

© Copyright 2006  
John Rhodes Thomas



**Investigation of Properties of Materials with Negative  
Permittivity and Permeability:  
Negative Refraction**

John Rhodes Thomas

A dissertation submitted in partial fulfillment of the  
requirements for the degree of  
Doctor of Philosophy

University of Washington

2006

Program Authorized to Offer Degree:  
Department of Electrical Engineering

UMI Number: 3224303

Copyright 2006 by  
Thomas, John Rhodes

All rights reserved.

### INFORMATION TO USERS

The quality of this reproduction is dependent upon the quality of the copy submitted. Broken or indistinct print, colored or poor quality illustrations and photographs, print bleed-through, substandard margins, and improper alignment can adversely affect reproduction.

In the unlikely event that the author did not send a complete manuscript and there are missing pages, these will be noted. Also, if unauthorized copyright material had to be removed, a note will indicate the deletion.

**UMI**<sup>®</sup>

---

UMI Microform 3224303

Copyright 2006 by ProQuest Information and Learning Company.

All rights reserved. This microform edition is protected against  
unauthorized copying under Title 17, United States Code.

ProQuest Information and Learning Company  
300 North Zeeb Road  
P.O. Box 1346  
Ann Arbor, MI 48106-1346

University of Washington  
Graduate School

This is to certify that I have examined this copy of a doctoral dissertation by

John Rhodes Thomas

and have found that it is complete and satisfactory in all respects,  
and that any and all revisions required by the final  
examining committee have been made.

Chair of the Supervisory Committee:

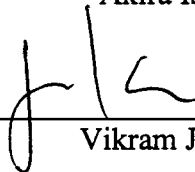


\_\_\_\_\_  
Akira Ishimaru

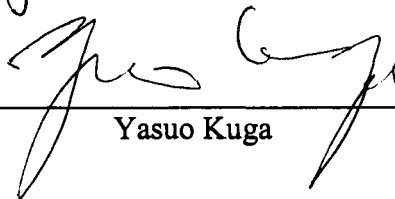
Reading Committee:



\_\_\_\_\_  
Akira Ishimaru



\_\_\_\_\_  
Vikram Jandhyala



\_\_\_\_\_  
Yasuo Kuga

Date: May 18, 2006

In presenting this dissertation in partial fulfillment of the requirements for the doctoral degree at the University of Washington, I agree that the Library shall make its copies freely available for inspection. I further agree that extensive copying of the dissertation is allowable only for scholarly purposes, consistent with "fair use" as prescribed in the U.S. Copyright Law. Requests for copying or reproduction of this dissertation may be referred to Proquest Information and Learning, 300 North Zeeb Road, Ann Arbor, MI 48106-1346, to whom the author has granted "the right to reproduce and sell (a) copies of the manuscript in microform and/or (b) printed copies of the manuscript made from microform."

Signature John R. Thomas

Date May 18, 2006

University of Washington

**Abstract**

**Investigation of Properties of Materials with Negative Permittivity and Permeability:  
Negative Refraction**

John Rhodes Thomas

Chair of the Supervisory Committee:  
Professor Emeritus Akira Ishimaru  
Department of Electrical Engineering

This thesis provides a study of electromagnetic wave properties of a uniform isotropic material with negative permittivity and permeability. No natural material has been found with this property, and none is expected. However, artificial materials made of periodic metallic structure have been shown to exhibit this behavior and have motivated much of this study. The acronym NIM for negative index medium is often used to denote such a metamaterial.

Chapter 2 provides interpretation of the meaning of permittivity and permeability in terms of measured values of reflection and transmission coefficients through a planar slab of an arbitrary homogeneous isotropic medium. Permittivity and permeability are frequency dependent. Consequently, this chapter and much of what follows are in the frequency domain.

Chapter 3 provides a comprehensive categorization of wave types at the boundary of a lossless normal dielectric with a half space of arbitrary permittivity and permeability in the low-loss limit. New wave types of backward surface waves and backward lateral waves are found for certain NIM combinations of permittivity and permeability.

Chapter 4 calculates the negative refraction expected at the interface with a NIM. The plane wave result given by Snell's law is shown to extend to a beam wave (a wave packet in the time domain) if the dominant beam wave frequencies are within a band in which the NIM is not too dispersive. Both an analytic approximate solution and numerical examples calculated from exact Fourier transform solutions are obtained.

Chapter 5 presents details of the phenomenon of negative index focusing by a planar NIM layer when the relative permittivity and permeability of the layer are both close to  $-1$ . Both an analytic approximation, based on expansions and asymptotics, and numerical results based on exact Fourier transform solutions are derived. Results of both approaches show good agreement in the appropriate parameter ranges.

Chapter 6 documents an approach to calculating reflection and transmission from a periodic layer of cylinders. This approach was not found to be useful for the challenge of calculating the properties of a metamaterial, nor in fact for any 3-dimensional structure.

# TABLE OF CONTENTS

List of Figures.....	iii
List of Tables.....	vii
1. Introduction .....	1
Notes to Chapter 1 .....	7
2. Issues in determining $\epsilon$ and $\mu$ from measured values of Reflection and Transmission.....	9
2.1. Meaning of an effective $\mu$ and $\epsilon$ and a gedanken experiment to measure them. ....	9
2.2. Some numerical examples.....	12
2.3. Sensitivity to small changes in R and T .....	20
2.4. Considerations concerning a metamaterial.....	24
2.5. Notes to Chapter 2 .....	26
3. Electromagnetic Waves over a Half Space of Arbitrary Permittivity and Permeability.....	27
3.1 Line Source over a semi-infinite metamaterial .....	29
3.2 Surface waves and lateral waves .....	30
3.3 Brewster's angle and Zenneck wave .....	35
3.4 Wave Types in $\epsilon'$ - $\mu'$ Diagram—Examples .....	39
3.5 Backward surface waves .....	47
3.6 Backward lateral wave and temporal wave packet.....	48
3.7 Notes to Chapter 3 .....	50
4. Negative refraction: Beam wave packet incident on NIM .....	51
4.1 Analytical formulation.....	52
4.2 Numerical solutions: Cases without a critical angle $\theta_c$ or with angle of incidence less than $\theta_c$ .....	60
4.3 Incidence beyond the critical angle: the backward lateral wave and Goos-Hanchen effect .....	68
4.4 Concluding remarks regarding negative refraction, BWLW, and negative Goos-Hanchen shift .....	75
4.5 Notes to Chapter 4 .....	77
5. Transmission and focusing by a planar slab with index close to $-1$ .....	78
5.1. Formulation of the analysis .....	81
5.2. Analytical approximations and limiting solutions.....	85
5.3. Approximations for transmitted $E_x$ in the space domain.....	93
5.4. Numerical calculation of $E_x$ fields and transverse focal widths .....	104
5.5. Z dependence of $E_x$ on axis and focal width in the propagation direction .	112
5.6. Variation of focal distance with $\text{Re}(n_2)$ .....	121
5.7. Focusing of the Poynting Vector and Energy Densities.....	125
5.8. Comparison to an alternate approach .....	141

5.9.	Summary and conclusions regarding focusing by a NIM slab .....	145
5.10.	Notes to Chapter 5 .....	147
6.	Lattice Sum Approach Combined with MoM to calculate scattering from a periodic layer of cylinders .....	148
6.1	Review of Yasumoto and Kushta's Approach .....	148
6.2	Calculation of T matrix from MoM calculation of scattered field .....	150
6.3	Calculations for a dielectric cylinder with $\epsilon_r$ not too large—some plotted results .....	153
6.4	Notes to Chapter 6 .....	162
7.	Conclusions and Implications for Future Work .....	163
	Notes to Chapter 7 .....	169
	Bibliography .....	170
	Appendix A: Derivation of Equation (2.7) .....	176
	Appendix B: Derivations for Section 5.3 .....	178
	To derive bounds on the integrand in (5.22) .....	178
	To show that $e(x)$ given by (5.25) is not greater than 1 in absolute value .....	180

## LIST OF FIGURES

Figure Number	Page
2.1 Solutions for $\mu_{2r}$ and $\varepsilon_{2r}$ for four material cases.....	14
2.2 Material of Case 1 with 8 physical solutions.....	15
2.3 Material of Case 2 with unique solution.....	16
2.4 Material of Case 3 with unique solution.....	17
2.5 Material of Case 4 with 8 physical solutions.....	18
2.6 Two solutions of $\mu_{2r}$ for measured values of $R$ , Case 1 .....	22
2.7 Two solutions of $\varepsilon_{2r}$ for measured values of $R$ , Case 1.....	23
3.1 Diagram of coordinate system for 2 media with line source.....	29
3.2 Regions in $\varepsilon' - \mu'$ plane to categorize poles and zeros of reflection .....	32
3.3 Regions in $\text{Real}(\varepsilon) - \text{Real}(\mu)$ plane by the sign of $\text{Im}(k_{z1})$ .....	34
3.4 (a) Regions of forward and backward surface wave (b) Regions of forward and backward lateral waves .....	35
3.5 Zenneck wave pole and Brewster's zero with relation to branch cuts .....	37
3.6 Propagation constant $k_{z1}$ at (a) Brewster's zero and (b) Zenneck wave pole .....	38
3.7 Complex S plane plot of pole or zero and branch cut to $n$ .....	39
3.8 Complex S plane plots of pole and branch cut for cases in Regions A and C of Figure 3.2 (b) .....	41
3.9 Complex S plane plots of pole and branch cut for cases in Regions A' and B' of Figure 3.2 (b) .....	42
3.10 Complex S plane plots of branch cut with zero or pole in proper Riemann surface for cases in regions c and of Figure 3.2 (b).....	44
3.11 Complex S plane plots of zero and branch cut for cases in Regions a' and b' of Figure 3.2 (b) .....	45
3.12 Regions for classification of asymptotic wave types .....	46

3.13	Backward surface wave diagram.....	47
3.14	Conventional forward lateral wave .....	48
3.15	Backward lateral wave (a) and wave packet (b).....	49
4.1	Wave packet incident on negative refractive index medium.....	54
4.2	Contour plots of $ \vec{H} $ for Lorentz model with $n_{2o} = -0.75 - 0.001j$ .....	63
4.3	Comparison of transmitted pulses for Lorentz vs linear variation .....	64
4.4	First step in the progression of a backward lateral wave.....	70
4.5	Second step in the progression of a backward lateral wave .....	71
4.6	Third (last) step in the progression of a backward lateral wave.....	72
4.7	Angle of the backward lateral wave .....	73
4.8	Goos Hanchen shift of reflected peaks .....	74
5.1	Illustration of geometric focusing .....	80
5.2	Transmission coefficient for propagating and evanescent parts of the spectrum through a $\frac{1}{2}$ -wavelength layer, p polarization .....	86
5.3	Comparison of the approximation formula and the complete formula for the transmission coefficient for cases in Figure 5.2(a) .....	88
5.4	Comparison of the approximation formula and the complete formula for the transmission coefficient for cases in Figure 5.2(b).....	89
5.5	Comparison of the approximation formula and the complete formula for the transmission coefficient for cases in Figure 5.2(c) .....	90
5.6	Spectrum of line source at focal plane through 2-wavelength layer .....	95
5.7	Asymptotic transverse field components for 2-wavelength layer .....	100
5.8	Asymptotic approximation for transverse focal width .....	104
5.9	Comparison of exact and asymptotic field in the focal plane for 2-wavelength layer.....	105
5.10	Focal tendency in and around focal plane for $E_x$ .....	106
5.11	Comparison of resonant spectral peaks for 1-wavelength layer.....	108
5.12	Transverse cut of $E_x$ in the focal plane for 1-wavelength layer .....	109

5.13	Transverse focal widths through layers of thickness 1 and 5 wavelengths and loss associated with permittivity.....	110
5.14	Transverse focal widths through layers of thickness 1 and 5 wavelengths and loss associated with permeability.....	111
5.15	Contour plot of $ E_x $ for a typical thin-slab case.....	113
5.16	$E_x$ in the theoretical focal plane for a $\frac{1}{2}$ -wavelength layer .....	114
5.17	Magnitude of $E_x$ on the Z axis for a $\frac{1}{2}$ -wavelength layer .....	114
5.18	Asymptotic low-spatial-frequency contribution to transmitted $E_x$ .....	117
5.19	Asymptotic high-spatial-frequency contribution to transmitted $E_x$ .....	118
5.20	Asymptotic calculation of $E_x$ evaluated on the Z axis .....	119
5.21	Numerical Fourier integral calculation of $E_x$ evaluated on the Z axis .....	120
5.22	Contour plot of $ E_x $ for a layer of thickness 5 wavelengths .....	121
5.23	Contour plot of $ E_x $ for same layer thickness, $n_2 \approx -0.98$ .....	122
5.24	Contour plot of $ E_x $ for same layer thickness, $n_2 \approx -1.02$ .....	123
5.25	Distance to peak and peak magnitude as a function of $n_2$ .....	124
5.26	Contour plot of Poynting vector magnitude for a 5-wavelength layer.....	127
5.27	Contour plot of $ E_x $ for same case as Figure 5.26 .....	127
5.28	Quiver plot of Poynting vector for same case as Figure 5.26 .....	129
5.29	Contour plot of magnitude of stored magnetic energy density, same case .	130
5.30	Contour plot of magnitude of stored electric energy density, same case ....	131
5.31	Contour plot of magnitude of total stored energy density, same case.....	132
5.32	Contour plot of real Poynting vector magnitude, thin slab .....	133
5.33	Contour plot of $ E_x $ , thin slab .....	134
5.34	Quiver plot of Poynting vector, thin slab .....	135
5.35	Contour plot of stored magnetic energy density, thin slab.....	136
5.36	Contour plot of stored electric energy density, thin slab.....	137
5.37	Contour plot of total stored energy density, thin slab .....	138

5.38	Magnitude of Fourier transform of focused field, comparison in a PIM-to-opposite-NIM case .....	142
5.39	Focused field component in the focal plane, comparison in a PIM-to-opposite-NIM case .....	143
5.40	Contour plot of $ E_x $ for comparison in a PIM-to-opposite-NIM case .....	144
6.1	MoM basis elements for cylinder cross section .....	154
6.2	Field scattered from a hollow dielectric pipe .....	156
6.3	Reflected and transmitted power fractions from lossless dielectric C-shaped cylinder .....	157
6.4	Details of reflected and transmitted power fractions from lossless C .....	158
6.5	Reflected and transmitted power from lossy dielectric C-shaped cylinder .....	159
6.6	Details of reflected and transmitted power fractions from lossy C .....	160

## LIST OF TABLES

Table Number	Page
Table 2.1 Four cases studied in four quadrants .....	13
Table 3.1 Wave types in the regions of Figure 3.2 (b) .....	40
Table 4.1 Progression of peaks in time .....	73
Table 5.1 Comparisons of exact and approximate locations of peak and magnitude of peak of $ T(k_x) $ .....	92
Table 5.2 Transverse widths of the focal peak in wavelengths .....	140
Table 5.3 Widths in the propagation direction .....	140

## Acknowledgements

Above all I would like to thank my advisor, Professor Akira Ishimaru, for so many aspects of my graduate work. First, he encouraged me to return to school in the Electrical Engineering Department. I enjoyed all the courses he taught including several that he taught for his last time before entering the emeritus ranks. His advice regarding which topics were worth investigating was invaluable and he always had helpful ideas when I had reached a difficult point in my research. He has been very kind in introducing me to many distinguished colleagues at meetings and I greatly enjoy what he has to report regarding the large number of meetings and conferences he attends. Also, Professor Ishimaru selected me to receive support from the National Science Foundation from grant ESC-9908849 and predecessor grants. I thank the National Science Foundation for this support.

Secondly I would like to thank my friend Sermsak Jaruwatanadilok who completed his Ph.D. three years ago and then, as a post-doc, was my office mate. Especially, he has helped me with so many issues concerning making computers work for me. There are several other graduate students who helped me in this aspect and I would like to acknowledge Junho Cha, Urachada “Dao” Ketprom, John Catton, and Sang Il Lee. Dao and Sang-II earned their doctorates and returned to their home lands.

All of the professors with whom I have had any significant interaction in the Department have been welcoming and helpful. In this regard I would like to mention three members of my committee from whom I also took very interesting courses: Professor Yasuo Kuga, Professor Leung Tsang, and Professor Vikram Jandhyala. Professor Kuga helped with much advice and found good computers for me to use so I might call him my second advisor.

I also thank many staff members. Noel Henry, our Program Manager for Electromagnetics, Optics and Acoustics, has been exceedingly helpful and has provided great insight into the workings of this University and our Department. I have enjoyed Stephen Graham's help with many departmental items over all my years here. Frankye Jones has been very helpful in setting forth requirements, as were the previous graduate advisors. Angel Bailey worked very hard to bring together computer audio-visual equipment for my General Examination.

Finally, I would like to acknowledge the continued encouragement from my daughter, Joanna Elizabeth Thomas-Osip. She started her Ph.D. research at the University of Florida a couple of years before I reached that stage here at the University of Washington. For a short while I was trying to catch up with her. She completed her Ph.D. in 2001 despite the significant obstacle of having to finish her work while living in Massachusetts. She gave me a book entitled "Writing Your Dissertation in 15 Minutes a Day." I hope I did not carry that too far.

## DEDICATION

To my mother and father:

Helen Harvey Rhodes Thomas, 1908-1979, B.A., *magna cum laude*, U.W., 1929  
Roscoe Gillespie Thomas, 1902-1986, B.A., U.W., 1925.

*Requiescant in pace.*

And to our *alma mater*

The University of Washington. *Lux sit.*

## 1. Introduction

This research started out to investigate the properties of what has been called photonic crystals (Joannopoulos, Meade *et al* 1995); that is, to understand the properties of a periodic structure of dielectric elements. As an approach to this problem, we made some preliminary calculations for a planar array of infinite conductive strips with the help of Floquet's theorem and MoM methods. Two papers (Yasumoto & Kushta 2000), (Yasumoto & Yoshitomi 1999), each with Professor Yasumoto of Kyushu University as one of two authors, presented an interesting idea for calculating the scattering from a layer of infinitely long cylinders (not just circular cylinders, but the more general definition of a cylinder). Their calculations were based on types of cylinders for which Yasumoto and his associates could calculate analytically the T-matrix for scattering off of an individual cylinder. This is a 2-dimensional theory, but we had hopes that the concept of separating the problem into one part that characterized the scattering from an individual object in the array and a second part that involved only the lattice geometry could be generalized to a 3-D problem. However, neither we nor others have been able to find a 3-D generalization of this separation. Hence, this approach does not appear helpful for 3-D cases. Chapter 6 presents a summary of our approach and results for a dielectric case.

At about this point in our studies, John B. Pendry published a paper (Pendry 2000) on the (somewhat amazing) possibility of obtaining perfect focusing from a layer of material with relative permittivity  $\epsilon_r$  and relative permeability  $\mu_r$ , both equal to  $-1$ . At about the same time, an experimental group that works with Pendry published results (Smith, Padilla *et al* 2000) of an experiment on arrays of slit rings and short wires. They showed it is possible to create a periodic structure of conducting elements (a metamaterial) that behaves as though it had both  $\epsilon_r$  and  $\mu_r$  negative over

a small band of frequencies. These two papers created a “torrent” of interest, and a new “hot topic” was established. Developments in (Pendry 2000) and (Thomas & Ishimaru 2002) were an outgrowth from the work of (Pendry, Holden *et al* 1999) that showed how an artificial material such as an array of metallic coiled sheets or split rings could resonate with the electric and magnetic fields to produce a material with negative effective permeability over a limited band of frequencies. All of the recent work on material with both  $\epsilon_r$  and  $\mu_r$  negative to some extent evolves from an almost overlooked paper by the Russian physicist Veselago (Veselago 1968).

In recent years there has been an increasing interest in development of new materials whose characteristics may not be found in nature (Veselago 1968) (Pendry, Holden *et al* 1999) (Smith, Padilla *et al* 2000) (Pendry 2000) (Ziolkowski & Heyman 2001) (Ishimaru, Lee *et al* 2003) (Ishimaru, Jaruwatanadilok *et al* 2005). Examples are metamaterials, in particular negative index materials (NIM), chiral media, photonic (PBG) or electromagnetic (EBG) band gap materials, and composite materials. A broad range of applications has been suggested including artificial dielectrics, lenses (Greegor, Parazzoli *et al* 2005, Parazzoli, Greegor *et al* 2003, Parazzoli, Greegor *et al* 2004), absorbers, antenna structures optical and microwave components, sensors and frequency selective surfaces.

Related work has become the main topic of my research. Chapters 3 through 5 concern what would be the properties of an ideal uniform isotropic material with negative  $\epsilon_r$  and  $\mu_r$ , with some consideration of cases with arbitrary  $\epsilon_r$  and  $\mu_r$ .

We verified that Pendry’s mathematical limit for transmission through a layer in which both  $\epsilon_r$  and  $\mu_r$  approach  $-1$  is correct. This limit predicts a plane of perfect focusing when the sum of the distance from the source to the incident side plus the distance from the exit side to the image is equal to the slab thickness. We wondered

just how such focusing occurs in the sense of how the limit was approached as losses and other deviations from  $-1$  were taken into account. As a quick overview, one can state that the limit of both  $\epsilon_r$  and  $\mu_r$  equal to  $-1$  is a highly singular point for the reflection and transmission coefficients. Of course,  $\epsilon_r$  and  $\mu_r$  both equal to  $+1$  is the vacuum state, and all physical problems can approach this limit in a smooth and well-known fashion as the density of the medium approaches zero.

Negative  $\epsilon_r$  and  $\mu_r$  is a very different situation. Chapters 3 and 4 examine the behavior of electromagnetic waves at the plane boundary between a half space of free space (vacuum) and a half space of idealized metamaterial with both  $\epsilon_r$  and  $\mu_r$  negative. Such a metamaterial has been called double negative (acronym DNG), (Ziolkowski & Engheta 2003) (Ziolkowski & Heyman 2001), negative index material (NIM), (Valanju, Walser *et al* 2002) and originally by (Veselago 1968) a left-handed medium (LHM). The latter term was chosen because the triad of vectors,  $(\vec{E}, \vec{H}, \vec{k})$  which is right handed in ordinary material, becomes left handed in a NIM. Although many authors, especially the physicists, continue to use the term LHM, we do not prefer this because it may be confused with left handed chiral media.

A DNG material must be a NIM. This fact is a fundamental point in establishing the existence of negative refraction. Chapter 3 will present a short proof based on the requirements of a passive material. Chapter 3 includes many portions of our paper (Ishimaru, Thomas *et al* 2005). In this chapter the source is taken in a free space or lossless region. The solution consists of a reflected wave in this source region and a transmitted wave in the other region, which is taken to have arbitrary  $\epsilon_r$  and  $\mu_r$ . Incident waves are taken as plane waves or the Fourier superposition of plane waves to create a 2-D line source. The types of reflected and transmitted waves are

classified. Backward surface waves and backward lateral waves are derived and discussed.

Chapter 4 provides details of negative refraction at the boundary of a half space of negative index material. This chapter investigates the transmission of a beam wave (a packet) into the NIM and shows that the beam is refracted negatively according to Snell's law, but its shape and orientation change and it propagates at a group velocity given by the known formula. We derive an analytic asymptotic expression that shows negative refraction and we present numerical calculations of exact solutions that verify the asymptotic theory. From calculations for cases with incidence beyond the critical angle we find phenomena identified as backward lateral waves and a negative Goos-Hänchen shift. This chapter is based on our paper "Wave Packet Incident on Negative-Index Media" (Thomas & Ishimaru 2005)

Chapter 5 gives detailed calculations of the transmission and focusing through a half-wavelength-thick layer of material with  $\epsilon_r$  and  $\mu_r$  both close to  $-1$ . We consider pure real deviations, pure imaginary deviations, and complex deviations. Some properties (such as a sharp peak in the transmission coefficient) varied considerably, but the basic limitation on focusing can be expressed by equations (5.30), (5.31) and (5.35) as described in Chapter 5. We show that focusing in the transverse direction has subwavelength size limited by the deviations of  $\epsilon_r$  and  $\mu_r$  from  $-1$ . But the focusing in the propagation direction is not subwavelength in size. The work described in Chapter 5 has been presented in three papers. One (Thomas & Ishimaru 2002) has an 8-page written version published in the SPIE Proceedings of that conference. The second is an oral paper (Ishimaru & Thomas 2002) and the third and most detailed is our paper "Evaluation of Focal Spot Widths for a Planar Slab with

Negative Index close to  $-1$ ” submitted to the Transactions of the Antennas and Propagation Society.

Chapter 2 provides a description of a method to determine the dielectric constant of a planar layer. In a sense, it provides a bridge between measured properties of a metamaterial or properties that may be calculated with methods discussed in Chapter 6 and the idealized DNG  $\epsilon_r$  and  $\mu_r$  of Chapters 3 and 4. The main purpose is to consider what the effective dielectric constant of a metamaterial would be when that interpretation must be made in terms of measurements of the waves scattered off a layer of the metamaterial. Chapter 2 shows that measurements of R and T at two angles of incidence almost uniquely determine the values of  $\epsilon_r$  and  $\mu_r$ . Presumably an additional measurement (at another angle, or possibly a very nearby frequency) would resolve the ambiguity.

Chapter 6 presents some of our first work based on the approach of Yasumoto et al. These calculations demonstrate an interesting technique, but we did not find a useful way to apply them to determine properties of metamaterials that are candidate NIM. Recently (Jia & Yasumoto 2004) published a paper on the scattering from a single periodic 2-D layer of metallic cylinders. They used a somewhat similar method where they apply Floquet’s theorem to the periodic structure and use standard boundary conditions just above and below the layer. The layer is divided into a finite number of periodic sublayers. Reflection and transmission coefficients are derived for each sublayer by treating the fields in the regions between rectangular metallic rods as composed of waveguide modes. Then, the overall reflection and transmission coefficients of the layer are calculated by recursion. The results are rearranged as double sums over the P rectangular metal objects in the periodic structure and an infinite inner sum that (Jia & Yasumoto 2004) find to be rapidly convergent for the

cases of circular cylinders sliced into 30 layers and an inner and outer rectangular double C that may be regarded as an approximation to the split ring structures to be discussed later. As our Chapter 2 shows, the R and T of this layer may be used to determine the epsilon and mu and they find a behavior of T with frequency characteristic of a negative index material.

We also summarize some of the other approaches to finding metamaterial structures with DNG property.

Chapter 7 summarizes what we conclude from our research so far and proposes several studies to clarify questions that have been raised by this completed work.

## ***Notes to Chapter 1***

- Greegor RB, Parazzoli CG, Nielsen JA, Thompson MA, Tanielian MH, Smith DR. 2005. Simulation and testing of a graded negative index of refraction lens. *Applied Physics Letters* 87: -
- Ishimaru A, Jaruwatanadilok S, Kuga Y. 2005. *Generalized surface plasmon resonance sensors using metamaterials and negative index materials*. Presented at Progress in Electromagnetics Research Symposium (PIERS)
- Ishimaru A, Lee SW, Kuga Y, Jandhyala V. 2003. Generalized constitutive relations for metamaterials based on the quasi-static Lorentz theory. *IEEE Transactions on Antennas and Propagation* 51: 2550-7
- Ishimaru A, Thomas JR. 2002. Transmission and focusing properties of a slab of negative refractive index. In *IEEE AP-S/URSI Symposium*. Dallas, Texas
- Ishimaru A, Thomas JR, Jaruwatanadilok S. 2005. Electromagnetic waves over half-space metamaterials of arbitrary permittivity and permeability. *IEEE Transactions on Antennas and Propagation* 53: 915-21
- Jia H, Yasumoto K. 2004. S-Matrix Solution of Electromagnetic Scattering from Periodic Arrays of Metallic Cylinders with Arbitrary Cross Section. *IEEE Antennas and Wireless Propagation Letters* 3: 41-4
- Joannopoulos JD, Meade RD, Winn JN. 1995. *Photonic Crystals*. Princeton, New Jersey: Princeton University Press. 137 pp.
- Parazzoli CG, Greegor RB, Li K, Koltzenbah BEC, Tanielian M. 2003. Experimental verification and simulation of negative index of refraction using Snell's law. *Physical Review Letters* 90: -
- Parazzoli CG, Greegor RB, Nielsen JA, Thompson MA, Li K, et al. 2004. Performance of a negative index of refraction lens. *Applied Physics Letters* 84: 3232-4
- Pendry JB. 2000. Negative refraction makes a perfect lens. *Physical Review Letters* 85: 3966-9
- Pendry JB, Holden AJ, Robbins DJ, Stewart WJ. 1999. Magnetism from conductors and enhanced nonlinear phenomena. *IEEE Transactions on Microwave Theory and Techniques* 47: 2075-84

- Smith DR, Padilla WJ, Vier DC, Nemat-Nasser SC, Schultz S. 2000. Composite medium with simultaneously negative permeability and permittivity. *Physical Review Letters* 84: 4184-7
- Thomas JR, Ishimaru A. 2002. *Transmission properties of material with relative permittivity and permeability close to -1*. Presented at Complex Mediums III: Beyond Linear Isotropic Dielectrics, Seattle, WA, United States
- Thomas JR, Ishimaru A. 2005. Wave packet incident on negative-index media. *IEEE Transactions on Antennas and Propagation* 53: 1591-9
- Valanju PM, Walser RM, Valanju AP. 2002. Wave refraction in negative-index media: Always positive and very inhomogeneous. *Physical Review Letters* 88: 187401
- Veselago VG. 1968. The electrodynamics of substances with simultaneously negative values of  $\epsilon$  and  $\mu$ . *Soviet Physics USPEKHI* 10: 509-14
- Yasumoto K, Kushta T. 2000. Efficient Analysis of Scattering by Periodic Arrays of Gyrotropic Cylinders. *Electromagnetic Waves & Electronic Systems* 5: 66-74
- Yasumoto K, Yoshitomi K. 1999. Efficient calculation of lattice sums for free-space periodic Green's function. *IEEE Transactions on Antennas and Propagation* 47: 1050-5
- Ziolkowski RW, Engheta N. 2003. Metamaterial special issue introduction. *IEEE Transactions on Antennas and Propagation* 51: 2546-9
- Ziolkowski RW, Heyman E. 2001. Wave propagation in media having negative permittivity and permeability. *Physical Review E* 64: 056625-1--15

## 2. Issues in determining $\varepsilon$ and $\mu$ from measured values of Reflection and Transmission

### 2.1 Meaning of an effective $\mu$ and $\varepsilon$ and a gedanken experiment to measure them.

For an ordinary uniform homogeneous substance, permittivity  $\varepsilon$  and permeability  $\mu$  can be defined in the basic cavity definitions on a fine scale, or measured by various experiments. There are well-known equations (Ishimaru 1991) pp. 43-45 (Chew 1990) pp. 49-53, that give the reflection coefficient  $R$  and transmission coefficient  $T$  from a planar layer of thickness  $d$  of this material. For an incident plane wave, these equations can be written in the following form:

$$R = \frac{j \left( \frac{Z_2}{Z_1} - \frac{Z_1}{Z_2} \right) \tan(k_{z_2} d)}{2 + j \left( \frac{Z_2}{Z_1} + \frac{Z_1}{Z_2} \right) \tan(k_{z_2} d)} \quad (2.1)$$

and

$$T = \frac{2}{2 \cos(k_{z_2} d) + j \left( \frac{Z_2}{Z_1} + \frac{Z_1}{Z_2} \right) \sin(k_{z_2} d)} = \frac{2 \sec(k_{z_2} d)}{2 + j \left( \frac{Z_2}{Z_1} + \frac{Z_1}{Z_2} \right) \tan(k_{z_2} d)} \quad (2.2)$$

where  $Z_2$  and  $Z_1$  are the wave impedances of medium 1 (free space for this example) and a general medium 2. For a plane wave of p-polarization (that is the electric field direction is in the plane of incidence) the wave impedance in medium 2 propagating at an angle  $\theta$  with respect to the  $Z$  axis (axis normal to the interface) is defined as  $Z_2 = k_{z_2} / (\omega \varepsilon_2)$ , and the same for medium 1 by change of subscripts from 2 to 1. However, we will choose material 1 as free space, so its permittivity is  $\varepsilon_0$  and permeability is  $\mu_0$ . In this definition  $\omega$  is the angular frequency of the plane wave

and  $k_z$  is the component of the propagation constant in the Z direction. Specifically in medium 2

$$k_{z2} = k_o \sqrt{\epsilon_{2r} \mu_{2r}} \cos \theta_2$$

with  $k_o = \omega / c$  and  $c$  being the speed of light in free space. The quantity  $n_2 = \sqrt{\epsilon_{2r} \mu_{2r}}$  is defined as the index of refraction, the ratio of the speed of phase propagation in medium 2 to that in free space. We have to choose the square root such that its imaginary part is negative (in our engineer's convention of time dependence proportional to  $\exp(j\omega t)$ ) to correspond to a passive medium. Further, to be explicit, the relative permittivity and permeability are defined as

$$\epsilon_{2r} = \epsilon_2 / \epsilon_o \quad \text{and} \quad \mu_{2r} = \mu_2 / \mu_o.$$

To complete the formulation, we need Snell's law to relate  $\theta_2$  to  $\theta_1$ . That is

$$n_2 \sin \theta_2 = n_1 \sin \theta_1 = \sin \theta_1.$$

With these equations it is well known that, given the parameters of the incident wave (polarization, frequency  $\omega$ , and incident angle  $\theta_1$ ) and the parameters of the layer (thickness  $d$  and constants  $\epsilon_2$  and  $\mu_2$ ), then R and T are determined.

However, the question of whether a measurement of  $R$  and  $T$  determines  $\epsilon_2$  and  $\mu_2$  is not so simple. There are indeed two equations in two unknowns, and in many ordinary cases equations (2.1) and (2.2) can be used in an inverse fashion. There is an explicit inverse set of equations, which are rather tricky to derive. First, one can see that there are really two variable combinations in equations (2.1) and (2.2) that depend on  $\epsilon_2$  and  $\mu_2$ . I shall call them  $g$  and  $\psi$ , where

$$g = \frac{Z_2}{Z_1} = \frac{\sqrt{n_2^2 - \sin^2 \theta_1}}{\epsilon_{2r} \cos \theta_1} \quad (2.3)$$

$$\psi = k_{z2} d = k_o d \sqrt{n_2^2 - \sin^2 \theta_1} \quad (2.4)$$

If we can solve for  $g$  and  $\psi$ , then easily we find

$$\varepsilon_{2r} = \frac{\psi}{g(k_0 d \cos \theta_1)} \quad (2.5)$$

and

$$\mu_{2r} = g^2 \cos^2 \theta_1 \varepsilon_{2r} + \sin^2 \theta_1 / \varepsilon_{2r} \quad (2.6)$$

I found by algebraic trial and various rearrangements that equations (2.1) and (2.2) yield one equation in which  $\psi$  has been eliminated in the form

$$g^2 = \frac{1 + R^2 - T^2 + 2R}{1 + R^2 - T^2 - 2R} \quad (2.7)$$

To show that (2.7) is correct is rather lengthy (Appendix A). This form has a typical ambiguity in determining  $g$  in that the square root has two values. It seems to be necessary in general to consider the consequences of both choices. There is a higher multi-valued function that then determines  $\psi$ . Substitution of a solution of (2.7) for  $g$  back into equation (2.1) yields

$$\tan \psi = \frac{2jR}{R(g + 1/g) - (g - 1/g)} \quad (2.8)$$

Equation (2.8) will yield a countable infinity of values for  $\psi$ , which differ by integer multiples of  $\pi$ . Numerically, I compute a sequence of these values for both solutions for  $g$ . Each one of these  $(g, \psi)$  solutions then yields a unique  $(\varepsilon_{2r}, \mu_{2r})$  pair. At this point I apply the requirement of a passive material in which the imaginary part of  $\varepsilon_{2r}$  and  $\mu_{2r}$  must be negative. In cases of layers that are only the order of a wavelength thick, I found that there are then only a relatively small number of solutions.

Furthermore, as the integer multiples of  $\pi$  deviate by larger and larger quantities from the allowed set, the imaginary parts of one or the other of  $\varepsilon_{2r}$  and  $\mu_{2r}$  will trend off in a positive direction.

## 2.2 *Some numerical examples*

The first point of these numerical examples is to show that, for a homogeneous uniform material with some values for  $\varepsilon_{2r}$  and  $\mu_{2r}$ , if one can then measure  $R$  and  $T$  with sufficient accuracy, the values of  $\varepsilon_{2r}$  and  $\mu_{2r}$  can be determined from equations (2.5) through (2.8). The solution would seem to be unique for a thin layer, but multi-valued for a thick layer. There are various practical problems with this experiment. For example, a thin layer of some materials may create very small reflection and thus make accurate measurements difficult.

To study these issues from a numerical viewpoint, I created small MATLAB programs to calculate:

- (1)  $R$  and  $T$  for given values of  $\varepsilon_{2r}$ ,  $\mu_{2r}$ , thickness in wavelengths (or equivalently  $k_0d$ ), and angle of incidence,  $\theta_i$ . This function program is

`RflTransGenMultIn(mu2rel,ep2rel,kod,thetainc).`

- (2) Another one to evaluate equations (2.7) and (2.8) and then plug into (2.5) and (2.6) to give multiple values of  $\varepsilon_{2r}$  and  $\mu_{2r}$  for selected values of  $R$  and  $T$ . This function program is

`EffConstsMultiPM(Rm,Tm,kod,thinc,Nt).`

The input variable  $N_t$  specifies the multiplicity of solutions examined. Specifically, there is an equation for the arc tangent of the right-hand side of equation (2.8). MATLAB produces a principal value with real part  $x$  between  $-\pi/2$  and  $\pi/2$ . This `EffConsts` program then generates internal values  $\{x - N_t * \pi, x - (N_t - 1) * \pi, \dots, x, \dots, x + N_t * \pi\}$ . It calculates a solution for each one of these. That is, it calculates  $2 * N_t + 1$  solutions for each square root involved in equation (2.7). Thus, the second program produces  $4 * N_t + 2$  solutions.

As a simple test we studied the cases shown in Table 2.1. We deliberately chose to include the double negative case and all combinations of positive with negative in the real part.

**Table 2.1** Four cases in four quadrants of  $\text{Re}(\varepsilon)$  vs.  $\text{Re}(\mu)$

Parameter	Case #1	Case #2	Case #3	Case #4
$\varepsilon_{2r}$	2-0.1j	2-0.1j	-2-0.1j	-2-0.1j
$\mu_{2r}$	3-0.2j	-3-0.2j	3-0.2j	-3-0.2j

We started at  $N_t = 5$  with a  $1/8^{\text{th}}$  wavelength thickness and normal incidence. Some results of the calculations are displayed in Figures 2.1 through 2.5. Figure 2.1 shows 11 solutions for all four cases. The other 11 solutions corresponding to the negative-real-part square root of equation (2.7) did not yield any solutions that had physical (passive) values of  $\varepsilon_{2r}$  and  $\mu_{2r}$ . The dots in each figure are solution values corresponding to the value  $n$  between  $-N_t$  and  $N_t$ , given along the abscissa. Physical solutions (looking across any row of figures) occur when for a given value  $n$  of  $N_t$ , both the  $\text{Imag}(\varepsilon_{2r})$  and  $\text{Imag}(\mu_{2r})$  are negative. Also I have plotted a horizontal line at the value for which the  $R$  and  $T$  were calculated as input to the EffConsts program. In all of these cases the line does intersect some point and thus that point represents the recovered Case parameter.

One important feature of Figure 2.1 is that the values of  $\text{Imag}(\mu_{2r})$  follow a slope of opposite sign compared to the values of  $\text{Imag}(\varepsilon_{2r})$ . Hence, there must be at most a finite number of physical solutions. If we go far enough to the left, the one with a negative slope must have positive values of imaginary part, and then when we go far enough to the right, the other one will have positive imaginary part. From the first row (first Case, this is a more or less normal magnetic and dielectric material) of Figure 2.1, we see that  $\text{Imag}(\mu_{2r})$  becomes negative for values of  $n \geq -3$  and  $\text{Imag}(\varepsilon_{2r})$  is negative for  $n \leq 4$ .

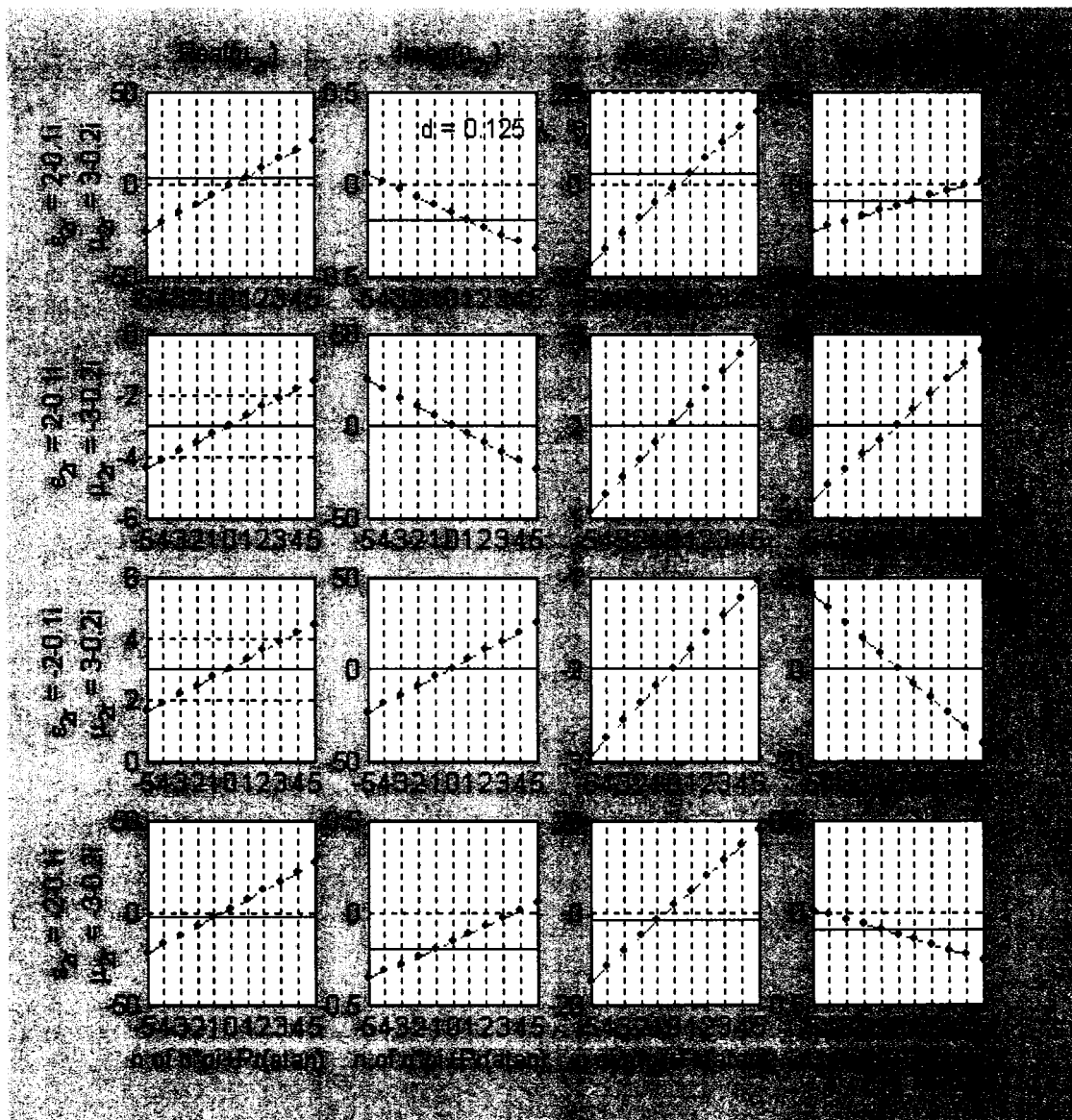


**Figure 2.1** Solutions for  $\mu_{2r}$  and  $\epsilon_{2r}$  for four material cases (referred to in the text as Cases 1 through 4) with a  $1/8^{\text{th}}$  wave layer. That is,  $R$  and  $T$  corresponding to the specified  $\epsilon_{2r}$  and  $\mu_{2r}$  are calculated. The inverse formula gives the plotted dot solutions for the limited range of  $n$  (from  $-5$  to  $5$ ), chosen arbitrarily. This range was found to be sufficient to show all the possible physical (passive) solutions for these cases. The physical solutions require that both the  $\text{Imag}(\mu_{2r})$  and  $\text{Imag}(\epsilon_{2r})$  be negative for a given  $n$ . Careful examination of rows 1 and 4 show that there are 8 solutions for Cases 1 and 4, whereas rows 2 and 3 show that there is a unique solution (the  $n = 0$  solution) for Cases 2 and 3.

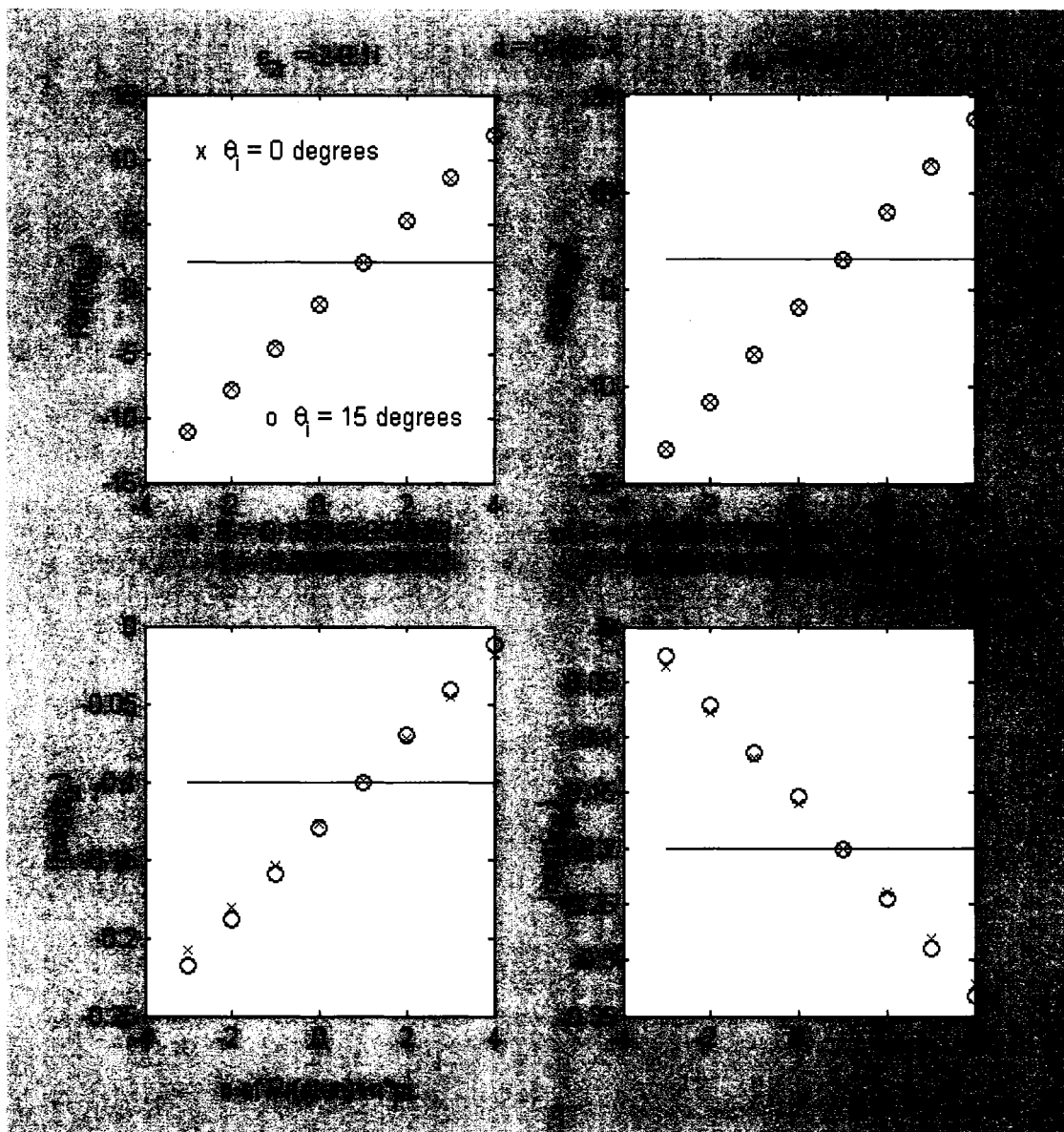


**Figure 2.2** Material of Case 1. There are 8 physical solutions for  $\epsilon$  and  $\mu$  at either normal (0 degrees) or 15 degrees for angle of incidence given accurate values of  $R$  and  $T$ . The horizontal line is at the constant of the original material. The imaginary parts agree only for one value of  $n$  ( $n = 1$ ). Thus, we have a proposed method for recovering the original values.

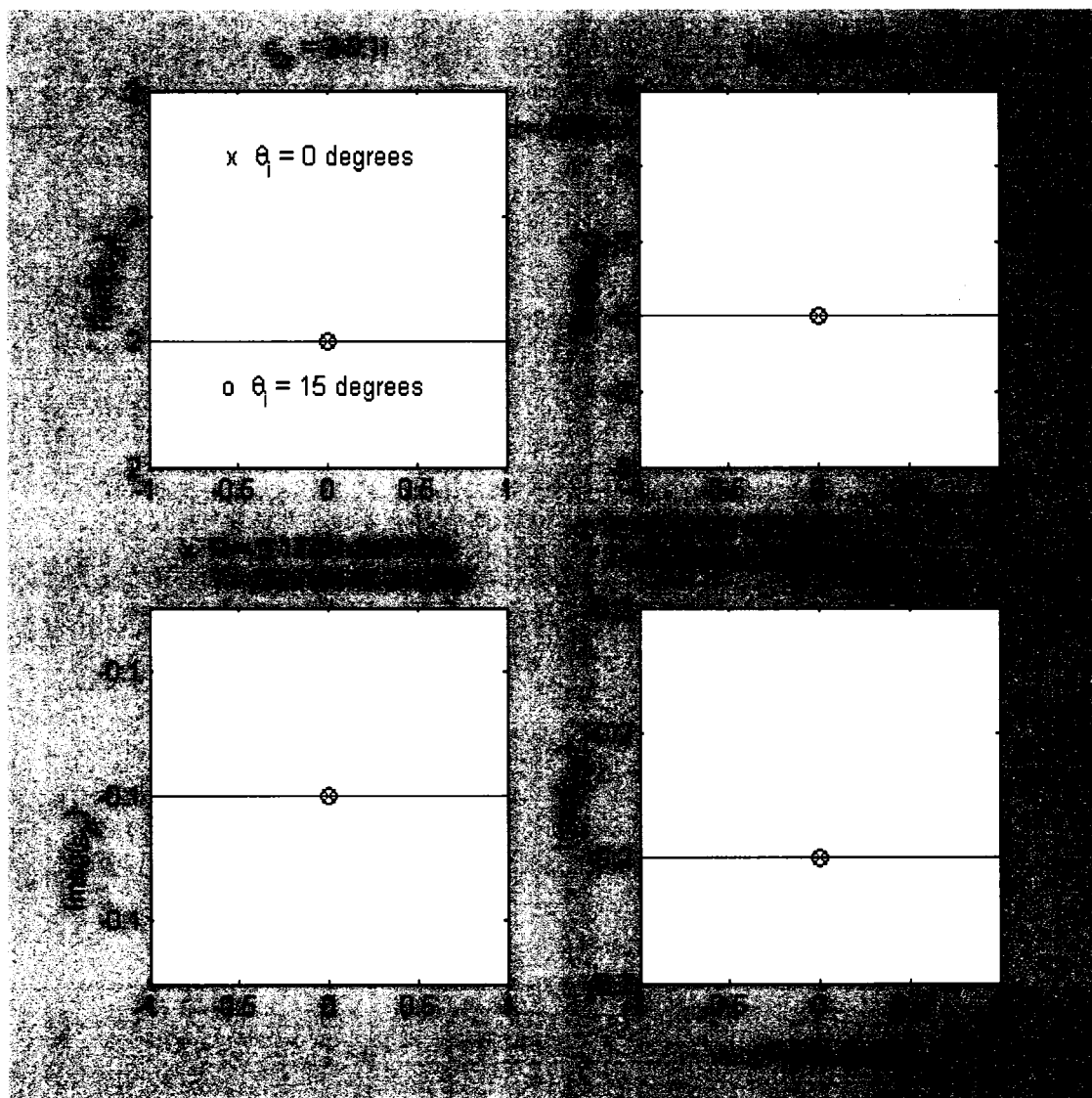


**Figure 2.3** Material of Case 2. There is exactly one solution at normal or 15 degrees angle of incidence given accurate values of  $R$  and  $T$ . The solution is for  $n = 0$ . It does occur at the original material constants indicated by the horizontal lines.

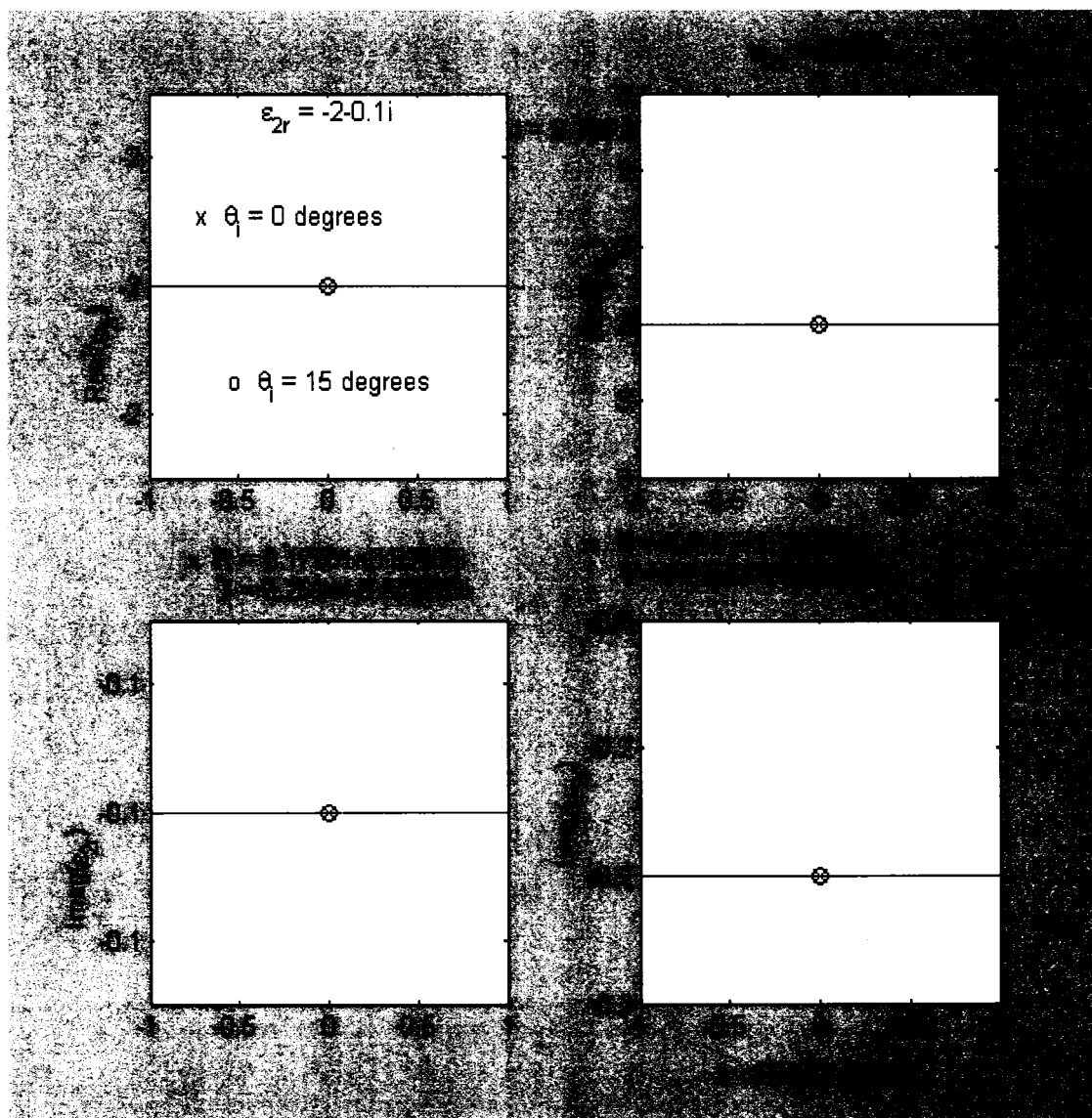


**Figure 2.4** Material of Case 3. There is exactly one solution at normal or 15 degrees angle of incidence given accurate values of  $R$  and  $T$ . The solution is for  $n = 0$ . It does occur at the original material constants indicated by the horizontal lines. This is symmetric to Case 2 because changing the sign of the real parts of both  $\varepsilon$  and  $\mu$  corresponds to the complex conjugates of  $R$  and  $T$ .

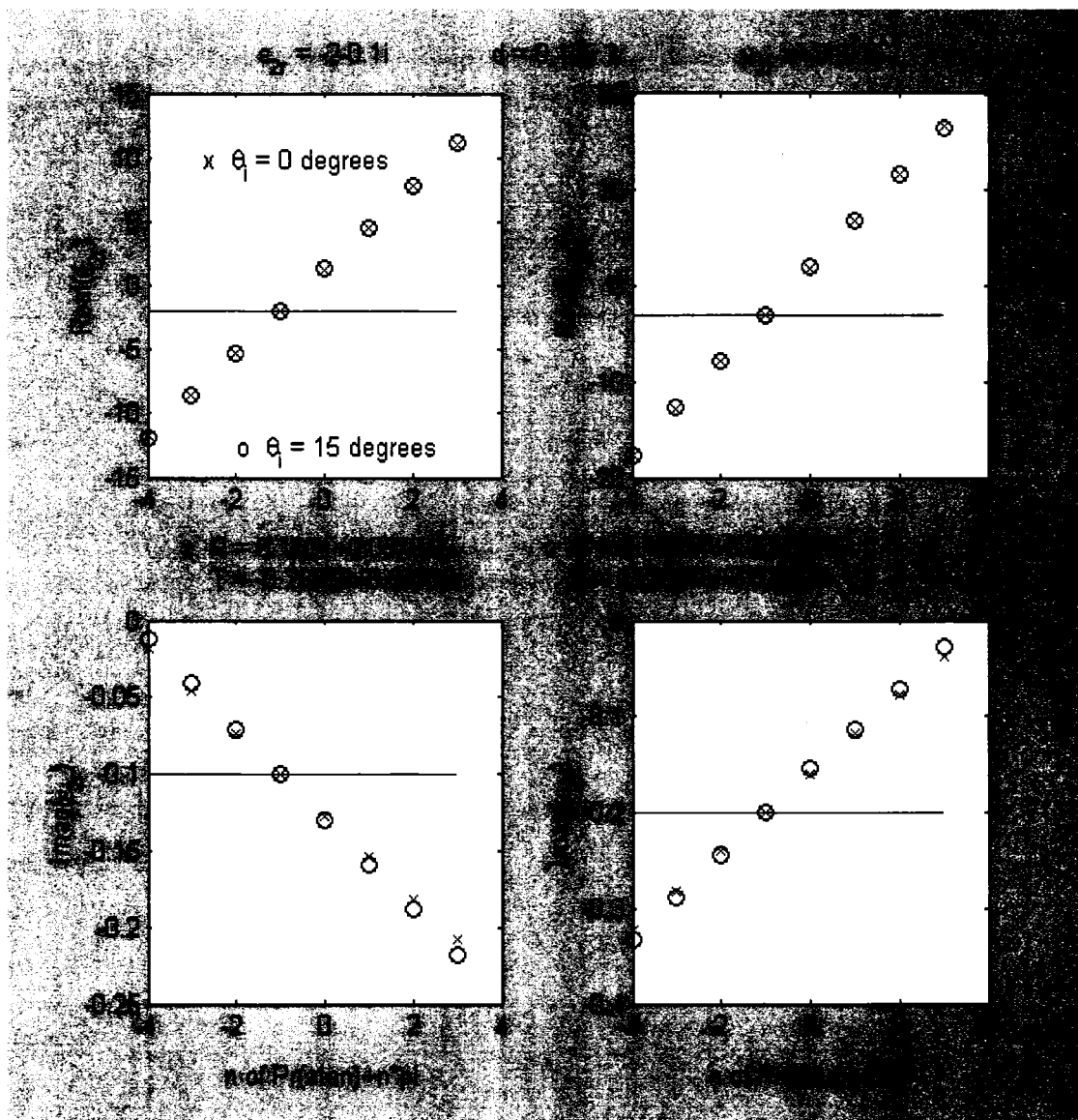


**Figure 2.5** Material of Case 4. This is symmetric to Case 1. There are 8 physical solutions for  $\varepsilon$  and  $\mu$  at either normal (0 degrees) or 15 degrees for angle of incidence given accurate values of  $R$  and  $T$ . The horizontal line is at the constant of the original material. The imaginary parts agree only for one value of  $n$  ( $n = -1$ ). Thus, we have a proposed method for recovering the original values.

Hence, there are 8 passive-material solutions (corresponding to the integers  $-3$  through  $+4$  inclusive). The one corresponding to  $n = 1$  recovers the original material. This is quite reasonable because for an index of refraction equal to  $\sqrt{2 \cdot 3} = 2.449$ , one probably would expect, through a  $1/8^{\text{th}}$  wavelength layer, a phase shift in the right-hand side of equation (2.8) that exceeds  $\pi/2$ .

Figures 2.2 through 2.5 show more details for these same four cases, with Figure 2.2 applying to Case 1, Figure 2.3 to Case 2, and so on. On each subfigure, only the physical (passive) cases are plotted. But the same set of calculations was redone for an incident angle of 15 degrees. The points plotted with an  $x$  correspond to the results of our gedanken experiment at normal incidence, and the points with an  $o$  to the experiment at 15 degrees. We note that the real parts do not appear to change, but the imaginary parts have increased slope magnitude as the angle of incidence goes off normal. Thus, we could use this as a method to select the correct (original) material constants as being the point where both experiments yield the same values.

There are a couple of other results that may be noted from these graphs. First, the change from Case 1 to Case 4 or the change from Case 2 to Case 3 leads to  $R$  and  $T$  changing as complex conjugates; that is, by the changing of the imaginary parts of  $R$  and  $T$ . Note that the interchange of Case 1 to Case 4 or Case 2 to Case 3 corresponds to changing the signs of the real parts of both  $\varepsilon$  and  $\mu$ . This is an interesting general property and should be true for the inverse calculation. Secondly, as the angle of incidence increases from 0 to 15 degrees, the real part of the reflection coefficient increases and the real part of the transmission coefficient decreases for all the cases. This result is well known for the normal Case 1, but it is interesting to see that it holds for all these different cases.

### 2.3 *Sensitivity to small changes in $R$ and $T$*

Unfortunately, the method proposed above of finding a unique solution for  $\varepsilon$  and  $\mu$  is not very stable numerically. It is quite sensitive to small changes in the (thought-experimental) values of  $R$  and  $T$ . Also, Figures 2.2 through 2.5 show cases in which the number of physical solutions is the same for both normal incidence and incidence at an angle of 15 degrees ( $\pi/12$ ). In more difficult cases (Thicker layers and more oblique incidence yield more phase shift.) to find the solution in which the imaginary parts of the calculated  $\varepsilon$  and  $\mu$  are the same requires comparison between sets of values of different length. This complicates the calculation. I developed a program (TestSensitivmueps) that works for cases that I have tried. The test runs have been done for the four cases of Table 2.1. As input, I calculated exact  $R$  and  $T$ , then approximated  $R$  by rounding up and down at 4 significant figures, and interpolating linearly with 100 values. Thus, these inaccurate values are not very inaccurate, but since the real part and imaginary part are generally not the same distance from the round-up and the round-down, these sets of values do not include the exact value. These calculations and roundings are done for both zero (normal) and 15-degree angles of incidence. Hence, the inverse solutions for the zero case will not be exactly the same as for the 15-degree case. Furthermore, there are now two different solutions, one obtained by finding the minimum difference between the imaginary parts of  $\mu$  (i.e., difference between the zero case and the 15-degree case) and one by finding the minimum difference between imaginary parts of  $\varepsilon$ . I called the former solution, solution a and the latter solution b.

In general, if we were trying to determine the solution for an unknown material, both would be acceptable and we would presumably need to make measurements at additional angles or perhaps at other nearby frequencies to resolve

the ambiguity. However, since in this case I am trying to recover values that are close to a known value, I found that solution b was much closer than solution a for cases 1 and 4 of Table 2.1. The solutions for case 1 are shown in Figure 2.6 and Figure 2.7. We can see from Figure 2.6 that solution b for the imaginary part of  $\mu$  is within about 2% of the starting value even though the differences in the rounded  $R$  are of the order of 0.01%. The real part of  $\mu$  for this approximate  $R$  is within about 1.5% of the starting value. Although the scale of the plots in Figure 2.7 does not allow one to read the values accurately enough to find these percentages, they are very close to the same for  $\varepsilon$ . The results for Case 4, the double negative case, are equivalent to case 1. This follows because of the symmetry mentioned earlier involving change of sign. Cases 2 and 3 have only one physical value of  $\varepsilon$  and  $\mu$  for each approximate value of  $R$  and  $\theta_1$ , but the accuracy of the retrieval is not any better. Difference in the real part is about the same; difference in the imaginary part is worse, about 10%.

Further investigation of this method is needed before it would be practical to use. However, truly practical methods involve measurements of  $R$  and  $T$  inside a section of waveguide or transmission line.

Two solutions of  $\mu_{2r}$  for “measured” values of  $R$ , Case 1,  $\mu_{2r} = 3 - 0.2j$

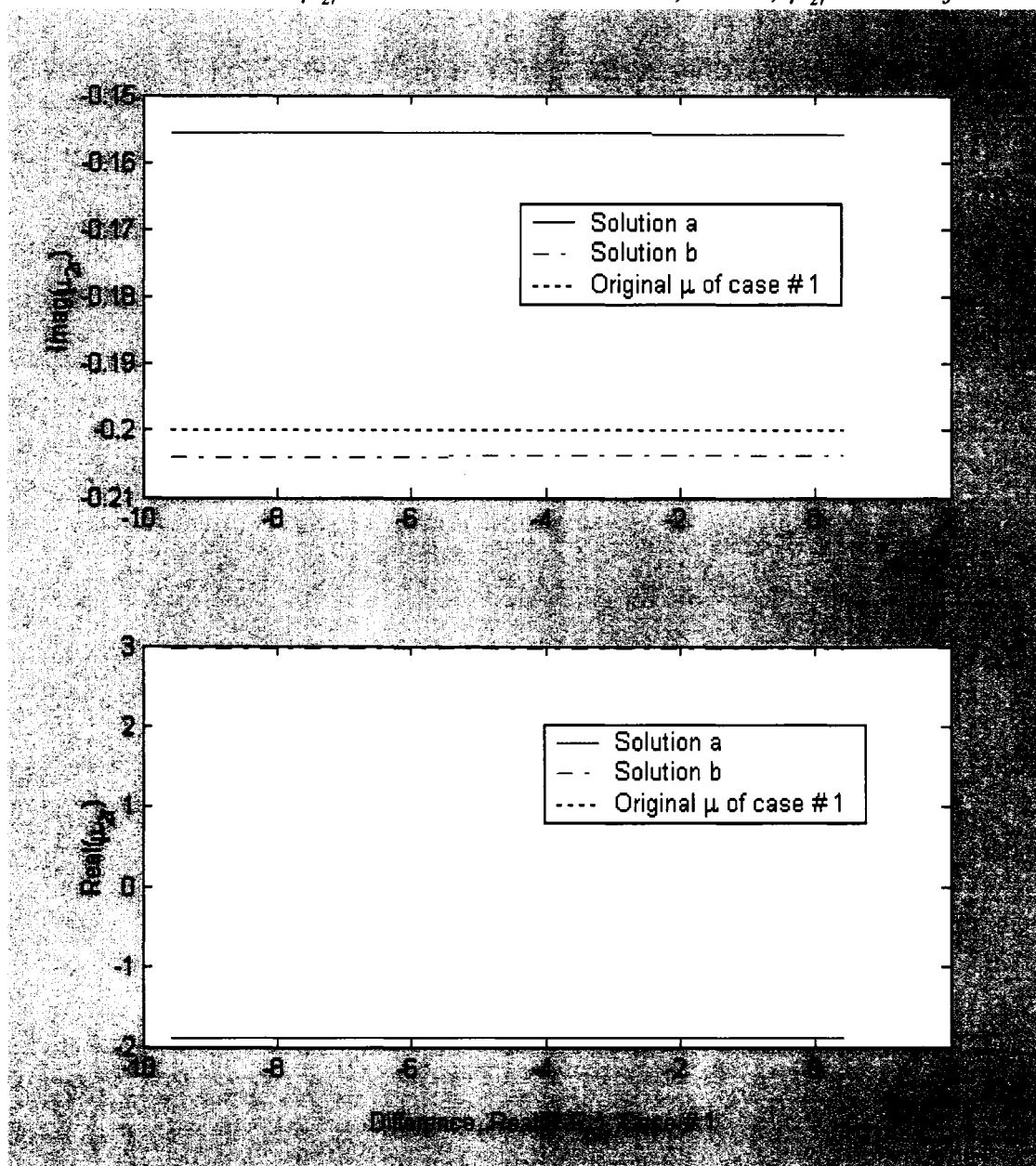


**Figure 2.6** Two solutions of  $\mu_{2r}$  for “measured” values of  $R$ , Case 1,  $\mu_{2r} = 3 - 0.2j$ . The two solutions appear to be independent of the small difference between the hypothetical measured  $R$  and the  $R_p$  of the exact original material. However, a plot of any one of these solutions alone reveals that there is a slope to each line, where the changes in  $\mu$  are about the same in magnitude as the Difference on the abscissa. Note that Solution b is fairly close to the original, while Solution a has opposite sign of the real part and a larger difference from the original imaginary part. In the general problem, one would not know whether the material is of DNG type.

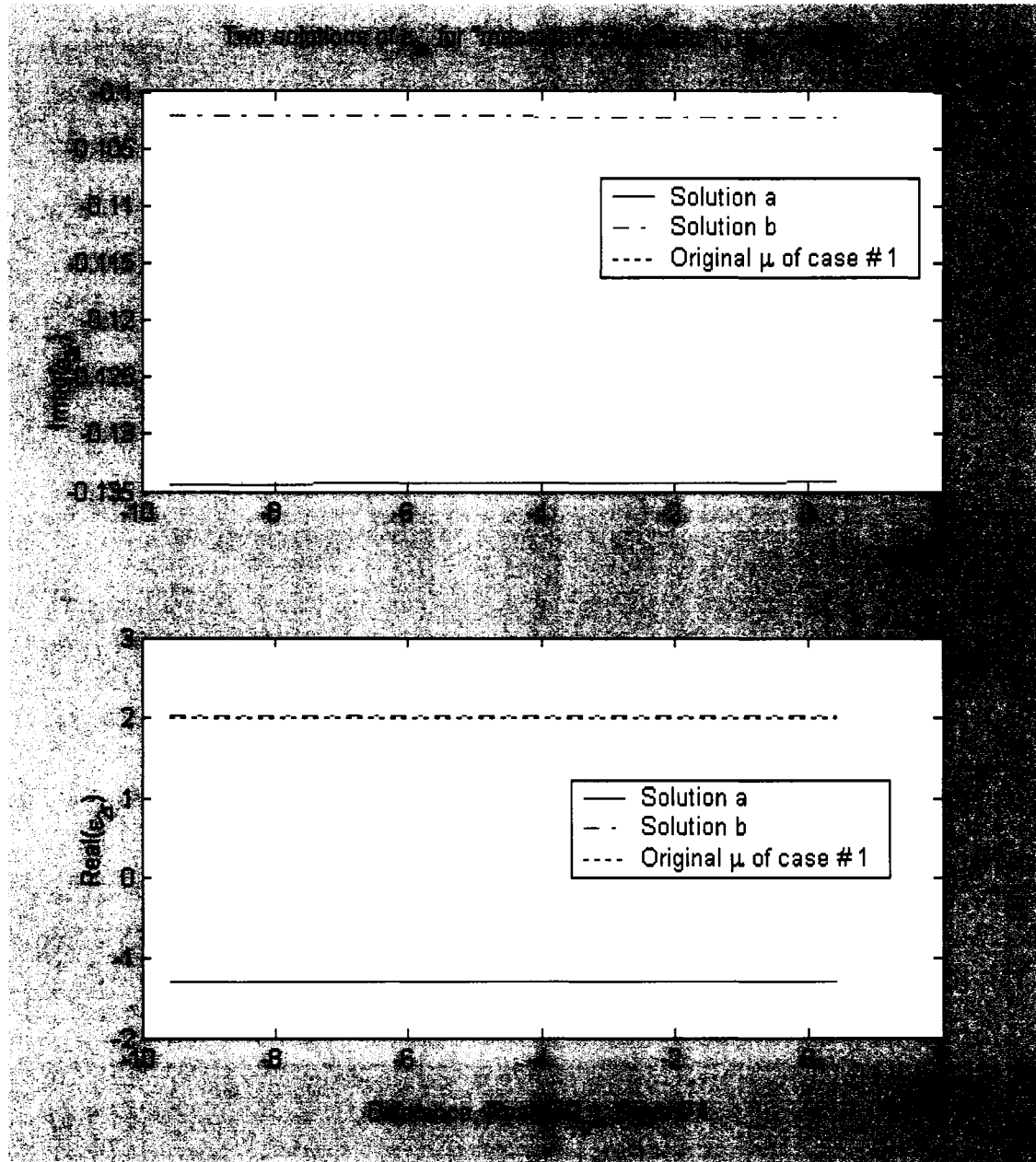


**Figure 2.7** Two solutions of  $\epsilon_{2r}$  for “measured” values of  $R$ , Case 1,  $\epsilon_{2r} = 2 - 0.1j$ . As in **Error! Reference source not found.**, the two solutions appear to be independent of the small difference between the hypothetical measured  $R$  and the  $R_p$  of the exact original material. However, a plot of any one of these solutions alone reveals that there is a slope to each line, where the changes in  $\mu$  are about the same in magnitude as the Difference on the abscissa. Again Solution b is fairly close to the original, while Solution a has opposite sign of the real part and a larger difference from the original imaginary part. Hence, if a third measurement were made to pick out the correct one of these two, it would appear to work for both  $\mu$  and  $\epsilon$ .

## 2.4 Considerations concerning a metamaterial

We were motivated to consider this layer reflection/transmission method of determining  $\varepsilon$  and  $\mu$  because we worked on computing the electromagnetic field propagation through a 2-dimensional periodic structure of infinite cylinders (in a layer). I shall return to the periodic structure in Chapter 6. Our computations were based on a T-matrix approach (Yasumoto & Kushta 2000), (Thomas & Ishimaru 2001), which seems to be limited to the 2-D case. In this approach, one finds that the reflected waves and transmitted waves at a distance (large compared to structure size within the artificial layered material) resolve into a sum of plane-wave modes that are Floquet modes for the period of the structure. Floquet's theorem applies to any periodic structure, so these considerations are more general than for a 2-D structure, but we use just one periodicity. The propagation constant parallel to the surface for the  $n$ th mode is given by

$$k_{zn} = -k_o \cos \phi_i + 2n\pi / h \quad (2.9)$$

where  $\phi_i = \pi / 2 - \theta_i$  is the complement of the angle of incidence we used above and  $h$  is the spatial period of the structure parallel to the surface. In Floquet's theorem,  $n$  ranges over all integers, positive, negative and 0.

We are considering a layer that is embedded on both sides in free space. Thus, by the phase matching requirement  $k_{zn}$  is the same for the transmitted wave as the incident wave, and equal in magnitude and of opposite sign for the reflected wave. Inside the periodic structure, generally all the Floquet modes will contribute to the solution. However for the transmitted and reflected waves, only modes in which  $k_{zn}$  is real will propagate. The longitudinal component (i.e., the Z-component in our coordinate system) of the propagation vector is given by

$$k_{zn} = \sqrt{k_o^2 - k_{xn}^2} = k_o \sqrt{1 - \left( -\cos(\phi_i) + \frac{n\lambda_o}{h} \right)^2} \quad (2.10)$$

where the sign of the square root must be chosen correctly to give attenuation in the outgoing wave direction if  $k_{xn} > k_o$ .

Modes will propagate away from (normal to) the surface if  $k_{zn}$  is real. For small values of  $h$  (measured in wavelength units), there will be only one propagating Floquet mode corresponding to  $n = 0$ . This would certainly be the case for radio waves on molecular crystals and it is true for any  $h < \lambda_o / 2$ . For  $1/2 < h / \lambda_o < 1$  (lattice spacing between  $1/2$  and 1 wavelength) the propagating modes of reflection and transmission are limited to the  $n = 0$  mode within a range of angles around normal incidence. If we let  $h / \lambda_o = f$  that range is given by  $\cos(\phi_i) > (1 - f) / f$  for positive  $n$  and  $\cos(\phi_i) < -(1 - f) / f$  for negative  $n$ . In other words, to exclude all positive and negative  $n$  modes,  $\cos(\phi_i)$  must be outside the interval

$$-(1 - f) / f \leq \cos \phi_i \leq (1 - f) / f .$$

As the lattice spacing  $f = h / \lambda_o$  increases to become larger than 1, at least one other Floquet mode will propagate for all angles of incidence. Moreover, when  $f$  is large, a large number of Floquet modes will propagate.

To obtain unusual propagation effects, we are considering metamaterials with lattice structure and spacing of the order of a wavelength, because that provides a possibility of interesting resonant interactions. To maintain a correspondence with dielectric and magnetic materials, we may limit the lattice spacing to maximum of one wavelength, so that around normal incidence there will be a unique reflected and transmitted wave, which can then be used to calculate  $\varepsilon$  and  $\mu$  according to the previous sections of this chapter. This motivation also led to keeping the off-normal “measured” values within 15 degrees of normal.

## 2.5 Notes to Chapter 2

Chew WC. 1990. *Waves and Fields in Inhomogeneous Media*. New York: IEEE PRESS (originally Van Nostrand Reinhold). 608 pp.

Ishimaru A. 1991. *Electromagnetic Wave Propagation, Radiation, and Scattering*. Englewood Cliffs, New Jersey: Prentice-Hall. 637 pp.

Thomas JR, Ishimaru A. 2001. Lattice sum approach to scattering by periodic structures. In *PIERS Symposium*. Boston, MA

Yasumoto K, Kushta T. 2000. Efficient Analysis of Scattering by Periodic Arrays of Gyrotropic Cylinders. *Electromagnetic Waves & Electronic Systems 5*: 66-74

### 3. Electromagnetic Waves over a Half Space of Arbitrary Permittivity and Permeability

This chapter is based to a large extent on our paper (Ishimaru, Thomas *et al* 2005) and includes numerous paragraphs and figures from that paper. Recent interest in metamaterials necessitates the study of wave characteristics in media with arbitrary permittivity and permeability whose real parts can be positive or negative. Metamaterials are artificial materials, made to be relatively homogeneous on the scale of a wavelength or so, with characteristics that may not be found in natural materials (Veselago 1968), (Pendry, Holden *et al* 1999), (Smith, Padilla *et al* 2000), (Pendry 2000), (Ziolkowski & Heyman 2001), (Ishimaru, Lee *et al* 2003), (Ishimaru, Jaruwatanadilok *et al* 2005). Examples include negative index materials (NIM), chiral media, and composite materials.

In the development of these materials there are at least four questions that need to be investigated: How do electromagnetic waves behave in metamaterials? What characteristics may be useful for practical applications? How does one construct a metamaterial with specified properties, particularly permittivity and permeability? What new applications can be identified to utilize the new wave characteristics? Treatments in this thesis deal primarily with the first of the above questions.

This chapter presents analysis of wave characteristics on semi-infinite metamaterials. Waves are excited by electric or magnetic line sources, and the problem is separated into the p (TM) and the s (TE) polarization, showing symmetries. The Fourier spectra of the reflection and transmission coefficients are examined and the poles, branch points, and zeros are shown in the  $\text{Real}(\mu)$ — $\text{Real}(\epsilon)$  diagram. We clarify the location of poles in proper and improper Riemann Surfaces, and the excitation of forward and backward surface waves, forward and backward Lateral

waves, and Zenneck waves, and the relations between Brewster's angle and Sommerfeld poles. This problem has been studied extensively for ordinary materials with  $\mu = 1$ . Since the permeability is no longer limited to 1 here, many new waves and new phenomena emerge. We include the behaviors of the backward surface waves and the temporal backward Lateral waves.

We first show that a material with negative real parts of permittivity and permeability must have negative real part of the index of refraction  $n$ . In our engineering convention of continuous wave time dependence derived from the real part of  $\exp(j\omega t)$ , the permittivity and permeability of a passive material must have negative imaginary parts and the index of refraction must have a negative imaginary part to insure convergent outgoing waves. Let the relative permittivity and permeability be  $\epsilon_r$  and  $\mu_r$  respectively. In the calculation of  $n = \sqrt{\epsilon_r \mu_r}$ , the correct sign of the square root must be chosen to yield a negative imaginary part. Constitutive parameters with negative real part must both lie in the third quadrant of the complex plane. On multiplication the sum  $\theta_m$  of the polar angles (modulo  $2\pi$ ) will lie in the first or second quadrant (polar angle  $\theta_m$  between 0 and  $\pi$ ). The square root then lies in either the first quadrant (half of the polar angle  $\theta_m$ ) or the negative of this choice, which will be in the third quadrant. To meet the requirement of a negative imaginary part, only the third quadrant choice is possible. Hence, the  $\text{Real}(n)$  is negative.

Next we present a comprehensive analysis of all CW wave types. New wave types such as backward surface waves and backward lateral waves are discussed and the relationship between Brewster's angle and the Zenneck wave is clarified. Our analysis is limited to 2-D problems with isotropic metamaterials. In general, however, metamaterials are anisotropic and highly dispersive, requiring further investigation

(Ziolkowski & Heyman 2001), (Ishimaru, Lee *et al* 2003), (Ishimaru, Jaruwatanadilok *et al* 2005), (Ishimaru & Thomas 2004), (Ziolkowski & Engheta 2003).

### 3.1 Line Source over a semi-infinite metamaterial

We consider an electric or a magnetic line source located over a metamaterial as shown in Figure 3.1.

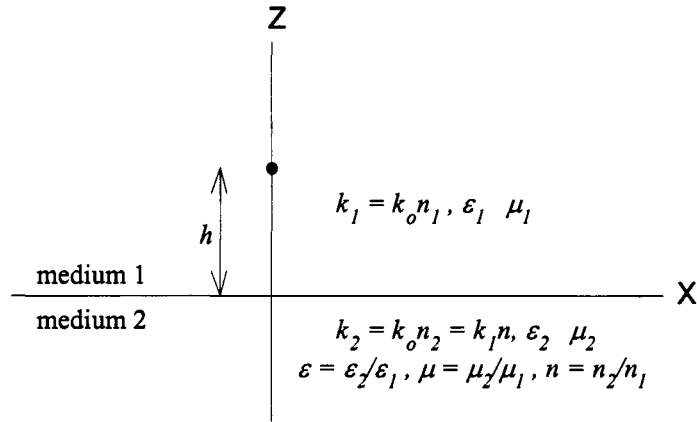


**Figure 3.1** Diagram of coordinate system for 2-media arrangement with line source. Medium 1 is ordinary lossless material. Both  $\epsilon_1$  and  $\mu_1$  are real and positive. Medium 2 is metamaterial with complex  $\epsilon_2$  and  $\mu_2$ .  $\epsilon$ ,  $\mu$ , and  $n$  are normalized with respect to medium 1. Line source is at  $x = 0$  and  $z = h$ .

For the p-polarization (TM), we have

$$\left( \frac{\partial^2}{\partial x^2} + \frac{\partial^2}{\partial z^2} + k_i^2 \right) H_y = -(-j\omega\epsilon_i I_m) \delta(x)\delta(z-h) \quad (3.1)$$

$$k_i^2 = k_o^2 \mu_i \epsilon_i$$

where  $I_m$  is the magnetic line current and we use the normalization  $-j\omega\epsilon_1 I_m = 1$ ,  $k_o$  is free space wavenumber,  $\mu_i$  and  $\epsilon_i$  are relative permeability and permittivity ( $i = 1, 2$  for medium 1 or 2).

Using the boundary condition that  $H_y$  and  $(1/\varepsilon)(\partial/\partial z)H_y$  are continuous at  $z = 0$ , we get the well known Fourier representation of the incident ( $H_{yi}$ ), the reflected ( $H_{yr}$ ) and the transmitted ( $H_{yt}$ ) fields (Ishimaru 1991).

$$\begin{aligned} H_{yi} &= \frac{1}{2\pi} \int \frac{\exp(-jk_{z1}|z-h| - jk_x x)}{2jk_{z1}} dk_x \\ H_{yr} &= \frac{1}{2\pi} \int R(k_x) \frac{\exp(-jk_{z1}(z+h) - jk_x x)}{2jk_{z1}} dk_x \\ H_{yt} &= \frac{1}{2\pi} \int T(k_x) \frac{\exp(-jk_{z1}h + jk_{z2}z - jk_x x)}{2jk_{z1}} dk_x \end{aligned} \quad (3.2)$$

where  $k_{zi} = \sqrt{k_i^2 - k_x^2}$

$$R(k_x) = \frac{Y_2 - Y_1}{Y_2 + Y_1} = \frac{Z_1 - Z_2}{Z_1 + Z_2}, \quad T(k_x) = \frac{2Y_2}{Y_2 + Y_1} = \frac{2Z_1}{Z_1 + Z_2}, \quad \text{and} \quad Y_i = \frac{\omega\varepsilon_i}{k_{zi}} = \frac{1}{Z_i}.$$

$Z_i$  and  $Y_i$  are the wave impedance and the wave admittance, respectively. First we note that for the s-polarization (TE), we have the same equation for  $E_y$  with the replacement of  $(-j\omega\varepsilon_i I_m)$  by  $(-j\omega\mu_i I = 1)$ . The boundary condition at  $z = 0$  is the continuity of  $E_y$  and  $(1/\mu)(\partial/\partial z)E_y$ . Therefore, the field for the s-polarization is identical to the field for the p-polarization with the interchange of  $\mu_i$  and  $\varepsilon_i$  in both media and the interchange of the E and H fields.

### 3.2 Surface waves and lateral waves

As a preliminary to this analysis, we need to pay close attention to the square root of various quantities. In the beginning of this chapter we noted that for a passive medium with our  $\exp(j\omega t)$  time dependence the imaginary parts of the constitutive parameters must be negative and that the imaginary part of the index of refraction must be negative for convergent outgoing waves. It follows that the characteristic

impedance  $Z_{oi}$  and admittance  $Y_{oi}$  must have positive real parts (like resistance and conductance) where

$$Z_{oi} = \frac{1}{Y_{oi}} = Z_o \sqrt{\frac{\mu_i}{\varepsilon_i}}, \quad Z_o = \sqrt{\frac{\mu_o}{\varepsilon_o}}.$$

Next,  $k_{zi}$ , which is expressed as a square root, needs to be chosen carefully. From the branch points at  $k_x = k_i$  in the complex  $k_x$  plane, we draw the branch cuts along  $\text{Im}(k_{zi}) = 0$ . Then, in the top surface of the  $k_x$  plane,  $\text{Im}(k_{zi}) < 0$  and the wave attenuates as  $|z| \rightarrow \infty$ . Thus, this is called the *proper Riemann surface*. Even though the branch cuts can be drawn in other ways, the above choice is most common (Felsen & Marcuvitz 1994). In the *improper Riemann surfaces*, one or both  $\text{Im}(k_{zi})$  become positive (Ishimaru 1991).

Let us examine the reflection coefficient  $R(k_x)$

$$R(k_x) = \frac{(k_{z1} / \varepsilon_1) - (k_{z2} / \varepsilon_2)}{(k_{z1} / \varepsilon_1) + (k_{z2} / \varepsilon_2)} \quad (3.3)$$

The zero and pole are given by

$$\frac{k_{z1}}{\varepsilon_1} = \pm \frac{k_{z2}}{\varepsilon_2} \quad \text{where} \quad \begin{cases} + & \text{Brewster's zero} \\ - & \text{Zenneck wave pole} \end{cases} \quad (3.4)$$

Solving for  $k_x$ , we get the pole at  $k_x = k_{xp}$ .

$$k_{xp} = k_1 S, \quad S^2 = \frac{\varepsilon^2 - n^2}{\varepsilon^2 - 1}, \quad \varepsilon = \frac{\varepsilon_2}{\varepsilon_1}, \quad n = \frac{n_2}{n_1}. \quad (3.5)$$

In order to determine whether the pole is in the proper Riemann surface, we first obtain

$$k_{z2} = \sqrt{k_2^2 - k_{xp}^2}. \quad (3.6)$$

The square root is taken such that  $\text{Im}(k_{z2}) < 0$ . We then use (3.4) to calculate

$$k_{z1} = -\frac{\varepsilon_1}{\varepsilon_2} k_{z2} = -\frac{1}{\varepsilon} k_{z2}. \quad (3.7)$$

If  $\text{Im}(k_{z1}) < 0$ , the pole is in the *proper* Riemann surface (I), and if  $\text{Im}(k_{z1}) > 0$ , the pole is in an *improper* Riemann surface (II). See (Ishimaru 1991).

Note that  $S^2$  in (3.5) corresponds to both zero and pole in (3.3). Brewster's angle occurs when the reflection coefficient is zero, and therefore the classification as pole or zero is based on (3.4). We shall discuss this further in the next subsection.

Let us now examine the location of the pole in the  $k_x$ -plane. For real  $\varepsilon$  and  $\mu$ ,  $S$  is pure real or pure imaginary so the pole  $k_{xp} = k_1 S$  lies on the real or imaginary axis in the  $k_x$ -plane. Figure 3.2 then shows the regions in the  $\varepsilon' - \mu'$  plane where different wave types can exist. We write

$$\varepsilon = \varepsilon' - j\varepsilon'' \quad \text{and} \quad \mu = \mu' - j\mu'' \quad (3.8)$$

to denote the real and imaginary parts of  $\varepsilon$  and  $\mu$  in a conventional fashion where  $\varepsilon''$  and  $\mu''$  are positive quantities.

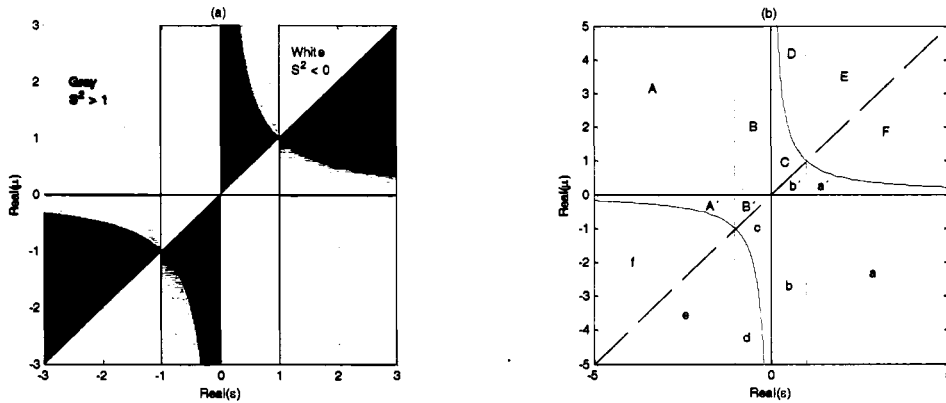


**Figure 3.2** Regions in  $\varepsilon' - \mu'$  plane to categorize poles and zeros of reflection coefficient. (a) region of  $S^2 > 1$  (gray),  $1 > S^2 > 0$  (black) where Zenneck waves or Brewster zeros occur, and  $S^2 < 0$  (white). (b) Regions in  $\varepsilon' - \mu'$  plane per Table 3.1.

If  $S^2 > 1$ , forward or backward surface waves can exist. If  $S^2 < 1$ , there may be Zenneck waves or a Brewster zero, and if  $S^2 < 0$ , the poles are on the imaginary axis and the wave may be exponentially decaying along the surface. However, this is not sufficient to describe the wave types. We also need to examine whether these poles are in the proper or improper Riemann surfaces by examining whether  $\text{Im}(k_{z1})$  is negative or positive with  $\text{Im}(k_{z2}) < 0$ . However, this depends greatly upon the ratio of the imaginary parts of  $\epsilon$  and  $\mu$ . We show in Figure 3.3 five cases where the ratio  $\epsilon'' / \mu'' = 10, 2, 1, 0.5, 0.1$ . We have found by many computations that the Riemann surface (or wave type) classification depends approximately only on the ratio  $\epsilon'' / \mu''$  if  $\mu''$  and  $\epsilon''$  are both small,  $\leq 0.01$ .

In Figure 3.2, there are four regions where  $S^2 > 1$  and surface waves can exist. However, as shown in Figure 3.3, the two regions (a and D in Figure 3.2(b)) with  $S^2 > 1$  on the right side ( $\epsilon' > 0$ ) of Figure 3.2(b) are in the improper Riemann surface. Hence, the surface wave can exist only in the region  $\epsilon' < 0$  where the poles are in the proper Riemann surface. In fact, we will show that the forward and backward surface waves exist in the two regions shown in Figure 3.4(a). We also note the forward  $L^+$  and the backward  $L^-$  lateral waves can exist in region  $1 > n > 0$  and  $0 > n > -1$ , respectively. See Figure 3.4(b).

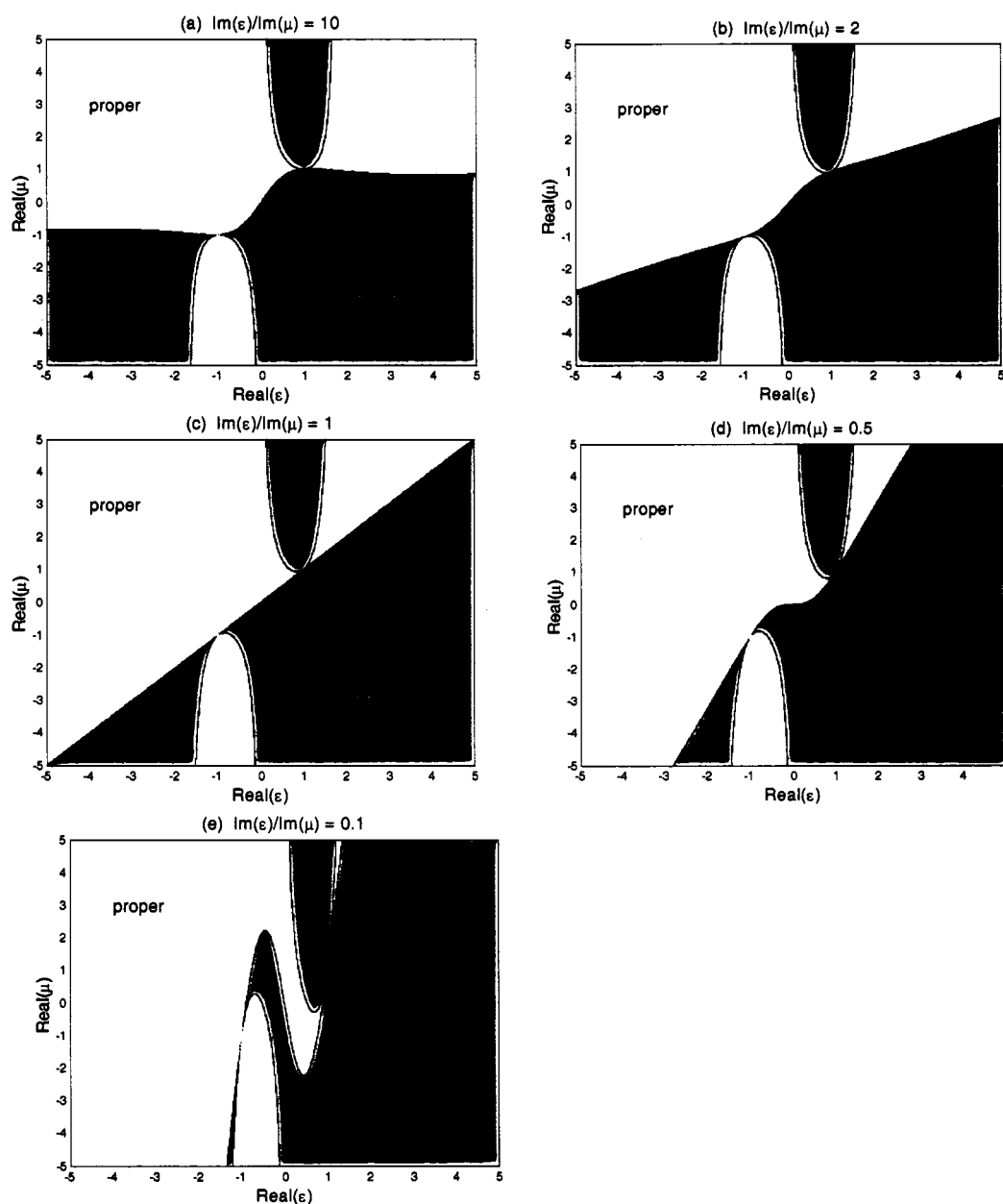


**Figure 3.3** Regions in the  $\text{Real}(\epsilon) - \text{Real}(\mu)$  plane where  $\text{Im}(k_{z1}) < 0$  (pole in proper Riemann surface) and  $\text{Im}(k_{z1}) > 0$  (pole in improper Riemann surface) for five values of the ratio  $\epsilon'' / \mu''$ . The plots are calculated with  $\mu'' = 0.001$ , but apply to small  $\epsilon''$ ,  $\mu''$ .

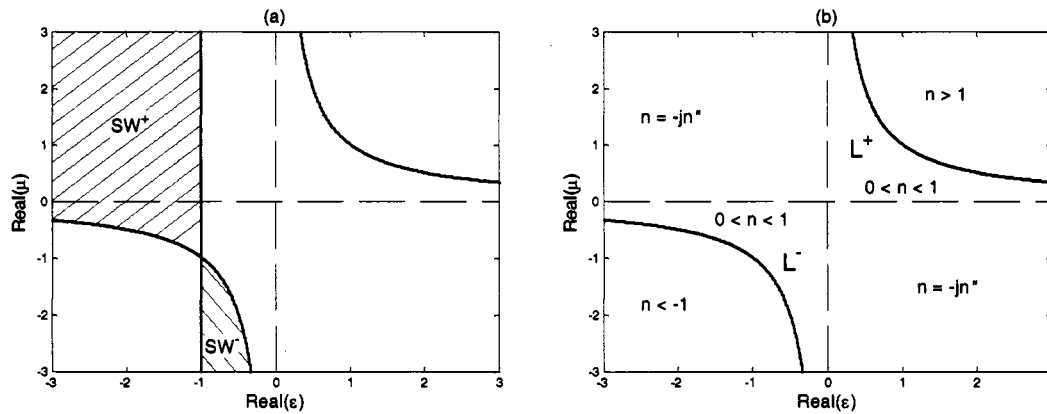


**Figure 3.4** (a) Regions in the  $\text{Real}(\mu)$  –  $\text{Real}(\epsilon)$  plane of forward surface waves ( $SW^+$ ) and backward surface waves ( $SW^-$ ). (b) Regions of forward lateral waves ( $L^+$ ) and backward lateral waves ( $L^-$ ). NIM correspond to points in the third quadrant.

### 3.3 Brewster's angle and Zenneck wave

It has been known that Brewster's angle and Zenneck wave are closely related. However their relationship is often not clearly explained. We first note that at Brewster's angle, the reflection coefficient is zero while at the Zenneck wave pole (sometimes called the *Sommerfeld pole*), the reflection coefficient is infinite. Brewster's angle is normally defined for plane wave incidence on lossless dielectric material, but here, we generalized it to include a lossy medium and complex angle, and call it *Brewster's zero*. This terminology was included in (3.4).

Now at the Zenneck wave pole, we have

$$\text{Im}(k_{z1}) < 0 \text{ and } \text{Im}(k_{z2}) < 0 \quad (3.9)$$

on Riemann surface I. At Brewster's zeros, we have

$$\text{Im}(k_{z1}) > 0 \text{ and } \text{Im}(k_{z2}) < 0 \quad (3.10)$$

on Riemann surface II.

In the  $k_x$  or  $S$  plane ( $k_x = k_1 S$ ;  $S$  may be regarded as a mnemonic for the sine of the polar angle between the  $k$  vector and the  $k_z$  direction.), both pole and zero are at the same point, but these two are on two different Riemann surfaces as shown in Figure 3.5. The upper part of Figure 3.5 shows a view looking down on the  $k_x$  plane with all four Riemann surfaces visible as though transparent. The dashed lines in the lower part of Figure 3.5 represent an end view of the 4 Riemann sheets, separated slightly as I, II, III and IV. The branch cuts to the branch points at  $k_1$  and  $k_2$  are drawn along the conventional  $\text{Im}(k_x)$  paths as mentioned above. These paths are hyperbolas. The dashed and dotted lines indicate connections to the respective Riemann surfaces in which the different branches and poles appear. The branch points  $k_1$  and  $k_2$  are the end points of the two branch cuts, and the point plotted with an x or an o represents the Sommerfeld pole or Brewster's zero. For a typical air-earth interface, the pole is on Riemann surface I, as shown, and represents the Zenneck wave in asymptotic analysis.

Physically, the spectral factors associated with the reflected wave in (3.2) have the same propagation constant along the surface at Brewster's zero and the Zenneck pole, but the phase front and the attenuation directions are different (Ishimaru 1991). The exponential form of the spectrum can be written as

$$\exp(-jk_{z1}z - jk_x x) = \exp(-j\vec{K}_r \cdot \vec{r} - \vec{\alpha} \cdot \vec{r}) \quad (3.11)$$

where  $\vec{K}_r$  and  $\vec{\alpha}$  represent the phase front propagation and the attenuation direction respectively, as shown in Figure 3.6. From the defining equation  $k_{z1}^2 + k_x^2 = k_1^2$  it follows that  $\vec{K}_r \cdot \vec{\alpha} = \text{Re}(n_1) \text{Im}(n_1) = n_1' n_1''$  and, hence,  $\vec{K}_r$  as drawn in Figure 3.6 is perpendicular to  $\vec{\alpha}$  if medium 1 is lossless.

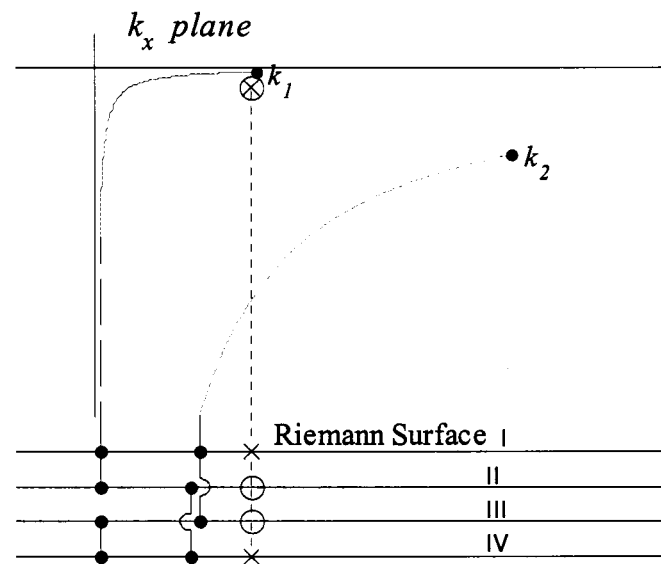


**Figure 3.5** Zenneck wave pole at  $x$  and Brewster's zero at  $o$  with relation to branch cuts. Riemann surface I:  $\text{Im}(k_{z1}) < 0$ ,  $\text{Im}(k_{z2}) < 0$ ; II:  $\text{Im}(k_{z1}) > 0$ ,  $\text{Im}(k_{z2}) < 0$ ; III:  $\text{Im}(k_{z1}) < 0$ ,  $\text{Im}(k_{z2}) > 0$ ; IV:  $\text{Im}(k_{z1}) > 0$ ,  $\text{Im}(k_{z2}) > 0$ .

The pole and the zero in Figure 3.5 are for a typical Sommerfeld problem of wave propagation over a conducting earth. For metamaterials, we need to reexamine Figure 3.5.

We label different regions shown in Figure 3.2(a) as in Figure 3.2(b). Then, from Figure 3.2(a), we note that  $1 > S^2 > 0$  in Regions C, F, c, and f. However, we shall see in the next section that the Zenneck wave occurs only in regions F and f. The boundaries of the regions shown in Figure 3.2(b) represent the limits for  $\varepsilon'' \rightarrow 0$  and  $\mu'' \rightarrow 0$ . In computations for a large sample of cases covering Figure 3.2(b), we have observed that for small imaginary parts these boundaries depend primarily on the ratio  $\varepsilon'' / \mu''$ .

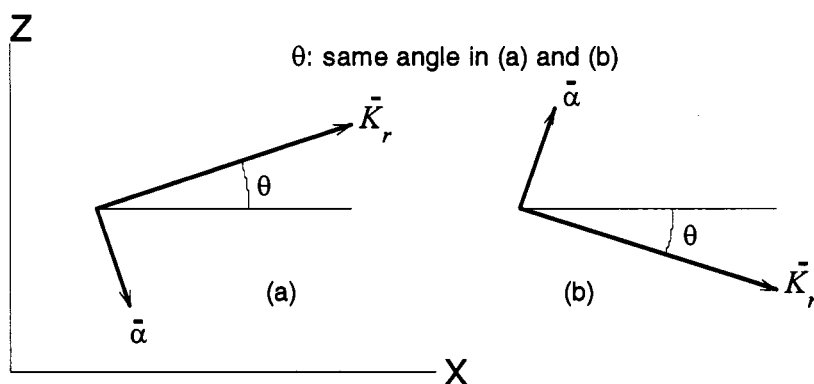


**Figure 3.6** Propagation  $k_{z1}$  constant at (a) Brewster's zero and (b) Zenneck wave pole. Note that  $\vec{K}_r$  is perpendicular to  $\vec{\alpha}$ .

The wave type in F and f depends on the ratio  $\epsilon''/\mu''$ . In Figure 3.7, we show that Zenneck wave poles exist for  $F_{10}$  ( $\epsilon''/\mu'' = 10$ ) and  $f_{0.1}$  ( $\epsilon''/\mu'' = 0.1$ ), but not for  $F_{0.1}$  ( $\epsilon''/\mu'' = 0.1$ ) and  $f_{10}$  ( $\epsilon''/\mu'' = 10$ ). In Figure 3.7 through Figure 3.11, to reduce crowded lines, we do not show the branch cut from  $S = (1,0)$  to  $(0,0)$  to  $(0, -\infty)$ , which is the cut from  $k_1$  shown in Figure 3.5. We have used the notation  $S = S_x + jS_y$  in Figure 3.7 through Figure 3.11; that is  $S_x = \text{Re}(S)$  and  $S_y = \text{Im}(S)$ . In the legend, the symbol x or o denotes a pole or zero of  $S$ , respectively. The diamond represents the branch point at  $S = n$ . The symmetric branch cuts and branch points in the upper half of the  $k_x$  plane are not shown.

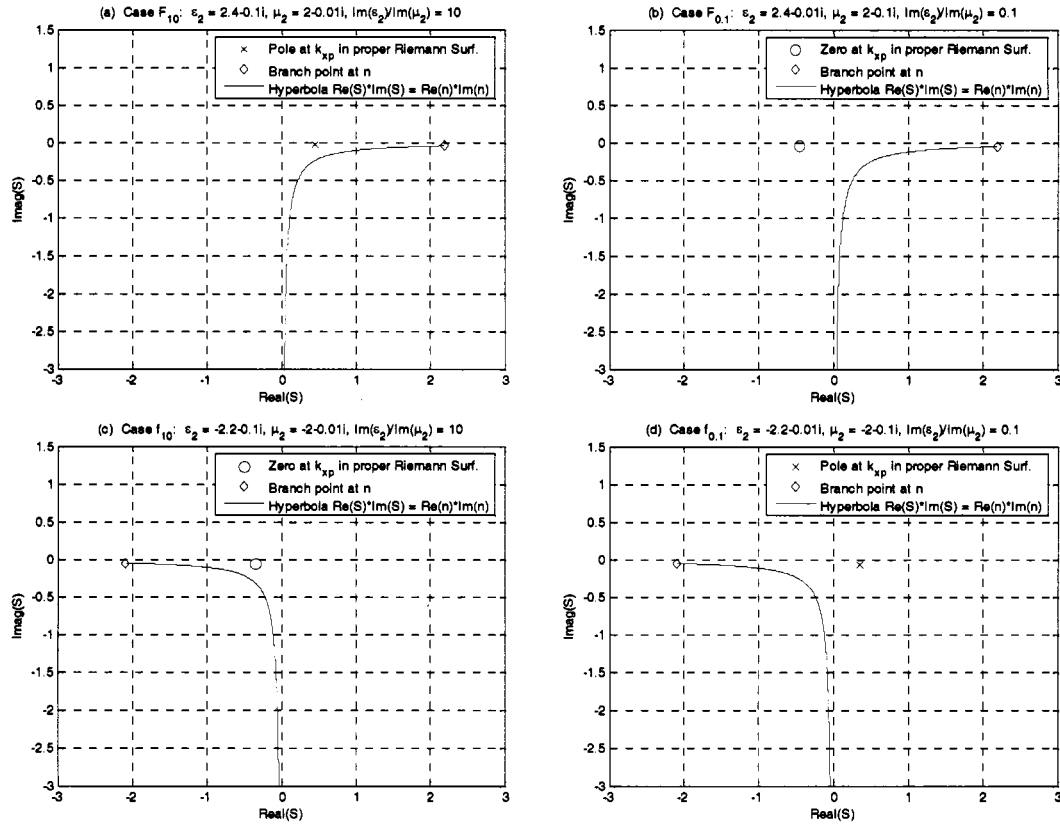


**Figure 3.7** Complex  $S$  plane ( $S = k_x / k_1$ ) plot of pole or zero and branch cut to  $n$  for four cases as labeled.

### 3.4 Wave Types in $\epsilon'' - \mu''$ Diagram—Examples

We have computed proper pole positions and branch cuts that determine the listed wave types for a large number of cases of  $(\mu, \epsilon)$ . We have explored the variation with real parts as shown by regions in the  $\epsilon'' - \mu''$  diagram, and we have explored variations with small negative imaginary parts. Our first calculations considered imaginary parts of the order of  $10^{-3}$  and we expanded to about 0.1. We noted that the boundary between regions of different wave type could change (e.g., region d expands with increasing  $\epsilon''$  to include a small part of region e where  $\epsilon''$  is less than  $-1$ ). We conclude that in the limit  $\epsilon'' \rightarrow 0$  and  $\mu'' \rightarrow 0$ , the boundaries are as shown in Figure 3.2(b), and the wave types by region are given in Table 3.1.

**Table 3.1 Wave types in the Regions of Error! Reference source not found.(b)**

Region label(s)	Wave Type	Abbreviation
A	forward surface wave	$SW^+$
B	evanescent wave	$E$
D and E	improper mode	$Im$
F	Zenneck wave or improper mode	
A'	backward lateral wave or forward surface wave	$L^-$ $SW^+$
B'	backward lateral wave	$L^-$
a and b	improper mode	$Im$
c	backward lateral wave	$L^-$
d	backward surface wave	$SW^-$
e	improper mode	$Im$
f	improper mode or Zenneck wave	
C, a', b'	forward lateral wave	$L^+$

We now show examples of various wave types for selected parts (not F nor f) of the  $\epsilon' - \mu'$  diagram (Figure 3.2(b)). These examples, shown in Figure 3.8 through Figure 3.11, are for the case of  $\epsilon'' = 0.1$  and  $\mu'' = 0.01$ . We use these rather large values for small quantities so that the branch-cut curves and poles lie far enough away from the axes to be readily visible. The choice of  $\epsilon''$  as larger than  $\mu''$  is partly motivated by our determination that  $\epsilon''$  is the controlling loss for our p-polarization (TM) case. However, the same wave type by region was found for other values that explored the range  $0.1 \leq \epsilon'' / \mu'' \leq 10$  and beyond. In each of these figures, we also show schematically the behaviors of the primary waves  $\psi_p$ , reflected waves  $\psi_r$ , surface waves  $\psi_{SW}$ , and lateral waves  $\psi_L$  in their asymptotic forms at large distance.

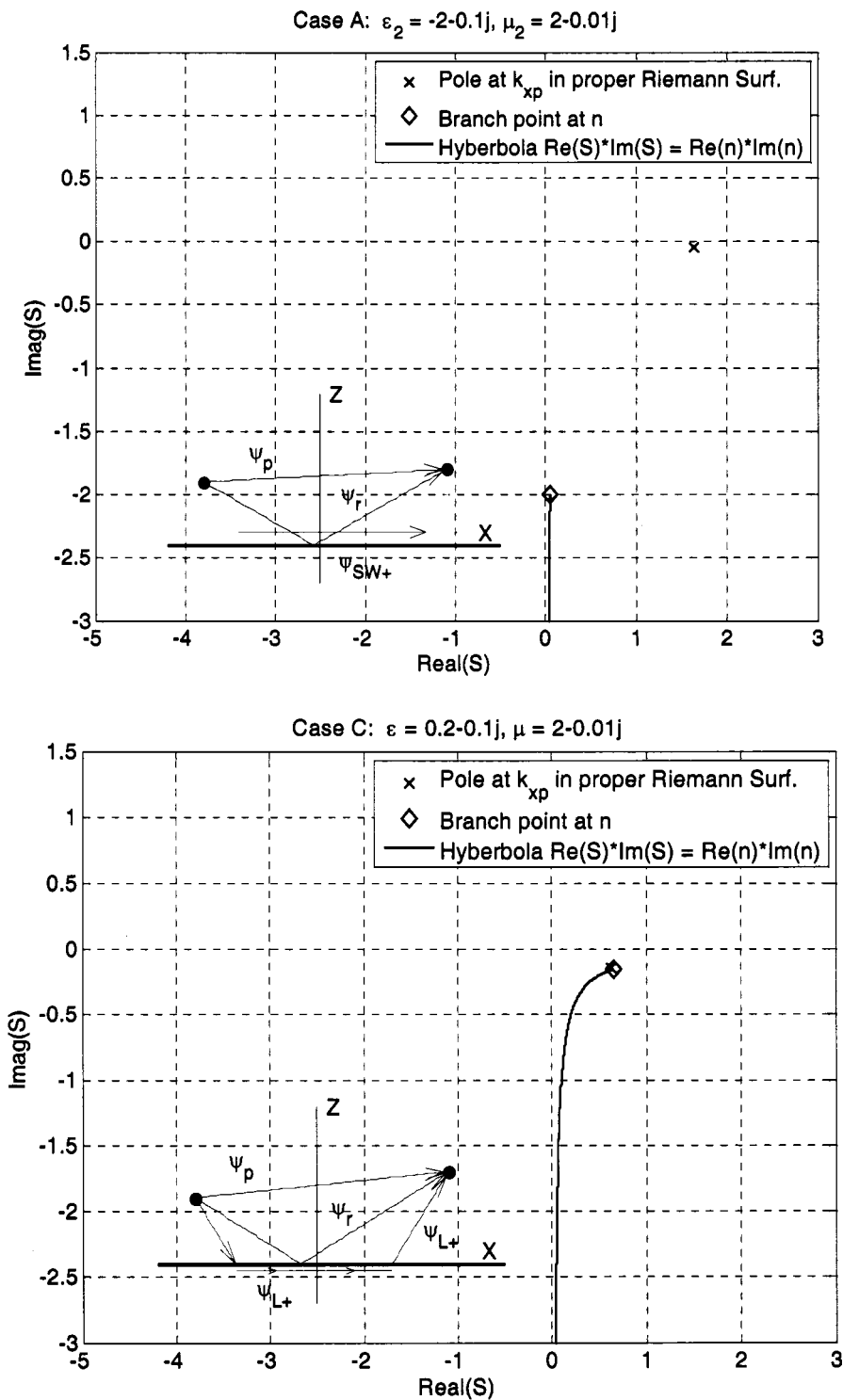


**Figure 3.8** Complex  $S$  plane ( $S = k_x / k_y$ ) plots of pole and branch cut to  $n$  for  $(\varepsilon, \mu)$  cases in regions A and C of Figure 3.2(b) with illustration of asymptotic wave types.

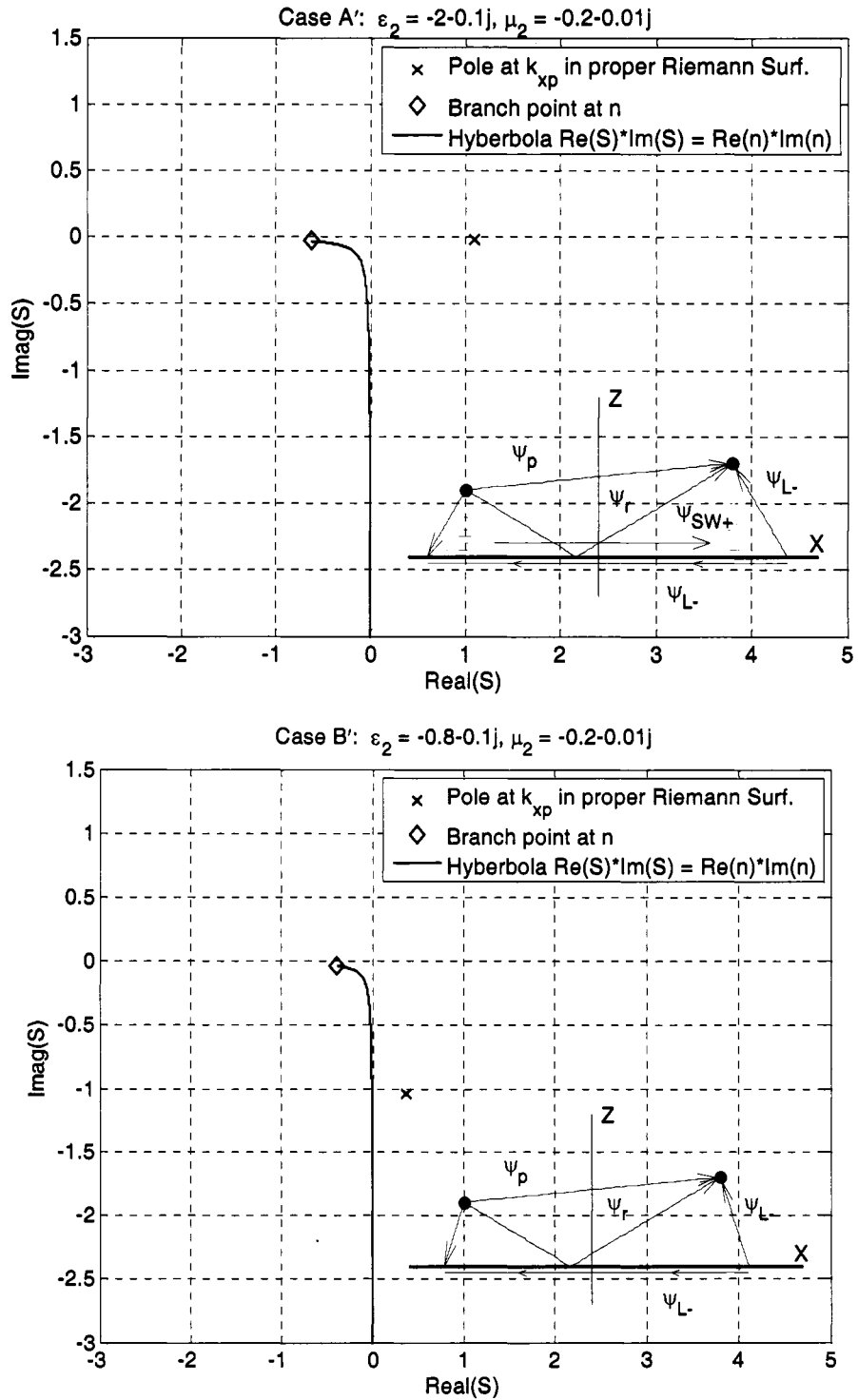
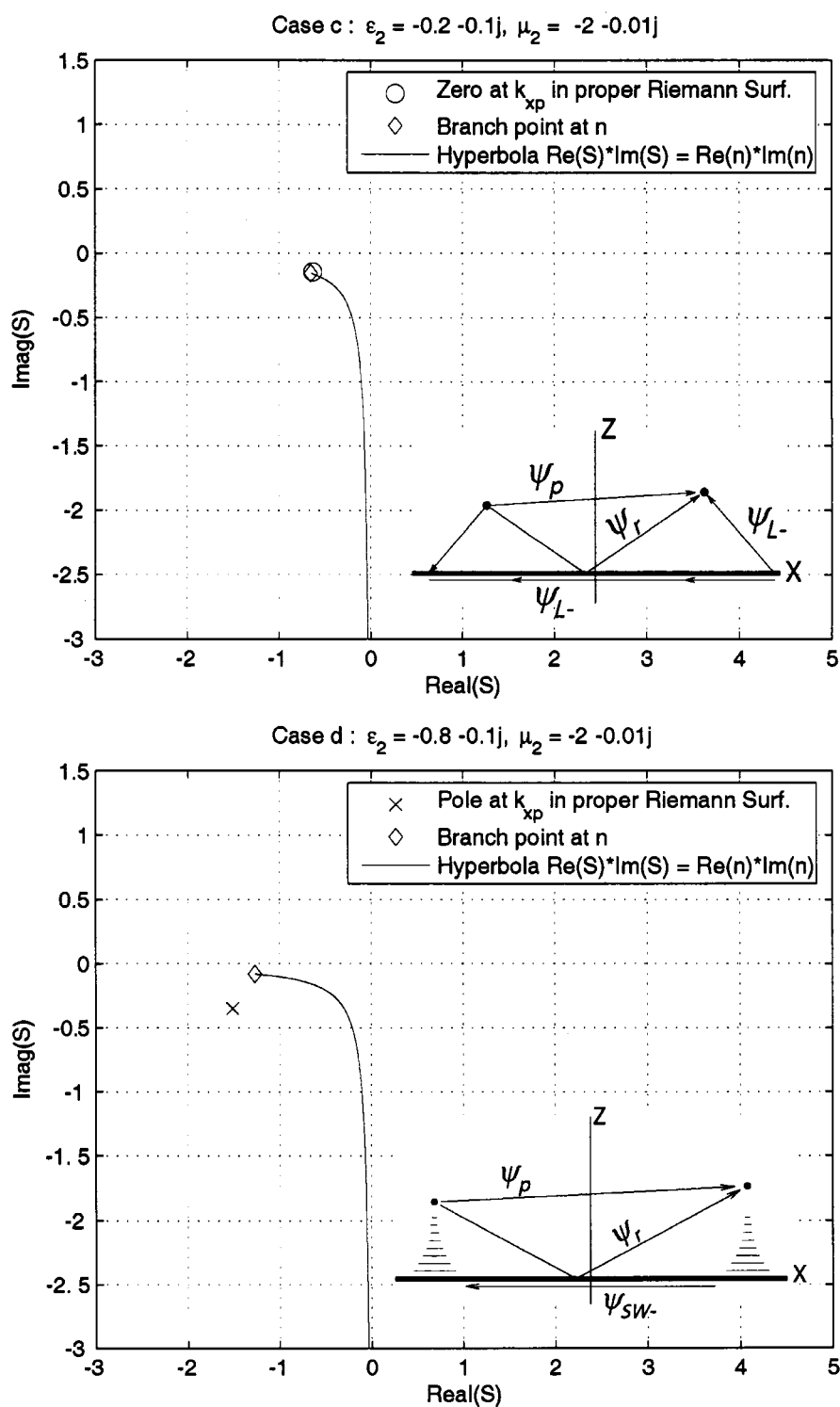


Figure 3.9 Complex S plane ( $S = k_x / k_y$ ) plots of pole and branch cut to  $n$  for  $(\epsilon, \mu)$  cases in regions A' and B' of Figure 3.2(b) with illustration of asymptotic wave types.

The usual dielectric range that produces Zenneck waves in Region F was illustrated in Figure 3.7(a). The well known surface wave (plasmon) for Region A is illustrated in Figure 3.8 case A. The forward lateral wave that occurs in conventional electromagnetics with propagation from a medium of higher refractive index to one of lower index is illustrated in Figure 3.9 case A', Figure 3.11 case a' and Figure 3.11 case b'.

The notation and diagram scheme of Figure 3.8 through Figure 3.11 deserves further explanation. In the inset diagrams, the interface at  $z = 0$  between a lossless medium of index  $n_1$  ( $z > 0$ ) and the arbitrary medium of index  $n_2$  ( $z < 0$ ) is shown as a heavy horizontal line. As mentioned above, the symbols  $\psi_p$  and  $\psi_r$  stand for the primary (direct) wave and reflected wave, respectively. The symbols  $\psi_L$  and  $\psi_{SW}$  stand for a lateral wave and a surface wave, respectively. The additional + or – in the subscript with the L or SW indicates whether the wave is of the previously well known positive type or the new negative type (negative phase velocity) we have found associated with negative index media.

The reflected waves are shown at the specular angle and the lateral waves are shown at the critical angle. The surface waves are shown propagating only parallel to the interface with an amplitude that decreases exponentially away from the surface (in the Z direction) represented by a series of decreasing short lines at two locations just above the surface. A surface wave on a lossless medium does not change amplitude in its propagation direction (X direction in the inset) and this idea is suggested by making the line series the same at both locations.



**Figure 3.10** Complex S plane ( $S = k_x / k_1$ ) plots of branch cut to  $n$  for  $(\epsilon, \mu)$  with zero or pole in proper Riemann surface for cases in regions c and d of Figure 3.2(b) with illustration of asymptotic wave types.

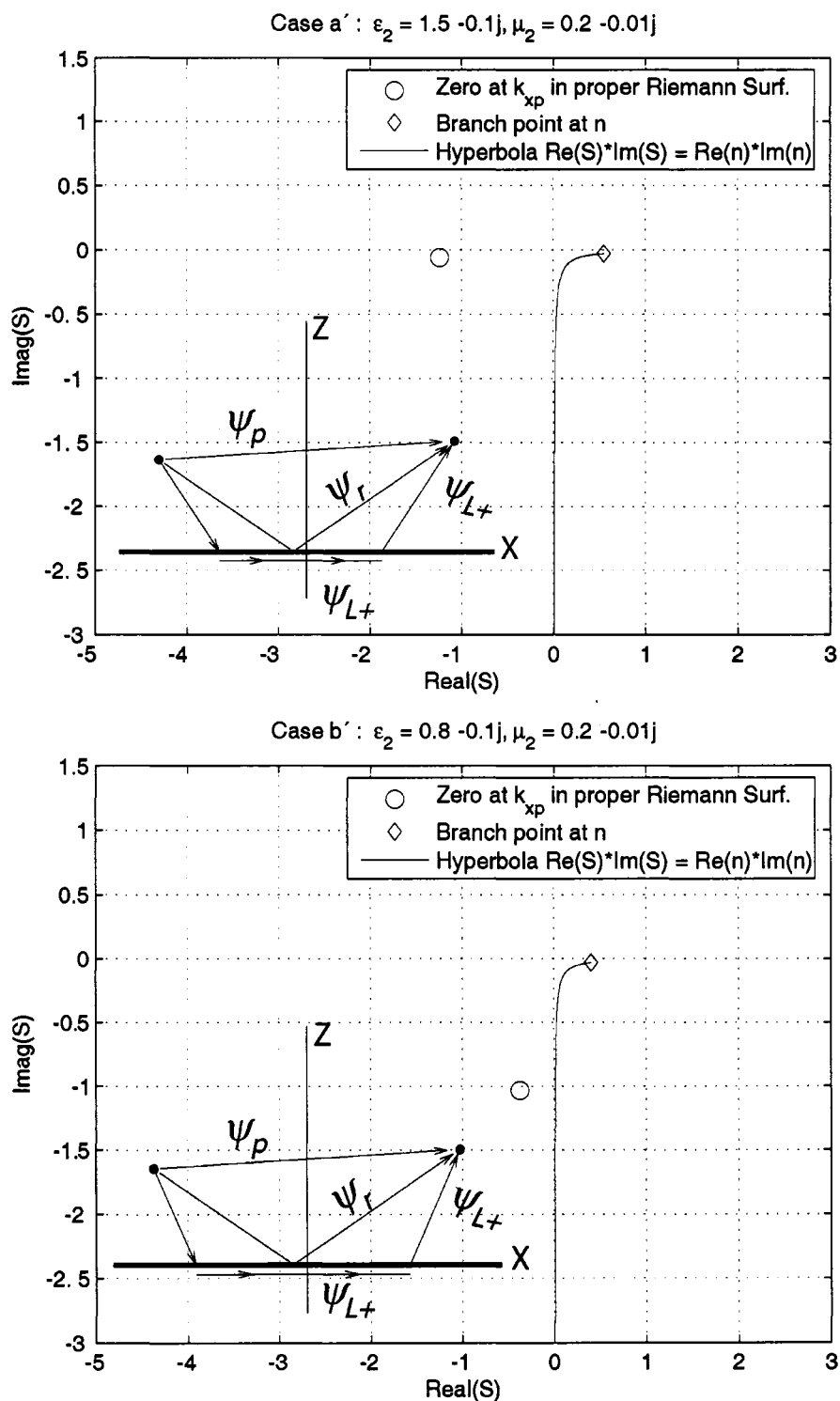


**Figure 3.11** Complex S plane ( $S = k_x / k_y$ ) plots of zero and branch cut to  $n$  for  $(\varepsilon, \mu)$  cases in regions a' and b' of Figure 3.2(b) with illustration of asymptotic wave types.

The wave types in Figure 3.7 through Figure 3.11 are determined by the topology of the pole locations relative to the branch cuts. Calculations to characterize the regions and determine the boundaries of the regions listed in Table 3.1 for the particular loss case of  $\text{Im}(\epsilon_{2r}) = -0.001$  and  $\text{Im}(\mu_{2r}) = 0$  were carried out in a MATLAB program `kz2pPropRiembyRegion.m`. A jagged overlay plot of the boundary of the regions for this particular loss case were then created with a program `GenrtBoundPlotsF50toF77.m`. Figure 3.12 shows how the boundaries of the regions listed in Table 3.1 change for this finite loss case. It is necessary to look at Figure 3.2(b) to see where the boundaries are without loss. The change in boundary may look large on this scale, but, in total, the plane extends to infinity and these boundary changes are small in that overall sense.

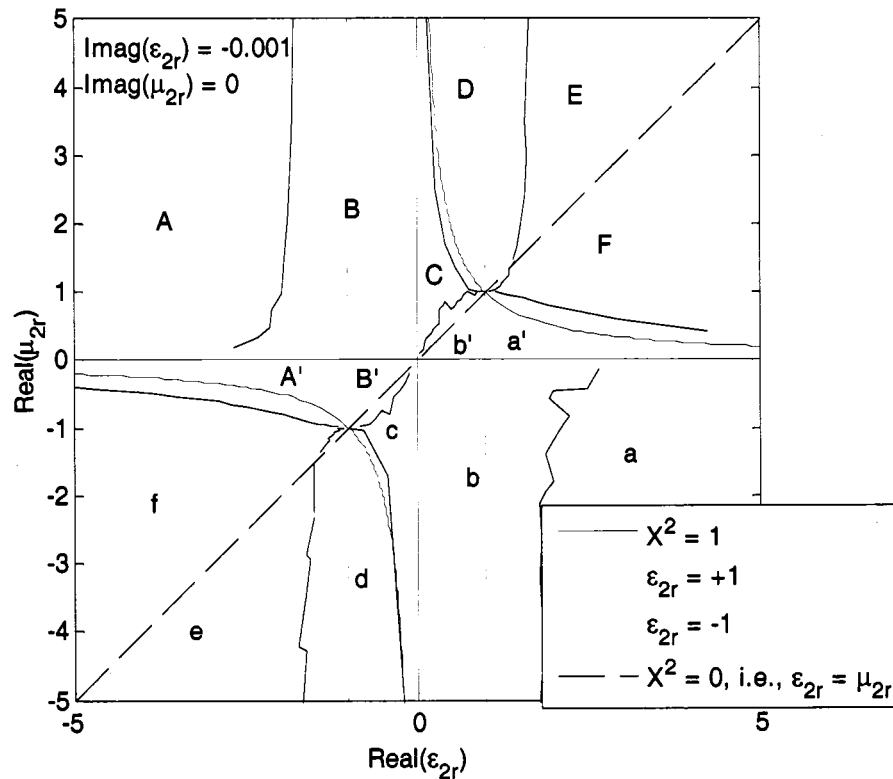


**Figure 3.12** Regions for classification of asymptotic wave types to be compared with Figure 3.2(b) and Table 3.1.

### 3.5 Backward surface waves

We have found a slow-wave pole (pole with  $\text{Re}(S_x) < -1$ ) occurs in region d of Figure 3.2(b) (also  $SW^-$  in Figure 3.4(a)). An example of the pole and branch cut configuration is shown in Figure 3.10 case d. For lossless cases, the phase velocity is in the negative  $x$  direction. However the Poynting vectors in medium 2 and medium 1 are pointed in  $+x$  and  $-x$  direction, respectively and the total power is pointed in  $+x$  direction. The Poynting vector in the  $x$  direction is given by

$$P_x = \frac{k_1 S}{2\omega\epsilon_0\epsilon_i} |H_y|^2 \quad \begin{cases} i=1 & \text{for medium 1,} \\ i=2 & \text{for medium 2.} \end{cases} \quad (3.12)$$

Since  $S < -1$ ,  $\epsilon_1$  is real and positive, and  $-1 < \epsilon_2 < 0$  in medium 2,  $P_x < 0$  in medium 1 and  $P_x > 0$  in medium 2. Furthermore, the total power in  $+x$  direction is given by

$$\begin{aligned} P_{total} &= \int_0^\infty P_x dz + \int_{-\infty}^0 P_x dz \\ &= \frac{1}{4} \frac{S}{\omega\epsilon_0\epsilon_1} \frac{1}{\sqrt{S^2 - 1}} \left[ 1 - \frac{1}{\epsilon^2} \right] \end{aligned} \quad (3.13)$$

which becomes positive as expected as shown in Figure 3.13.

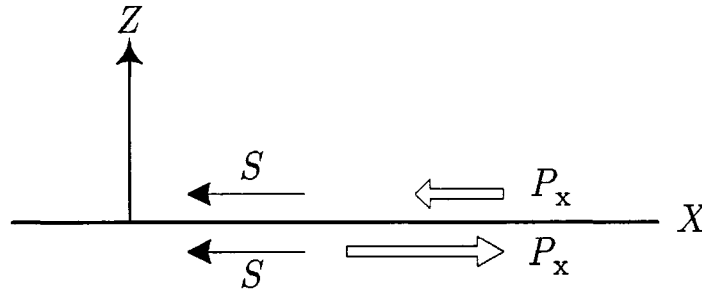


**Figure 3.13** Backward surface wave diagram.  $S$  is normalized value of  $k_{xp}$  and is therefore continuous across the boundary. The  $x$  component of Poynting vector  $P_x$  has opposite signs in the different media and is of different magnitude as discussed in text.

### 3.6 Backward lateral wave and temporal wave packet

In Figure 3.2(b) and Figure 3.8 through Figure 3.11, the backward lateral wave is shown as occurring in NIM regions A', B' and c. A conventional forward lateral wave, which occurs in region C, a', and b' of Figure 3.8 and Figure 3.11 is pictured in Figure 3.14.

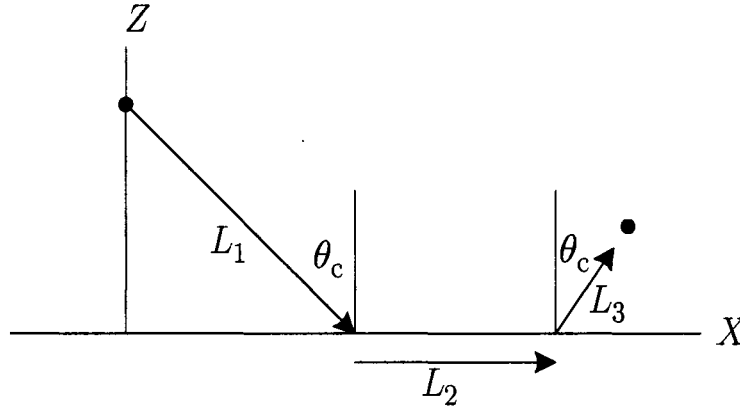


**Figure 3.14** Conventional forward lateral wave.

The forward lateral wave is given by

$$H_y \propto \exp(-jk_1 L_1 - jk_2 L_2 - jk_1 L_3) \quad (3.14)$$

and  $\theta_c$  is the critical angle ( $= \sin^{-1}(\text{Re}(n))$ ). The backward lateral wave is given by the same expression, but  $k_2 = k_1 n$ ,  $0 > n > -1$ , and  $\theta_c < 0$ . This is pictured in Figure 3.15(a).

As illustrated in Figure 3.14 and Figure 3.15(a), the lateral wave is created by rays propagating from the source to medium 2 at the critical angle  $\theta_c$  along the path shown as  $L_1$ . Then the lateral wave travels along the surface to where it radiates from medium 2 at angle  $\theta_c$  to reach the observation point shown at the end of the path  $L_3$ . With a NIM the phase velocity in medium 2 is negative (i.e., opposite the X component of the incident wave). It should, however, be noted that NIM is highly

dispersive and therefore the wave in NIM over  $L_2$  propagates with group velocity rather than phase velocity. If a wave packet is incident on NIM, the wave packet propagates as shown in Figure 3.15(b). In this figure, the backward lateral wave emerges from a source point that travels along the X-axis at group velocity  $v_g$  as shown. The lateral wave radiates into medium 1 (shown as freespace) at the critical angle  $\theta_c$ . Then,  $\theta_l$  represents the angle between the front of the lateral wave packet and the X-axis.

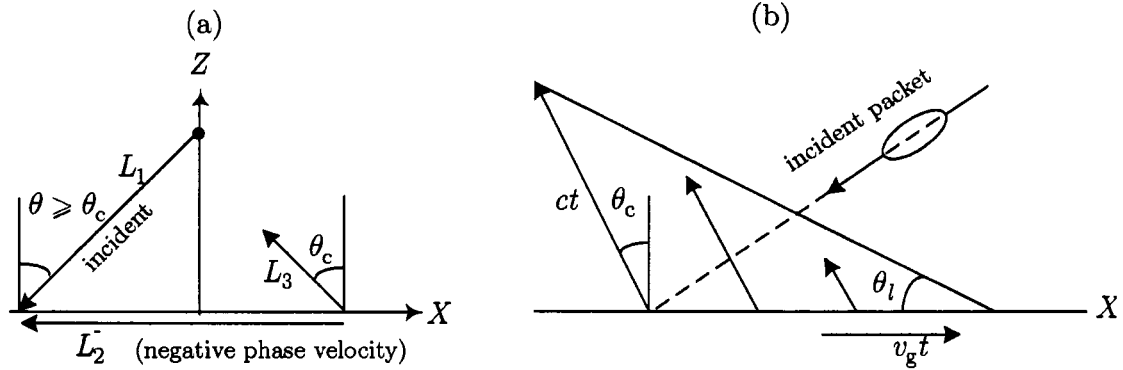


**Figure 3.15** Backward lateral wave (a) and wave packet (b).

The group refractive index  $n_g$  is given by

$$n_g = \frac{\partial}{\partial \omega} (n\omega) = \frac{c}{v_g} \quad (3.15)$$

The law of sines applied to the triangle in Figure 3.15(b) then gives (Ishimaru & Thomas 2004)

$$\sin^2 \theta_l = \frac{n_g^2 (1 - |n|^2)}{1 + 2n_g |n| + n_g^2} \quad (3.16)$$

Exact numerical calculation of the space-time wave packet confirms this behavior of the backward lateral wave (Ishimaru & Thomas 2004).

### 3.7 Notes to Chapter 3

- Felsen LB, Marcuvitz N. 1994. *Radiation and Scattering of Waves*. New York: IEEE Press. 888 pp.
- Ishimaru A. 1991. *Electromagnetic Wave Propagation, Radiation, and Scattering*. Englewood Cliffs, New Jersey: Prentice-Hall. 637 pp.
- Ishimaru A, Jaruwatanadilok S, Kuga Y. 2005. *Generalized surface plasmon resonance sensors using metamaterials and negative index materials*. Presented at Progress in Electromagnetics Research Symposium (PIERS)
- Ishimaru A, Lee SW, Kuga Y, Jandhyala V. 2003. Generalized constitutive relations for metamaterials based on the quasi-static Lorentz theory. *IEEE Transactions on Antennas and Propagation* 51: 2550-7
- Ishimaru A, Thomas JR. 2004. *Waves in layered negative index media excited by space-time localized source*. Presented at URSI International Symposium on Electromagnetics Theory, Proceedings, Pisa, Italy
- Ishimaru A, Thomas JR, Jaruwatanadilok S. 2005. Electromagnetic waves over half-space metamaterials of arbitrary permittivity and permeability. *Ieee Transactions on Antennas and Propagation* 53: 915-21
- Pendry JB. 2000. Negative refraction makes a perfect lens. *Physical Review Letters* 85: 3966-9
- Pendry JB, Holden AJ, Robbins DJ, Stewart WJ. 1999. Magnetism from conductors and enhanced nonlinear phenomena. *IEEE Transactions on Microwave Theory and Techniques* 47: 2075-84
- Smith DR, Padilla WJ, Vier DC, Nemat-Nasser SC, Schultz S. 2000. Composite medium with simultaneously negative permeability and permittivity. *Physical Review Letters* 84: 4184-7
- Veselago VG. 1968. The electrodynamics of substances with simultaneously negative values of  $\epsilon$  and  $\mu$ . *Soviet Physics USPEKHI* 10: 509-14
- Ziolkowski RW, Engheta N. 2003. Metamaterial special issue introduction. *IEEE Transactions on Antennas and Propagation* 51: 2546-9
- Ziolkowski RW, Heyman E. 2001. Wave propagation in media having negative permittivity and permeability. *Physical Review E* 64: -

## 4. Negative refraction: Beam wave packet incident on NIM

This chapter presents calculations of the refraction and reflection of a wave packet in time and space at the plane boundary between free space and a negative index medium (NIM). Most of this chapter has been published in (Thomas, Ishimaru 2005b). When a single-frequency (CW) plane wave is incident on NIM, the wave is refracted negatively according to Snell's law, a direct consequence of phase matching. It has also been shown that the group front of a plane wave refracts positively, but a modulated Gaussian beam refracts negatively (Smith, Schurig *et al* 2002). So, there has been controversy regarding the refraction of finite packets.

Consequently, in this work we use a space-time domain approach to clarify the refraction, causal requirements, and dispersion that apply to a space-time beam wave packet. In so doing we discuss the refraction of a beam packet for cases when the incident angle is less or greater than the critical angle. This approach leads to a study of the Goos-Hänchen effect and to confirmation of a new wave, the "backward lateral wave," which we predicted in Chapter 3 and our paper (Ishimaru, Thomas *et al* 2005).

We study the propagation of a space-time wave packet (a pulsed beam wave) that has nearly planar properties near the middle of the beam and nearly cw properties near the mid-point in time of the pulse. We treat here a 2-D Gaussian beam wave modulated with a Gaussian time dependence. In free space this wave packet has negligible change in cross section or time-domain envelope for distances such that  $\lambda_0 z' \ll \pi W_0^2$  where  $\lambda_0$  is the wavelength at the central frequency of the pulse,  $z'$  is distance along the direction of propagation of the central direction of the beam, and  $W_0$  is the beam cross section. For example, if  $W_0 = 10\lambda$ , then the beam wave will retain its coherence for several 10's of wavelengths. We will show that this packet, incident on a planar boundary of a NIM, exhibits negative refraction plus a skewing and

distortion of the elliptical cross section of the incident pulse. The skewing effect is due to the positive refraction of what we call the wavefront normal, but which is also identified as the interference front normal by (Smith, Schurig *et al* 2002). We have obtained an analytic first-order asymptotic approximation that shows the roles of the group velocity, the phase velocity and the wave fronts of the beam. From this expression, we find that the center of the wave packet refracts negatively according to Snell's law and propagates with the group velocity. However, the wave normal, which is a vector normal to the wave front, refracts positively and propagates with a velocity different from the group velocity. We will use a p-polarized wave packet, but the results apply equally to the s-polarized packet.

We have implemented numerical calculations to confirm the approximations and to show smaller second-order effects. This numerical calculation has also been applied to a case for which we predicted the existence of a backward lateral wave. The backward lateral wave occurs in a NIM when the angle of incidence is beyond the critical angle. With incidence from free space on a lossless NIM, existence of a critical angle (Ishimaru, Thomas *et al* 2005) requires  $-1 < n < 0$ .

#### 4.1 Analytical formulation

We consider the interface between a half space of a NIM and free space, with the normal direction to the boundary plane being the Z direction, positive into the NIM. The incident wave packet is taken as p-polarized, completely determined by one component of the magnetic field, which we take to be in the Y direction. The incident wave packet in free space ( $E_x, E_z, H_y$ ) is then given by  $H_y(x, z, t) = \text{Re} \psi_i(x, z, t)$  with

$$\psi_i = \exp \left[ j\omega_o \left( t - \frac{z'}{c} \right) - \frac{(t - z'/c)^2}{T_o^2} - \frac{x'^2}{W_o^2} \right] \quad (4.1)$$

where  $\omega_0$  = carrier frequency,  $c$  = speed of light,  $T_0 = 2/\Delta\omega$ ,  $\Delta\omega$  = frequency band, and  $W_0$  is the half width of the packet at  $1/e$  of its peak amplitude in the  $x'$  direction. As shown in Figure 4.1, the incident packet propagates along the  $z'$  direction coordinate, and  $x'$  is the transverse coordinate of the packet. The  $(x', z')$  coordinates are related to  $(x, z)$  through rotation by the angle of incidence  $\theta_0$  of the beam centerline. The electric field is obtained as  $\vec{E} = (1/(j\omega\epsilon_0))\nabla \times (H_y \hat{y})$ . This is a collimated wave packet applicable when  $W_0 \gg \lambda$  and  $\Delta\omega \ll \omega_0$ . To obtain the analytical expression for the packet in the medium, we first rotate the coordinate system from  $(x', z')$  to  $(x, z)$  and take a double Fourier transform with respect to direction  $x$  and time  $t$  at  $z = 0$ .

$$\begin{aligned} \bar{\psi}_i(k_x, 0, \omega) &= \int_{-\infty}^{\infty} \int_{-\infty}^{\infty} \psi_i(x, z, t) \exp(-j\omega t + jk_x x) dt dx \\ &= \frac{\pi W_0 T_0}{\cos \theta_0} \exp \left[ -\frac{(\omega - \omega_0)^2 T_0^2}{4} - \frac{(k_x - \frac{\omega}{c} \sin \theta_0)^2 W_0^2}{4 \cos^2 \theta_0} \right] \end{aligned} \quad (4.2)$$

To obtain the field in the NIM where  $z > 0$  (medium 2), we multiply  $\bar{\psi}_i$  by the transmission coefficient  $T(k_x, \omega)$  and the propagation factor  $\exp(-jk_{z2}z)$ , and then take the inverse Fourier transform. We obtain

$$\psi_t(x, z, t) = \frac{1}{(2\pi)^2} \int_{-\infty}^{\infty} \int_{-\infty}^{\infty} T(k_x, \omega) \bar{\psi}_i(k_x, 0, \omega) \exp(-jk_{z2}z - jk_x x + j\omega t) dk_x d\omega \quad (4.3)$$

where

$$\begin{aligned} T(k_x, \omega) &= \frac{2k_{z1} / \epsilon_0}{\frac{k_{z1}}{\epsilon_0} + \frac{k_{z2}}{\epsilon}} \\ k_{z1} &= \sqrt{k^2 - k_x^2}, \quad k_{z2} = \sqrt{(kn)^2 - k_x^2}, \quad k = \omega/c \end{aligned}$$

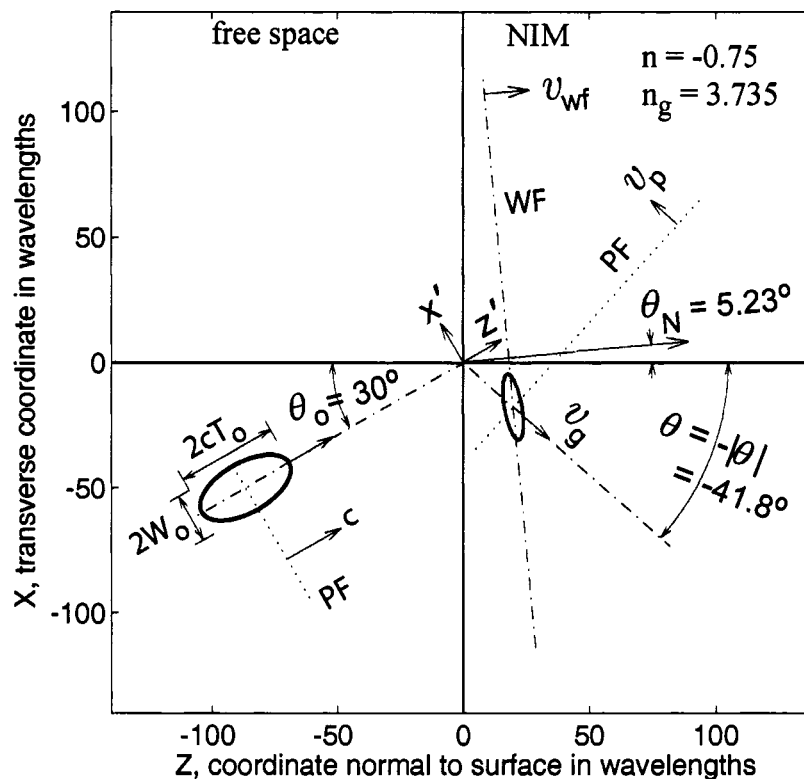


**Figure 4.1** Wave packet incident on negative refractive index medium. Wave packets are shown as heavy contour lines of  $|\vec{H}|$  at a level of  $1/e$  from the peak. The incident packet is shown at time  $-5T_0$  and the refracted packet at time  $5T_0$  relative to time of incidence of the peak. The wave packet propagates with the group velocity  $v_g$  in the direction  $\theta = -|\theta|$ . The wave front (WF) propagates with the wavefront velocity  $v_{wf}$  in the direction of the wave normal  $\vec{N}(\theta_N)$ . The phase front (PF) propagates with the phase velocity  $v_p$  in the direction opposite to the group velocity.

In the computation of  $k_{z1}$  and  $k_{z2}$ , care must be taken to choose the square root which corresponds to attenuation of the outgoing wave; that is a negative imaginary part for the  $\exp(+j\omega t)$  convention used here. Similarly the reflected wave is obtained by multiplying by the reflection coefficient  $R(k_x, \omega)$  and a propagation factor  $\exp(+jk_{z1}z)$  for a negative-going wave in the free-space medium. Thus, in the time domain

$$\psi_r(x, z, t) = \frac{1}{(2\pi)^2} \iint R(k_x, \omega) \bar{\psi}_i(k_x, 0, \omega) \exp(+jk_{z_0}z - jk_x x + j\omega t) dk_x d\omega \quad (4.4)$$

Assuming that  $T(k_x, \omega)$  is a slowly varying function of  $k_x$  and  $\omega$ , we can evaluate (4.3) by an approximation method that is essentially an application of the method of steepest descent. The approximation is asymptotic in the large parameters  $W_0$  and  $T_0$ . Noting that  $\bar{\psi}_i$  in (4.2) is highly peaked near  $\omega_0$  and  $\frac{\omega_0}{c} \sin \theta_0$ , we expand  $k_{z2}$  and keep the first-order terms.

$$k_{z2} = k_{z0} + k_x' \frac{\partial k_{z2}}{\partial k_x} + \omega' \frac{\partial k_{z2}}{\partial \omega} \quad (4.5)$$

where  $k_x' = k_x - \frac{\omega_0}{c} \sin \theta_0$ ,  $\omega' = \omega - \omega_0$ , and  $\frac{\partial k_{z2}}{\partial k_x}$  and  $\frac{\partial k_{z2}}{\partial \omega}$  are evaluated at  $\omega_0$  and  $k_{x0} = \frac{\omega_0}{c} \sin \theta_0$ . With  $T(k_x, \omega) = T(k_{x0}, \omega_0)$  the inner integral on  $k_x$  is a straightforward example of completing the square in ( $k_x$  – linear shift term) and finding the remaining term that is independent of  $k_x$  times a known definite integral that gives a factor of  $2\sqrt{\pi} \cos(\theta_0)/W_0$ . Then, the outer integral on  $\omega$  can be done by the same method. This second integral has many terms, and requires considerable manipulation to reduce it to obtain this final analytical expression for  $\psi_t(x, z, t)$ .

$$\begin{aligned} \psi_t(x, z, t) &= T(k_{x0}, \omega_0) e^{-j\phi} F_b F_a \\ \phi &= k_{z0}z + k_{x0}x - \omega_0 t \\ F_b &= \exp \left[ - \left( x + \frac{\partial k_z}{\partial k_x} z \right)^2 \frac{\cos^2 \theta_0}{W_0^2} \right] \\ F_a &= \exp \left[ - \frac{(t - \vec{N} \cdot \vec{r})^2}{T_0^2} \right] \end{aligned} \quad (4.6)$$

where the vector  $\vec{N}$  is defined as

$$\vec{N} = \frac{\sin \theta_o}{c} \hat{x} + \frac{1}{c} \frac{(nn_g - \sin^2 \theta_o)}{\sqrt{n^2 - \sin^2 \theta_o}} \hat{z}$$

and the other subsidiary quantities are

$$\begin{aligned} k_{x_o} &= \frac{\omega_o}{c} \sin \theta_o = \frac{\omega_o}{c} n \sin \theta_2, \quad k_o = \frac{\omega_o}{c} \\ k_{z_o} &= \sqrt{k_o^2 n^2 - k_{x_o}^2} = k_o \sqrt{n^2 - \sin^2 \theta_o} = k_o n \cos \theta_2 \\ \frac{\partial k_z}{\partial k_x} &= -\frac{k_{x_o}}{k_{z_o}} = -\tan \theta_2 \end{aligned}$$

$$n_g = \text{group refractive index} = \frac{\partial(\omega n)}{\partial \omega} \quad (4.7)$$

Derivation of the group refractive index<sup>1</sup> in (4.7) has been presented by many classic authors including (Brillouin 1960) and (Born & Wolf 1989). From the equations following (4.6) until Section 4.2 we will use short notation that  $n = n(\omega_o)$  and

$$n(\omega) = n + \frac{(n_g - n)\omega'}{\omega_o} \quad (4.8)$$

---

<sup>1</sup> The formula  $n_g = \frac{\partial(\omega n)}{\partial \omega}$  is well known. It follows from the basic derivation of the group velocity of a packet made up of sine waves of two frequencies  $\omega + d\omega$  and  $\omega - d\omega$ , for which the wave numbers in the direction of propagation are  $k + dk$  and  $k - dk$ . If two waves of equal amplitude are added, the result is a modulated wave with carrier frequency  $\omega$  and modulation frequency  $\Delta\omega$  proportional to  $\sin(kz - \omega t) \cos(\Delta k \cdot z - \Delta\omega \cdot t)$ . The pure sine wave of the form  $\sin(kz - \omega t) = \sin(k(z - v_p t))$  has evident velocity (the phase velocity of the complex wave) of  $v_p = \omega / k$ , and similarly the pure cosine modulation has evident velocity of  $v_g = \Delta\omega / \Delta k$ . The group velocity is the limit as  $\Delta k \rightarrow 0$ , i.e.,  $v_g = \partial\omega / \partial k$ . The medium in which the wave propagates determines the function  $\omega = \omega(k)$ , but, at least over limited ranges in which the inverse relation is not double valued, this may also be regarded as an inverse function  $k = k(\omega)$ . It is a well known theorem that  $1/v_g = \partial k / \partial \omega$ . Thus,  $n_g = c/v_g = \partial(kc) / \partial \omega$ . But with the phase velocity as expressed above and the definition of index of refraction as  $n = c/v_p$ , then  $kc = \omega n$ , and we obtain (4.7). This derivation has been presented by many classic authors, including (Brillouin 1953) and (Born & Wolf 1989).

This first-order approximation is used in the analytic asymptotic approximation and also later in what we call the linear model.

The angle  $\theta_2$  is the angle of refraction given by Snell's law for incidence at the central angle  $\theta_0$  of the packet. The indexes  $n$  and  $n_g$  as well as  $\frac{\partial k_z}{\partial k_x}$  are to be evaluated at  $\omega_0$  and  $k_{x0}$ . The square root choice for  $k_{z0}$  is now well understood. It is plus or minus for  $n$  plus or minus, respectively. More rigorously, it is chosen so that  $\text{Im } k_{z0} < 0$  and that  $\text{Im } \varepsilon < 0$  and  $\text{Im } \mu < 0$ . Also note that since  $n$  is negative, the phase velocity  $v_p = c/n$  is negative. However, the group refractive index  $n_g$  and the group velocity  $v_g$  are positive. These are consistent with (Smith, Schurig *et al* 2002).

We note that this approximation applies when the transmitted wave is not evanescent, that is when there is no critical angle for total reflection or when the incident angle is not greater than this critical angle. We shall return to incidence at angles beyond the critical angle in Section 4.3.

The equation for the reflected field can be evaluated by the same method as described for the transmitted wave. If one makes only the approximation that  $R(k_x, \omega) = R(k_{x0}, \omega_0)$ , the resulting reflected field is the specular reflection of the incident wave with all frequency components having this central reflection coefficient. Thus, that approximation would correspond to a beam wave propagating coherently for distances small compared to  $\pi W_o^2 / \lambda_o$  and then showing dispersion. However, if the further approximation is made as to  $k_{zi} = \sqrt{k_{zo}^2 - k_x^2}$ , then the elliptical beam cross section will just move uniformly outwards at the specular reflection angle with speed of light  $c$ .

Equation (4.6) and the following term definitions show three features of wave propagation in the NIM due to the product of three functions. (1) The phase term  $\exp(-j\phi) = \exp(-jnk_o[\cos\theta_2 z + \sin\theta_2 x - (c/n)t])$  shows phase progression according

to Snell's law with  $n \sin \theta_2 = \sin \theta_o$ . Thus, the angle of refraction  $\theta_2$  and the phase velocity are negative because the index of refraction is negative. (2) The factor  $F_b$  clearly shows that the peak of the transmitted packet follows the line  $x = z \tan \theta_2$ . That is, the energy associated with the E and H fields of the packet is refracted negatively. (3) The factor  $F_a$  exhibits planar fronts given by

$$t - \vec{N} \cdot \vec{r} = \text{constant}. \quad (4.9)$$

The transmitted packet's skewed oval amplitude contour results from the product of the factors  $F_b$  and  $F_a$ . The vector  $\vec{N}$  is in the direction of the normal to the fronts of  $F_a$ . In connection with analysis of a modulated plane wave these fronts have been called interference fronts by other authors (Smith, Schurig *et al* 2002), (Pendry & Smith 2003) and also group fronts (Zhang & Park 2004). The angle  $\theta_N$  between the vector  $\vec{N}$  and the Z-axis is given by (Figure 4.1)

$$\tan \theta_N = \frac{N_z}{N_x} = \frac{\sin \theta_o \sqrt{n^2 - \sin^2 \theta_o}}{nn_g - \sin^2 \theta_o} \quad (4.10)$$

Here, we need to choose the correct sign for the square root, which comes from the occurrence of  $k_{z2o} = k_o \sqrt{n^2 - \sin^2 \theta_o}$ . This propagation factor must have a negative imaginary part for attenuation of the outward going wave. To have transmission into the NIM and not total reflection, we must have  $n^2 > \sin^2 \theta_o$ . For completeness we now consider the cases of both positive and negative index. For positive  $n$  the square root must be positive in its dominant real part, and we expect the group velocity to be smaller than the phase velocity, so  $n_g > n$ . Thus, the numerator and denominator of the fraction in (4.10) are positive and  $\theta_N$  is positive. For negative  $n$ ,  $k_{z2o}$  and the square root must be negative in its (dominant) real part. Since the group index must be positive and greater than 1 for causal signal propagation

(Brillouin 1960), the fraction on the right of equation (4.10) is positive and again  $\theta_N$  is positive.

Figure 4.1 illustrates these asymptotic-approximation results for a case  $n = -0.75$  and  $n_g = 3.735$ . These index values are chosen in a somewhat arbitrary way. We have chosen to study negative indexes somewhere near  $-1$ . With the choice of  $n = -0.75$ , the group index of  $3.735$  corresponds to that of a Drude-Lorentz model discussed below. The angle of incidence is chosen as  $30$  degrees, well below the critical angle of approximately  $48.6$  degrees. The beam wave packet of (4.1) is chosen to have a transverse half-width  $W_o = 10 \lambda$  and a half-length along the direction of propagation of  $cT_o = 20\lambda$ . The width and length are taken to the  $1/e$  amplitude relative to the peak, and this choice of  $T_o$  amounts to a bandwidth  $\Delta f$  to the  $1/e$  amplitude in frequency  $\Delta f / f_o = 0.05\pi$ . This is a reasonably narrow bandwidth and the choice of  $n_g$  as a constant across the integral in equation (4.4) is a reasonable approximation. Any material (metamaterial) with negative index of refraction will have strong dispersion. Variations with frequency may be modeled with a Drude (plasmonic) model (Drude 1900), a Drude-Lorentz model, or possibly a still more complex model. However, a Drude-Lorentz model, also referred to as a Lorentz model or Lorentz medium, provides what we may call a physical model with 3 parameters for permittivity. As also considered by (Ziolkowski & Heyman 2001), we shall use the same form to characterize the negative permeability. In the next section we shall consider cases that correspond to a Lorentz model, and carry out numerical solutions of the exact integral equations (4.3) and (4.4) for a single-resonance Drude-Lorentz behavior of both permittivity and permeability. To show the generality of the approach,  $\varepsilon$  and  $\mu$  are taken to be somewhat different.

The term Drude-Lorentz (or Lorentz) model refers to a classical model for electrons, bound with a simple-harmonic-oscillator potential, interacting with a cw electromagnetic field. The relative permittivity of such a medium has the form

$$\varepsilon_r = 1 + \frac{\omega_{pe}^2}{\omega_e^2 - \omega^2 + j\omega\Gamma_e} \quad (4.11)$$

where  $\omega_{pe}$  is the plasma frequency of the electrons,  $\omega_e$  is the harmonic oscillator frequency, and  $\Gamma_e$  the collision frequency. In the low-loss case  $\Gamma_e \ll \omega_{pe}$ . We also use this frequency variation with assigned parameters for the relative permeability  $\mu_r$ . For the low-loss case the real part of (4.11) has a negative minimum at a frequency slightly above  $\omega_e$  given by  $\omega^2 = \omega_e(\omega_e + \Gamma_e)$ . This minimum is

$$\min(\text{real}(\varepsilon_r)) = 1 - \frac{\omega_{pe}^2}{2\omega_e\Gamma_e + \Gamma_e^2} \approx 1 - \frac{\omega_{pe}}{2\omega_e} \frac{\omega_{pe}}{\Gamma_e}$$

Since  $\omega_{pe} \gg \Gamma_e$  and  $\omega_e$  is typically of the same order as  $\omega_{pe}$ , it is possible to set  $\varepsilon_r$  equal to any reasonable negative value at some frequency in the normal dispersion region slightly above this minimum.

#### **4.2 Numerical solutions: Cases without a critical angle $\theta_c$ or with angle of incidence less than $\theta_c$**

We have calculated solutions to (4.3) and (4.4) with brute-force numerical integrations. The standard computations are based on a grid of 2066 values of  $k_x$  by 1811 values of  $\omega$ . It is a variable-step grid with finer steps near the central peak of the Gaussian and coarser steps out towards the edge of the rectangular integration area. The integration method is trapezoidal. We note that (4.3) and (4.4) could be considered as scaling in frequency relative to center frequency  $\omega_o$  and x component of wavenumber relative to the center  $k_{xo} = (\omega_o / c) \sin \theta_o = k_o \sin \theta_o$  if

- the Gaussian widths are expressed in wavelengths, that is  $W_o = W_n \lambda_o$  and  $cT_o = T_n \lambda_o$  with  $\lambda_o = 2\pi / k_o$  and the subscript  $n$  denoting normalized;
- the permittivity and index of refraction are scaled as functions of frequency relative to this normalized frequency.

This result essentially follows from the electrodynamic similitude of Maxwell's equations (Stratton 1941). We carried out computations for a specific center frequency  $f_o = 10^{11}$  Hz, but we show results plotted in wavelength units for  $x$  and  $z$ , which would then apply to any center frequency so long as the index of refraction and permittivity are scaled correspondingly.

We consistently computed cases with  $W_o = 10\lambda_o$  and  $cT_o = 20\lambda_o$  as in Figure 4.1. With these fairly rapid Gaussian cutoffs, we found that we could obtain good results with a grid where  $(k_x - k_{x_o})W_o / (2 \cos \theta_o)$  extends from  $-14$  to  $+16$  and where  $(\omega - \omega_o)T_o / 2$  extends from  $-13$  to  $+13$ . These choices make the Gaussian factors become  $\exp(-14^2) \approx 7.6 \cdot 10^{-86}$ ,  $\exp(-16^2) \approx 6.6 \cdot 10^{-112}$ , and  $\exp(-13^2) \approx 4.0 \cdot 10^{-74}$  on the outer edges along the center lines of the other variable, respectively. We found these limits and the grid fineness by trial and error where we required that the main parts of the transmitted and reflected fields change by less than 1 part in  $10^6$  as we went to a next test with larger limits or finer grids.

We limited our computations to times such that  $ct < 10\lambda_o$ , where  $t = 0$  is the time when the incident pulse is centered at the origin, per equation (4.1). Hence, the maximum values of  $x$  and  $z$  where the pulse is of interest in the cases we examined is limited to about  $200\lambda_o$ . Finer grids would be required for larger values of  $x$  and  $z$ . Also, a finer grid is required for some small-amplitude fields considered in the last section on backward lateral waves.

We present a selection of cases to illustrate the following features of reflection from and refraction in a NIM.

- The asymptotic approximation gives a very accurate description of the motion of the peak of the transmitted wave. The peak follows the line at the Snell's law angle of the center frequency, and it moves with the speed of the group velocity of the center frequency. The peak amplitudes are fairly close to the approximate prediction.
- The elliptical amplitude distribution is skewed and rotated in coarse agreement with the asymptotic approximation. The size of the contour at  $1/e$  of the peak is quite close to that predicted by the asymptotic approximation.
- As expected, the reflected wave is well predicted by specular reflection of the pulse with the reflection coefficient of the center frequency.
- The curved variation of index of refraction in a Lorentz model provides some asymmetry to the transmitted pulse, but still leads to a pulse that reasonably follows the asymptotic approximation.

Figure 4.2 and Figure 4.3 show comparisons of numerical solutions to the exact Fourier integral equations (4.3) and (4.4) for cases corresponding to the asymptotic solution shown in Figure 4.1. Because the reflection and transmission coefficients  $R$  and  $T$  depend on  $\epsilon_{2r}$  as well as  $n_2$ , it is necessary to specify this additional quantity at the band center as well as functions to determine their variation across the frequency band of integration. We chose a band-center value  $\epsilon_{2r_0} = -0.8 - 0.002j$ . Then, the band-center value of relative permeability is  $\mu_{2r_0} = n_{2_0}^2 / \epsilon_{2r_0} = -0.70312 - 0.000117j$ . To specify the variation of  $n$  and  $\epsilon$  across the band we consider two cases. They are: (a) a single-resonance Lorentz model for  $\epsilon_{2r}$  and  $\mu_{2r}$  and (b) a linear model for  $\epsilon_{2r}$

and  $n_2$ . We include just one linear model calculation. It shows that the transmitted pulse in the NIM is relatively insensitive to details of the variation of  $n$  and  $\varepsilon_r$  about the center frequency if the relatively wide-band condition applies.

We have chosen a single-resonance Lorentz model for several reasons. It has only 3 parameters for the permittivity and another 3 for the permeability. Also, the Lorentz model has been considered as a simple physical example by several

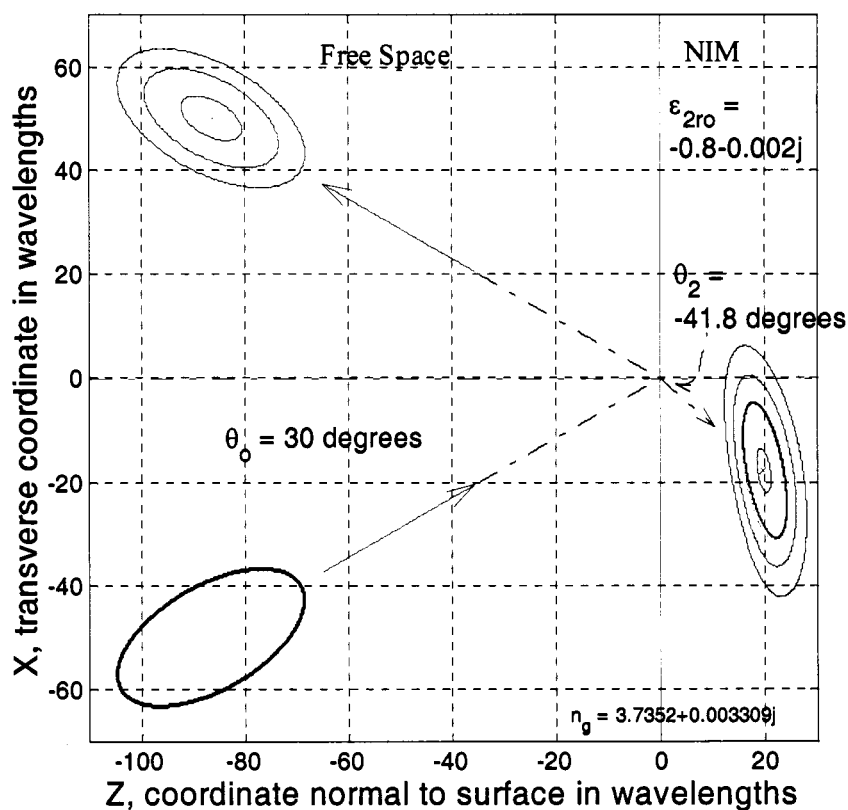


**Figure 4.2** Contour plots of  $|\vec{H}|$  for Lorentz model with  $n_{2o} = -0.75 - 0.001j$  at time  $= 5T_o$  for transmitted and reflected fields. The incident contour is at time  $-5T_o$ . From exact theory numerical field calculations, the transmitted contours are at levels of 0.9, 0.6,  $1/e$ ,  $0.4*1/e$ , and  $0.1*1/e$  relative to the peak of 0.8855 and reflected contours at 0.9, 0.6, and  $1/e$  relative to this peak of 0.1085. For the analytic asymptotic approximation only the  $1/e$  contours of the incident and transmitted wave are shown (in black). (Incident peak = 1.0, transmitted peak = 0.9358.)

other researchers in the study of NIM; e.g., (Ziolkowski & Heyman 2001), (Smith, Schurig *et al* 2002). Two of the three conditions to determine these parameters are set by the choice of real and imaginary parts of  $\epsilon_{2ro}$  and  $n_{2o}$  (which determine  $\mu_{2ro}$ ). The third condition we shall take arbitrarily is a moderately wide-band condition.

Thus, we take  $\epsilon_r(\omega)$  as given by (4.11). The analogous Lorentz form of the permeability is taken as

$$\mu_r = 1 + \frac{\omega_{pm}^2}{\omega_m^2 - \omega^2 + j\omega\Gamma_m}. \quad (4.12)$$

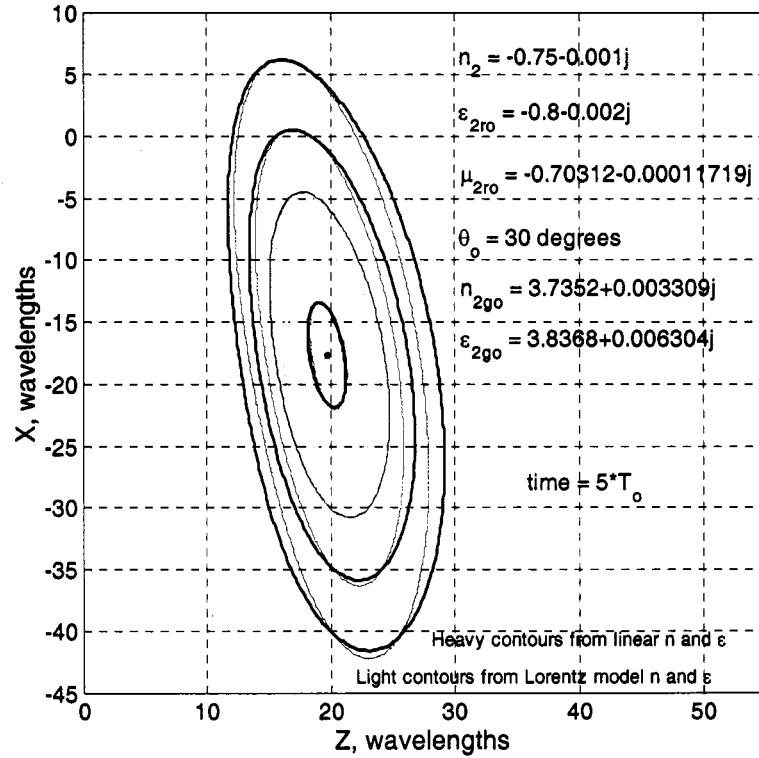


**Figure 4.3** A close comparison of transmitted (refracted) pulses. Comparison is of Lorentz model variation of  $n_2$  and  $\epsilon_{2r}$  versus a model with linear variation of  $n_2$  and  $\epsilon_{2r}$  with matching  $n_g$  and  $\epsilon_{2rg}$  at central frequency. Contour levels are 0.9, 0.6,  $1/e$ ,  $0.4*1/e$ ,  $0.1*1/e$  relative to the respective peaks.

We have chosen a wide-band condition  $\omega_{pe} / \omega_e = \omega_{pm} / \omega_m = 2.5$ . The larger the choice of this ratio, the wider the band of the resonance. The limit of this ratio approaching infinity leads to a pure Drude (plasma) model.

The group index at frequency  $\omega_o$  is given by

$$n_g = \frac{n(\omega_o)}{2} \left[ \frac{1}{\epsilon_r} \frac{\partial(\omega\epsilon_r)}{\partial\omega} + \frac{1}{\mu_r} \frac{\partial(\omega\mu_r)}{\partial\omega} \right] = \frac{n(\omega_o)}{2} \left[ \frac{\epsilon_{rg}}{\epsilon_r} + \frac{\mu_{rg}}{\mu_r} \right] \quad (4.13)$$

where the term in square brackets is evaluated at  $\omega_o$ . We define the group relative permittivity by analogy as  $\epsilon_{rg} = \partial(\omega\epsilon_r) / \partial\omega$  and similarly for permeability. In the linear model, the group index matches the slope of  $n(\omega)$  at  $\omega_o$ . For our case of  $n_{2o} = -0.75 - 0.001j$ ,  $\epsilon_{2ro} = -0.8 - 0.002j$ ,  $\mu_{2ro} = n_{2o}^2 / \epsilon_{2ro}$  and the wide-band condition as stated, then  $n_{2go} = 3.7352 + 0.003309j$ . The linear model also requires the value of the linear fit to  $\epsilon_{2r}$  at  $\omega = \omega_o$  given by  $\epsilon_{2rg}$ , which from (4.11) and (4.13) is

$$\epsilon_{2rg} = \epsilon_{2ro} \left[ 1 + \frac{\omega_o \omega_{pe}^2 (2\omega_o - j\Gamma_e)}{(\omega_e^2 - \omega_o^2 - j\omega_o \Gamma_e)^2 \epsilon_{2ro}} \right] = 3.8368 + 0.006304j \quad (4.14)$$

The Lorentz model gives a positive imaginary part for  $\epsilon_{2rg}$  and  $n_g$ . This is evident from classic Lorentz model dispersion curves—in the normal dispersion region above the resonant frequency, the magnitude of the imaginary part of  $\epsilon(\omega)$  is decreasing. However, this result will not violate the outgoing radiation condition within our band of approximation. In this band  $n(\omega)$  is given by (4.8) and

$$\epsilon(\omega) = \epsilon(\omega_o) + (\epsilon_{2rg} - \epsilon(\omega_o))(\omega - \omega_o) / \omega_o.$$

If  $\text{Im}\{\epsilon\} = \epsilon''$  and  $\epsilon''(\omega_o) = -\Delta_1$  where  $\Delta_1$  is a small positive quantity, then  $\epsilon_{2rg} = \Delta_2$  where  $\Delta_2$  is a positive quantity of the order of  $\Delta_1$  and

$$\epsilon'' = -\Delta_1 + \frac{(\Delta_2 + \Delta_1)(\omega - \omega_o)}{\omega_o} \quad (4.15)$$

within our band of integration. In other words, (4.15) shows that even though the  $\text{Im}\{\varepsilon_{2r}\}$  is positive,  $\text{Im}\{\varepsilon\}$  is negative. The same reasoning applies to  $\text{Im}\{n\}$ .

Figure 4.2 shows the numerically calculated contours of the magnitude of the transmitted field and reflected field at a time  $t = 5T_o$  as in Figure 4.1. Figure 4.2 also shows black contours at  $1/e$  of the peak for the incident wave at time  $t = -5T_o$  and for the asymptotic approximation for the transmitted wave at  $5T_o$ . The third numerical contour at  $1/e$  of the transmitted peak is very close to the black  $1/e$  contour from the analytic approximation. This illustrates that the asymptotic approximation works well for the Lorentz model with incidence not beyond the critical angle. We want to emphasize this point since the asymptotic approximation utilizes only the linear variation as given by (4.13) and is given analytically by (4.6) and (4.7).

There are several significant points concerning these calculations.

The peak of the numerical integral calculation for the transmitted wave follows very closely along the Snell's angle line at the group velocity. The "x" in Figure 4.2 at the location of the transmitted peak has coordinates  $x / \lambda_o = -17.67$  and  $z / \lambda_o = 19.65$ . The asymptotic approximation has its peak at  $X_p / \lambda_o = (5cT_o / n_g) \sin \theta_2 = -17.85$  and  $Z_p / \lambda_o = (5cT_o / n_g) \cos \theta_2 = 19.95$ . With an incident peak normalized to 1, the amplitude of the peak from numerical integration is 0.831, as compared to the asymptotic approximation value of 0.936. In general, we find the magnitude of the transmitted asymptotic peak to agree only within about 10% of the result found by numerical integration. The numerical integration depends on the value and variation of the relative permittivity  $\varepsilon_{2r}$ , whereas the asymptotic approximation does not.

The time duration of the pulse (as measured by the length of the  $1/e$  contour along the direction of propagation, the line at angle  $\theta_2$  is very close to that of the

asymptotic approximation. However, the width (minor axis) of the numerically integrated peak is somewhat greater than that of the asymptotic approximation. Also, the contours are slightly egg-shaped with a little more width farther from the origin than closer relative to a symmetric shape. But the slope of the major and minor axes of the contours, predicted by the interaction of the factors  $F_b$  and  $F_a$  in (4.6), appears to be in good agreement.

The reflected pulse, as expected, is very close to symmetric with the incident pulse. The reflected peak is at  $x / \lambda_o = 50.14$  and  $z / \lambda_o = -86.38$  as compared to specular values  $100 \cdot \sin(\pi / 6) = 50$  and  $-100 \cdot \cos(\pi / 6) \approx -86.6$ . The magnitude of the reflected peak computed from inverse transform is 0.1057 compared to the asymptotic approximation of 0.1069. In summary for this case, the asymptotic approximation gives a qualitatively and heuristically satisfactory explanation of the refracted and reflected waves.

Figure 4.1 and Figure 4.2 show that the wave in the Lorentz model medium, with  $n_g = 3.735$ , is moving much more slowly than the wave in free space because the transmitted contours are visibly much closer to the origin and the length to the  $1/e$  contour is much smaller. In addition, the reflected peak shows better agreement between the asymptotic specular reflection and the numerical integration. In Figure 4.2 the peaks as found from numerical integration (on a grid of  $0.01\lambda_o$  by  $0.01\lambda_o$ ) are plotted as an "x" in the center of the contours.

Figure 4.3 shows details of the comparison of the Lorentz model results of Figure 4.2 with a numerical integration of the case of constant  $n_g = 3.7352 + 0.003309j$  and constant  $\epsilon_{2rg} = 3.8368 + 0.006304j$ , which we call a linear model. Figure 4.3 presents an enlargement of the fourth quadrant region of Figure 4.2, but with comparison of two numerical integration solutions. There is at

least as much difference between these two numerical solutions as between the asymptotic approximation and the Lorentz model solution. The Lorentz model solution has a higher peak, by about 6%, and has more asymmetry than the linear model, but qualitatively the solutions are similar.

We have calculated reflected and transmitted waves for the case of a medium with  $n_{2o} = -1.25 - 0.001j$  and with various positive values of  $n_g$  and we find similar results. The asymptotic solution provides a good qualitative understanding and prediction of the velocity of the transmitted peak and the approximate size and orientation of the  $1/e$  contour. If  $n_2 < -1$ , there is no critical angle, and the asymptotic approximation given by (4.6) is valid for all angles of incidence.

### ***4.3 Incidence beyond the critical angle: the backward lateral wave and Goos-Hänchen effect***

For two positive-index dielectric materials with a planar boundary, with incidence from a medium of larger positive index onto one of smaller index, there is a critical angle for total internal reflection. At angles slightly larger than this critical angle, there are two known, yet somewhat unusual, phenomena known as the lateral wave and the Goos-Hänchen shift (Ishimaru 1991). We consider here a backward lateral wave and find numerical solutions that demonstrate this behavior for the case of incidence from free space to NIM of index between  $-1$  and  $0$ , specifically for  $n_{2o} = -0.75 - 0.001j$  as considered in the previous section. There is a critical angle

$$\theta_c = \sin^{-1}(|\operatorname{Re}\{n_{2o}\}|) = 48.59^\circ.$$

We present here results for  $\theta_o = 5\pi/16$  radians =  $56.25^\circ$ . In this solution the small transmitted-wave peak moves backwards along the surface (compared to the usual positive index case) and causes a small amplitude lateral wave on this backwards side of the main reflected pulse. We call this the backward lateral wave (BWLW).

The lateral wave is separated from the radiated-wave term in an asymptotic expansion as the part of the complex integral contributed by the path around a branch point. When incidence is not beyond the critical angle, the branch point lies in a part of the complex plane of integration that does not come close to the steepest-descent curve and thus does not make a significant contribution. The standard theory of these asymptotic expansions is done in terms of single-frequency (cw) waves. From a study of continuous waves at the interface of a normal dielectric and a NIM, we predicted in Chapter 3 the existence of backward lateral waves and other asymptotic phenomena (Ishimaru, Thomas *et al* 2005). The numerical case presented here shows the features of a backward lateral wave examined in a region fairly close to the origin, that is, the (2-D) point of incidence of the center of the pulse.

Figures 4.4 through 4.6 show contour plots of the reflected and transmitted waves (the transverse component  $H_y$ ) at times  $t = 3T_o, 6T_o$  and  $9T_o$ , respectively, after the peak of the incident pulse (same width and duration as in previous section) arrives at the origin. To illustrate the scale, the incident  $1/e$  contour is shown at time  $= -t$ . Recall that  $cT_o = 20\lambda_o$  so that at  $t = 3T_o$  the reflected peak is about  $60\lambda_o$  from the origin, and the reflected wave has taken its elliptic shape quite accurately within  $1/e$  of its peak. However, the outer contours are still forming in Figure 4.4.

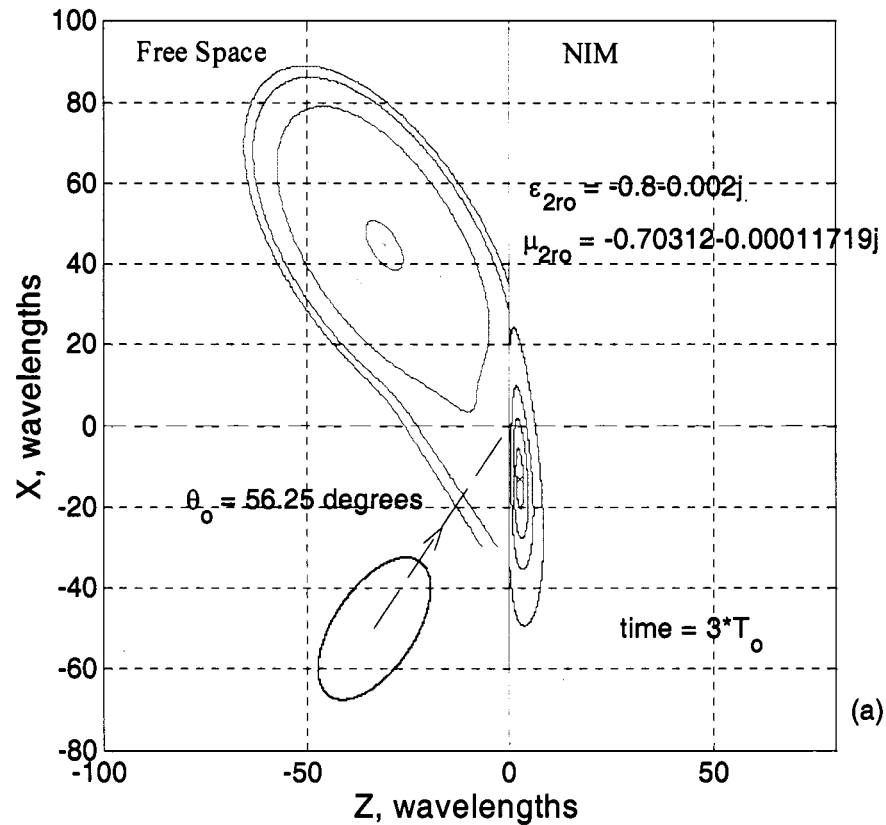


**Figure 4.4** First step in the progression of a backward lateral wave for a Lorentz model with  $n_2 = -0.75 - 0.001j$ . The contours shown are of the transverse field  $|H|$ . Transmitted and reflected wave contours are shown at time  $= 3T_0$ . One incident wave contour is shown at time  $= -3T_0$ .

In all three of these figures, the reflected contours are at 0.9, 0.65, 1/e, 0.1\*1/e, 0.02\*1/e, and 0.01\*1/e of reflected peak. The transmitted contours are at 0.9, 0.65, 1/e, and 0.2\*1/e of peak at x in the NIM, and the incident contour is at 1/e of the incident peak. Heavy contours denote the 1/e levels.

The asymptotic theory has a heuristic interpretation for this low-amplitude transmitted wave propagating near the surface as the source of the backward lateral wave, which shows up as the asymmetric tails in Figures 4.4 through 4.6. The surface source point moves in the backwards direction at approximately the group

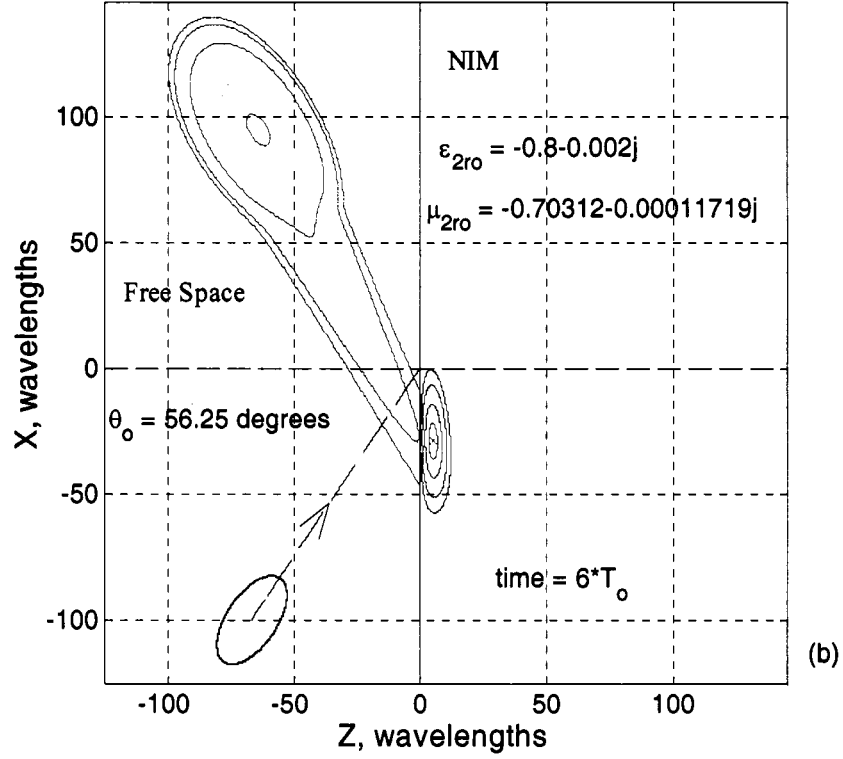


**Figure 4.5** Second step in the progression of a backward lateral wave for a Lorentz model with  $n_2 = -0.75 - 0.001j$ . The contours shown are of the transverse field  $|H|$ . Transmitted and reflected wave contours are shown at time  $= 6T_0$ . One incident wave contour is shown at time  $= -6T_0$ .

velocity for the dispersive NIM. Asymptotically, the BWLW radiates outwards from the surface source point at an angle to the normal equal to the critical angle. Thus, the similar triangles shown in Figure 4.7 lead to the result (Ishimaru, Thomas *et al* 2005) that the asymptotic BWLW will create a wave front emerging at an angle  $\theta_l$ . The law of sines applied to this triangle gives, for our Lorentz case with  $n = -0.75$  and  $n_g = 3.735$

$$\sin^2(\theta_l) = \frac{n_g^2(1 - |n|^2)}{1 + 2n_g|n| + n_g^2}; \quad \text{thus, } \theta_l \approx 33^\circ. \quad (4.16)$$

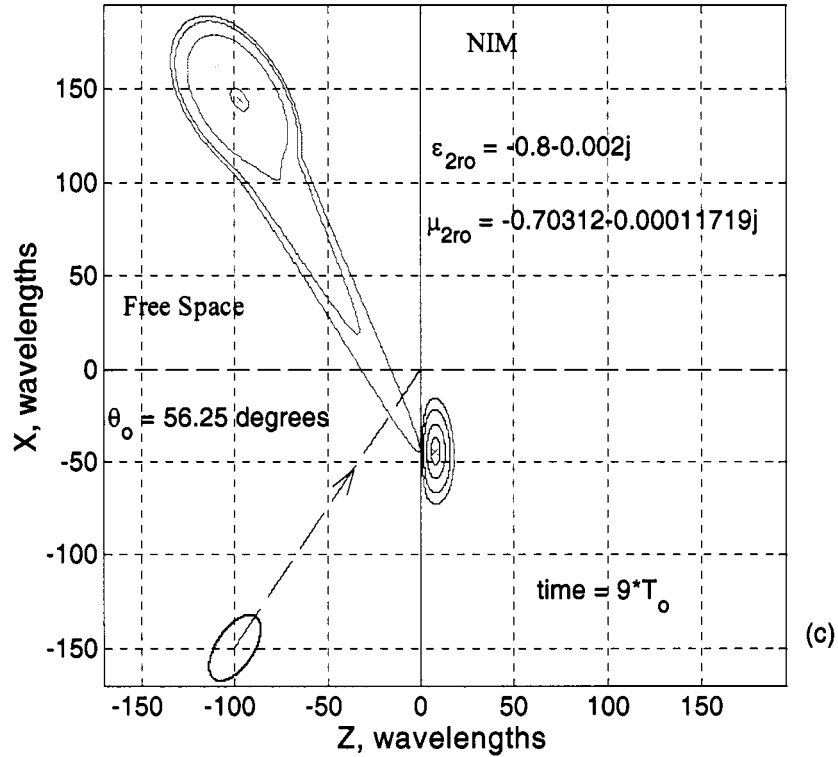


**Figure 4.6** Third (last) step in the progression of a backward lateral wave for a Lorentz model with  $n_2 = -0.75 - 0.001j$ . The contours shown are of the transverse field  $|H_y|$ . Transmitted and reflected wave contours are shown at time  $= 9T_0$ . One incident wave contour is shown at time  $= -9T_0$ .

Equation (4.16) provides an approximate explanation of the angle of the asymmetric tails in Figures 4.4 through 4.6, as one may read off these true-angle plots.

We compile in Table 4.1 a summary concerning the peaks in Figures 4.4 through 4.6. The peak locations ( $X$  and  $Z$ ) are given in wavelength units (taken as  $c/10^{11}$  in our computations), the time is given in terms of the  $1/e$  time duration of the Gaussian pulse ( $T_0 = 2 \cdot 10^{-10}$  s) and the amplitudes are all normalized to the unit incident  $H = 1$  A/m. The BWLW contour is taken from a judgment of the appearance

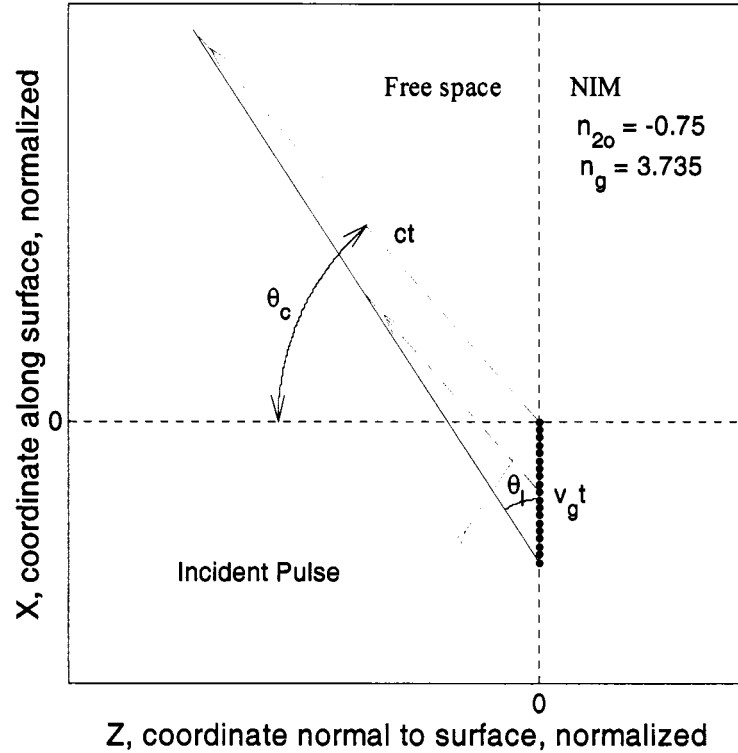


**Figure 4.7** Angle of the backward lateral wave. The small transmitted peak travels down the X axis and radiates at each point at the angle  $\theta_c$  relative to the surface normal.

of the plots as the  $0.02 \cdot (1/e) \cdot (\text{Peak})$  contour level. It is qualitatively the highest contour where the extended tail appears.

**Table 4.1** Progression of Peaks in Time

Time <sup>1</sup>	$3T_0$	$6T_0$	$9T_0$
$X_t (\lambda_0)$	-13.007	-28.885	-44.209
$Z_t (\lambda_0)$	2.5215	5.2335	7.923
Amplitude	0.090569	0.058165	0.042926
$X_r (\lambda_0)$	44.724	94.610	144.491
$Z_r (\lambda_0)$	-30.789	-64.019	-97.290
Amplitude	0.941092	0.918465	0.885763
BWLW contour level	0.00692	0.00676	0.00652

<sup>1</sup> The first three rows refer to the transmitted peak, the next three refer to the reflected peak, and the last row is the approximate BWLW amplitude.

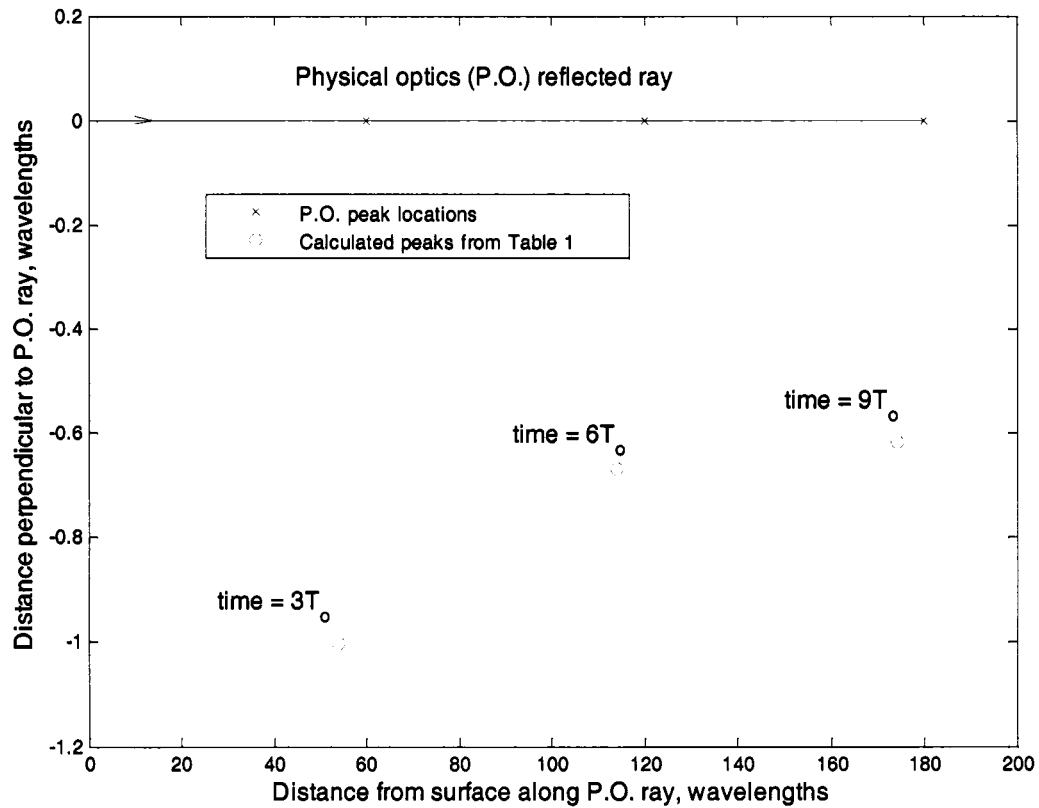


**Figure 4.8** Goos Hänchen shift of reflected peaks. The shift is towards the negative  $x$  direction by slightly less than a wavelength. The calculated peaks lag behind the P.O. peaks by about 5 wavelengths.

Least-mean-square linear fits to the three transmitted peak points give constant  $x$  and  $z$  components of velocity  $V_x = -7.7951 \cdot 10^7$  m/s and  $V_z = 1.3494 \cdot 10^7$  m/s that fit the data very closely. The resulting index  $n_g = c / \sqrt{V_x^2 + V_z^2} = 3.7896$  is satisfactorily close to 3.7352 with allowance for the second-order dispersion effects.

In Figure 4.8 we plot the location of the points  $(Z_r, X_r)$  compared to the straight line of the ideal physical optics reflection of the center of the incident pulse. The points where the physical optics peak would be at times  $t = 3T_0$ ,  $6T_0$  and  $9T_0$  are denoted by an  $x$  on the straight line, and the calculated points are shown by a small circle. The vertical displacement for large  $t$  between these two positions is interpreted

as the Goos-Hänchen shift of the NIM, with the shift being in the negative X direction (Lakhtakia 2004), (Qing & Chen 2004). The delay involved in the shift accounts for the calculated pulse lagging behind the instantaneous physical optics points.

#### **4.4 Concluding remarks regarding negative refraction, BWLW, and negative Goos-Hänchen shift**

We have demonstrated that an asymptotic analytic first-order approximation to the calculation of transmission and reflection at a plane boundary between free space and a NIM gives a good estimate of the negative refraction that occurs. We have provided an exact calculation of the negative refraction phenomenon for a pulse in time and 2-D space. We have also calculated a case that demonstrates the phenomenon of a backward lateral wave (as predicted on general theoretical grounds (Ishimaru, Thomas *et al* 2005)) and also a small negative displacement of the peak of the reflected wave that we interpret as a Goos-Hänchen shift.

The criterion for validity of the asymptotic approximation may be stated as:  $n_g$  and  $\epsilon_{rg}$  must not change greatly over the band of integration. The assumed choice of a Lorentz model with  $\omega_{pe} / \omega_e = 2.5$  met this criterion for our particular choice of a time pulse with 20 cycles from maximum sinusoidal peak to the sinusoidal peak with amplitude  $1/e$  of the maximum. However, when we look at what metamaterial designers may have achieved so far, we find considerably narrower bandwidths. For example, if we try to characterize roughly the resonances found by (Ishimaru, Lee *et al* 2003), we find that the resonances would have  $\omega_{pe} / \omega_e \approx 0.5$ . Then, the asymptotic approximation would not work at all for our pulse. On the other hand, a more monochromatic pulse with at least 300 cycles from maximum sinusoid to the  $1/e$  amplitude sinusoid would satisfy the condition for validity of the asymptotic approximation. This narrower-band pulse would again exhibit negative refraction

with propagation at the speed given by the group index. The calculational method should go through as in our simpler case, but the number of intervals would increase and consequently the computation time, too.

An important related conclusion is that we need to find methods to make wider-band metamaterials for practical use with pulses that are not extremely narrow band. In other words we need to find a way to increase the plasma frequency relative to the resonant frequency (for both electric and magnetic Lorentz models). That statement does not have an obvious practical solution, but it has some interpretation in that the plasma frequency of a natural material is related to its electron density, whereas the resonant frequency is typically an atomic or molecular property.

#### 4.5 Notes to Chapter 4

- Born M, Wolf E. 1989. *Principles of Optics: Electromagnetic Theory of Propagation, Interference and Diffraction of Light*. Cambridge, U.K.: Cambridge University Press
- Brillouin L. 1960. *Wave Propagation and Group Velocity*. New York: Academic Press
- Drude P. 1900. Zur Electronentheorie der Metalle. *Annalen der Physik* 1: 566
- Ishimaru A. 1991. *Electromagnetic Wave Propagation, Radiation, and Scattering*. Englewood Cliffs, New Jersey: Prentice-Hall. 637 pp.
- Ishimaru A, Lee SW, Kuga Y, Jandhyala V. 2003. Generalized constitutive relations for metamaterials based on the quasi-static Lorentz theory. *IEEE Transactions on Antennas and Propagation* 51: 2550-7
- Ishimaru A, Thomas JR, Jaruwatanadilok S. 2005. Electromagnetic waves over half-space metamaterials of arbitrary permittivity and permeability. *IEEE Transactions on Antennas and Propagation* 53: 915-21
- Lakhtakia A. 2004. Positive and negative Goos-Hanchen shifts and negative phase-velocity mediums (alias left-handed materials). *AEU-International Journal of Electronics and Communications* 58: 229-31
- Pendry JB, Smith DR. 2003. Comment on "Wave refraction in negative-index media: Always positive and very inhomogeneous". *Physical Review Letters* 90: 029703-1
- Qing DK, Chen G. 2004. Goos-Hanchen shifts at the interfaces between left- and right-handed media. *Optics Letters* 29: 872-4
- Smith DR, Schurig D, Pendry JB. 2002. Negative refraction of modulated electromagnetic waves. *Applied Physics Letters* 81: 2713-5
- Stratton JA. 1941. *Electromagnetic Theory*. New York: McGraw-Hill. 615 pp.
- Zhang ZM, Park K. 2004. On the group front and group velocity in a dispersive medium upon refraction from a nondispersive medium. *Journal of Heat Transfer-Transactions of the Asme* 126: 244-9
- Ziolkowski RW, Heyman E. 2001. Wave propagation in media having negative permittivity and permeability. *Physical Review E* 64: 056625-1--15

## 5. Transmission and focusing by a planar slab with index close to $-1$

We calculate in considerable detail the transmission and focusing through a planar slab of metamaterial with relative permittivity and relative permeability both close to  $-1$ . As shown at the beginning of Chapter 3, the index of refraction will then also be negative, and close to  $-1$ . We start with a treatment of plane waves in the spatial Fourier domain and proceed to calculate the focusing of a 2-D line source.

As has been shown (Pendry 2000), (Thomas & Ishimaru 2002) in the limit of  $\epsilon_{2r} \rightarrow -1$  and  $\mu_{2r} \rightarrow -1$  the transfer function of a negative-index planar slab provides amplification of the evanescent spectral components from a finite or point source such that the mathematical limit yields a perfect image in the image plane  $z = 2d_2 - d_1$  shown geometrically in Figure 5.1. However, as pointed out by several authors (Thomas & Ishimaru 2002), (Ziolkowski & Heyman 2001), (Smith, Schurig *et al* 2003), (Chew 2004), (Podolskiy & Narimanov 2005), loss terms or any deviations from the singular case with  $\epsilon_{2r} = \mu_{2r} = -1$  limit the focal spot width.

We treat the transmission of a delta-function line source through a layer with classical continuous-wave reflection and transmission formulas. This source includes all spatial wave numbers. For this 2-D problem, the electromagnetic propagation can be completely separated into a p-polarization (incident E field parallel to the plane of incidence) and s-polarization (incident E field perpendicular (senkrecht) to the plane of incidence). As in Chapters 3 and 4, we analyze the case of p-polarization and note that the s-polarization solution can be obtained by interchanging  $\epsilon$  and  $\mu$ , which is possible in principle with a metamaterial.

We shall show that a delta-function line source has one field component that images to a delta function in the specified limit. The longitudinal component  $k_z$  of the

propagation vector normal to the surface assumes values that are negative real (corresponding to all angles from normal to grazing) and imaginary for the evanescent modes. Transmission in a medium of  $\varepsilon_r = \mu_r = -1$  amplifies the Fourier components for imaginary  $k_z$  and, thus, restores the evanescent waves and bypasses the usual diffraction limit of an ordinary lens. However, for slight deviations from the limit, the magnitude of the transmission coefficient for the evanescent spectrum peaks and then starts to fall off exponentially (instead of continuing its exponential rise).

A 2-dimensional magnetic current line source provides the p-polarized incident E field and corresponds to a delta function in the transverse E field in the source plane. In other words, for the incident field it is equivalent to slot source of infinitesimal width with E field across the slot. We denote this transverse component as  $E_x$ . The exact calculations include details of the side lobes in this transverse direction. Also, we have obtained analytic approximations for the spatial amplitude function of  $E_x$  in and near the focal plane and for the resulting peak widths at half maximum. We present some numerical results for the other components in terms of Poynting vectors and energy densities but have not obtained similar analytic asymptotic approximations.

Figure 5.1, a ray-image diagram following (Pendry 2000), is helpful for visualizing how a metamaterial planar slab of index of refraction  $n_2 = -1$  focuses ordinary rays as shown. We present exact numerical solutions for several slab thicknesses covering a fairly densely sampled range of real parts of  $\varepsilon_{2r}$  and  $\mu_{2r}$  from  $-0.9$  to  $-1.1$ . We have derived analytic approximations that allow estimates of focal width for any small deviations from the mathematically singular case with  $\varepsilon_{2r} = \mu_{2r} = -1$ . We concentrate mostly on cases with  $\text{Re}\{n_2\} = -1$ , but we consider briefly the effect of a change in this real part in Section 5.6.

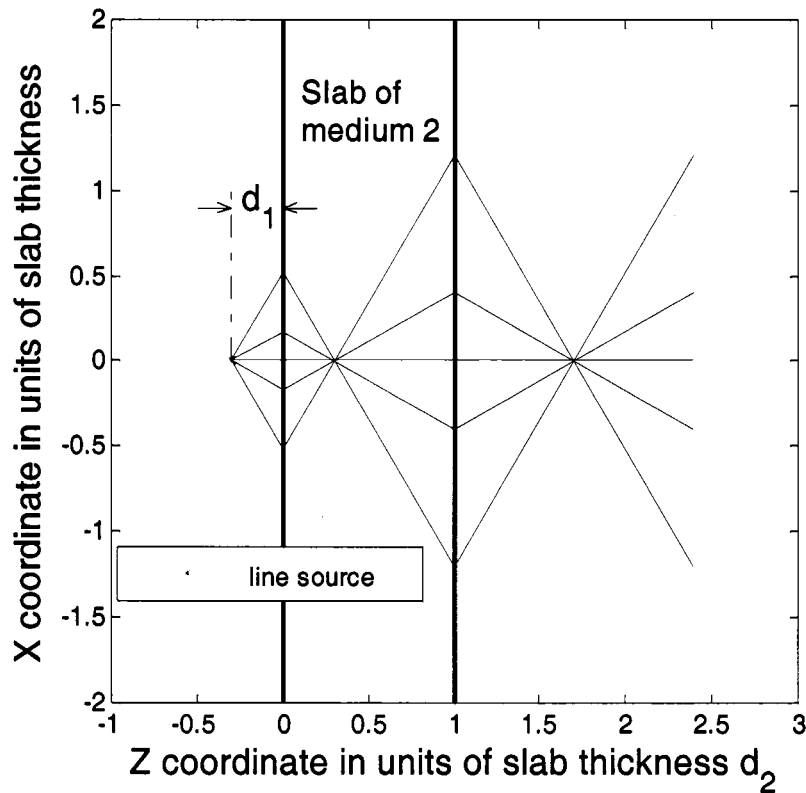


**Figure 5.1** Illustration of geometric focusing for  $n_2 = -1$  and coordinate system for following calculations.

Variations in  $\epsilon_{2r}$  and  $\mu_{2r}$  such that  $\text{Re}\{n_2\}$  deviates from  $-1$  destroy the geometric ray image focus in unusual ways, with an appearance of focusing at distances different from  $z = 2d_2 - d_1$ . To introduce the concept of how the focal limiting is produced we studied an analytic asymptotic approximation to the solution. We have limited our investigations to the 2-dimensional case because then the s and p polarizations (TE and TM as classified by incident field vectors) have independent solutions. The 3-D case has a similar limit to the transfer function, which produces a perfect focusing limit, but the polarization separation only applies to a dipole with orientation normal to the surface of the slab.

### 5.1. Formulation of the analysis

For the 2-D case the CW transmission coefficient  $T(k_x)$  of a slab of thickness  $d_2$  (also given by (2.2)) is

$$T(k_x) = \frac{1}{\cos(k_{z_2}d_2) + (j/2)(Z_2/Z_1 + Z_1/Z_2)\sin(k_{z_2}d_2)} \quad (5.1)$$

where  $k_{z_2} = \sqrt{n_2^2 k_o^2 - k_x^2}$  and the square root must be chosen such that the imaginary part is negative to satisfy the outgoing radiation condition. (We use  $e^{j\omega t}$  time variation.)  $Z_1$  and  $Z_2$  are the wave impedances in medium 1 (free space) and medium 2 (the slab of negative index), respectively. Equation (5.1) is derived from standard boundary conditions providing continuity of tangential electric field  $E$  and magnetic field  $H$ . There is a symmetry between the cases of s and p polarization because of the term  $Z_2/Z_1 + Z_1/Z_2$  so we have chosen to evaluate p polarization. In this case  $Z_i = k_{z_i}/(\omega\epsilon_i)$  for media  $i = 1, 2$ . (The equivalent formula for s polarization is  $Z_i = \omega\mu_i/k_{z_i}$ .) We define  $\delta_c = n_2^2 - 1$ ,  $\delta_e = \epsilon_{2r} + 1$ , and  $\delta_m = \mu_{2r} + 1$ . All three of these will be considered small magnitude quantities in this chapter. When  $\epsilon_{2r}$  and  $\mu_{2r}$  are close to  $-1$  in the complex plane and  $\delta_e$  and  $\delta_m$  are of the same order, then  $n_2^2 = \mu_{2r}\epsilon_{2r}$  is close to  $+1$  in complex value and  $\delta_c$  will be of the same order as the other two  $\delta$ 's.

The coefficients giving the amplitudes of the other waves created from the incident wave in this finite slab problem, namely  $R$  for the reflected wave and  $A$  and  $B$  for the forward- and backward-going waves in medium 2, have formulas related to (5.1). If we let  $D =$  the denominator, so  $T = 1/D$ , then

$$A = (1/2)(1 + Z_1/Z_2)\exp(jk_{z_2}d_2)/D, \quad B = (1/2)(1 - Z_1/Z_2)\exp(-jk_{z_2}d_2)/D, \text{ and}$$

$$R = 1 - \frac{\cos(k_{z_2}d_2) + j(Z_1/Z_2)\sin(k_{z_2}d_2)}{D}.$$

Thus, all the wave components have the same denominator, and, therefore, the same poles. These poles may be called plasmons or polaritons or discrete modes in the Fourier spectrum (Chew 2004) (Yannopoulos & Moroz 2005). If the poles have small imaginary parts so they are close to the real axis, they are realized as surface waves. As (Lu, Grzegorzczak *et al* 2005) have noted, this  $D$  leads to a countably infinite set of poles in the upper Riemann sheet, but with small  $\delta$ 's, only one is close to the Sommerfeld Integration Path (along the real  $k_x$  axis in our numerical calculations). In the following analysis we find a  $k_p$  where the denominator is nearly a minimum and thus are finding approximately where this pole occurs along the real axis.

We have calculated power series expansions of (5.1) in two separate regions along the real  $k_x$  line: (a)  $|k_x| < k_o$  and  $|k_x|/k_o$  is small enough that a power series expansion in  $\delta_c/[1 - (k_x/k_o)^2]$  converges fairly rapidly, and limiting the expansion to second order is reasonable. (b)  $|k_x| > k_o$  and  $|k_x|/k_o$  is large enough that a power series expansion in  $\delta_c/[(k_x/k_o)^2 - 1]$  converges fairly rapidly, and limiting the expansion to second order is reasonable. Obviously what is small enough or large enough for  $k_x/k_o$  depends on  $\delta_c$ , but as  $\delta_c$  gets small enough, the upper limit of validity of case (a) approaches the lower limit of validity of case (b). The result of these expansions is that  $(Z_2/Z_1 + Z_1/Z_2) = 2 + R_a$  in region a and  $(Z_2/Z_1 + Z_1/Z_2) = -2 - R_b$  in region b, where  $R_a$  and  $R_b$  are small quantities of second order in  $\delta_c$  and  $\delta_e$ . For this presentation we assume  $\delta_e$  and  $\delta_c$  are of the same order in deciding what to call second order, third order and so forth. Note that the first order terms cancel in these expansions.

Thus, we obtain to third order

$$R_a \approx \left( \delta_e + \frac{1}{2} \frac{\delta_c k_o^2}{k_o^2 - k_x^2} \right)^2 + \left( \delta_e + \frac{1}{2} \frac{\delta_c k_o^2}{k_o^2 - k_x^2} \right) \left( \delta_e^2 - \frac{1}{2} \frac{\delta_c^2 k_o^4}{(k_o^2 - k_x^2)^2} \right) \quad (5.2)$$

$$R_b \approx \left( \delta_e - \frac{1}{2} \frac{\delta_c k_o^2}{k_x^2 - k_o^2} \right)^2 + \left( \delta_e - \frac{1}{2} \frac{\delta_c k_o^2}{k_x^2 - k_o^2} \right) \left( \delta_e^2 - \frac{1}{2} \frac{\delta_c^2 k_o^4}{(k_x^2 - k_o^2)^2} \right). \quad (5.3)$$

Formally, these expressions are identical, but the first applies where  $|k_x| < k_o$  and the second where  $|k_x| > k_o$ . Then the transfer function has the following forms that lead to the asymptotic approximations that follow.

$$T(k_x) = \frac{\exp(-jd_2 \sqrt{k_2^2 - k_x^2})}{1 + j(R_a / 2) \sin(d_2 \sqrt{k_2^2 - k_x^2}) \exp(-jd_2 \sqrt{k_2^2 - k_x^2})} \quad \text{in region (a)} \quad (5.4)$$

$$T(k_x) = \frac{\exp(d_2 \sqrt{k_x^2 - k_2^2})}{1 - (R_b / 4) (\exp(2d_2 \sqrt{k_x^2 - k_2^2}) - 1)} \quad \text{in region (b)} \quad (5.5)$$

where  $k_2 = n_2 k_o$  and the sign of  $\sqrt{k_2^2 - k_x^2}$  must be chosen to give a negative imaginary part, which turns out to mean  $-\sqrt{k_2^2 - k_x^2}$  if the usual (e.g., MATLAB) convention is used that picks the square root with a positive real part. In region (b) the requirement for negative imaginary part of this same square root leads to the result that the  $\sqrt{k_x^2 - k_2^2}$  is transparent in that the conventional positive real part square root is the proper choice.

In the formulation of the calculations here we use the coordinate system and distances shown in Figure 5.1. The magnetic current line source at  $z = -d_1$ ,  $x = 0$ , is normalized for convenience as

$$J_m = -2\delta(x)\delta(z + d_1). \quad (5.6)$$

The three incident-field components produced by this line source are given in a solution by Fourier transform with respect to  $x$  as

$$H_y^{inc}(x, z) = -\frac{\omega \epsilon_o}{2\pi} \int_{-\infty}^{\infty} \frac{\exp(-jk_x x - jk_{z1} |z + d_1|)}{k_{z1}} dk_x \quad (5.7)$$

$$E_x^{inc}(x, z) = \frac{1}{2\pi} \int_{-\infty}^{\infty} \exp(-jk_x x - jk_{z1} |z + d_1|) dk_x \quad (5.8)$$

$$E_z^{inc}(x, z) = \frac{-1}{2\pi} \int_{-\infty}^{\infty} \frac{k_x}{k_{z1}} \exp(-jk_x x - jk_{z1} |z + d_1|) dk_x \quad (5.9)$$

where  $k_{z1} = \sqrt{k_o^2 - k_x^2}$  with the sign of the square root chosen as positive real for the forward going wave with  $|k_x| < k_o$  and in the form  $k_{z1} = -j\sqrt{k_x^2 - k_o^2}$ , with positive real square root in the region  $|k_x| > k_o$  for the evanescent wave components.

In the source plane where  $z = -d_1$  we recognize that (5.8) becomes an expression for the delta function. That is  $E_z^{inc}(x, -d_1) = \delta(x)$ . The other components have singularities in the plane  $z = -d_1$ , but have significant amplitudes away from  $x = 0$ . For example,  $H_y^{inc}(x, -d_1) = (\omega\epsilon_o / 2)H_0^{(2)}(k_o x)$  where  $H_0^{(2)}$  is the zero-order Hankel function of the second kind.

The transmitted fields are determined from the incident fields by multiplying incident plane wave components inside the Fourier integrals given in (5.7) through (5.9) by the transmission coefficient (5.1) and adjusting for a  $z$  coordinate origin shift. That is,  $T(k_x)$  is the transmission coefficient for a  $z$  coordinate measured from the exit side of the slab, and to retain  $z$  as measured from the origin shown in Figure 5.1 we have to make the translation  $z \rightarrow z - d_2$ . Thus, in the region  $z \geq d_2$  the  $x$  component of the electric field is

$$E_x^r = \frac{1}{2\pi} \int_{-\infty}^{\infty} T(k_x) \exp(-jk_{z1}(z - d_2 + d_1) - jk_x x) dk_x. \quad (5.10)$$

This is the field component that becomes a delta function in the image plane  $z = 2d_2 - d_1$  in the limit as  $\epsilon_{2r} \rightarrow -1$  and  $\mu_{2r} \rightarrow -1$ . The only place where  $z$  and  $d_1$  show up in (5.10) is in the exponential as  $z - d_2 + d_1$ . This shows that for a fixed slab thickness  $d_2$ , the solution has an invariance property as the slab is moved back and forth between the source and its image. The extent of the solution that corresponds to the physical space beyond the exit plane of the slab does change, but the transmitted solution that is in the physical range of  $z$  has the same functional form.

## 5.2. Analytical approximations and limiting solutions

With  $k_x$  in region (a) and with the assumptions that  $|\delta_e| \ll 1$ ,  $|\delta_c| \ll 1$  and that the absorption through the slab as measured by  $k_o d_2 \text{Im}(\delta_c)$  is fairly small, then with an error term of the order of  $R_a$ ,  $T(k_x) \approx \exp(-jk_{z_2} d_2)$ . Further as explained just after (5.5) in the limit  $n_2 \rightarrow -1$ ,  $k_{z_2} \rightarrow -k_{z_1}$  in this region, but  $k_{z_2} \rightarrow k_{z_1}$  in region (b). We examine the behavior of  $|T(k_x)|$  for the case of small  $\delta$ 's. From (5.4)  $|T(k_x)| \approx 1$  in region (a). In region (b), (5.5) shows that  $|T(k_x)|$  starts to increase as  $|\exp(d_2 \sqrt{k_x^2 - k_2^2})|$  for  $k_x$  just slightly larger than  $|k_2| = |n_2| k_o$ , but changes to a decreasing behavior approximately equal to  $|(4/R_b) \exp(-d_2 \sqrt{k_x^2 - k_2^2})|$  for sufficiently large  $k_x$ . As a function of  $k_x$  the magnitude peaks near where the denominator of (5.5) is a minimum. We denote the location of the peak as  $k_x = k_p$ . With several approximations to ignore small terms

$$k_p^2 \approx k_o^2 + \frac{1}{d_2} \ln \left| \frac{2}{\sqrt{R_b}} \right| \approx k_o^2 + \frac{1}{d_2} \ln \left| \frac{2}{\delta_e} \right| \quad (5.11)$$

The subscript p is a mnemonic for peak and also for pole, since this is also an approximation to the real part of the location of the pole in the  $k_x$  plane.

To illustrate the behavior of  $|T|$  we have programmed complete equations for the transmission coefficient and show the behavior of  $|T|$  as a function of  $k_x / k_o$  for three sequences of  $\varepsilon_{2r}$  and  $\mu_{2r}$  in Figure 5.2. All the graphs in Figure 5.2 include the limit curve for the perfect focusing case,  $\varepsilon_r = \mu_r = -1$ . The Figure 5.2(a) graph also shows the curve that is the result of no layer at all; i.e., where  $\varepsilon_r = \mu_r = +1$ . The magnitude of the propagating part of the transmitted wave is the same for both of these cases, but with no layer the evanescent spectrum shows its "standard" (for a point source) exponentially decreasing amplitude factor in propagation.

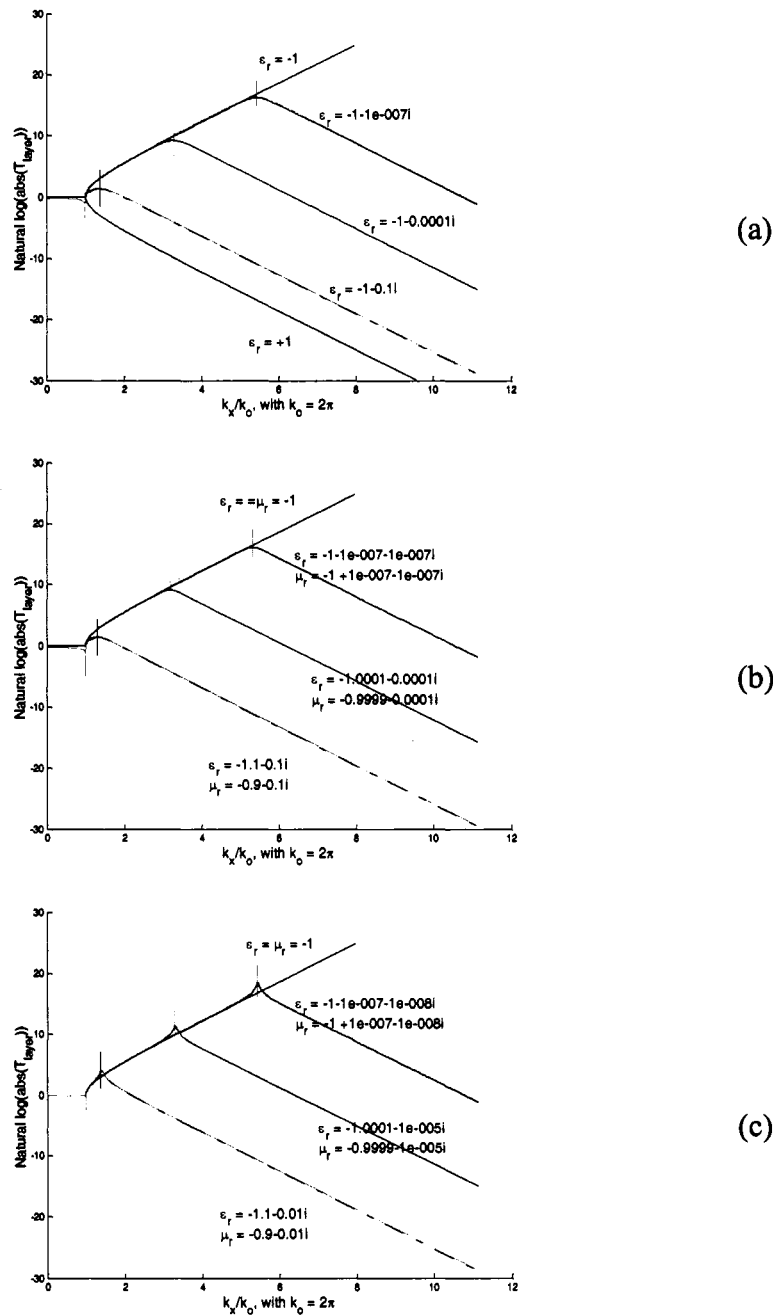


**Figure 5.2** Transmission coefficient for propagating and evanescent parts of the spectrum through a half-wavelength layer, p polarization. In 3(a), each case has  $\mu_r = \epsilon_r$  and deviations from  $-1$  are only in the imaginary part. In 3(b), the deviation in  $\epsilon_r$  is of the form  $\delta(-1-j)$ , and the deviation in  $\mu_r$  is of the form  $\delta(1-j)$ . In 3(c) the deviation in  $\epsilon_r$  is of the form  $\delta(-1-0.1j)$ , and the deviation in  $\mu_r$  is of the form  $\delta(1-0.1j)$ . The small parameter  $\delta$  is positive. The vertical ticks at or near the peaks show the value of  $k_p$  along the horizontal axis.

Figure 5.2 also includes overlays in region b of the approximate  $T(k_x)$  given by (5.5) and (5.3). Further, the location of  $k_p$  from (5.11) is plotted as a vertical bar around the peak it locates. Although these logarithmic plots do not have sufficient resolution to show the details, the agreement of the approximations with the complete formula is quite good. More details of the comparison of the approximate and complete formulas are shown in Figure 5.3 through Figure 5.5. These are not logarithmic plots so the vertical scales of each pane within the figures are significantly different. In Figure 5.3 corresponding to cases where deviation of  $\varepsilon_{2r}$  and of  $\mu_{2r}$  from  $-1$  is pure imaginary, the real part of the transmission coefficient of the layer is much larger than the corresponding imaginary part. The approximation formula is much better for the large (real) part than for the imaginary part. The first pane of Figure 5.3 shows most drastically the jitter due to loss of significant figures in the computer calculation of the denominator of (5.1) in the exact formula. In Figure 5.4 where the deviations of  $\varepsilon_{2r}$  and of  $\mu_{2r}$  from  $-1$  have equal real and imaginary parts,  $T(k_x)$  has peaks in the real part and in the imaginary part that are roughly equal. The agreement of approximation and exact formulas is quite good except for the large deviation case (magnitude about 0.1) in the region  $k_x$  fairly close to  $k_o$ . In this case the peak is fairly close to  $k_o$  so the approximation is only fair in the region around the peak. Finally, in Figure 5.5 the deviations of  $\varepsilon_{2r}$  and of  $\mu_{2r}$  from  $-1$  are mostly real, the pole of  $T(k_x)$  is getting close to the real  $k_x$  axis and so  $T(k_x)$  has noticeable spikes at  $k_p$ . In this figure the peaks in the imaginary parts are several times larger than the peaks in the real parts and the approximation formula agrees better in imaginary part with the exact formula.

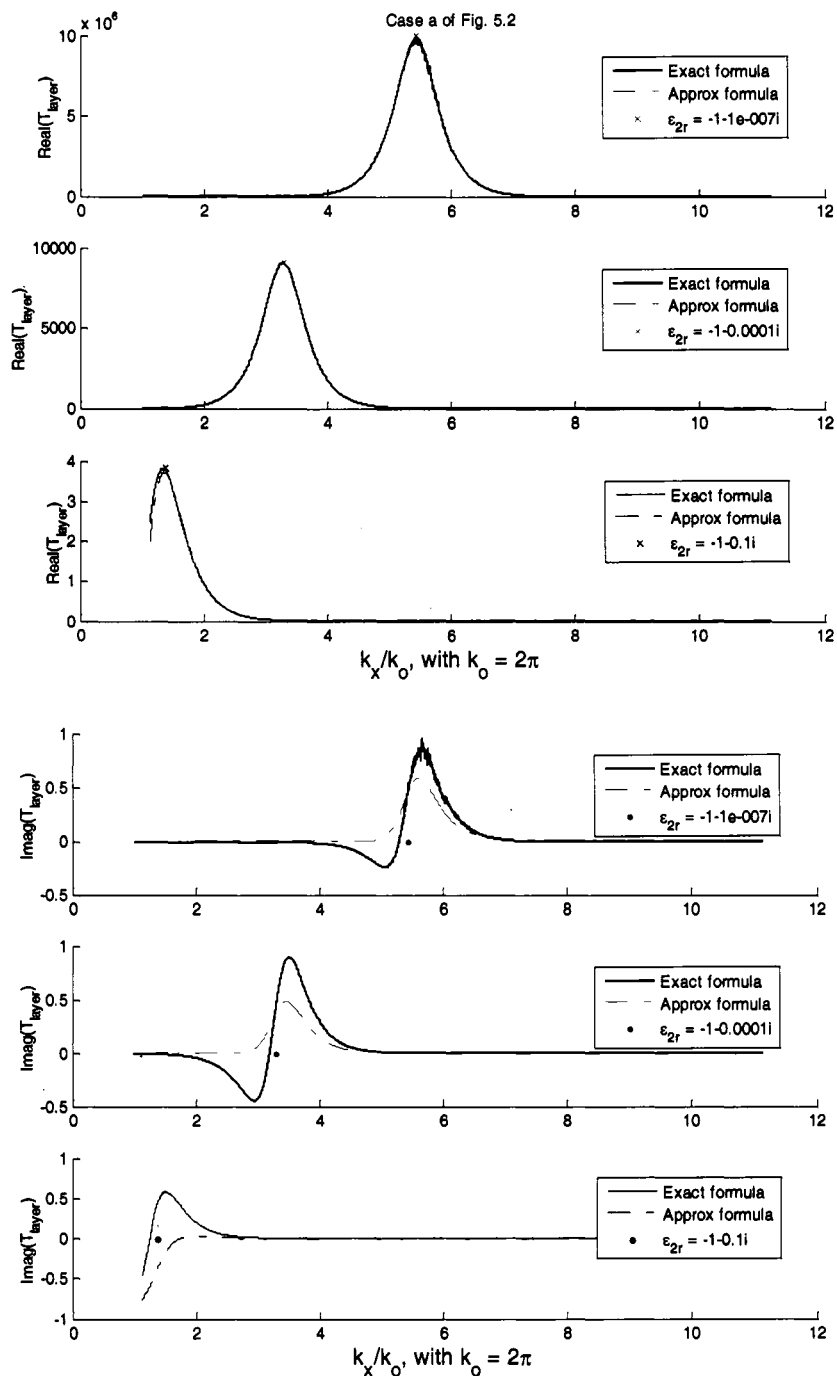


**Figure 5.3** Comparison of the approximation formula and the complete formula for the imaginary and real parts of the transmission coefficient  $T(k_x)$  for cases in Figure 5.2(a). The x's in the upper three panes (real parts) are the absolute value of the approximation formula (5.5) evaluated at  $k_p$  as given by (5.11), right-most approximation. The dots in the lower three panes locate the value of  $k_p$  along the axis.

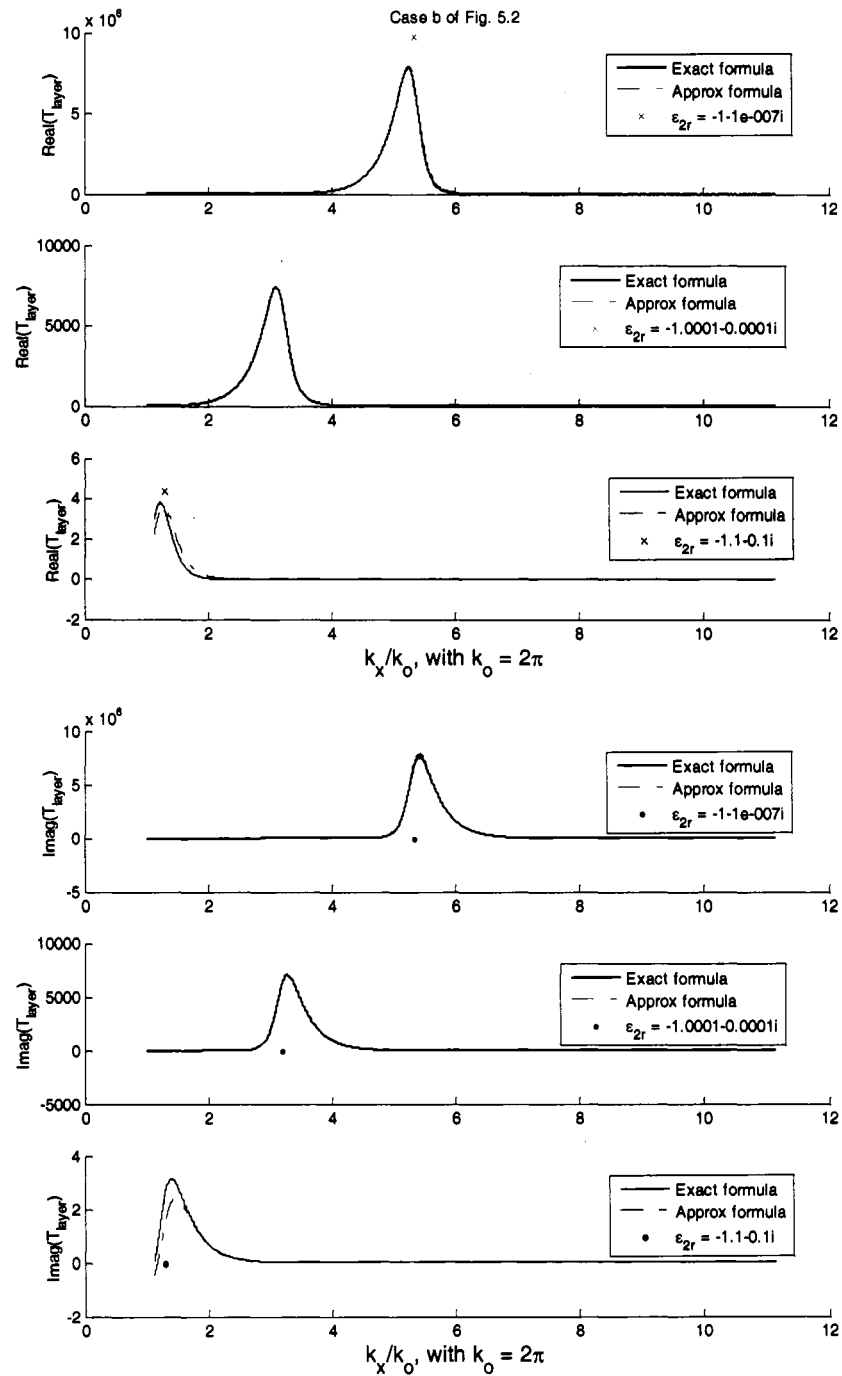


**Figure 5.4** Comparison of the approximation formula and the complete formula for the imaginary and real parts of the transmission coefficient  $T(k_x)$  for cases in Figure 5.2(b). The x's in the upper three panes (real parts) are the absolute value of the approximation formula (5.5) evaluated at  $k_p$  as given by (5.11), right-most approximation. The dots in the lower three panes locate the value of  $k_p$  along the axis.

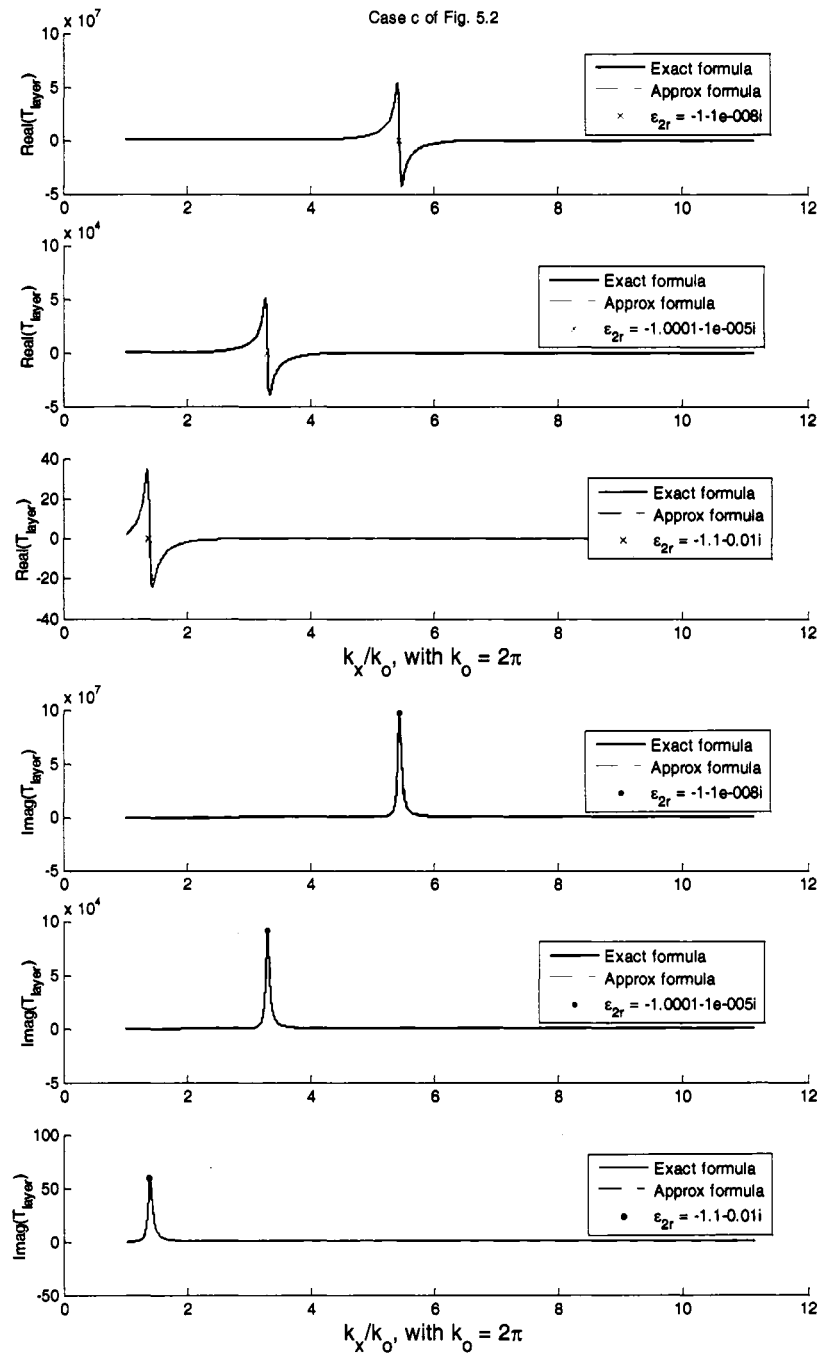


**Figure 5.5** Comparison of the approximation formula and the complete formula for the imaginary and real parts of the transmission coefficient  $T(k_x)$  for cases in Figure 5.2(c). The x's in the upper three panes locate the value of  $k_p$  along the axis. The dots in the lower three panes (imaginary parts) are the absolute value of the approximation formula (5.5) evaluated at  $k_p$  as given by (5.11), right-most approximation.

Cases with pure real values of the deviations  $\delta_e$  and  $\delta_m$  lead to poles on the real axis (i.e., infinite spikes). Although the Fourier integrals have finite values per the Sommerfeld prescription, our brute force integration does not work in these cases. Table 5.1 summarizes the accuracy of the approximation of  $T(k_x)$  from (5.5) and (5.3) for the peak of  $|T(k_x)|$ . The entries in Table 5.1 need some explanation. The format repeats for each of the three subplots a, b and c of Figure 5.2. The first, fourth, and fifth columns correspond to cases shown in the plots. The second and third columns correspond to cases that would clutter the plots in between the smallest loss case and the next case shown. However, the calculations were carried out for all the  $(\varepsilon_{2r}, \mu_{2r})$  cases of Table 5.1. The rows labeled  $a = k_{peak} / k_o$  give the value of  $k_x$  at which the largest value of  $|T(k_x)|$  occurred in the fine-mesh grid of  $k_x$  values for which the computations were carried out. The rows labeled  $b = k_p / k_o$  give the values of the quantity  $k_p$  computed from (5.11), which is approximately at the peak. Then, row  $d = \max |T|$  gives the largest value of  $|T(k_x)|$  and row  $e = \max |T_{appr}|$  gives the magnitude of the approximation (5.5) evaluated at  $k_p$  given in row  $b$ . The percentage differences of the approximation and the value calculated from the complete formula are shown as indicated. Note that in the first percentage we calculate the lower row minus the upper row as a percentage of the upper (exact formula) row, whereas in the second percentage we calculate the upper row minus the lower row as a percentage of the upper (exact formula) row. This choice was made to make most of the percentages positive. Finally the trend is for the approximation to get more accurate as the deviation gets smaller, i.e., as the cases move from the right column towards the left column. However, for the first (left) column, the computer calculation of the exact formula is losing significant figures of accuracy and so the per cent difference increases. In this case the approximation is numerically more accurate.

**Table 5.1** Comparisons of location of peak and magnitude of peak of  $|T(k_x)|$  for cases shown in Figure 5.2 plus intermediate cases for each subplot.

Plot 5.2 a					
$\varepsilon_{2r}$	-1-1e-7j	-1-1e-4j	-1-0.001j	-1-0.01j	-1-0.1j
$\mu_{2r}$	-1-1e-7j	-1-1e-4j	-1-0.001j	-1-0.01j	-1-0.1j
$a = k_{peak} / k_o$	5.44210	3.28340	2.58310	1.90670	1.34450
$b = k_p / k_o$	5.44380	3.30720	2.61800	1.96070	1.38180
%diff( $b - a$ )	0.03080	0.72550	1.35000	2.83290	2.77520
$d = \max  T $	9.94E+06	9.07E+03	8.49E+02	7.20E+01	3.83E+00
$e = \max  T_{aprx} $	9.66E+06	9.07E+03	8.49E+02	7.19E+01	3.74E+00
%diff( $d - e$ )	-2.82420	0.00000	-0.00017	-0.02367	-2.31260
Plot 5.2 b					
$\varepsilon_{2r}$	-1-1e-7-1e-7j	-1.0001-1e-4j	-1.001-0.001j	-1.01-0.01j	-1.1-0.1j
$\mu_{2r}$	-1+1e-7-1e-7j	-0.9999-1e-4j	-0.999-0.001j	-0.99-0.01j	-0.9-0.1j
$a = k_{peak} / k_o$	5.33170	3.18950	2.49710	1.83660	1.29820
$b = k_p / k_o$	5.33540	3.20220	2.51640	1.86660	1.30810
%diff( $b - a$ )	0.06991	0.39950	0.76955	1.63340	0.75782
$d = \max  T $	9.75E+06	9.02E+03	8.41E+02	7.15E+01	4.34E+00
$e = \max  T_{aprx} $	9.65E+06	9.02E+03	8.40E+02	7.05E+01	3.89E+00
%diff( $d - e$ )	1.03520	0.00935	0.11519	1.43050	10.26100
Plot 5.2 c					
$\varepsilon_{2r}$	-1-1e-7-1e-8j	-1.0001-1e-5j	-1.001-1e-4j	-1.01-0.001j	-1.1-0.01j
$\mu_{2r}$	-1+1e-7-1e-8j	-0.9999-1e-5j	-0.999-1e-4j	-0.99-0.001j	-0.0-0.01j
$a = k_{peak} / k_o$	5.44210	3.30550	2.61650	1.96080	1.39900
$b = k_p / k_o$	5.44230	3.30570	2.61650	1.95930	1.38070
%diff( $b - a$ )	0.00219	0.00571	-0.00051	-0.07451	-1.30740
$d = \max  T $	9.71E+07	9.09E+04	8.56E+03	7.56E+02	6.04E+01
$e = \max  T_{aprx} $	9.66E+07	9.09E+04	8.55E+03	7.45E+02	5.22E+01
%diff( $d - e$ )	0.53426	0.00906	0.11083	1.36560	13.56300

To summarize what is important for following calculations of integrals involving  $T(k_x)$ , the approximation is accurate around the peak to within about 1% for cases with deviations  $|1 + \varepsilon_{2r}|$  and  $|1 + \mu_{2r}|$  both in the range of  $10^{-3}$  to  $10^{-4}$ , and it is reasonably accurate as shown by Figure 5.3 through Figure 5.5 for  $k_x \geq k_o + |\delta_c|$ . The accuracy becomes very good for  $k_x$  large compared to  $k_p$ .

### 5.3. Approximations for transmitted $E_x$ in the space domain

As noted at the beginning of Section 5.2 and illustrated in Figure 5.2 in region (a) of  $k_x$  space,  $T(k_x) \approx \exp(-jk_{z2}d_2)$  and  $k_{z2} \approx -k_{z1}$  for  $n_2 \approx -1$ . From (5.10) we readily identify the Fourier transform of  $E_x$  in the transmitted region ( $z > d_2$ ) as

$$\tilde{E}_x^{tr} = T(k_x) \exp(-jk_{z1}(z - d_2 + d_1)). \quad (5.12)$$

Hence, in the focal plane defined as  $z = 2d_2 - d_1$ ,

$$\tilde{E}_x^{tr} \approx \exp(-jk_{z2}d_2) \exp(-jk_{z1}d_2) \rightarrow 1 \quad \text{for } k_x < k_o - |\delta_c|. \quad (5.13)$$

For  $k_x > k_o + |\delta_c|$  with the approximation of  $k_z \approx k_o$  in (5.5) we obtain

$$\tilde{E}_x^{tr} \approx \frac{\exp\left(-\sqrt{k_x^2 - k_o^2}(z - 2d_2 + d_1)\right)}{1 - (R_b/4)\left(\exp(2d_2\sqrt{k_x^2 - k_o^2}) - 1\right)}. \quad (5.14)$$

In the focal plane

$$\tilde{E}_x^{tr} \approx \frac{1}{1 - (R_b/4)\left(\exp(2d_2\sqrt{k_x^2 - k_o^2}) - 1\right)}. \quad (5.15)$$

$R_b$  is a small quantity, given approximately by (5.3), and it becomes arbitrarily small as  $\varepsilon_{2r} \rightarrow -1$  and  $\mu_{2r} \rightarrow -1$ . Thus, for any fixed  $k_x$  we can make  $\tilde{E}_x^{tr}$  arbitrarily close to 1. Hence, in the focal plane the Fourier transform of  $E_x$  has a limiting value of 1. In this formal sense  $E_x(z = 2d_2 - d_1, x) \rightarrow \delta(x)$ . However, in any physical

situation,  $\varepsilon_{2r}$  and  $\mu_{2r}$  have values with at least some loss that leads to finite deviations  $\delta_e$  and  $\delta_m$  from  $-1$ . For  $k_x$  at least moderately large compared to  $k_o$ , the exponential function in the denominator will make  $(R_b / 4) \left( \exp(2d_2 \sqrt{k_x^2 - k_o^2}) \right)$  large. So for  $k_x > k_p$

$$\tilde{E}_x^{nr} \approx \frac{-4}{R_b} \exp(-2d_2 \sqrt{k_x^2 - k_o^2}) \quad (5.16)$$

There is a transition region between region (a) where (5.13) is a good approximation and the region where (5.16) becomes a good approximation. This transition region contains the interval where the effects of branch points at  $k_o$  and  $k_2$  and the pole near  $k_p$  cause some sharp variations. In all cases where  $\delta_e$  and  $\delta_m$  are small, the interval around the branch points contributes negligibly to the inverse Fourier transform because the length of the interval is the order of  $\delta_c$  and the integrand is well behaved.  $T(k_x)$  vanishes at the branch points with a square root behavior. If the deviation  $\delta_e$  or  $\delta_m$  has a moderate loss as the example in Fig 5.6 illustrates, the pole effect is not large. Several other figures illustrating this behavior were published in (Thomas & Ishimaru 2002).

Figure 5.6 shows the amplitude and phase of the spectrum of the  $E_x$  field in the focal plane for a selected low-loss case with  $d_2 = 2$ . The solid curves show the exact solution (5.10), and the dotted curves represent the asymptotic approximation given by (5.13) and (5.16) with the further approximation that  $R_b \approx (\delta_e)^2$ . The approximation (5.13) is extended upwards from small  $k_x$  and the approximation (5.16) is extended downwards from large  $k_x$  to the point where they intersect in magnitude. The value of  $k_x$  where the magnitudes intersect is  $k_p$ , the approximation given by the right-most side of (5.11). Specifically,

$$k_p = \sqrt{k_o^2 + (M / d_2)^2} \quad \text{where } M = \ln(2 / |\delta_e|) \quad (5.17)$$

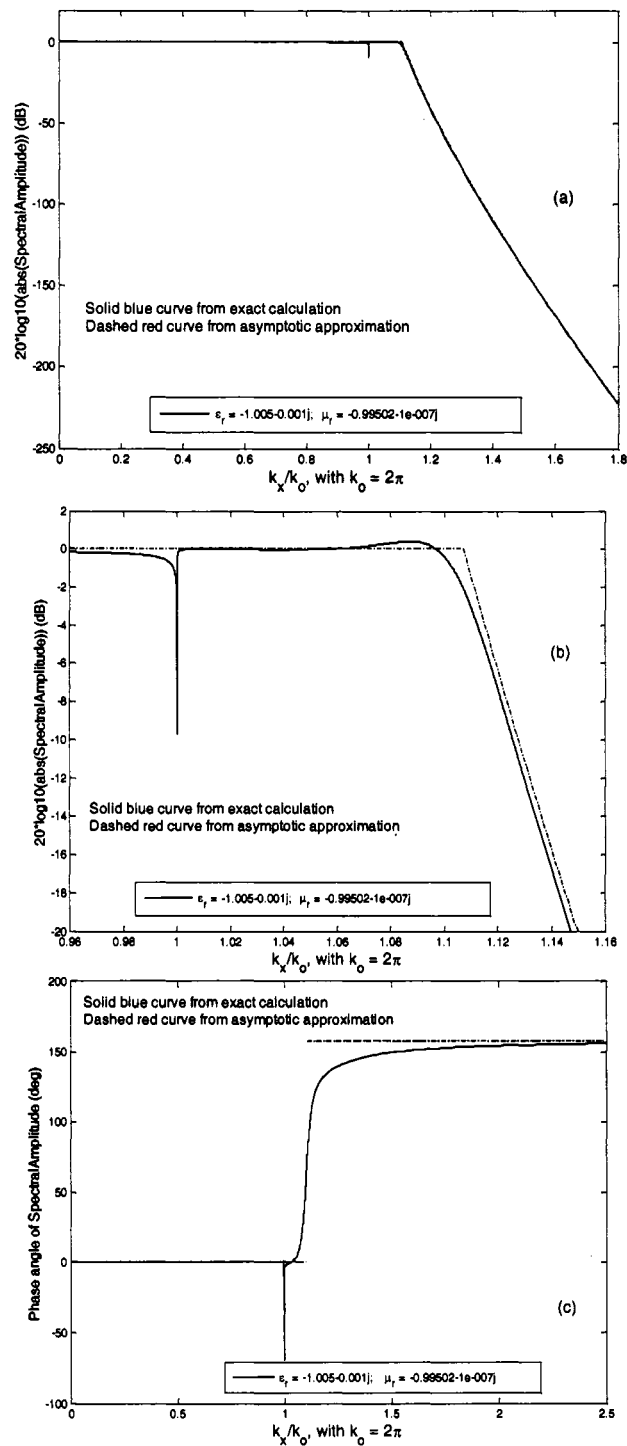


**Figure 5.6** Spectrum of line source at focal plane through a layer of thickness 2 wavelengths, p polarization. (a) and (b) are amplitude plots in dB. (b) is an enlarged portion of (a) for a region around the interval  $k_o$  to  $k_p$ . (c) is phase in degrees.  $\epsilon_{2r}$  and  $\mu_{2r}$  related so that  $\text{Re}(n_2) = -1$ .

These curves were calculated for a particular case of  $\varepsilon_{2r} = -1.005 - 0.001j$ ,  $\text{Im}(\mu_{2r}) = -10^{-7}$  and  $\text{Re}(n_2) = -1$ . This makes  $\text{Re}(\mu_{2r}) = -0.9950246$  and  $\text{Im}(n_2) = -4.9756 \cdot 10^{-4}$ . The resulting  $k_p / k_o$  is 1.107176. Also, the particular case assumed the thickness of the slab to be  $d_2 = 2\lambda_o$  with the source at a distance  $d_1 = \lambda_o$  in front of the slab. The resulting image plane is at a distance  $\lambda_o$  beyond the slab. The phase curve of the approximate solution shown in Figure 5.6(c) exhibits a discontinuity at  $k_p$ , whereas the exact solution has a sharp dip at the branch point (not in the approximate solution) and then a fairly rapid transition from zero phase at low  $k_x$  to the constant phase of  $-1/R_b \approx -1/(\delta_e)^2$  at high frequency.

The major conclusion we draw from Figure 5.6 is that the asymptotic approximations with connection by extrapolation represent the essential behavior of the exact spectrum except for a resonant peak and a sharp dip at the  $k_o$  branch point. The resonant peak does not occur for cases where  $\delta_e$  and  $\delta_c$  are predominantly imaginary (lossy). Hence, we evaluate analytically (with some further approximation) the inverse transform of the asymptotic spectrum of  $E_x$  in the focal plane. The spectrum given by (5.13) and (5.16) with connection by extrapolation to the point where the magnitudes intersect is

$$\tilde{E}_x = \tilde{E}_1(k_x) + \tilde{E}_2(k_x) \quad (5.18)$$

where

$$\begin{aligned} \tilde{E}_1(k_x) &= 1, \quad \tilde{E}_2(k_x) = 0, & \text{for } |k_x| \leq k_p \\ \tilde{E}_1(k_x) &= 0, \quad \tilde{E}_2(k_x) = \frac{-4}{(\delta_e)^2} \exp(-2d_2 \sqrt{k_x^2 - k_o^2}), & \text{for } |k_x| > k_p \end{aligned} \quad (5.19)$$

and  $k_p$ , the wavenumber where the magnitude of  $\tilde{E}_2$  in the upper interval equals 1, is given by (5.17). Then

$$E_x(x) = \frac{1}{2\pi} \int_{-\infty}^{\infty} \tilde{E}_x(k_x) \exp(-jk_x x) dk_x = E_1(x) + E_2(x) \quad (5.20)$$

where

$$E_1(x) = \frac{1}{2\pi} \int_{k_p}^{k_o} \exp(-jk_x x) dk_x = \frac{1}{\pi x} \sin(k_p x) \quad (5.21)$$

$$E_2(x) = \frac{-4}{\pi \delta_e^2} \int_{k_p}^{\infty} \exp(-2d_2 \sqrt{k_x^2 - k_o^2}) \operatorname{Re}(e^{-jk_x x}) dk_x. \quad (5.22)$$

Bounds on  $\sqrt{k_x^2 - k_o^2} / k_x$  over the range of the integrand for  $E_2$  and the mean value theorem lead to strict bounds on  $E_2$  in terms of an elementary integral. See Appendix B. Define  $\Delta = k_p - \sqrt{k_p^2 - k_o^2}$ . Then,

$$E_2(x) = \frac{-4F \exp(-2k_p d_2) (2d_2 \cos(k_p x) - x \sin(k_p x))}{\pi \delta_e^2 (4d_2^2 + x^2)} \quad (5.23)$$

where

$$1 \leq F \leq \exp(2d_2 \Delta). \quad (5.24)$$

The complex function  $E_2(x)$  has a constant phase, determined by  $\delta_e^2$ . This phase is the asymptotic phase that corresponds to large  $k_x$ . All the other factors are real, and this real function has a peak at  $x = 0$ . Consider the  $x$  dependence as given by the dimensionless function

$$e(x) = \frac{E_2(x)}{E_2(0)} = \frac{4\Theta^2 \cos X - 2X\Theta \sin X}{4\Theta^2 + X^2}. \quad (5.25)$$

where we have used scaled variables  $X = k_p x$  and  $\Theta = k_p d_2$  to show the 2-parameter dependence of  $e(x)$ . It is easy to see that  $e(0) = 1$ , and that this is a relative maximum in the neighborhood of  $x = 0$ .

We can show that  $|e(x)| \leq 1$  for all positive  $\Theta$ , and the inequality is strict unless  $X = 0$  (Appendix B). Thus,  $E_2(x)$  can generally be characterized as a

function which has its maximum absolute value at  $x = 0$ , has sinusoidal oscillations with shifting phase, and has decreasing amplitude oscillations as  $|x| \rightarrow \infty$ . The damping is rapid for small  $\Theta$ , but slow for large  $\Theta$ . Since  $E_1(x) = \sin(k_p x)/(\pi x)$  by (5.21), then the sum  $E_x = E_1 + E_2$  has this same general characterization. We now show that  $E_2(0) \ll E_1(0)$  for a large set of cases of interest. For this set of cases in the focal plane close to the focal point at  $x = 0$  the transmitted  $E_x$  is reasonably well approximated by  $E_1$ .

The cases for which  $E_2(0) \ll E_1(0)$  correspond to slab thicknesses that are not thin compared to a wavelength, or roughly with thickness  $d_2 \geq 0.5\lambda_o$ . These non-thin cases are important because they provide for three circumstances that could be particularly useful. First, the sum of the source distance (as measured on the incident side) plus the image distance (as measured on the transmitted side) equals the slab thickness so for cases where the source and image need to be separated by a wavelength, the slab thickness needs to be  $\geq 0.5\lambda_o$ . Secondly, if the slab is a metamaterial made of structures small compared to a wavelength, but constructed on a periodic grid with lattice constant of the order of 0.1 wavelength, then to have at least 5 periods within the structure, the thickness would be about  $0.5\lambda_o$ . Third, we shall show that thin layers do not provide focusing in the Z direction (the direction normal to the slab) but rather exhibit a monotonically decreasing field on axis. So we limit our considerations in the following analysis to  $d_2 \geq 0.5\lambda_o$  and put emphasis on  $d_2 \geq \lambda_o$ . We examine

$$\left| \frac{E_2(0)}{E_1(0)} \right| = \frac{2F \exp(-2k_p d_2)}{|\delta_e^2| k_p d_2} \quad (5.26)$$

with the bounds on  $F$  given by (5.24). Also by (5.17)  $k_p > k_o$  and more so for smaller  $d_2$ . From the definitions of  $\Delta$  before (5.23) and  $k_p$  in (5.17) and (5.11) we use (5.24) to find the maximum  $F_{\max}$ .

$$F_{\max} \exp(-2k_p d_2) = \exp\left(-2d_2 \sqrt{k_p^2 - k_o^2}\right) = \frac{|\delta_e^2|}{4} \quad (5.27)$$

so

$$\frac{|E_2(0)|_{\max}}{|E_1(0)|} = \frac{1}{2k_p d_2}. \quad (5.28)$$

Whereas for the minimum  $F_{\min}$  with use of the quantity  $M$  defined in (5.17)

$$\frac{|E_2(0)|_{\min}}{|E_1(0)|} = \frac{\exp\left[-2\left(\sqrt{M^2 + (k_o d_2)^2} - M\right)\right]}{2k_p d_2} \quad (5.29)$$

The right-hand side of (5.29) clearly expresses that the minimum is less than the maximum given by (5.28). Even for the maximum case  $\frac{|E_2(0)|_{\max}}{|E_1(0)|}$  is less than  $1/(2\pi)$

for  $d_2 \geq 0.5\lambda_o$ .

The important conclusion of this analysis is that  $E_x(x)$  is reasonably well approximated (in units of volts per wavelength) as  $E_x(x) = 2(k_p / k_o) \sin(k_p x) / (k_p x)$ .

The central peak of this field has a full width  $\Delta W$  at half maximum of

$$k_p \Delta W = 3.790988534. \quad (5.30)$$

This quantity may be called the 6-dB width, since the dB ratio for a field component is  $20 \log_{10}(\text{Ratio}) \cong -6$  for a ratio of  $1/2$ . We shall also consider the 3-dB width  $\Delta W_3$  (at 0.70795 of the max). The  $E_1$  asymptotic approximation gives

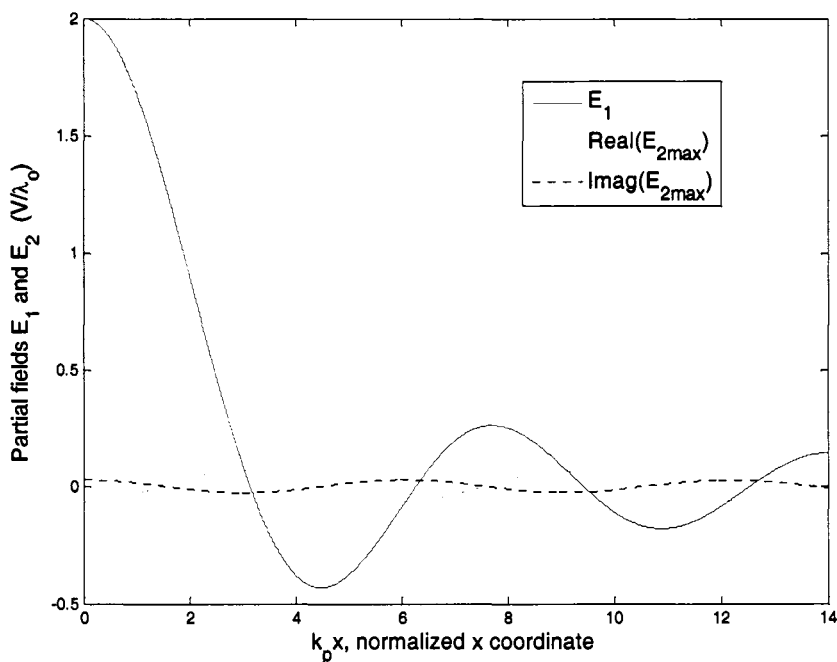
$$k_p \Delta W_3 = 2.77869717. \quad (5.31)$$

Figure 5.7 illustrates  $E_1$ ,  $E_2$ , and the sum  $E_x$  for the case that matches Figure 5.6.

The peak of  $E_2$  at  $x = 0$  is less than the peak of  $E_1$  by a factor greater than  $k_p d_2 > 4\pi$  for this case. Our numerical calculations will illustrate that (5.30) gives a reasonable estimate of  $\Delta W$  for many cases of interest. The asymptotic approximation does not

show any dependence on  $\mu_{2r}$  (including  $n_2$ ) and hence the approximation has limitations on validity.

We chose the width of  $|E_x(x)|$  at half maximum as our measure of the width of the focus because we found that in the cases we calculated with  $\epsilon_{2r}$  and  $\mu_{2r}$  both very



**Figure 5.7** Asymptotic transverse field components in the focal plane for slab thickness  $d_2 = 2\lambda_o$  and  $\epsilon_{2r} = -1.005 - 0.001j$ .  $E_1$  is real.

close to  $-1$ , then the width at half maximum did not recur in more distant sidelobes. However, this is not true for widths measured to a lower value, such as the  $1/e$  value. Also, we chose to concentrate on  $E_x$  because with the chosen polarization the perfect focus limit maps the transverse delta function in  $E_x$  to a transverse delta function, but not so for the other components. We shall show in a particular case how this makes the focusing much worse in terms of Poynting vector magnitude or energy density.

## Relation to uncertainty principle

The uncertainty principle relates the rms widths of  $|E_x(x)|^2$  and  $|\tilde{E}_x(k_x)|^2$  about their respective means, where  $E_x$  and  $\tilde{E}_x$  are a Fourier transform pair. This principle gives the result that

$$\Delta W^* \Delta k^* \geq 1/2 \quad (5.32)$$

where

$\Delta k^*$  = rms width of the  $k_x$  spectrum of the image, and

$\Delta W^*$  = rms width of the field  $E_x(x)$  of the image.

This uncertainty relation comes from quantum mechanics and the relation between two canonically conjugate coordinates (e.g., the coordinate  $x$  and the momentum  $p_x = \hbar k_x$ ). The main point is that the momentum representation, say  $a(p_x)$ , is the Fourier transform of Schrödinger's wave function  $\psi(x)$  in coordinate space. The probabilities of the particle (photon) being located at  $x$  within  $dx$  is  $|\psi(x)|^2 dx$  and of having momentum  $p_x$  within  $dp_x$  is  $|a(p_x)|^2 dp_x$ . So the uncertainty principle is a result concerning the probability distributions that are the absolute squares of wave functions.

The uncertainty principle does imply limits on the focal width. However, for the photon momentum spectrum  $\tilde{E}_1$  in (5.19) (a uniform distribution over a finite interval),  $\Delta k^* = k_p / \sqrt{3}$  and the corresponding coordinate distribution is a damped sine that does not have a finite mean square value. With the sharp roll off of the spectrum as shown in Figure 5.6,  $\Delta k^*$  is only slightly larger than  $k_p / \sqrt{3}$ . So the relation (5.32) says that the rms uncertainty of the image position of the exact solution

$$\Delta W^* \geq \sqrt{3} / (2k_p) = 0.866 / k_p.$$

However, the uncertainty relation can be used for an order of magnitude

estimate by considering just the dominant parts of the two conjugate spectra, with the assumption that a small additional function will bring smoothness and rapid rolloff beyond the main lobe in both domains. Then, the uncertainty relation may be used to estimate the width  $\Delta W$  from  $\Delta k$ . In addition, there are several well known widths of this sort. In particular for a rectangular  $k_x$  spectrum of  $\tilde{E}_1$  with width  $k_o = 2\pi$ , which applies for the case where all real components are focused, but evanescent components do not contribute,

$$\Delta W = 0.6 \quad (\text{two-significant figure accuracy}). \quad (5.33)$$

Also, the width  $\Delta W_1$  between the first zeros of  $E_1$  is given exactly by

$$k_p \Delta W_1 = 2\pi,$$

which may be used as a measure of the width of the central peak of  $E_1$  but is not so useful for our general case where the  $E_2$  contribution (or the complete solution) has a significant effect on the zero location.

There is another Fourier transform pair for which the relation of widths at half height (the 3-dB width) is often used as an approximation in the estimation of the transform of a function that has many peaks. This pair consists of the damped exponential in time and the simple pole in the frequency domain. The prototypical pair may be taken as

$$G(t) = \exp(-j\omega_o t) e^{-\Gamma t} \quad \text{and} \quad g(\omega) = \frac{j}{\omega - \omega_o + j\Gamma}. \quad (5.34)$$

Since  $G(t)$  is assumed as a causal function starting at  $t = 0$ , the width  $\tau$  at half height of  $|G(t)|^2$  is  $\tau = \ln(2)/(2\Gamma)$ . The 3-dB width of  $|g(\omega)|^2$  about its peak value of  $1/\Gamma^2$  is  $\Delta\omega = 2\Gamma$  and thus  $\tau\Delta\omega = \ln(2)$ . However, the uncertainty relation (5.32) does not

provide a useful estimate here because the probability distribution corresponding to  $\text{const}|g(\omega)|^2 = (\pi/\Gamma)|g(\omega)|^2$  has an infinite variance.

From (5.17) the transverse width at half height (6-dB width) can be written as

$$\Delta W = \frac{3.791}{\sqrt{k_o^2 + [\ln(2/|\delta_e|)/d_2]^2}}. \quad (5.35)$$

This asymptotic formula shows that  $\Delta W$  can be made arbitrarily small as  $|\delta_e| = |\varepsilon_{2r} + 1| \rightarrow 0$ . The asymptotic approximation requires that  $|\delta_m| = |\mu_{2r} + 1|$  be of the same order as  $|\varepsilon_{2r} + 1|$ . Equation (5.17) and a less-specific width estimate comparable to (5.35) were derived in (Thomas & Ishimaru 2002). Similar formulas have been obtained by (Smith, Schurig *et al* 2003), (Podolskiy & Narimanov 2005), and (Lu, Grzegorzczuk *et al* 2005). Also, the approach to small  $\Delta W$  is quite slow because of the logarithmic dependence and because other calculations indicate that to have a peak in the Z direction (the propagation direction),  $d_2$  must be somewhat greater than a wavelength. A thin slab can provide a sharp transverse focus, but the  $|E_x|^2$  pattern will form a ridge along the Z axis with peak falling off gradually with distance from the slab.

To emphasize the significance of (5.35) we show in Figure 5.8 the transverse focal width  $\Delta W$  versus slab thickness for four values of the parameter  $|\delta_e|$ . If the slab thickness is greater than about 3 wavelengths and  $|\delta_e| \geq 10^{-4}$ , the transverse focal width is a substantial fraction of the large thickness limit of 0.6 wavelengths. On the other hand, if the slab is quite thin in wavelengths, then  $\Delta W$  can be small in wavelengths. We believe this explains certain experimental results, e.g., (Melville & Blaikie 2005), where a very thin slab of silver was used as a quasistatic approximation to a negative index medium to obtain subwavelength resolution. However, we caution that the limit  $d_2 = 0$  means there is no slab and the image plane becomes the source

plane. We have substantiated the asymptotic formula by many exact Fourier transform calculations. That is, if  $|\delta_e| > |\delta_m|$  or both are of the same order, then the formula (5.35) is a good approximation. If  $|\delta_m| \gg |\delta_e|$ , a rough estimate is obtained by using  $\delta_c = -\delta_e - \delta_m + \delta_e \delta_m$  in place of  $\delta_e$ .

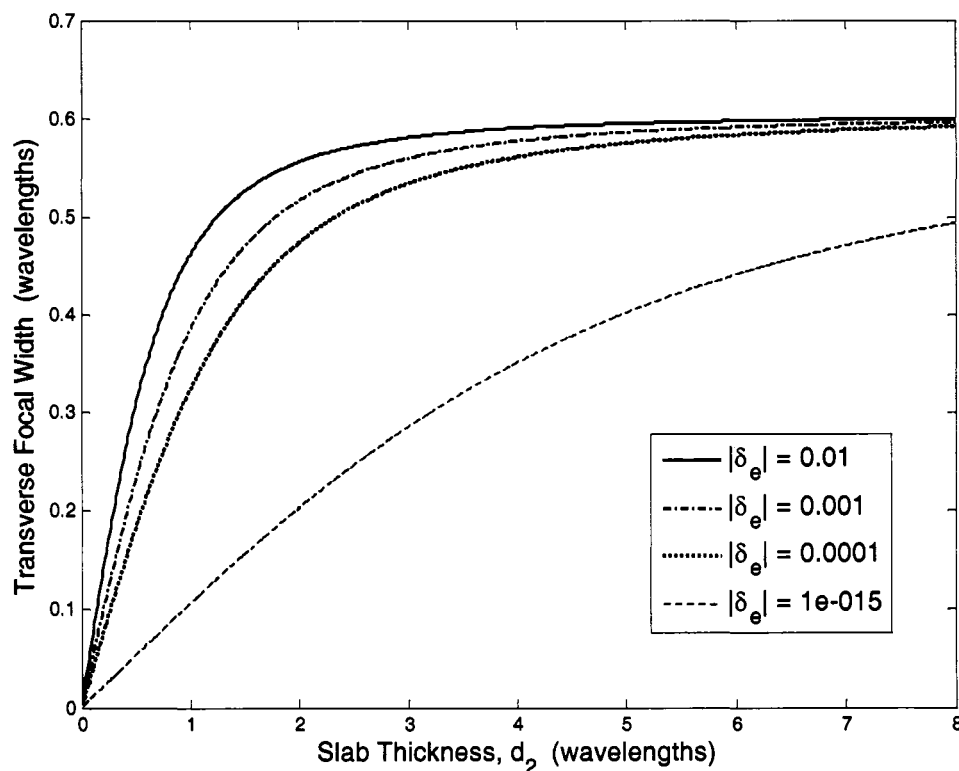


**Figure 5.8** Asymptotic approximation for transverse focal width at half maximum of  $|E_x|$ . The larger three deviation parameters  $\delta_e$  are estimates of achievable possibilities. The smallest  $\delta_e$  may be a sublime goal.

#### 5.4. Numerical calculation of $E_x$ fields and transverse focal widths

We have evaluated the transmitted  $E_x$  field accurately for many cases over a fairly broad region of the 2-D X-Z space. The calculations are limited somewhat in distance from the subsurface line because the oscillations of the integrand become very rapid for large  $x$  or  $z$ . We have explored out to  $z = 15 \lambda_0$  and to  $x \approx 12 \lambda_0$ . For the most part we have explored cases where the imaginary part of  $\epsilon_{2r}$  or  $\mu_{2r}$  is around

$10^{-3}$ , which keeps the resonance that occurs near  $k_p$  to be reasonably smooth as we shall illustrate.

As a first example, Figure 5.9 shows a comparison of the exact solution for the case corresponding to that shown in Figure 5.6 and Figure 5.7 with a modified plot of Figure 5.7. Recall that  $E_1$  is a purely real function and  $E_2$  is a function with constant phase. The  $E_2$  quantity plotted in Figure 5.9 is the  $E_2$  function multiplied by the inverse of its constant phase to produce a real quantity (with choice of positive real at  $x = 0$ ). Figure 5.9 then shows that the  $\text{Re}(E_x)$  is roughly within  $E_2$  of  $E_1$  and the  $|\text{Im}(E_x)| \approx |E_2|$ . This is consistent with the spectral comparisons shown in Figure 5.6. Further details of  $E_x$  in the region near the focal point are shown in Figure 5.10. Note that the scale for  $x$  in Figure 5.10 and subsequent figures is in wavelengths.

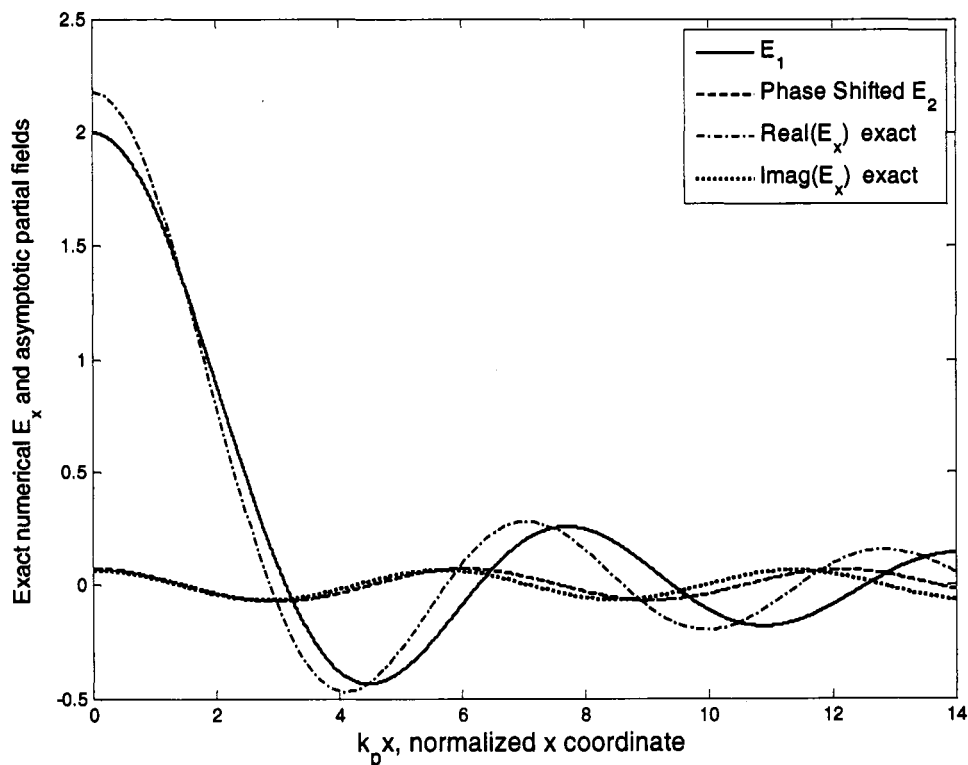


**Figure 5.9** Comparison of exact ( $E_x$ ) and asymptotic field ( $E_1$  and  $E_2$ ) in the focal plane for slab thickness  $d_2 = 2\lambda_o$ ,  $\varepsilon_{2r} = -1.005 - 0.001j$ ,  $\mu_{2r} = -0.99502 - 1e-007j$ .  $E_1$  is real.

For this case where  $k_p/k_o = 1.10718$  and  $k_o = 2\pi/\lambda_o$ , the conversion factor for Figure 5.9 is to divide  $k_p x$  by 6.9566. The peak value of  $|E_x|$  in the focal plane  $z_{fromExit} = 1\lambda_o$  is 2.177 V/wavelength and the magnitude of  $E_x$  reaches half this value at  $X_{hf} = 0.2752$  wavelengths. Since  $E_x$  is symmetric in  $x$ , the full width at half maximum is  $\Delta W = 2X_{hf} = 0.5504\lambda_o$ . By (5.30), the asymptotic estimate for the full width at half maximum is  $\Delta W = 3.791/k_p = 3.791/(1.10718(2\pi)/\lambda_o) = 0.5449\lambda_o$ , within 1% of the accurate calculation.

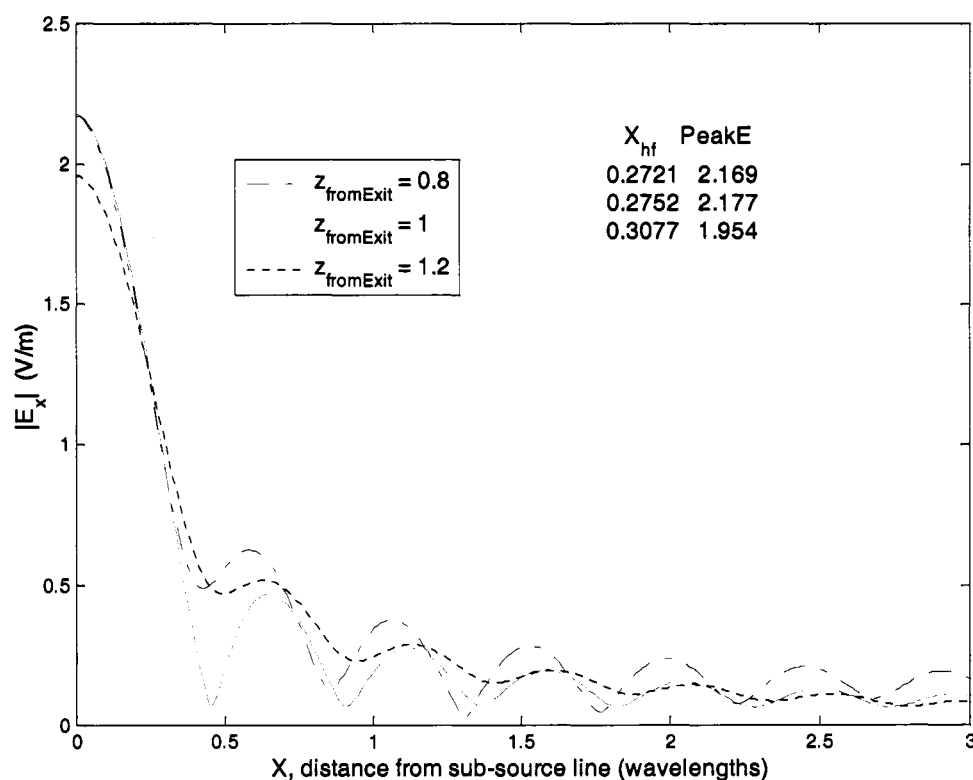


**Figure 5.10** Focal tendency for  $E_x$ . Slab width is  $2\lambda_o$ . Source distance is  $1\lambda_o$  in front of slab.  $\epsilon_{2r} = -1.005 - 0.001j$ ,  $\mu_{2r} = -0.99502 - 10^{-7}j$ . The included table gives values of  $X_{hf}$ , the half width at half height, and of the peak of  $E_x$  in  $V/\lambda_o$  for the 3 curves in legend order.

Figure 5.10 represents cuts through planes at  $0.8\lambda_o$ ,  $1.0\lambda_o$  and  $1.2\lambda_o$  from the

exit plane, respectively. For this example these correspond to 0.8, 1.0 and 1.2 times the distance from the exit plane to the focal plane. Figure 5.10 shows that the width of the central peak at half height is approximately a minimum in the focal plane. Actually this measure of width is slightly smaller somewhat inwards of (closer to the exit plane than) the focal plane. But there is deterioration in the quality of focus as measured by higher sidelobes or by an integral measure of the intensity at greater distances. This effect can be much more extreme in resonant cases.

More extreme cases occur for our p-polarization when the  $\text{Im}(\varepsilon_{2r}) = 0$ . All the loss is associated with the permeability. A case on which we carried out a careful study to determine the fineness of the grid required for accurate numerical Fourier transform integrals shows a much more peaked resonance near  $k_p$ . The parameters of this case are  $\varepsilon_{2r} = -1.0065$ ,  $\mu_{2r} = -0.99354 - 0.001j$ , and slab thickness  $d_2 = 1\lambda_o$ . Part of the explanation for this choice is that  $k_p$  increases with decreasing  $d_2$  and thus leads to a higher peak and a larger region where the grid must be fine-meshed. Figure 5.11 shows the spectral peak for this case at about 15 dB compared to a peak at about 5 dB for a medium with the previous values of  $\varepsilon_{2r}$  and  $\mu_{2r}$ .

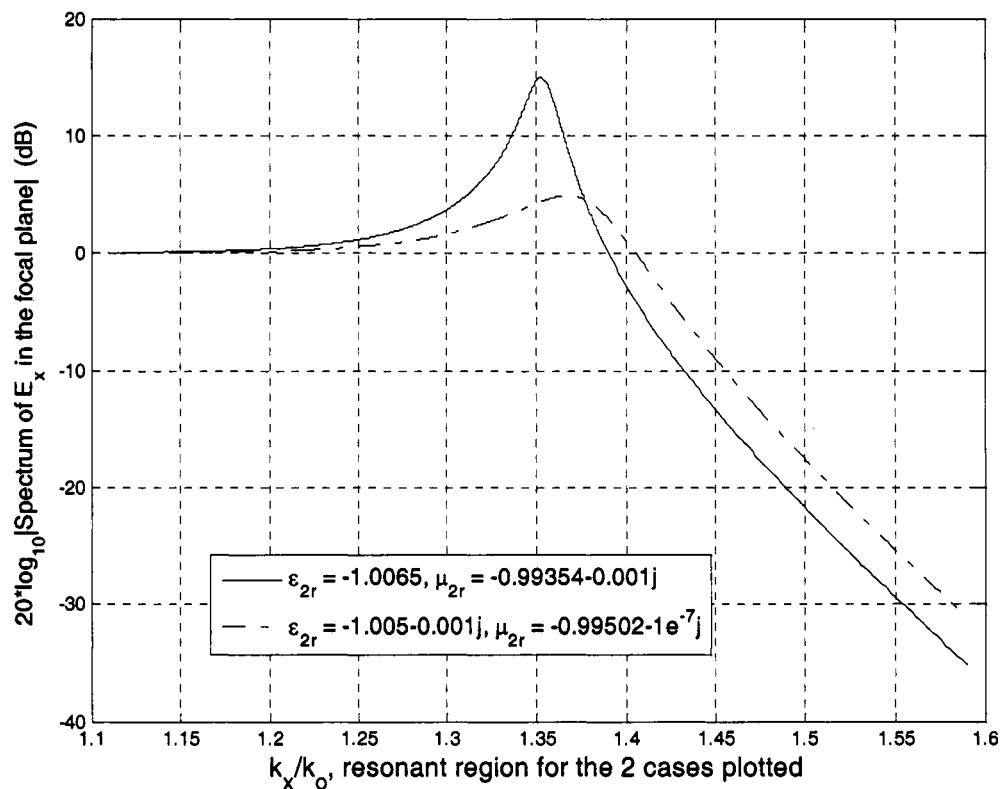


**Figure 5.11** Comparison of resonant spectral peaks for slab of thickness  $d_2 = 1 \lambda_o$ .

For the resonant case with a pure real  $\epsilon_{2r}$ , Figure 5.12 shows the space domain plot of  $E_x$  in the focal plane. These curves show many features in common with the asymptotic solution where for this case  $k_p = 8.503$ , or  $k_p / k_o = 1.3533$ : The real part is the dominant part of the solution, and its peak is approximately the peak of  $E_1$ , which is  $2 \cdot k_p / k_o = 2.707$ . The imaginary part of  $E_x$  resembles the function  $E_2$ . The full half width  $\Delta W = 2X_{hf} = 0.4529 \lambda_o$  is reasonably close to the asymptotic prediction of  $0.4458 \lambda_o$  given by (5.30).

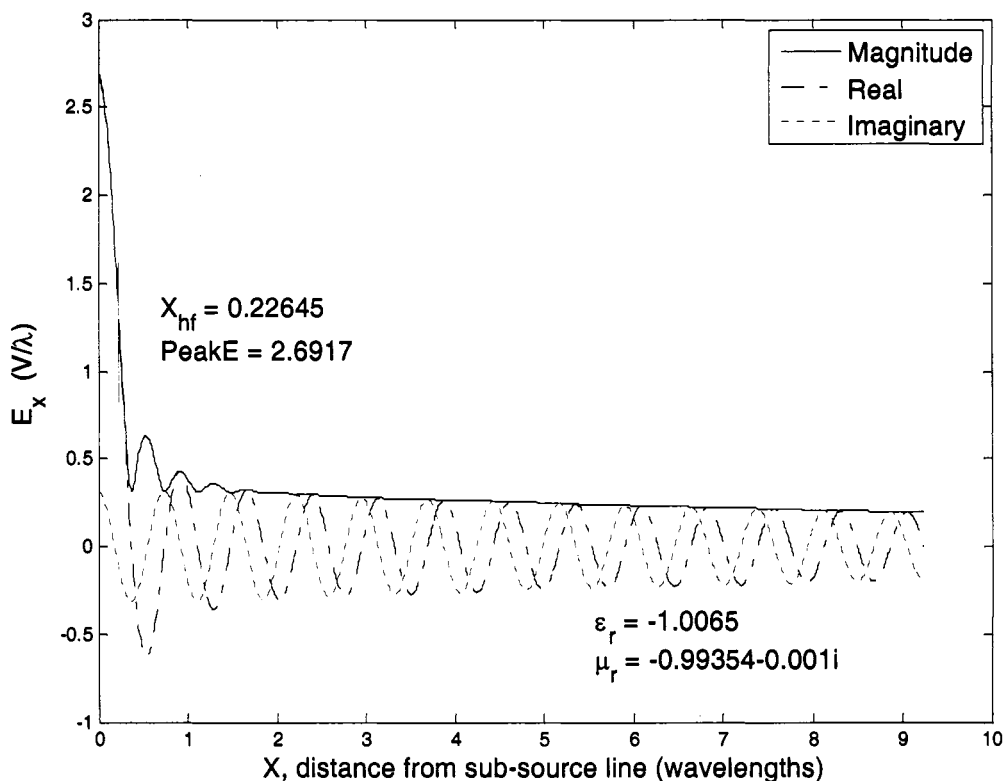


**Figure 5.12** Transverse cut of  $E_x$  in the space domain with central peak and oscillations for slab of  $1\lambda_0$  thickness and no loss in the permittivity term.

We have calculated transverse widths for many thousands of combinations of constitutive parameters and slab thickness. One convenient method to summarize the results is to look at a set of values of  $\epsilon_{2r}$  and  $\mu_{2r}$  that are related so that  $\text{Re}(n_2)$  is a constant,  $-1$  in most cases to follow. The imaginary parts of  $\epsilon_{2r}$  and  $\mu_{2r}$  are also held constant. Then  $\epsilon_{2r}$  and  $\mu_{2r}$  are related by a hyperbolic curve in the  $\text{Re}(\epsilon_{2r})$  versus  $\text{Re}(\mu_{2r})$  plane. For cases corresponding to the solid-line curve in Figure 5.12 the transverse width plotted versus the  $\text{Re}(\epsilon_{2r})$  is shown in the lower pair of plots in Figure 5.13. The solid curve is the result of the numerical Fourier transform calculations and the dotted curve is the asymptotic formula (5.30). The upper pair of plots show the same transverse focal widths for a slab of thickness  $d_2 = 5\lambda_0$ . The

asymptotic formula is within 1% of the detailed calculation except if  $|\delta_e| \ll |\delta_m|$ , where  $\delta_e = 1 + \varepsilon_{2r}$ ,  $\delta_m = 1 + \mu_{2r}$ . Equation (5.17) and further approximations leading to (5.23) require more than the general asymptotic approximation; the further requirement is that  $|\delta_e|$  be not small compared to  $|\delta_c|$  where  $\delta_c = -\delta_e - \delta_m + \delta_e \delta_m$ . Analysis of the relationship between  $\varepsilon_{2r}$  and  $\mu_{2r}$  required by fixing  $\text{Re}(n_2) \approx -1$  and the imaginary parts of  $\varepsilon_{2r}$  and  $\mu_{2r}$  leads to understanding that  $|\delta_e| \approx |\delta_m|$  unless  $\text{Re}(\delta_e)$  is small compared to the larger of  $\text{Im}(\delta_m)$  or  $\text{Im}(\delta_e)$ . So, in Figure 5.13, the region where the approximation is not good is where  $|\text{Re}(\varepsilon_{2r}) + 1| \ll 10^{-3}$ .

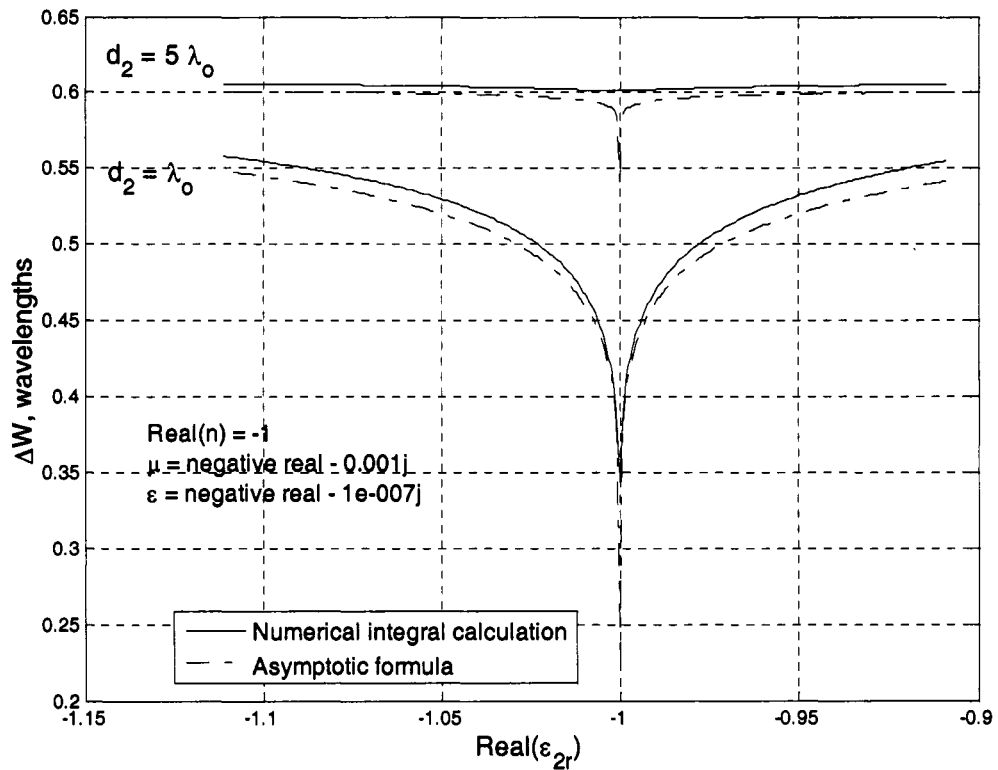


**Figure 5.13** Transverse focal widths through a slab of thickness  $1\lambda_0$  and  $5\lambda_0$  with small loss associated with permittivity.

Figure 5.14 shows the same type of plot for the case where the dominant loss

term is associated with permittivity and not with permeability. In this case the asymptotic approximation is quite accurate across the range of  $\text{Re}(\epsilon_{2r})$ . We have chosen to show cases with slab thickness  $d_2 = 1\lambda_o$  in Figure 5.13 and Figure 5.14 because we consider these as tight transverse focal distances for reasons given just before equation (5.26) and also because lack of focusing in the propagation (Z) direction for thin slabs could make the thin cases less useful. For thicker slabs, the transverse half width is somewhat greater, as shown by the upper pair of curves in Figure 5.13 and Figure 5.14. Except for exceedingly small  $|\delta_e|$ , (5.35) shows that the transverse focal width for fairly thick slabs ( $d_2 \geq 5\lambda_o$ ) becomes close to constant at  $3.791/(2*\pi) \approx 0.6$  wavelengths.

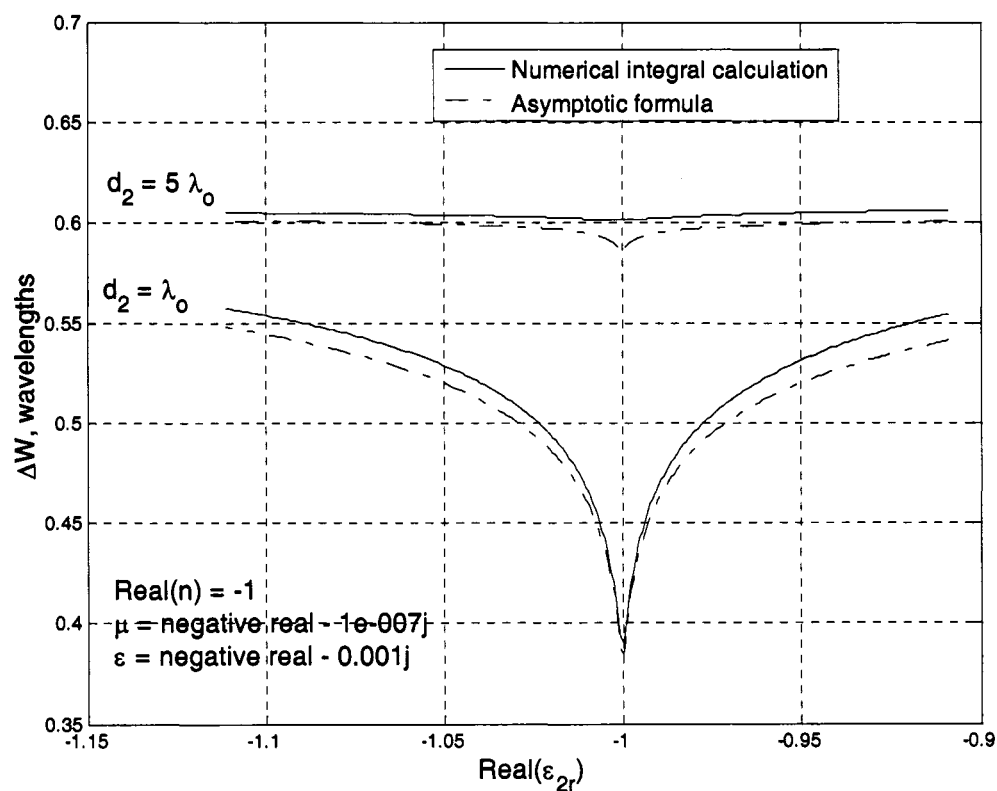


**Figure 5.14** Transverse focal widths through slabs of thickness  $1\lambda_o$  and  $5\lambda_o$  with small loss associated with permeability.

### 5.5. *Z dependence of $E_x$ on axis and focal width in the propagation direction*

For thin slabs with  $n_2 \approx -1$  we noticed that  $E_x$  on the Z axis is very strong at the exit surface of the slab and falls off monotonically with distance  $z$  from the slab. This behavior occurs even though in the transverse direction  $|E_x|$  is going from a wide-spread oscillatory function on the surface to a rather tight transverse focus in the focal plane and then on to a smooth wide-spread function for large  $z$ . On the other hand, for slabs of thickness greater than about 5 wavelengths, we found that  $E_x$  peaks on the Z axis at about the distance of the focal plane and has a width at half height of about 2 wavelengths, a width that is almost constant, increasing slightly as the slab thickness increases from 5 to 15 or more wavelengths.

The thin slab case with low loss appears in a contour plot as a sharp ridge with maximum value at the exit point and peak of the ridge on the Z axis. The width as measured to the half magnitude point (the 6-dB width) stays approximately constant out to the (defined) transverse focal plane. Figure 5.15 shows a contour plot based on numerical Fourier integrals of the exact solution for a slab thickness  $d_2 = 0.5 \lambda_o$  with small deviations from  $-1$ ; that is, with  $\epsilon_{2r} = -1.0005 - 0.0001j$  and  $\mu_{2r} = -0.99950025 - 10^{-7} j$ . The real part of  $\mu_{2r}$  (carried to more significant figures) is selected to make  $\text{Re}(n_2)$  equal to  $-1$  to machine accuracy. Figure 5.15 shows how the thin slab case does not provide a spot focus as usually imagined. This ridge focus is another reason why we have concentrated our calculations on thicker slabs. To provide data on this thin-slab case for direct comparison to other cases shown in this Chapter, Figure 5.16 shows exact numerical calculations of  $E_x$  in the focal plane. In this plane, the focal width (at the 6-dB level) is significantly less than a wavelength, with  $\Delta W = 0.108 \lambda_o$  as indicated on the plot. The plot of  $|E_x|$  on the Z-axis shown in Figure 5.17 shows in another way that there is no sensible focal width in the

propagation direction for these thin slab cases.

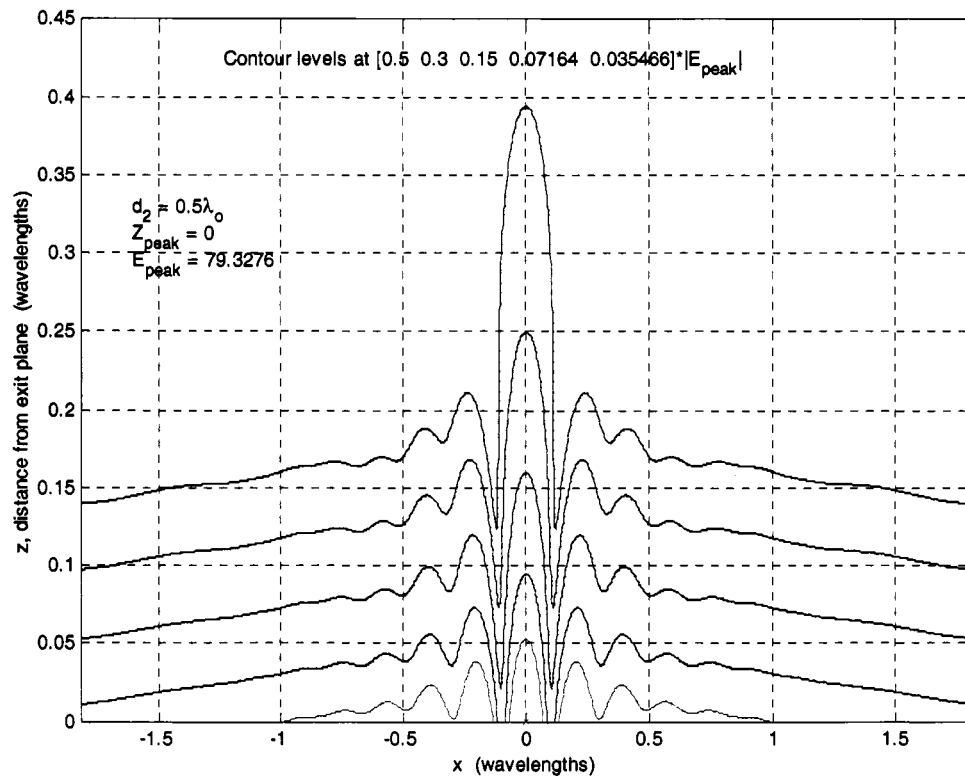


**Figure 5.15** Contour plot of  $|E_x|$  for a typical thin-slab case with  $n_2 = -1 - 5.025 \cdot 10^{-5} j$ . The peak of the transmitted field occurs at  $x = z = 0$  (position indicated by an 'x') with magnitude 79.3 V/wavelength as annotated. The next-to-lowest contour level is chosen to go through the defined focal plane ( $z = 0.25 \lambda_0$ ) and the lowest contour is at half of this level. All the contour levels are chosen to increase by about a factor of 2 as the contours get closer to the exit plane.

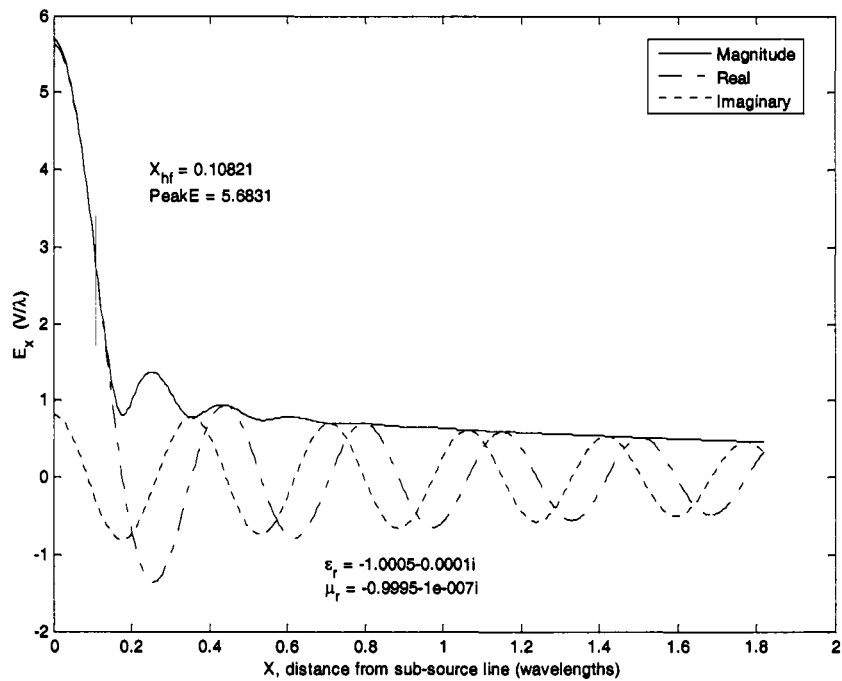


Figure 5.16  $E_x$  at  $z_{fromExit} = 0.25 \lambda_o$  with  $d_2 = 0.5 \lambda_o$  and  $d_1 = 0.25 \lambda_o$

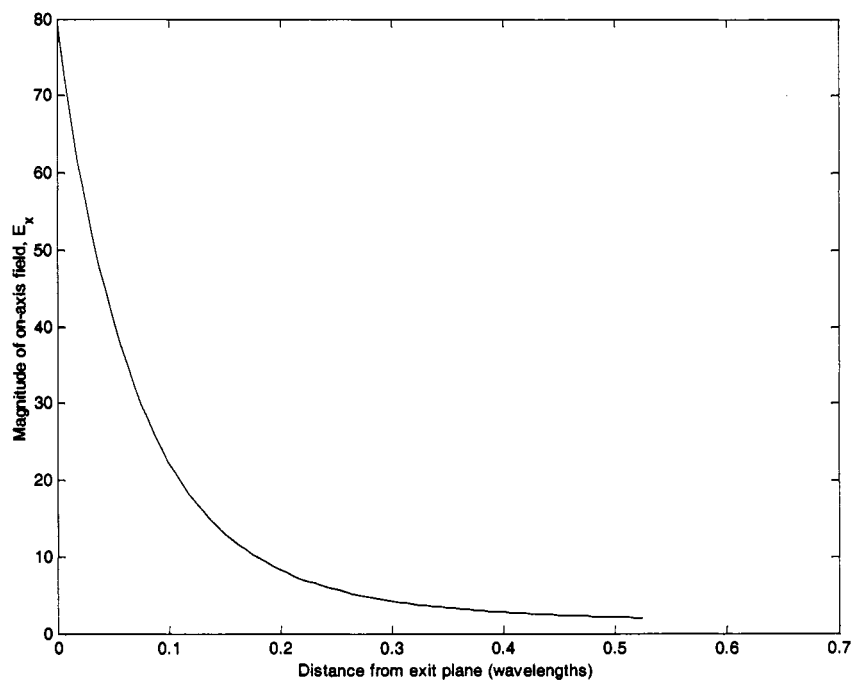


Figure 5.17 Magnitude  $|E_x|$  on the Z axis in  $V/\lambda_o$  for same case as Figure 5.15 and Figure 5.16.

We can understand this change in behavior from asymptotic analysis following somewhat along the developments of Section 5.2. The Fourier transform for the field on the Z-axis (i.e., at  $x = 0$ ) is the zero-spatial-frequency value of the integral given by (5.10). The invariance of (5.10) with respect to  $z - d_2 + d_1$  in the physical region  $z > d_2$  is a reason why we concentrated on just the one value of  $d_1 = 0.5d_2$  for the distance of the source to the incident plane of the slab, with the symmetric result for the distance from the exit plane to the focal plane.

An asymptotic evaluation of (5.10) with  $x = 0$  again breaks the integral into two regions. Region (a) will use the approximation (farthest right)

$$T(k_x) \approx \exp(-jd_2\sqrt{k_2^2 - k_x^2}) \approx \exp(jd_2\sqrt{k_o^2 - k_x^2}), \quad (5.36)$$

and region (b) will use the equations of (5.5) and (5.3). However, the boundary between (a) and (b) will be at  $k_x = k_o$  (instead of  $k_p$ ) because this choice provides a good approximation over the full range of  $z$  except in a small interval of length  $\delta_c$  about  $k_o$ . The integrand does not get large in this small interval, but has two branch points where  $T(k_x)$  vanishes so the contribution to the complete integral is small. The integral over region (a) will be denoted as  $E_1$  and over (b) will be  $E_2$ . Thus,

$$E_1 = \frac{1}{2\pi} \int_{k_o}^{k_p} \exp\left(-j\sqrt{k_o^2 - k_x^2}(z - 2d_2 + d_1)\right) dk_x. \quad (5.37)$$

To calculate the remaining  $E_2$  contribution to  $E_x$  on axis, we use (5.5) with the replacement  $\sqrt{k_x^2 - k_2^2} \approx \sqrt{k_x^2 - k_o^2}$ . Since  $\exp(-jk_x x)$  does not occur in the on-axis integral, the integrand is symmetric in  $k_x$  and we obtain twice the integral over the upper range.

$$E_2 = \frac{2}{2\pi} \int_{k_o}^{\infty} \frac{\exp\left(-\sqrt{k_x^2 - k_o^2}(z - 2d_2 + d_1)\right)}{1 - (R_b/4) \left[ \exp\left(2d_2\sqrt{k_x^2 - k_o^2}\right) - 1 \right]} dk_x. \quad (5.38)$$

In numerical calculations we used  $4k_p$  for the upper limit because the integrand is extremely small and decreasing rapidly beyond that point. We recognize that the focal distance in this  $z$  coordinate measured from the incident surface of the slab is  $z_f = 2d_2 - d_1$ . We can make (5.37) and (5.38) more general by replacing  $z - 2d_2 - d_1$  by  $z - z_f$  so we can now use the exit plane or the image plane for the  $z$  coordinate origin. This form emphasizes the translational invariance of the solution in the sense that, as the source and image are kept a distance  $2d_2$  apart and the slab of thickness  $d_2$  is translated parallel to itself in the intervening region, the solution for the transmitted field remains the same relative to the image point. Only the cutoff of the transmitted region, or in other words, how far the solution extends from the image towards the slab, changes.

$E_1$  has a very nice form in that it is independent of the constitutive parameters and of slab thickness except for focal plane location. This “universal” function is shown in Figure 5.18. The real part is symmetric and the imaginary part is antisymmetric about the focal distance, so the magnitude is symmetric as shown. It should be noted that the width of  $E_1$  about the focal point as measured at the half maximum level is

$$\Delta W_z = 1.9142 \lambda_o. \quad (5.39)$$

It is this “universal” width of  $E_1$  that accounts for the fact that for all fairly thick slabs the focal width along the  $Z$  direction is about  $2 \lambda_o$ .

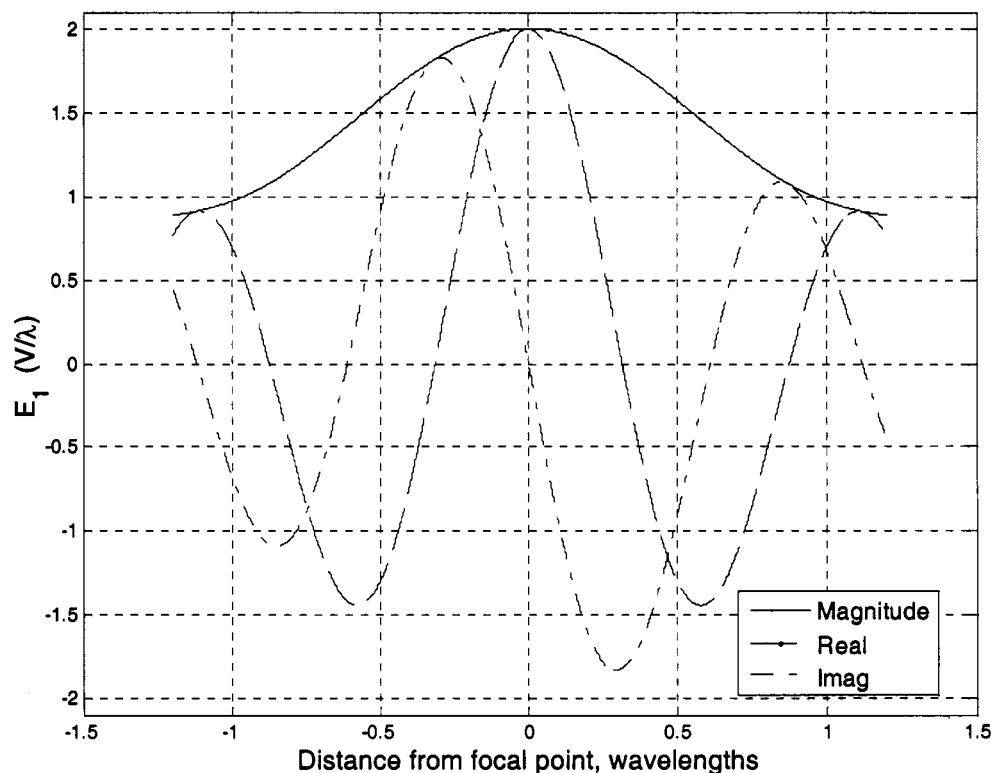


**Figure 5.18**  $E_1$  is the asymptotic low-spatial-frequency contribution to the transmitted  $E_x$  component evaluated on the  $Z$  axis. The plot is translated to be centered on the focal plane. Negative distance is towards the slab. The half maximum value occurs at  $D = \pm 0.95707$ .

To understand when and how  $E_1$  determines the focal width in these cases, the contribution of  $E_2$  must be examined. We evaluated (5.38) with what we call the third-order approximation (5.3) for  $R_b$ . Again, we have assumed the symmetric case with the source at a distance  $d_1 = d_2/2$  away from the incident side of the slab.  $E_2$  is largest at the exit plane of the slab and falls off rapidly with distance from the exit plane. Also, it is much larger when the slab is thin. Figure 5.19 illustrates how severely  $E_2$  changes as the slab thickness increases from  $1\lambda_0$  to  $8\lambda_0$ . It is important to note the change of scale (both vertical and horizontal) for the different slab thicknesses.

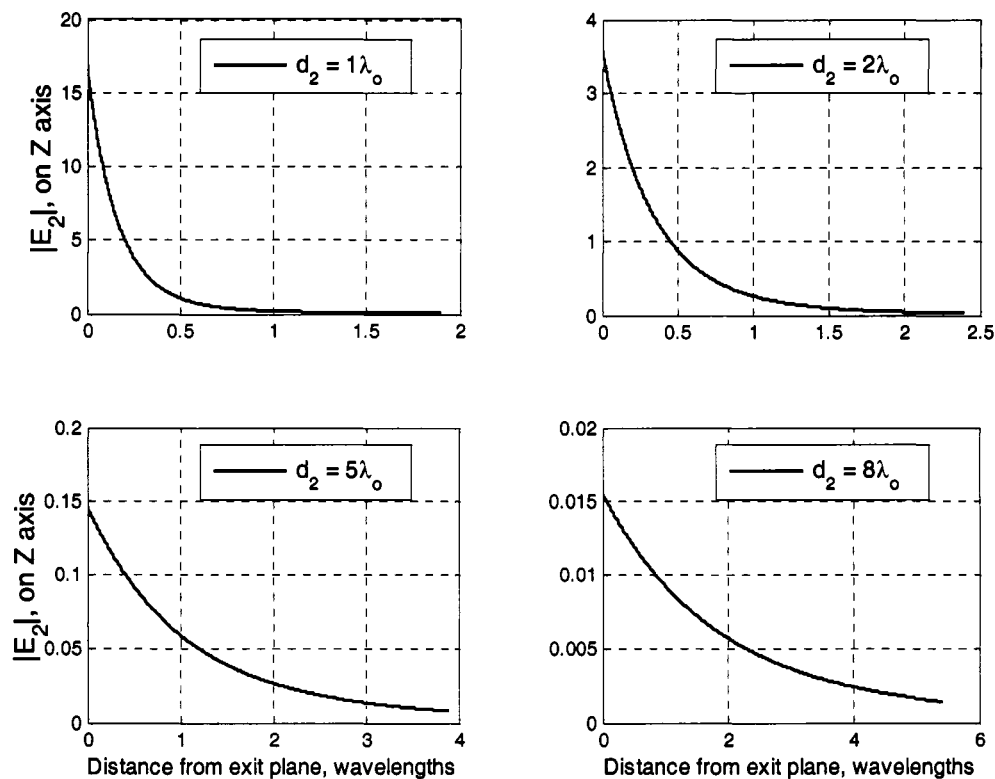


**Figure 5.19**  $E_2$  is the asymptotic high-spatial-frequency contribution to the transmitted  $E_x$  component. The  $z$  origin is translated so that  $z$  is measured from the exit plane of the slab. These calculations are for the case  $\epsilon_{2r} = -1.0005 - 0.001j$  and  $\mu_{2r} = -0.9995 - 10^{-7}j$ .

The asymptotic calculation of  $E_x(z) = E_1 + E_2$  on the  $Z$  axis then reveals no peak for thin (approximately  $d_2 \leq 1$ ) slabs and a shifting but near constant peak for thick slabs. Figure 5.20 shows the results for the cases of Figure 5.19. The exact calculation of  $E_x(z)$  from numerical integration of (5.10) is shown in Figure 5.21 for the same cases. The magnitudes are quite close except near the exit plane for the thin slab with  $d_2 = 1$ , where the exact calculation has a peak (not shown in the figure due to scaling for comparison to Figure 5.20) of  $49.36 \text{ V}/\lambda_0$  at the exit plane. In general, the approximation for  $E_2$  is somewhat rough because it is used to approximate to lower spatial frequencies than the derivation indicates to be valid.

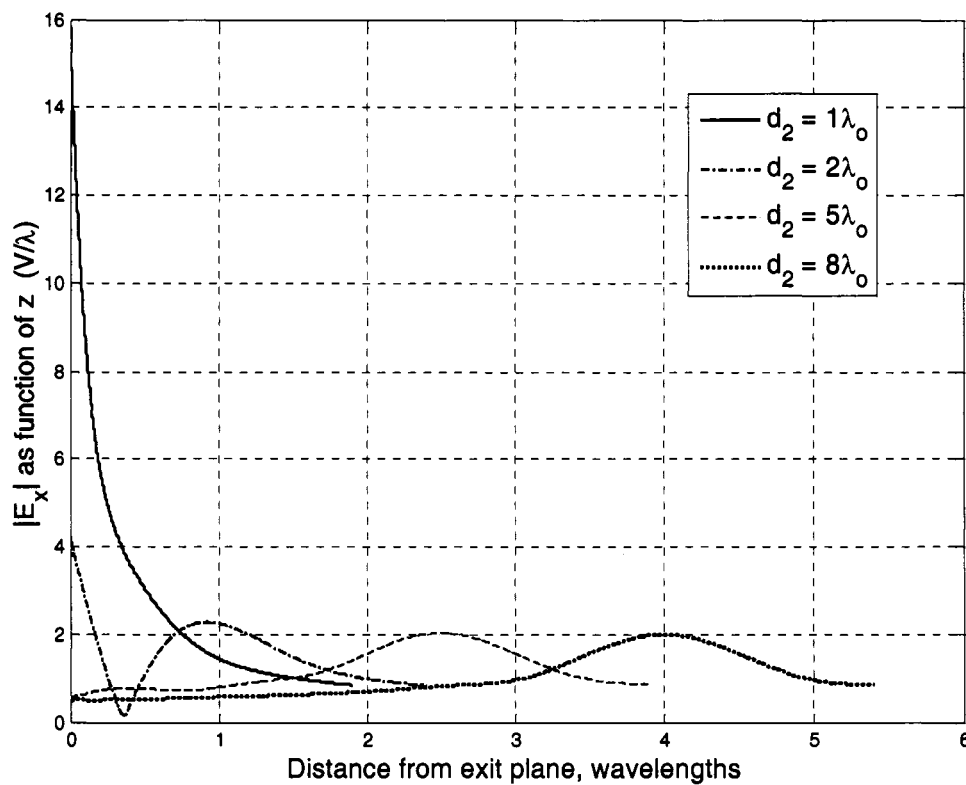


**Figure 5.20** Asymptotic calculation of  $E_x$  evaluated on the Z axis translated so that z is measured from the exit plane of the slab. For the case  $\epsilon_{2r} = -1.0005 - 0.001j$  and  $\mu_{2r} = -0.9995 - 10^{-7}j$ .

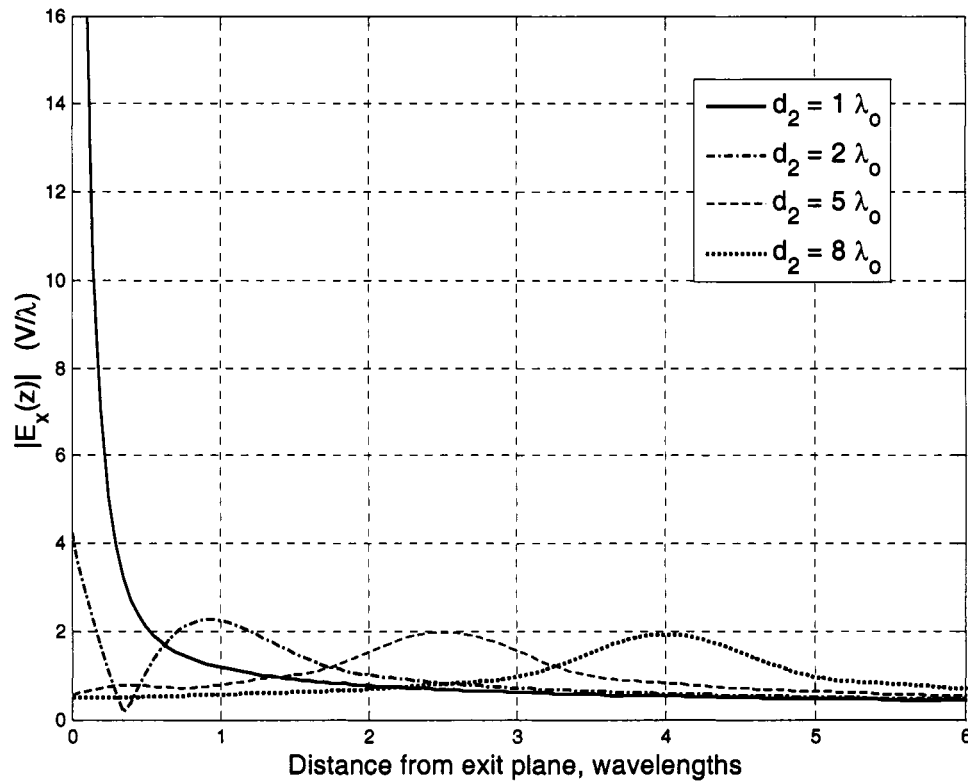


**Figure 5.21** Numerical Fourier integral calculation of  $E_x$  evaluated on the  $Z$  axis translated so that  $z$  is measured from the exit plane of the slab. For the case  $\varepsilon_{2r} = -1.0005 - 0.001j$  and  $\mu_{2r} = -0.9995 - 10^{-7}j$ .

To summarize the focusing typical of a thick slab with  $d_2 = 5 \lambda_0$  Figure 5.22 shows a contour plot of  $E_x$  in  $X$ - $Z$  space with equal-length axes. The plot data come from a numerical evaluation of the exact Fourier integral solution. The distance of the source from the incident plane is  $d_1 = d_2 / 2$ .

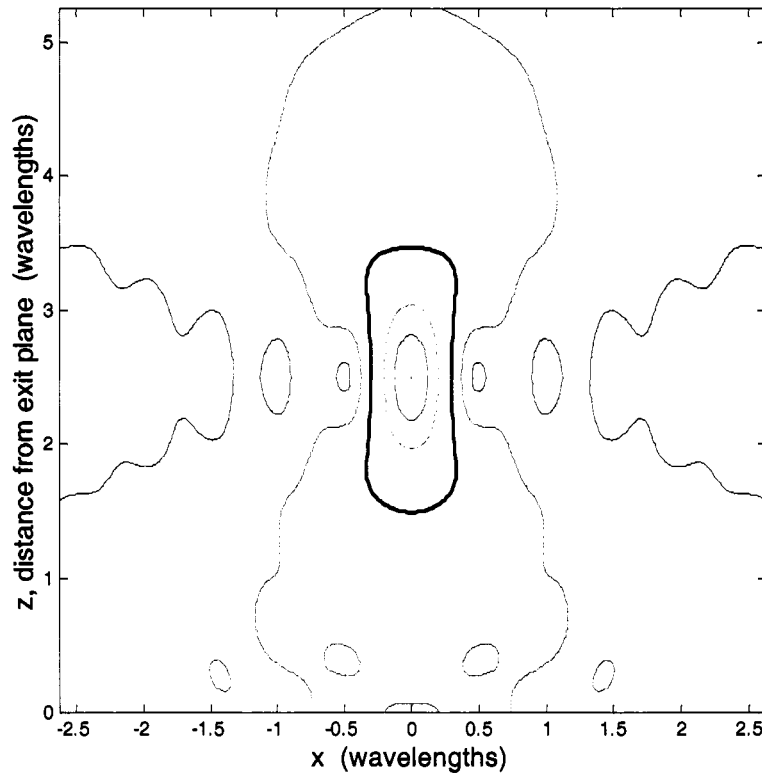


**Figure 5.22** Contour plot of  $|E_x|$ . For the case  $d_2 = 5$ ,  $\epsilon_{2r} = -1.0005 - 0.001j$  and  $\mu_{2r} = -0.9995 - 10^{-7}j$ . The contours are at 0.9, 0.75, 0.5, 0.3 and 0.1 of peak value. The peak location is at the point plotted with an x. The heavy contour is the  $\frac{1}{2}$ -height contour.

### 5.6. Variation of focal distance with $Re(n_2)$

We use here the term focal distance for the  $Z$  distance from the exit plane to the point where the maximum of transmitted  $E_x$  occurs. By symmetry the peak is on the  $Z$  axis. From the discussion of invariance of the transmitted solution with translation of the slab between source and theoretical  $n_2 = -1$  image point, the focal distance could more generally refer to the distance from the ideal image point inside medium 2 (at  $z = d_2 - d_1$  as measured from the incident plane) to this peak of  $E_x$ .

Also, previously in this Chapter we used focal point to mean the theoretical geometrical focal point of the  $n_2 = -1$  slab. Since we have computed only cases with  $d_1 = 0.5d_2$ , there is just an additive shift of  $0.5d_2$  between these two definitions for our computations.

The program that generates the calculations and plot of Figure 5.23 is very useful to visualize how the shape and position of the peak of  $|E_x|$  change with changes in the index of refraction and in the constitutive parameters. We find that the focal distance increases for small increases in  $\text{Re}(n_2)$  from  $-1$  (i.e., decreasing  $|n_2|$ ) and the focal distance decreases as  $\text{Re}(n_2)$  goes from  $-1$  towards more negative values.

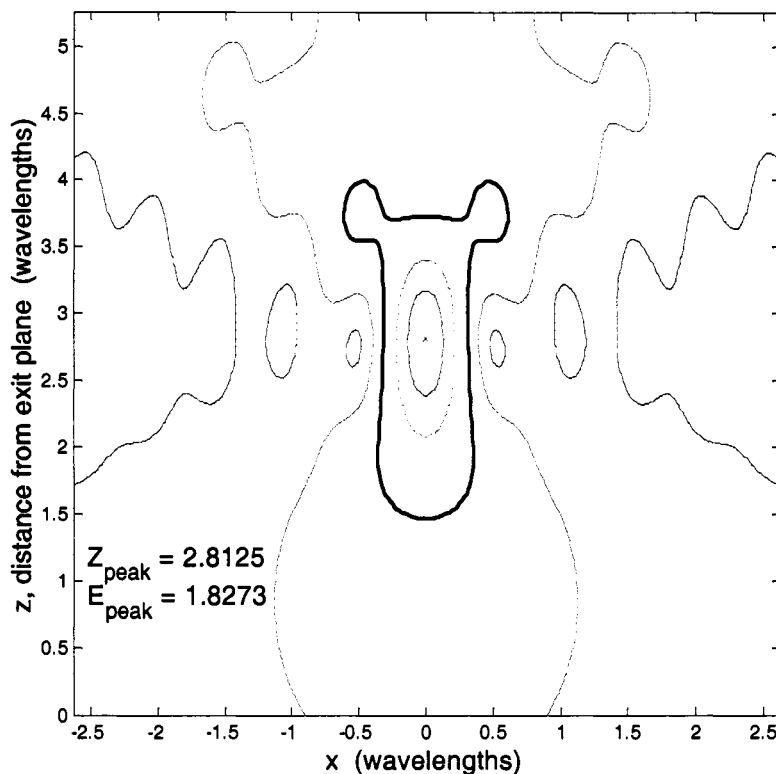


**Figure 5.23** Contour plot of  $|E_x|$ . For the case  $n_2 = \epsilon_{2r} = \mu_{2r} = -0.98 - 0.00098j$  with  $d_2 = 5$ . Contour levels and peak  $x$  as in Figure 5.22. The quantity  $Z_{peak}$  refers to distance from exit plane to peak at  $E_{peak} = \max|E_x|$  in  $V/\lambda$ .

Also, as Figure 5.23 and Figure 5.24 show, the half-height contour develops “ears” on the end in the Z direction towards which the contour is moved relative to the  $n_2 = -1$  case. This means that small peaks above half height are developing in these ears. These peaks represent a general trend toward higher side lobes. Our calculations show that to visible levels the contours in Figure 5.23 and Figure 5.24 depend only on  $\text{Re}(n_2)$  and not on particular  $\epsilon_{2r}$ ,  $\mu_{2r}$  combinations as long as the two are reasonably close to each other. In Figure 5.23 and Figure 5.24 we chose  $n_2 = \epsilon_{2r} = \mu_{2r}$  and

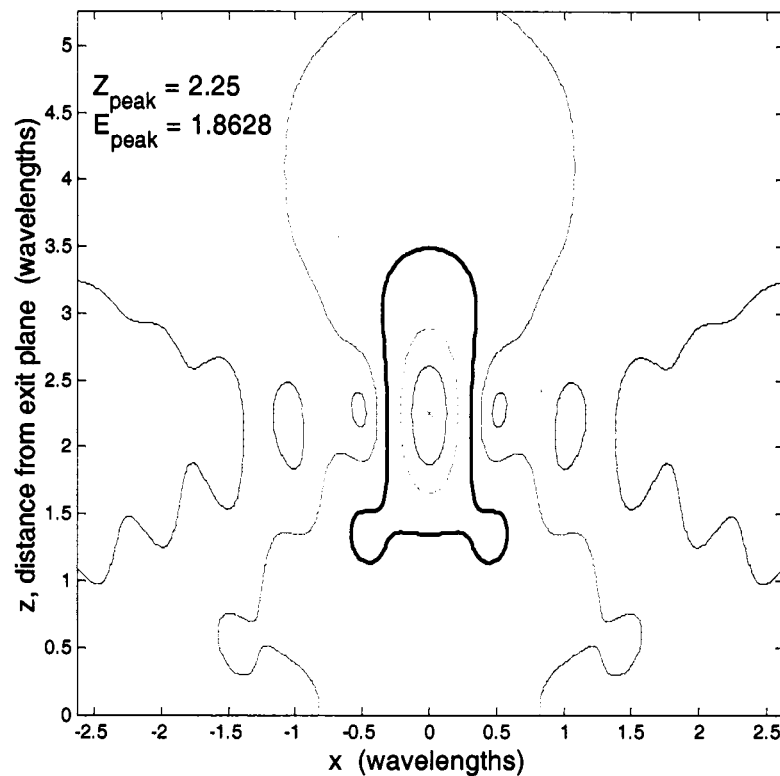


**Figure 5.24** Contour plot of  $|E_x|$ . For the case  $n_2 = \epsilon_{2r} = \mu_{2r} = -1.02 - 0.00102j$  with  $d_2 = 5$ . Contour levels and peak  $x$  as in Figure 5.22. The quantity  $Z_{peak}$  refers to distance from exit plane to peak at  $x$ .  $E_{peak} = \max(|E_x|)$  in  $V/\lambda$ .

set the loss tangent for all of these to be 0.001.

Figure 5.25 summarizes the results of many runs of the types shown in Figure 5.23 and Figure 5.24 and also results for slab thicknesses of 4 and 6 wavelengths.

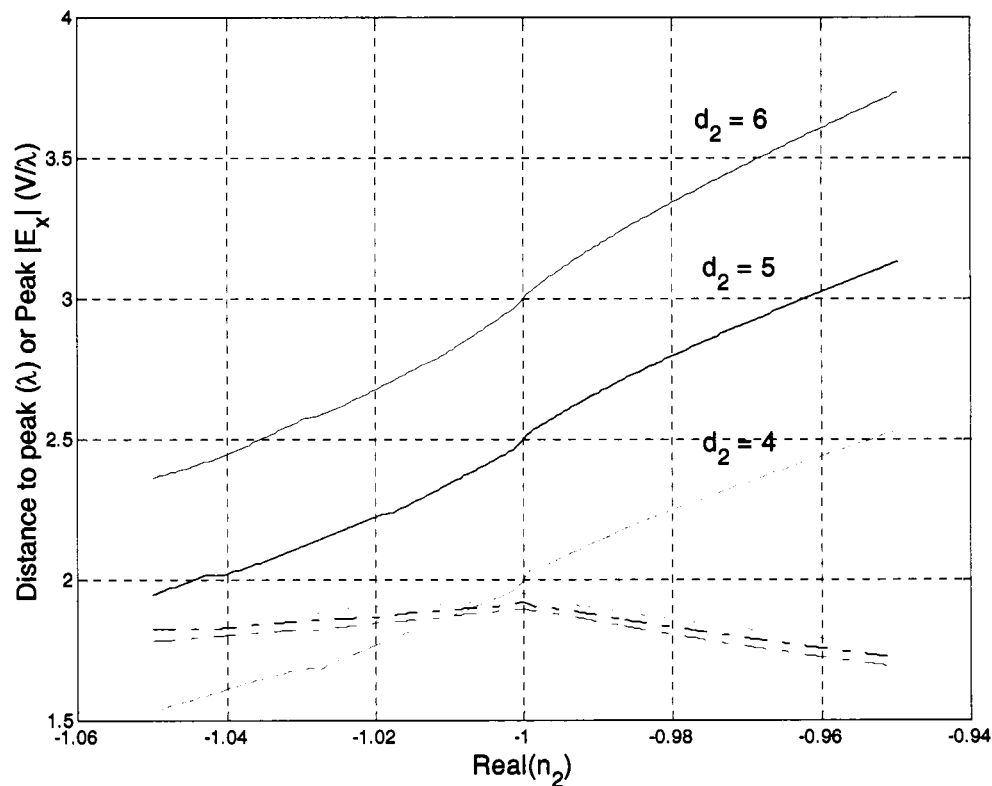


**Figure 5.25** Solid curves show  $Z$  distance from exit to peak of  $E_x$ . The dash-dot curves give the value of the peak. The peak-value curves are inverted in order from top to bottom relative to the focal distance curves. (Thicker slabs provide more attenuation.) Calculations for case  $n_2 = \epsilon_{2r} = \mu_{2r}$ . Loss tangent = 0.001.  $d_1 = 0.5d_2$ .

The small kinks and inflections in the focal length curves in the region  $n_2 < -1$  (most pronounced for the thinnest slab) were unexpected. For a selected value of slab thickness  $d_2$  the curves of peak  $E_x$  have corresponding inflections at the same values of  $n_2$  (barely visible at the scale shown in Figure 5.25. This behavior appears related to the growth of sidelobes and changing patterns as shown in Figure 5.22 through

Figure 5.24. The region  $n_2 < -1$  has greater complexity introduced by the finiteness of the region into which the higher-amplitude sidelobes are being squeezed and the fact that all the non-evanescent waves are transmitted through medium 2.

If  $n_2 = -1 + \delta_n$ ,  $|\delta_n| \ll 1$ ,  $n_2$  real, then near axial rays focus geometrically at the point  $z_f = 2d_2 - d_1 + \delta_n d_2$  (measured from the origin in the plane of incidence), but farther from axial rays deviate increasingly more from this point in their axis crossing as the incident angle  $\theta$  increases. In contrast, for  $-1 < n_2 < 0$  a portion of the pulse incident at large angles (angles greater than the critical angle) become evanescent in the transmission region.

### 5.7. *Focusing of the Poynting Vector and Energy Densities*

These results are from numerical calculations of fields based on (5.10) for  $E_x$  and the similar Fourier inverse transforms for the transmitted components  $H_y^r$  and  $E_z^r$ . From here on we omit the superscript where we are dealing only with transmitted components. Explicitly,

$$H_y = \frac{-\omega \epsilon_o}{2\pi} \int_{-\infty}^{\infty} T(k_x) \frac{\exp[-jk_{z1}(z - d_2 + d_1) - jk_x x]}{k_{z1}} dk_x \quad (5.40)$$

$$E_z = \frac{-1}{2\pi} \int_{-\infty}^{\infty} T(k_x) \frac{k_x}{k_{z1}} \exp[-jk_{z1}(z - d_2 + d_1) - jk_x x] dk_x \quad (5.41)$$

where  $k_{z1} = \sqrt{k_o^2 - k_x^2}$  and the correct sign of the square root must be chosen to attenuate outgoing waves.

From a set of a dozen cases for which all the components were calculated and from them the Poynting vector and energy densities, we have found a few properties of the focus that are probably general. Since in the limit of  $\epsilon_{2r} \rightarrow -1$  and  $\mu_{2r} \rightarrow -1$  all the components in the theoretical focal plane are restored to their values in the source plane, the Poynting vector should show a focusing peak near the theoretical

focus. We find that this Poynting peak of  $\text{Re}\{|\vec{S}|\}$  is

- (a) closer to the exit plane than the peak of  $|E_x|$ . This has meaning only if there is a peak relative to the Z direction (the propagation direction).
- (b) In these cases, the peak of  $\text{Re}\{|\vec{S}|\}$  is tighter than the peak of  $|E_x|$ . By this we mean that the half widths at 3 dB and 6 dB below the peak are smaller in both the transverse (X) and propagation (Z) direction. The dB measure is taken per the appropriate definition so that, for example, the -6 dB level is about half the peak for  $|E_x|$  and about one quarter the peak for  $\text{Re}\{|\vec{S}|\}$ .
- (c) When there is no peak in the Z direction (This corresponds to a case with a relatively thin negative index layer, thickness less than about 1 wavelength.), the transverse focusing of  $\text{Re}\{|\vec{S}|\}$  is broader (i.e., has larger 3-dB and 6-dB widths) than that of  $|E_x|$  as calculated in the theoretical focal plane.

We shall now present a series of plots to illustrate cases that are chosen to be comparable to previous calculations in this chapter, or with variations from these. We start with results for the case shown in Figure 5.22, where the NIM layer of width  $d_2 = 5$  has  $\epsilon_{2r} = -1.0005 - 10^{-3}j$  and  $\mu_{2r} = -0.9995 - 10^{-7}j$ . (More precisely, the  $\text{Re}(\mu_{2r})$  is chosen to make  $\text{Re}(n_2) = -1$  to machine accuracy.)

Figure 5.26 is a contour plot of  $\text{Re}\{|\vec{S}|\}$  for this case with the 2 heavy contours being at 3 dB and 6 dB below the peak. The one outer contour shown (at 10 dB below the peak) can be interpreted as illustrating that the power is flowing into the focal point along several paths, but one strong path is at an approximately constant angle that appears to come from  $x = 5$  on the exit plane. This flow accounts for the extension of the 6-dB contour in this direction. The next figure, Figure 5.27, is a

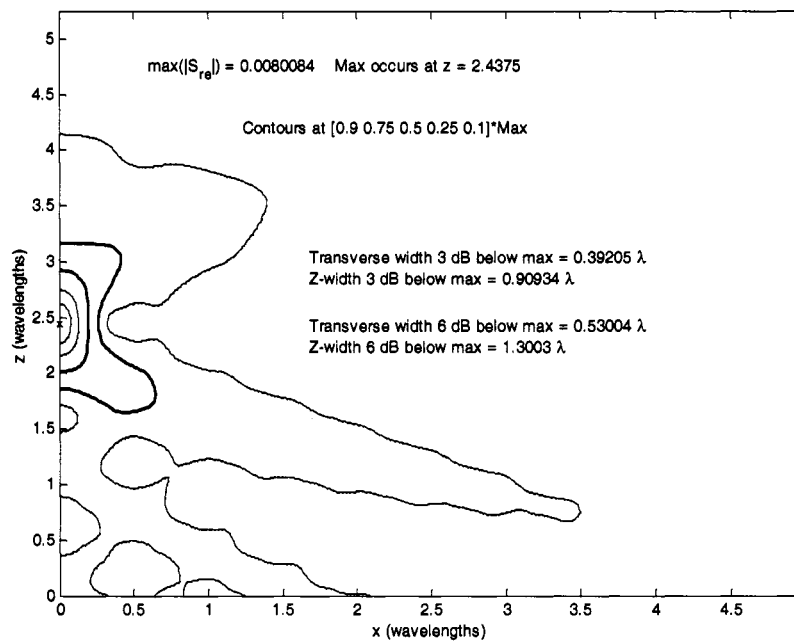


**Figure 5.26** Contour plot of real part of the Poynting vector, for case with  $d_2 = 5 \lambda_o$ ,  $\epsilon_{2r} = -1.0005 - 10^{-3} j$  and  $\mu_{2r} = -0.9995 - 10^{-7} j$ .

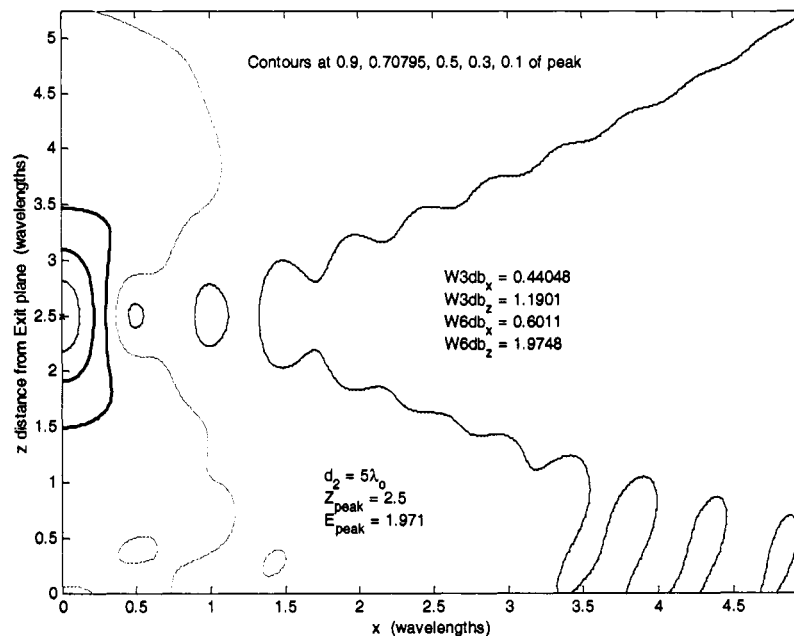


**Figure 5.27** Contour plot of  $|E_x|$ , for case with  $d_2 = 5 \lambda_o$ ,  $\epsilon_{2r} = -1.0005 - 10^{-3} j$  and  $\mu_{2r} = -0.9995 - 10^{-7} j$ . In both Figure 5.26 and Figure 5.27 the heavy contours are at 3 dB and 6 dB below the peak.

replot of Figure 5.22 with just the half space in  $x$  and  $z$  shown, to be comparable to Figure 5.26, and with contour levels chosen to allow better dB comparison to Figure 5.26 because the heavy contours are also at the level of 3 dB and 6 dB below the peak. One may easily see that the width of the corresponding contours in Figure 5.27 are larger as measured along the  $Z$  axis and slightly fatter as measured in the transverse ( $x$ ) direction along the line through the peak. The numerical values given on the plot are for the full widths (i.e., in the  $x$  direction the symmetric part of the contour in negative  $x$  is included) in wavelengths. In Figure 5.27, further abbreviations of these widths were used; for example,  $W_{3\text{db}_x}$  refers to the transverse or  $x$  direction width 3 dB below the peak. The transverse widths of  $\text{Re}\{|\vec{S}|\}$  are slightly less than 0.9 times the transverse widths of  $|E_x|$ , while the width 6 dB down for  $\text{Re}\{|\vec{S}|\}$  in the  $Z$  direction is only 0.66 times this width of  $|E_x|$ . This ratio is 0.76 at 3 dB below the peak. In Table 5.2, to be presented after more detailed considerations, we shall gather these widths for a number of cases. In Figure 5.27, it is difficult to separate the two outer contours. The next-to-outer contour at roughly 10 dB below the peak includes the left-most contour from top to bottom of the figure plus two small closed ovals near the bottom (left and right of this long contour) plus a short segment about the origin.

Next, Figure 5.28 shows the direction of the flow of  $\text{Re}\{\vec{S}\}$  corresponding to the magnitudes in Figure 5.26. Figure 5.28 is a MATLAB quiver plot, which plots vectors with length proportional to  $\text{Re}\{|\vec{S}|\}$  and direction of  $\text{Re}\{\vec{S}\}$  on a rectangular grid. Upon exiting the NIM at  $z = 0$  the Poynting vector flows alternately towards and away from the  $Z$  axis and forms complex patterns to reach a peak magnitude with direction flowing outwards in the vicinity of the focal point. The details of the complex pattern change noticeably from case to case, but the general properties remain.

The magnetic and electric stored energy densities and the total energy density also show interesting patterns in contour plots. The time-averaged electric and magnetic energy densities  $W_e$  and  $W_m$  in free space (the transmitted-field region) for the single-frequency cases we are considering in this chapter are given by

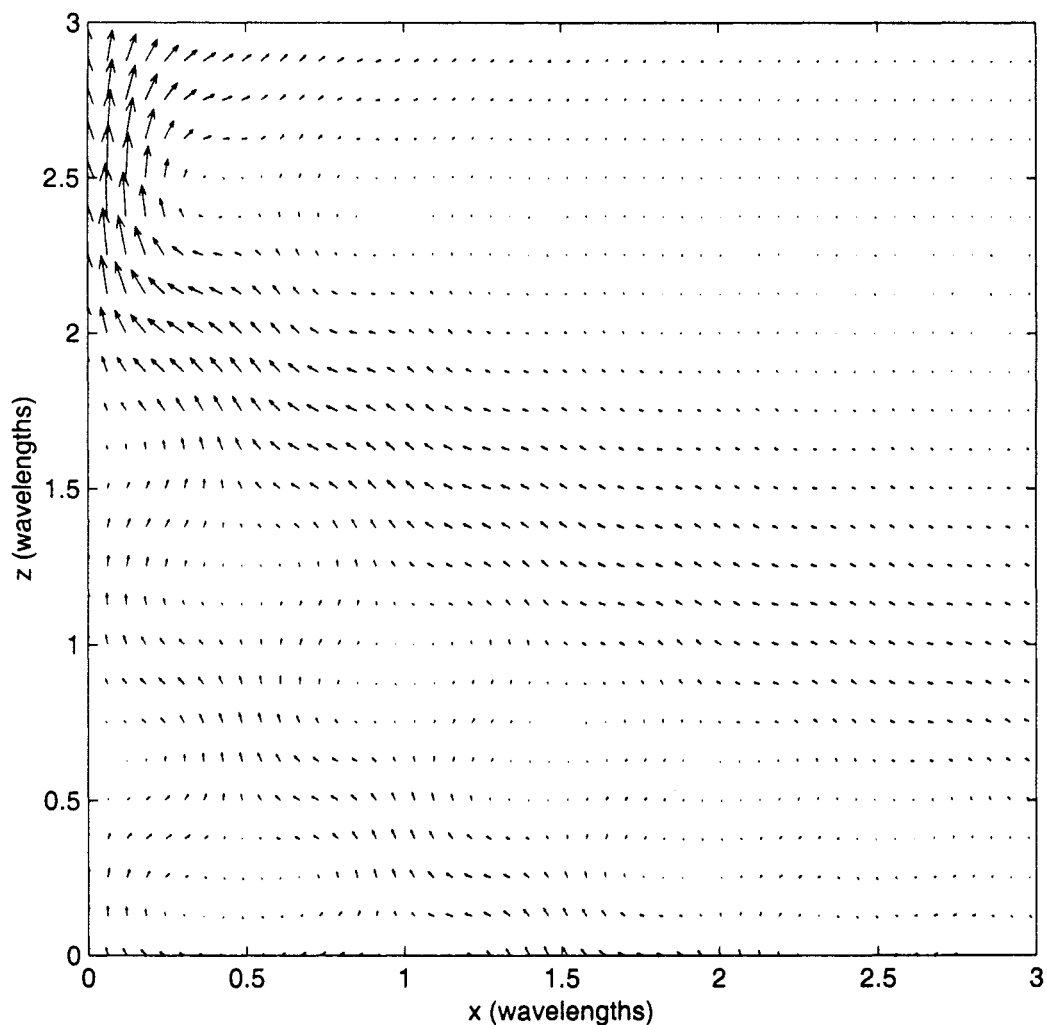


**Figure 5.28** Quiver plot of  $\text{Re}\{\vec{S}\}$  for same case with  $d_2 = 5 \lambda_0$ ,  $\epsilon_{2r} = -1.0005 - 10^{-3} j$  and  $\mu_{2r} = -0.9995 - 10^{-7} j$ .

$$W_e = \frac{\epsilon_o}{4} |\vec{E}|^2 \quad \text{and} \quad W_m = \frac{\mu_o}{4} |\vec{H}|^2 \quad (5.42)$$

respectively, where  $\vec{E}$  and  $\vec{H}$  are the vector phasor amplitudes of the electric and magnetic field in accordance with the notation we have been using. Then, a total stored energy density may be defined as  $W = W_e + W_m$ . Since we calculated all the fields to get the Poynting vector, these densities are evaluated directly from (5.42).

For the same case as shown in Figures 5.26 through 5.28, a contour plot of  $W_m$  is shown in Figure 5.29 and of  $W_e$  in Figure 5.30. Figure 5.29 shows that  $W_m$  forms a compact focal pattern about a peak at  $z \cong 2.44 \lambda_o$  just inwards of the

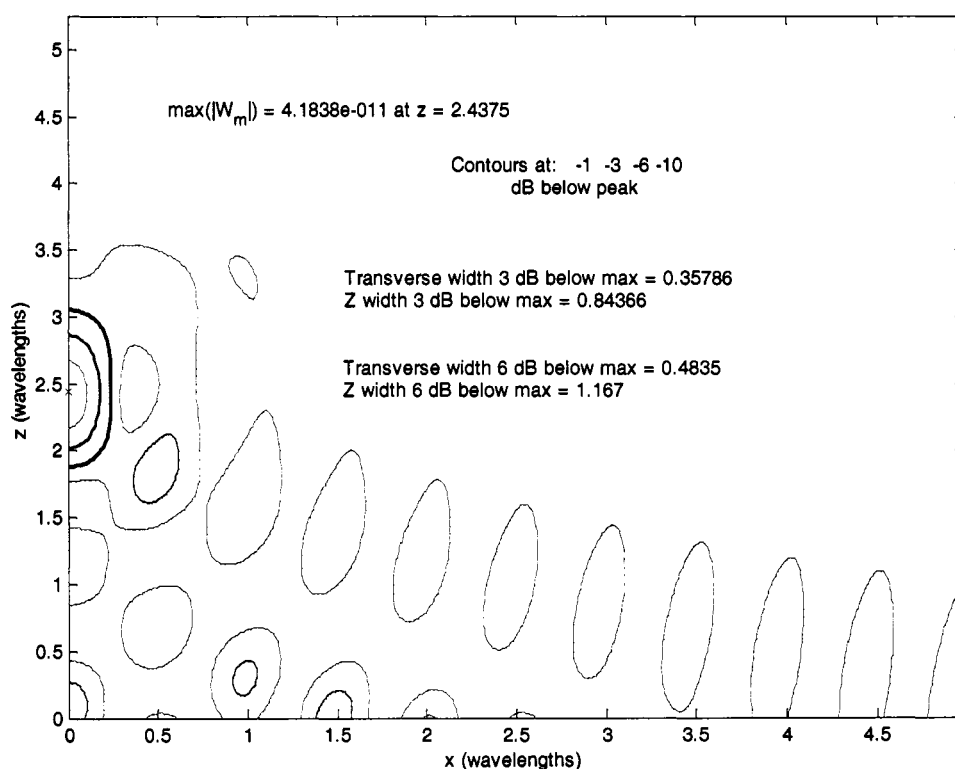


**Figure 5.29** Contour plot of stored magnetic energy density for  $d_2 = 5$ ,  $\epsilon_{2r} = -1.0005 - 10^{-3} j$ , and  $\mu_{2r} = -0.9995 - 10^{-7} j$ . The contours at  $-3$  dB and  $-6$  dB relative to the peak are shown in heavy line widths. The peak location is indicated with an x. Note that the widths of the peak at these two levels are somewhat (8% to 10%) smaller than the corresponding levels for  $\text{Re}\{\vec{S}\}$  shown in Figure 5.26.

theoretical focal point. In contrast  $W_e$  has a broader pattern and, at the  $-6$  dB level, the contours show a standing wave pattern that extends beyond  $x = 4 \lambda_o$ . Hence, we calculated transverse- and propagation-direction widths for the contours of  $W_m$ , but did not want to make such a choice for the complex pattern of Figure 5.30. One other interesting feature of these two plots is that the standing-wave pattern (at the  $-10$  dB level) for  $W_m$  alternates positions of peaks and valleys compared to the standing wave pattern (at the  $-6$  dB level) for  $W_e$ . The peaks of  $W_m$  and  $W_e$  are such that the total stored energy  $W$  shown in Figure 5.31 has long streaming patterns (at the  $-10$  dB level) that appear to correspond to the regions where the Poynting vector is strongly carrying energy into the focal zone.

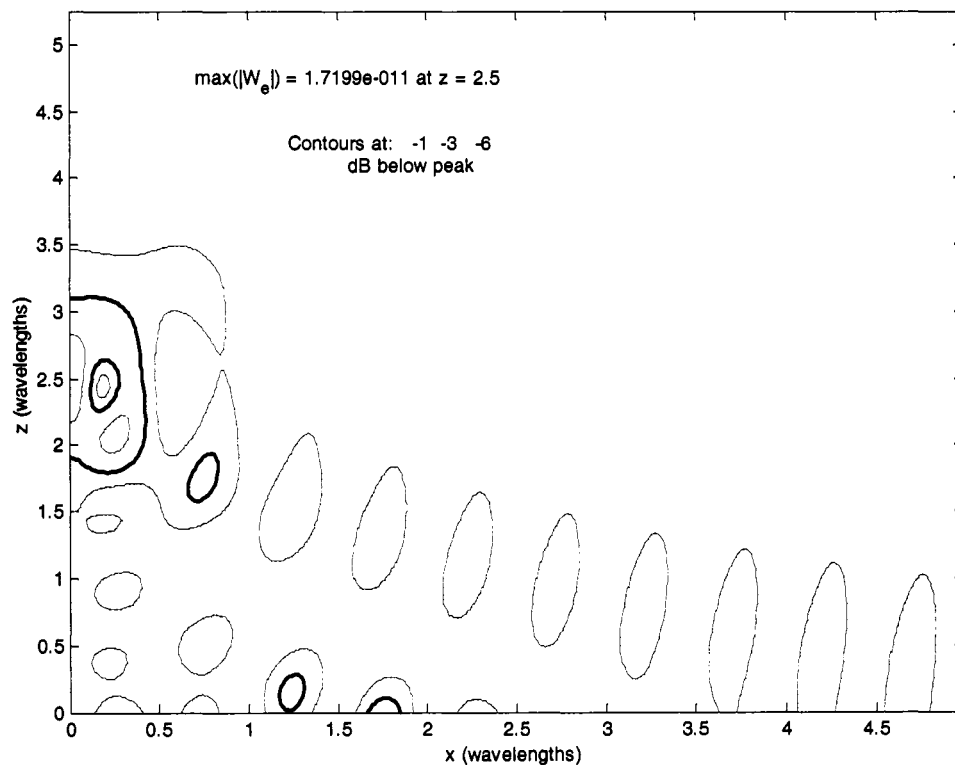


**Figure 5.30** Contour plot of stored electric energy density for  $d_2 = 5$ ,  $\epsilon_{2r} = -1.0005 - 10^{-3} j$ , and  $\mu_{2r} = -0.9995 - 10^{-7} j$ . Only the contour at  $-3$  dB is shown in heavy line width. There is a small valley inside the principal  $-3$  dB curve that extends from about  $z = 1.9$  to  $z = 3.1$  and there are three peaks above the  $-3$  dB level exterior to the principal contour.

The calculations and graphics shown in Figures 5.26 through 5.31 represent a thick-layer case where the asymptotic approximation of (5.39) gives a close estimate of the Z-direction width of the peak of  $|E_x|$  (at the level of 6 dB below the peak). A contrasting thin-layer case with  $d_2 = 0.5 \lambda_0$  will be illustrated in the next three figures. The characteristic feature of the thin case is what may be called ridge focusing. That is, there is no relative peak in the Z direction along the Z axis. Along this axis there is a sharply focused ridge out to the theoretical focal point and somewhat beyond with a

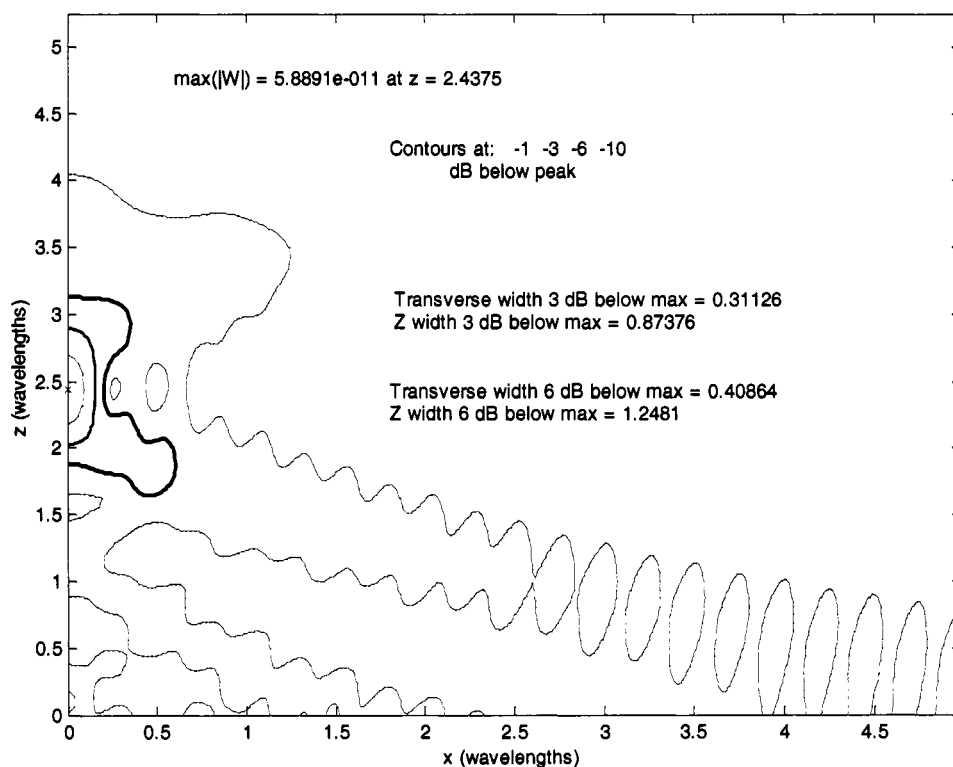


**Figure 5.31** Contour plot of total stored electromagnetic energy density for  $d_2 = 5$ ,  $\epsilon_{2r} = -1.0005 - 10^{-3} j$ , and  $\mu_{2r} = -0.9995 - 10^{-7} j$ . The contours at  $-3$  dB and  $-6$  dB relative to the peak are shown in heavy line widths. The peak location is indicated with an x. Note that the transverse widths are smaller than those of  $W_m$  given in Figure 5.29, but the propagation-direction widths are larger.

monotonic decline in intensity with increasing  $z$ . This ridge feature applies to both  $|E_x|$ , as noted previously in Sections 5.3 and 5.5, and to  $\text{Re}\{\bar{S}\}$ . Further, the relative steepness of the ridge in the theoretical focal plane is steeper for  $|E_x|$  than for  $\text{Re}\{\bar{S}\}$ , which is a reversal compared to the thick-layer case. The contours shown in Figure 5.32 and Figure 5.33 are not scaled relative to the value at the theoretical focal point, but rather to the maximum of  $\text{Re}\{\bar{S}\}$  or  $|E_x|$ . In both cases this maximum is at the origin (the sub-image point in the exit plane of the NIM). Therefore, the contours that are at  $-3$  dB and  $-6$  dB relative to this maximum do not give a direct measure of the width of the peak in the focal plane.

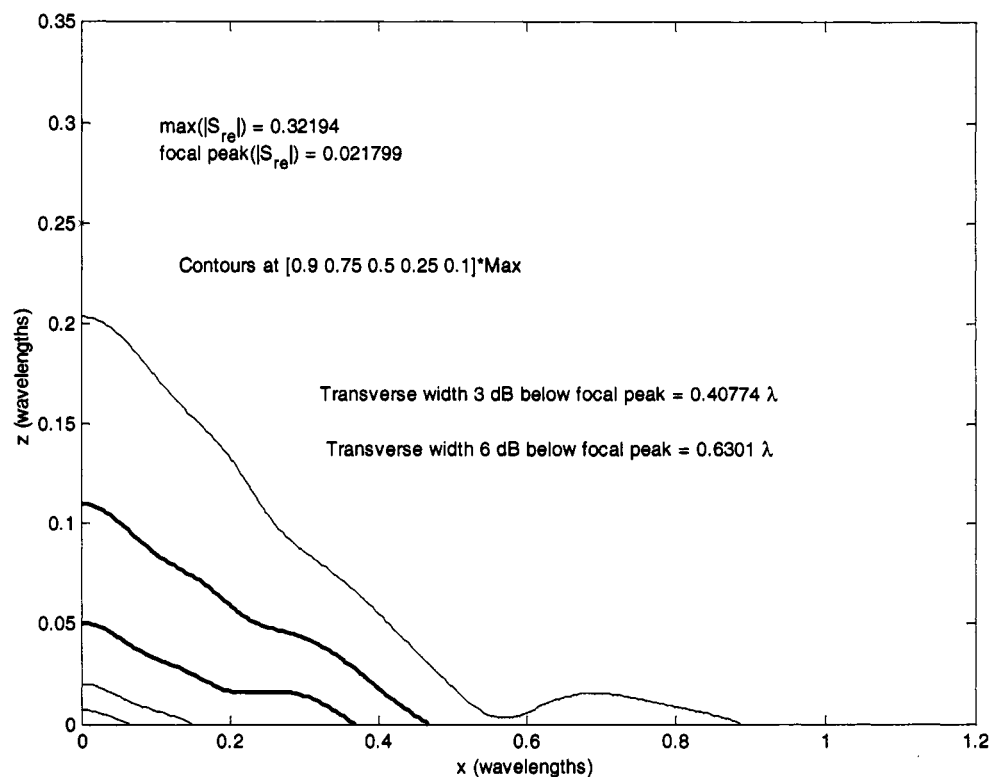


**Figure 5.32** Contour plot of real part of the Poynting vector, for thin slab case with  $d_2 = 0.5 \lambda_0$ ,  $\epsilon_{2r} = -1.0005 - 10^{-3} j$  and  $\mu_{2r} = -0.9995 - 10^{-7} j$ .

The width values have been calculated from our standard complete set of values of  $\text{Re}\{\bar{S}\}$  and  $|E_x|$  calculated on a fine grid covering for this case the region out to  $x = 2\lambda_o$  and  $z = 1.05d_2$ , where (to reiterate)  $d_2 =$  the slab thickness and the source is at a distance  $d_1 = 0.5d_2$  to the left of the slab; thus, the theoretical image plane is at  $z = d_1$  to the right of the slab.

The (theoretical) focal plane for Figure 5.32 is at  $z = 0.25\lambda_o$ , as indicated by an x on the  $z$  axis. This plot reveals a rather broad ridge focus for  $\text{Re}\{\bar{S}\}$  compared to  $|E_x|$  as shown in Figure 5.33.

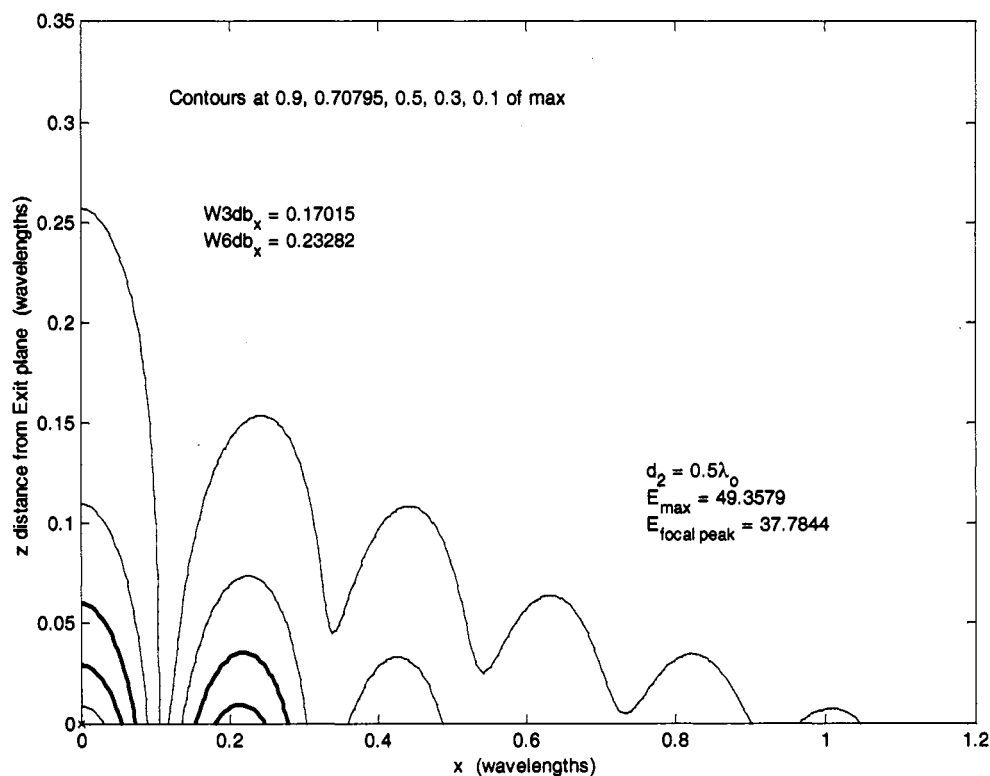


**Figure 5.33** Contour plot of  $|E_x|$ , for thin slab case with  $d_2 = 0.5\lambda_o$ ,  $\epsilon_{2r} = -1.0005 - 10^{-3}j$  and  $\mu_{2r} = -0.9995 - 10^{-7}j$ .

For this thin case the widths of the  $|E_x|$  peak in the  $x$  direction, measured in the

theoretical focal plane, are significantly smaller than (about 40% of) the values for  $\text{Re}\{|\bar{S}|\}$ . The  $|E_x|$  focus is quite a bit tighter than the limit for a large positive-index lens, which would correspond to the asymptotic results (5.30) and (5.31) with  $k_p = k_o$ , which give a 3-dB width of  $0.442 \lambda$  and a 6-dB width of  $0.603 \lambda$ .

The Poynting vector flow for this thin slab case is also quite different from the thick case. Figure 5.34 is a quiver plot of this vector flow. It shows a large amplitude Poynting vector coming out of the sub-image point in the exit plane and a strong drop in amplitude with increasing  $x$  in any fixed  $z$  plane between the exit and the

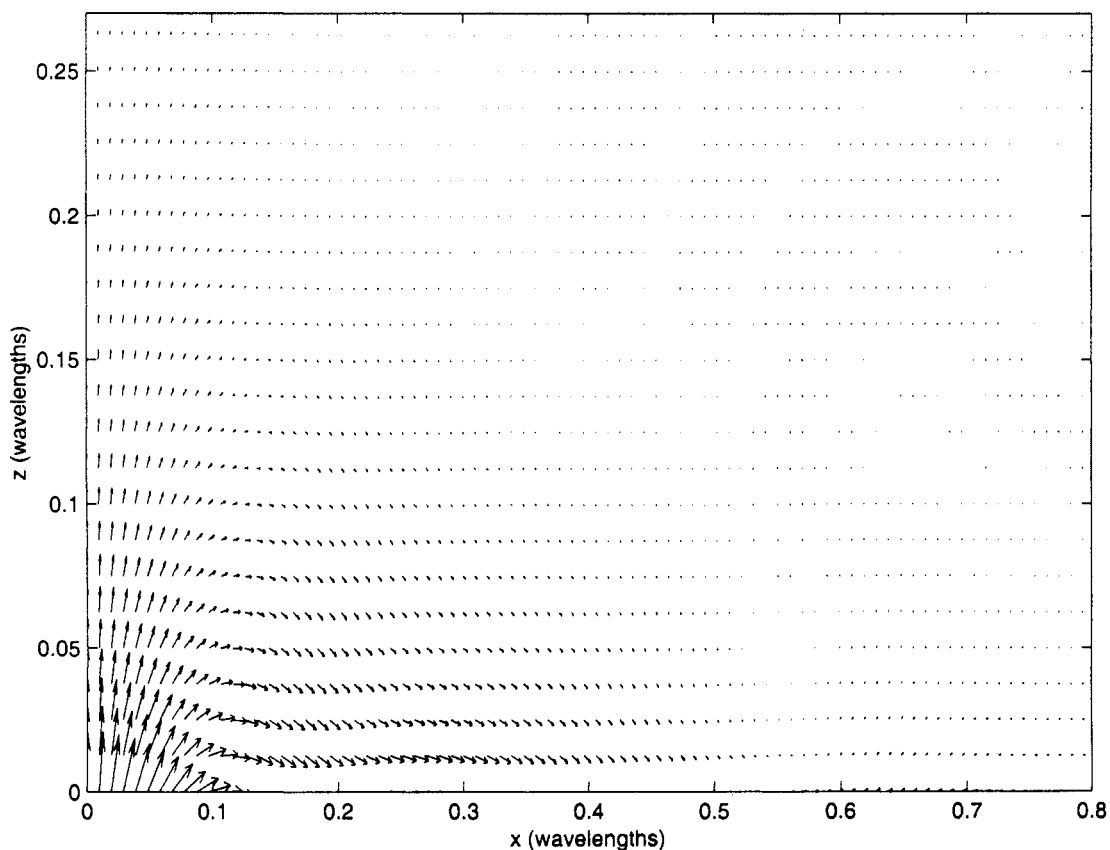


**Figure 5.34** Quiver plot of real part of Poynting vector for thin slab case with  $d_2 = 0.5 \lambda_o$ ,  $\epsilon_{2r} = -1.0005 - 10^{-3} j$  and  $\mu_{2r} = -0.9995 - 10^{-7} j$ .

theoretical focus at  $z = 0.25 \lambda_0$ .

The x-dependent behavior is seen much more easily in plots of  $\text{Re}\{|\vec{S}|\}$  versus x because the quiver plot rapidly loses sensitivity to show variations in  $\text{Re}\{\vec{S}\}$  wherever the magnitude is less than about 0.2 of the peak. However, we wanted to show this flow pattern and to note that there are regions along the exit plane where the flow of real energy appears to go back into the NIM and then reemerge at larger x values. We have noticed this feature in all of our thin slab cases.

Contour plots of stored energy, electric, magnetic and total, for the thin-slab case of Figure 5.32 through Figure 5.34 are shown in Figure 5.35 through Figure 5.37.

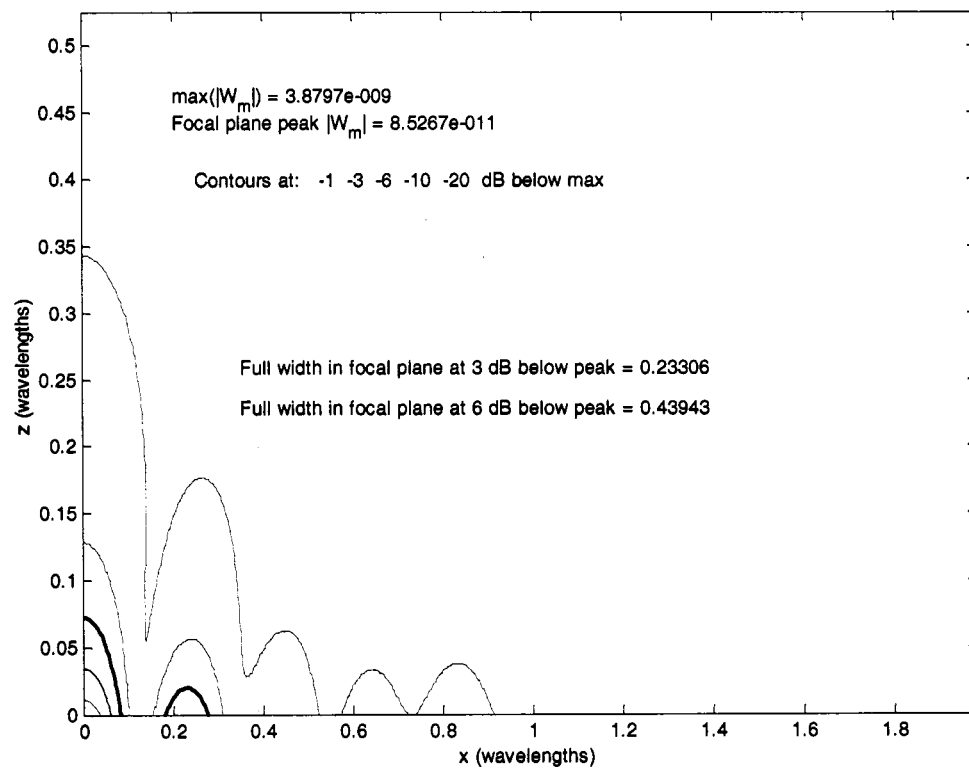


**Figure 5.35** Contour plot of stored magnetic energy density for case  $d_2 = 0.5 \lambda_0$ ,  $\epsilon_{2r} = -1.0005 - 10^{-3} j$ ,  $\mu_{2r} = -0.9995 - 10^{-7} j$ . The heavy contour is at 6 dB below the maximum.

These plots all show a broad ridge behavior with a narrow width in the theoretical focal plane. The electric energy density, Figure 5.36, and the total energy density, Figure 5.37, have maximum values on the exit plane away from the sub-image point at  $z = 0$ .

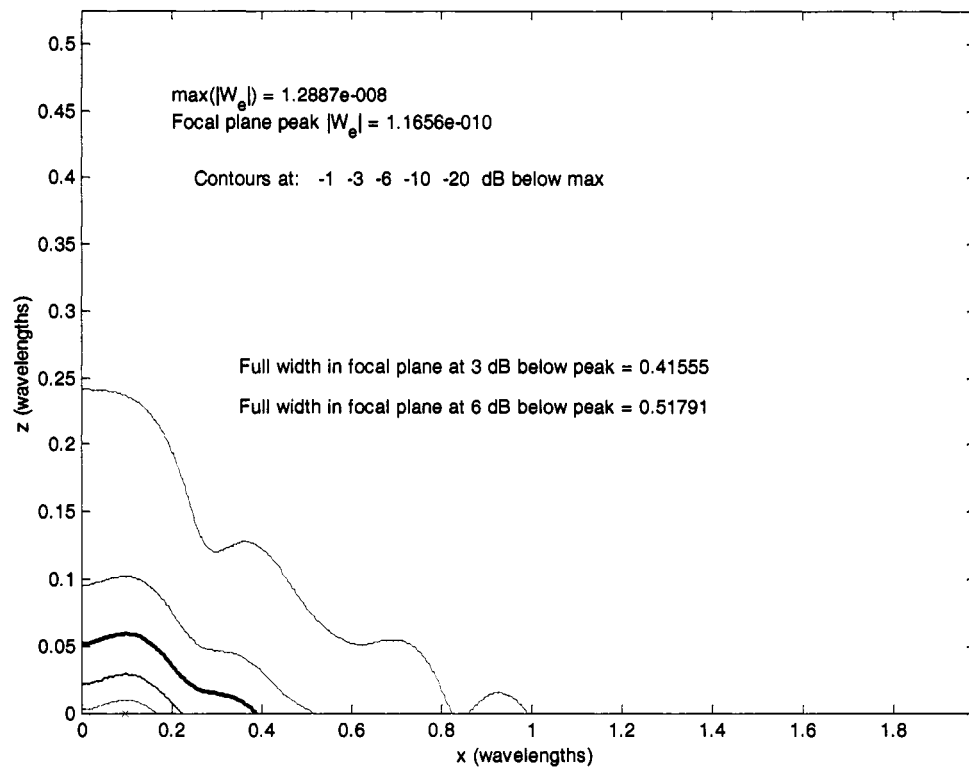


**Figure 5.36** Contour plot of stored electric energy density for case  $d_2 = 0.5 \lambda_o$ ,  $\epsilon_{2r} = -1.0005 - 10^{-3} j$ ,  $\mu_{2r} = -0.9995 - 10^{-7} j$ . The heavy contour is at 6 dB below the maximum. The maximum point, denoted by an x, occurs at  $x = 0.0967 \lambda_o$ .

For all three stored energies, the magnitudes at the theoretical focal point are roughly 15 to 20 dB down from the maximum in the exit plane. By comparison with values in Table 5.2 (see following), the transverse widths of these energy densities in

the focal plane is intermediate between the width of  $|E_x|$  (narrowest) and that of the magnitude of the Poynting vector (broadest).

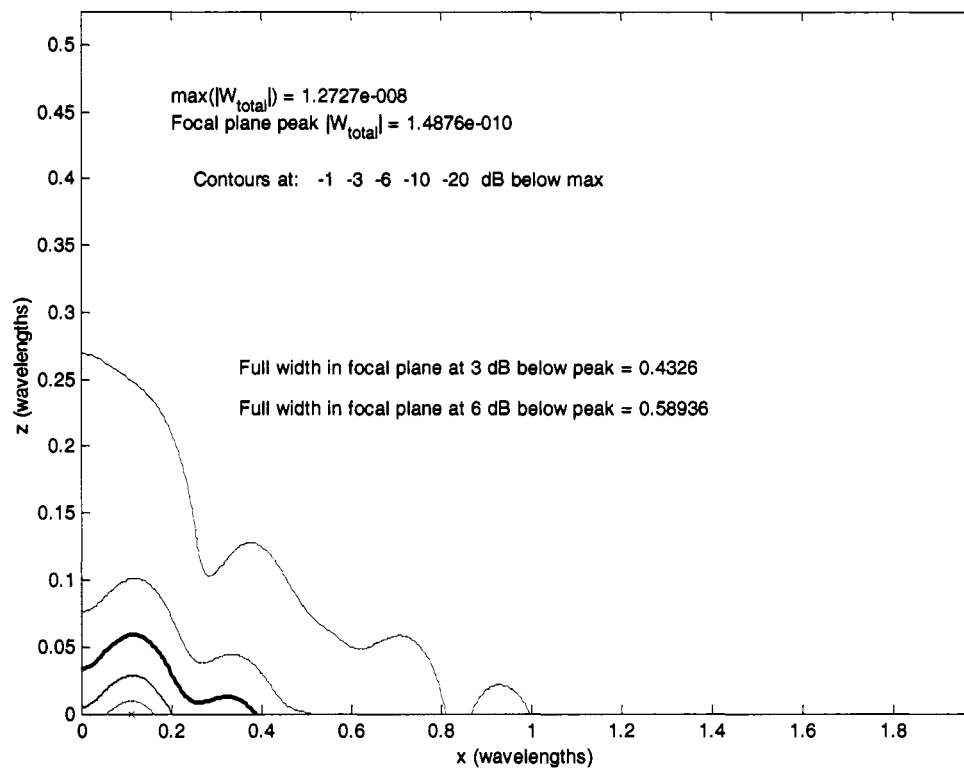


**Figure 5.37** Contour plot of total stored electromagnetic energy density for case  $d_2 = 0.5 \lambda_o$ ,  $\epsilon_{2r} = -1.0005 - 10^{-3} j$ ,  $\mu_{2r} = -0.9995 - 10^{-7} j$ . The heavy contour is at 6 dB below the maximum. The maximum point, denoted by an x, occurs at  $x = 0.1112 \lambda_o$ .

Several interesting variations on these patterns can be seen in the 10 other cases that have been run through the complete calculation of all components and a large set of plots to show the behavior clearly in all dimensions. One particular difference is in the gyres, clockwise or counterclockwise, tight or broad, found in the quiver plots.

We summarize the focal width behavior for 12 cases in Table 5.2 and Table 5.3. Thickness is given in wavelength units as are the width entries. The column headings in the second row (third through eighth columns) designate the quantity for which the width is calculated; namely, the asymptotic approximation of  $|E_x|$ , the full numerical integration calculation of  $|E_x|$ , and the calculation of  $\text{Re}\{\bar{S}\}$  from the full numerical integration calculation of all three field components.

In Table 5.2 the asymptotic widths are calculated from formulas (5.30), (5.31), and (5.17). This table shows that these formulas provide excellent estimates of the transverse widths of peaks of  $|E_x|$ . The transverse widths of the peaks of  $\text{Re}\{\bar{S}\}$  are less regular in their dependence on  $\delta_e$ . Note that  $\delta_m$  and  $\delta_n$  are completely determined by the conditions that  $\text{Re}(n_2) = -1$  and  $\text{Im}(\mu_{2r}) = -10^{-7}$ . However, the peak widths of  $\text{Re}\{\bar{S}\}$  may depend functionally on all these quantities and the layer thickness.

In Table 5.3 the asymptotic widths are for the thick case only. They are the “universal” widths of  $|E_x|$  on axis in the Z (propagation direction) given by the function shown in Figure 5.18. The 6-dB half width was given specifically in (5.39). They are in fact the limits possible without evanescent wave restoration. Note that there are no entries for the thin case because the ridge focusing does not show a decrease in  $|E_x|$  or  $\text{Re}\{\bar{S}\}$  inwards of the theoretical focal plane along the Z axis.

The DNE entry for the intermediate thickness  $d_2 = 2.5$  and  $\epsilon_{2r} = -0.995 - 10^{-3}j$  at 6 dB below the peak stands for Does Not Exist. That is, the minimum of  $|E_x|$  between the exit plane and the theoretical focal point on the Z axis is noticeably more than half of the peak value.

**Table 5.2** Transverse Widths of the Focal Peak in Wavelengths

Thickness	$\epsilon_{2r}$	At 3 dB below peak			At 6 dB below peak		
		Asy $ E_x $	$ E_x $	Real $ S $	Asy $ E_x $	$ E_x $	Real $ S $
$d_2 = 5$	$-1.005 \cdot 10^{-3}j$	0.4345	0.4406	0.3928	0.5927	0.6012	0.5312
	$-0.995 \cdot 10^{-3}j$	0.4345	0.4408	0.3915	0.5927	0.6015	0.5293
	$-1.0005 \cdot 10^{-3}j$	0.4302	0.4408	0.3920	0.5869	0.6011	0.5301
	$-0.9995 \cdot 10^{-3}j$	0.4302	0.4405	0.3919	0.5869	0.6011	0.5299
$d_2 = 2.5$	$-1.005 \cdot 10^{-3}j$	0.4134	0.4149	0.3707	0.5640	0.5665	0.5015
	$-0.995 \cdot 10^{-3}j$	0.4134	0.4181	0.3706	0.5640	0.5707	0.4992
	$-1.0005 \cdot 10^{-3}j$	0.3992	0.4107	0.3667	0.5446	0.5607	0.4943
	$-0.9995 \cdot 10^{-3}j$	0.3992	0.4111	0.3663	0.5446	0.5614	0.4938
$d_2 = 0.5$	$-1.005 \cdot 10^{-3}j$	0.2059	0.2072	0.5449	0.2809	0.2858	0.9704
	$-0.995 \cdot 10^{-3}j$	0.2059	0.2073	0.3891	0.2809	0.2860	0.6150
	$-1.0005 \cdot 10^{-3}j$	0.1711	0.1702	0.4077	0.2334	0.2328	0.6301
	$-0.9995 \cdot 10^{-3}j$	0.1711	0.1702	0.3856	0.2334	0.2328	0.5739

**Table 5.3** Widths in the Propagation Direction

Thickness	$\epsilon_{2r}$	At 3 dB below peak			At 6 dB below peak		
		Asy $ E_x $	$ E_x $	Real $ S $	Asy $ E_x $	$ E_x $	Real $ S $
$d_2 = 5$	$-1.005 \cdot 10^{-3}j$	1.219	1.190	0.9093	1.9142	1.975	1.3003
	$-0.995 \cdot 10^{-3}j$	1.219	1.193	0.9012	1.9142	1.982	1.289
	$-1.0005 \cdot 10^{-3}j$	1.219	1.190	0.9094	1.9142	1.975	1.300
	$-0.9995 \cdot 10^{-3}j$	1.219	1.190	0.9076	1.9142	1.977	1.298
$d_2 = 2.5$	$-1.005 \cdot 10^{-3}j$		0.9914	0.8564		1.526	1.237
	$-0.995 \cdot 10^{-3}j$		0.9388	0.7767		DNE	1.124
	$-1.0005 \cdot 10^{-3}j$		0.9315	0.8033		1.445	1.164
	$-0.9995 \cdot 10^{-3}j$		0.9216	0.7896		1.438	1.145

### 5.8. Comparison to an alternate approach

Recently Grbic and Eleftheriades published an investigation of the focal limitations of negative-refractive-index transmission-line lenses. They treated a similar 2-dimensional source with their discrete-type of approximation to a negative-index medium, and they constructed a square grid of inductors and capacitors to model their network. Thus, they established the following parameters for the source and transmitted field regions:

$$\mu_p = 2.539 - 0.006j \quad \varepsilon_p = 1.458 - 0.003j. \quad (5.43)$$

Then with a conjugate structure in the simulated NIM region, they obtained

$$\mu_n = -2.539 - 0.038j \quad \varepsilon_n = -1.456 - 0.071j. \quad (5.44)$$

Our Fourier transform methods can be applied to continuous media having these permittivities and permeabilities with appropriate care in the choice of the  $k_x$  grid for the numerical integration. The negative-index focusing property can be derived for any real index of refraction in a similar fashion to our derivation in Chapter 3 of the types of waves possible at a planar boundary (Ishimaru, Thomas *et al* 2005). That work shows the waves depend only on the ratio of the indexes of refraction of the two media.

Hence, we calculated the transmitted  $E_x$  due to our standard line source in the positive medium (5.43) through a slab of NIM (5.44). The other parameters of the calculation per (Grbic & Eleftheriades 2005) are:

Frequency  $f = 1$  GHz

Slab thickness  $d_2 = 5$  cell units =  $4.2 \cdot 10^{-2}$  m

Source distance  $d_1$  from incident side = theoretical image distance from exit side

$$d_1 = 0.5d_2.$$

Derived parameters are then

Index of refraction of the PIM (source region and transmitted region)

$$n_1 = 1.92402 - 0.004253j$$

Index of refraction of the slab  $n_2 = -1.92298 - 0.06126j$

Wavelength in the PIM  $\lambda_1 = \text{Re}(2\pi / k_1) = 0.155815 \text{ m}$ .

Thus, the thickness of the NIM slab is  $0.26955 \lambda_1$ , which is definitely a thin slab, and so we expect ridge focusing. Figure 5.38 and Figure 5.39 show results in the focal plane.

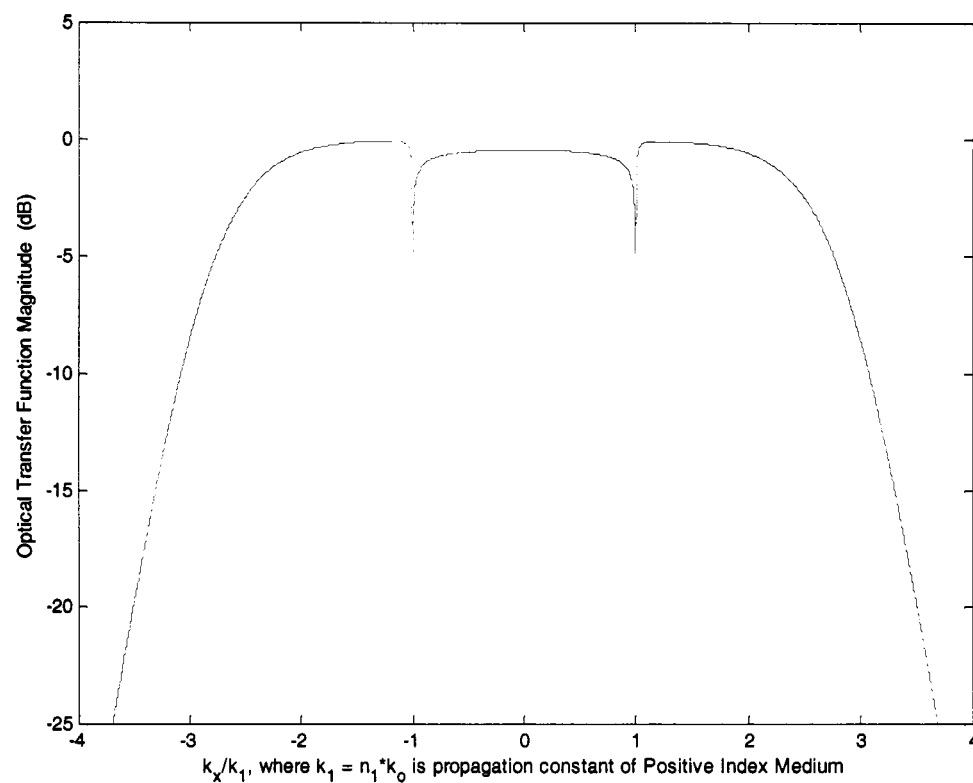


**Figure 5.38** Magnitude of Fourier transform of focused field in the theoretical focal plane. The focal plane is at a distance  $0.5d_2 = 0.13478 \lambda_1$  from the exit plane of the slab. Constitutive parameters for the case of (Grbic & Eleftheriades 2005).

Figure 5.38 gives the magnitude of the Fourier transform of  $E_x$  in dB. With a point source this quantity is conventionally called the Optical Transfer Function. Figure 5.38 is to be compared with Theoretical OTF A of Figure 4 of (Grbic & Eleftheriades 2005) because they derived OTF A for an unbounded slab, whereas their OTF B was derived to estimate the effect of the finite grid that they had in their experiment. Their OTF A agrees well with Figure 5.38 because, as they note, their OTF A drops to  $-6$  dB at approximately  $k_x / k_1 = 3$ .

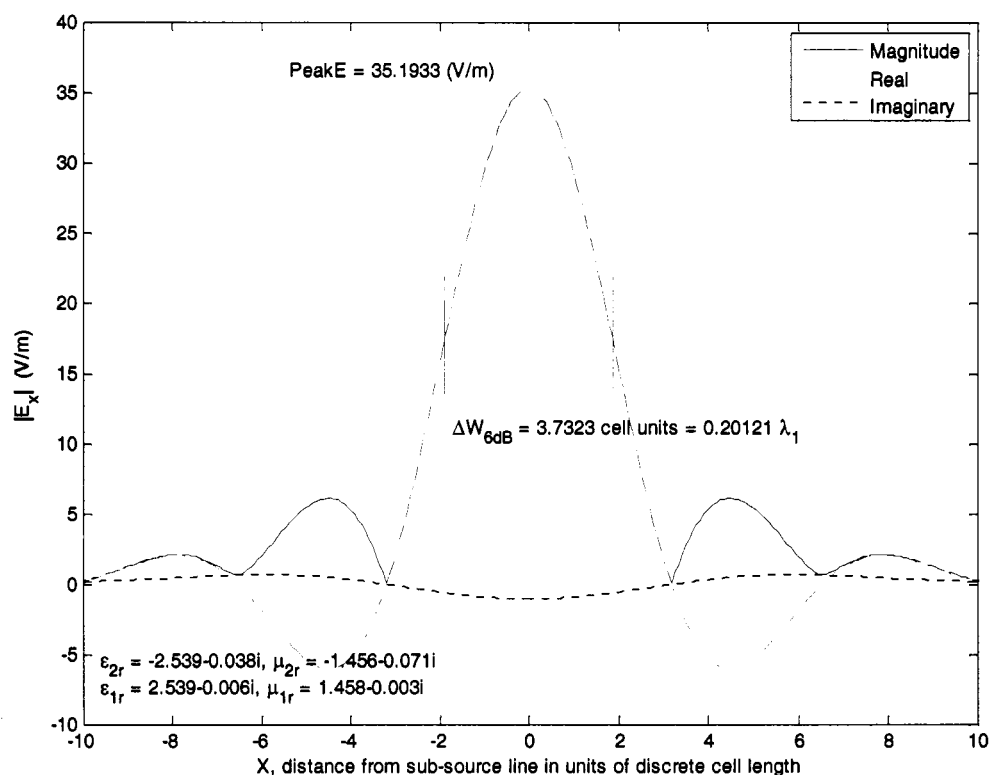


**Figure 5.39** The focused field component in the focal plane at  $z_{fromExit} = 0.5d_2 = 0.13478 \lambda_1$ . This result is the inverse transform of the optical transfer function, the magnitude of which is shown in Figure 5.38. The field values correspond to our delta-function magnetic current line source of  $-2$  V.

Figure 5.39 is to be compared with Figure 5 of (Grbic & Eleftheriades 2005). However, their experimental source had a finite width (width at half peak estimated to be about 1.5 cell units =  $0.08 \lambda_1$ ). Hence, their focal plane curves (experimental and theoretical) are somewhat wider (roughly 40% to 50%) than ours in Figure 5.39. Also, our focused peak should be tighter because of the finite size of their slab and because the continuous-medium approach would be expected to give a result slightly closer to the NIM limit.

Finally, in Figure 5.40 we illustrate the field variation over the transmitted region from the exit plane out to about 1.5 times the slab thickness, or 3 times the focal distance.

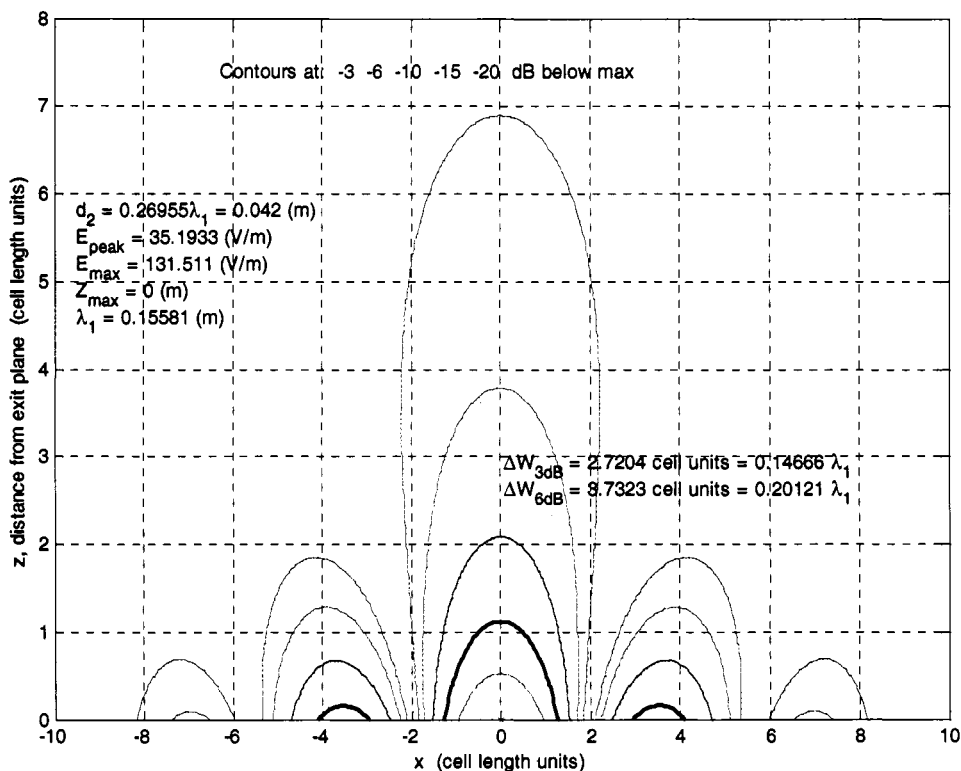


**Figure 5.40** Contour plot of  $|E_x|$  for case  $\mu_{2r} = -2.539 - 0.038j$ ,  $\varepsilon_{2r} = -1.456 - 0.071j$  and  $\mu_{1r} = 2.539 - 0.006j$ ,  $\varepsilon_{1r} = 1.458 - 0.003j$ . Heavy contour is at  $-6$  dB. Max is at exit point (origin) and peak refers to peak field in the focal plane at  $z = 2.5$  cell units.

Note that there are two different references for the dB units in Figure 5.40. The contour levels are calculated with reference to the maximum of  $|E_x|$  throughout the transmitted region, which is noted on the plot as  $E_{\max}$ . However, the 3-dB and 6-dB widths for the focal plane are relative to the peak in the focal plane, given as  $E_{\text{peak}}$  in this figure. Figure 5.40 illustrates quite clearly the ridge nature of the focusing where the steepness of the ridge in the neighborhood of its crest on the  $Z$  axis stays about the same for  $0 < z < 0.5d_2$ .

### 5.9. *Summary and conclusions regarding focusing by a NIM slab*

Our asymptotic approximations and supporting exact calculations show that the transverse focal width of a uniform material with  $n_2$  very close to  $-1$  and with  $\epsilon_{2r}$  and  $\mu_{2r}$  fairly close to  $-1$  is somewhat smaller than the limit provided by a large positive index lens, which can focus all the non-evanescent rays. This conventional lens limit may be specified by the focal widths at 3 dB and 6 dB below the peak for the delta-function source field. These widths are  $0.442 \lambda_o$  (5.31) and  $0.603 \lambda_o$  (5.30) respectively. The improved focusing results from amplification and focusing of evanescent rays out to a wave number  $k_p$  beyond  $k_o$  given approximately by (5.17). The transverse focusing improves only logarithmically with the smallness of the deviations of the relative constitutive parameters from  $-1$  but inversely with the thickness  $d_2$  of the slab. So for substantially reduced focal widths, thin slabs are necessary.

However, we show that thin slabs provide what we call ridge focusing. That is, there is no peak in the propagation direction (the  $Z$  direction). To obtain a peak in the  $Z$  direction the slab thickness must be greater than about 2 wavelengths because in all cases where there is a focal peak relative to the  $Z$  direction, the focal width in this direction is approximately  $2 \lambda_o$  at half maximum.

Many numerical computation of the exact Fourier transform solutions show that the approximate widths and the computed widths of  $\text{abs}(E_x)$  are quite close. Therefore, equation (5.35) and Figure 5.8 provide useful estimates of the transverse width of  $|E_x|$  for any case.

In the thick slab cases we investigated numerically, we found that the Poynting vector magnitude focuses more tightly than the magnitude of  $E_x$ , the component which is a delta function in our line source. But the opposite result that the Poynting vector focusing is broader than the focusing of  $\text{abs}(E_x)$  holds for thin slabs. The fields out to the theoretical focal plane of an  $n_2 = -1$  slab and beyond are near fields relative to the source for slabs of thickness  $5\lambda_0$  and even more. Hence, the Poynting vector behavior differs significantly from the square of  $|E_x|$ .

The half-peak-level contour moves away from the exit plane if  $n_2$  increases from  $-1$  to  $-0.98$  and moves closer to the exit plane if  $n_2$  decreases from  $-1$  to  $-1.02$ . With the source set at a fixed distance in front of the slab, the distance to the peak of the transmitted image contours (what we have called the focal distance) moves in and out with  $\text{Re}(n_2)$  generally as the contours do. The inflections and small peaks in these computed curves are attributed to the complexities of the changing contour patterns with development of many sidelobes or subpeaks.

We have presented cases with minimum deviations of  $\epsilon_{2r}$  or  $\mu_{2r}$  from  $-1$  of about  $10^{-3}j$  to  $10^{-4}j$ . Figure 5.8 and (5.35) show that the transverse focal width could be reduced significantly from  $0.6\lambda_0$  only by use of a thin slab or by making the logarithm of the deviations noticeably smaller; e.g., to reduce the deviation to  $\approx 10^{-15}j$ . Such a low loss seems improbable with metallic lattice structures. Furthermore, since source plus image distance (from their respective sides of the slab) equals the slab thickness, a thin slab implies that the source and image are very close.

### 5.10. Notes to Chapter 5

- Chew WC. 2004. Sommerfeld integrals for left-handed materials. *Microwave and Optical Technology Letters* 42: 369-73
- Grbic A, Eleftheriades GV. 2005. Practical limitations of subwavelength resolution using negative-refractive-index transmission-line lenses. *IEEE Transactions on Antennas and Propagation* 53: 3201-9
- Ishimaru A, Thomas JR, Jaruwatanadilok S. 2005. Electromagnetic waves over half-space metamaterials of arbitrary permittivity and permeability. *IEEE Transactions on Antennas and Propagation* 53: 915-21
- Lu J, Grzegorzczak TM, Wu B-l, Pacheco J, Chen M, Kong JA. 2005. Effect of poles on subwavelength focusing by an LHM slab. *Microwave and Optical Technology Letters* 45 49-53
- Melville DOS, Blaikie RJ. 2005. Super-resolution imaging through a planar silver layer. *Optics Express* 13: 2127-34
- Pendry JB. 2000. Negative refraction makes a perfect lens. *Physical Review Letters* 85: 3966-9
- Podolskiy VA, Narimanov EE. 2005. Near-sighted superlens. *Optics Letters* 30: 75-7
- Smith DR, Schurig D, Rosenbluth M, Schultz S, Ramakrishna SA, Pendry JB. 2003. Limitations on subdiffraction imaging with a negative refractive index slab. *Applied Physics Letters* 82: 1506-8
- Thomas JR, Ishimaru A. 2002. *Transmission properties of material with relative permittivity and permeability close to -1*. Presented at Complex Mediums III: Beyond Linear Isotropic Dielectrics, Seattle, WA, United States
- Yannopapas V, Moroz A. 2005. Negative refractive index metamaterials from inherently non-magnetic materials for deep infrared to terahertz frequency ranges. *Journal of Physics-Condensed Matter* 17: 3717-34
- Ziolkowski RW, Heyman E. 2001. Wave propagation in media having negative permittivity and permeability. *Physical Review E* 64: 056625-1--15

## 6. Lattice Sum Approach Combined with MoM to calculate scattering from a periodic layer of cylinders

This investigation was done prior to all the study for the previous chapters. It provides an interesting method for treating a very special class of 2-D problems, but it did not lead us to a method for calculating the layer properties of a periodic structure that could form a negative index media (NIM) structure.

### 6.1 *Review of Yasumoto and Kushta's Approach*

(Yasumoto & Kushta 2000) derived a T-matrix-based method for calculating the scattering by a periodic array (a single layer) of cylinders. This method provides a separation of the problem of scattering from the array into two parts. One is the scattering from an individual cylinder of the array. This solution must be expressed in transition matrix (T-matrix) form to be used with the second part. The second part is the lattice sum function of the array. The lattice sum function was originally derived by Rayleigh, but it was not considered very useful because, in the brute force approach, this sum is very slowly convergent. However, in a companion paper, (Yasumoto & Yoshitomi 1999) found an efficient method to calculate these sums as evaluations of a reasonably convergent contour integral.

One reason that the approach has not led to a 3-D generalization is that it is based on a scalar wave function, so it is limited to problems that can be described by a TE or TM solution, with one field component that determines all the others. The T-matrix approach is based on cylindrical harmonic (2-D) or spherical harmonic (3-D) representations of the waves. For the 2-D case, if the incident wave is given by

$$\Psi_{inc} = \sum_{n=-\infty}^{\infty} a_n^i J_n(kr) e^{-jn\phi} \quad (6.1)$$

then the vector  $a^i = [a_n^i]$  fully describes the incident wave. For example, a plane wave is given by  $a_n^i = \exp(jn(\phi_o - \pi/2))/(\omega\mu k)$ . A general scattered (outgoing) wave is given in cylindrical harmonics by

$$\Psi_s = \sum_{n=-\infty}^{\infty} b_n H_n^{(2)}(kr) e^{-jn\phi} \quad (6.2)$$

where the vector  $b = [b_n]$  fully describes the scattered wave. The  $T$  matrix is then defined as the matrix which produces the scattered wave from the incident wave; that is  $b = Ta^i$ . (Yasumoto & Kushta 2000) established the following theorem for a periodic layer of cylindrical scatterers, with a TE or TM wave so that a scalar wave function can describe the problem,

$$b = (I - T \cdot L)^{-1} Ta^i \quad (6.3)$$

where  $L$  is the lattice sum function. The lattice sum function (matrix) is defined by the following relations:

$$L_{mn} = S_{m-n}(kh, \phi^i)$$

$$S_n(kh, \phi^i) = \sum_{\ell=1}^{\infty} e^{j\ell kh \cos \phi^i} H_n^{(2)}(\ell kh) + (-1)^n \sum_{\ell=1}^{\infty} e^{-j\ell kh \cos \phi^i} H_n^{(2)}(\ell kh)$$

Thus,  $L_{mn}$  depends only on the lattice spacing  $h$ , or the non-dimensional version of it which is  $kh = 2\pi h / \lambda$ , and the angle of incidence  $\phi^i$  relative to the plane of the lattice.

This appears to be a very general formula and it seemed reasonable to hope to find a 3-D version of this theorem. The proof involves Floquet's theorem and Graf's Addition Theorem for Bessel or Hankel functions. The extra complications of spherical harmonics with another angular variable seem to lead to a problem that does not translate to a similar approach.

In principle, an individual cylinder could be several cylindrical structures lined up within the cell of the lattice. This feature attracted us to pursue this general method to solve the problem of scattering (that is, both reflection and transmission) through a structure that could be of interest in metamaterial studies. The method is limited to 2-D structures. There was some hope of extension to a 3-D case, but we have not found that inspiration and Yasumoto, who has continued to work on this, also has not had success.

I successfully programmed calculations of the lattice sum function and thereby verified the calculations of (Yasumoto & Yoshitomi 1999). Yasumoto found this verification helpful. The calculations were based on numerical evaluation of contour integrals where the integrand has the form

$$I(t) = [G_n(t) + G_n(-t)] F(t, kh, \pm \cos \phi) \quad \text{where} \quad G_n(t) = \left(1 - \sqrt{j+t^2}\right)^n e^{jn\pi/4}$$

$$\text{and} \quad F = \frac{je^{-khF_1}}{F_1 \left(1 - e^{-khF_1} e^{jkh \cos \phi}\right)} \quad \text{with} \quad F_1 = e^{j\pi/4} \sqrt{j+t^2}$$

The convergence on the variable of integration  $t$  is assured by the appearance of  $F_1$  in the exponential (along with the 45-degree path). A complication is that  $G_n(-t)$  gets close to  $-G_n(t)$  when  $n$  gets large.

## 6.2 Calculation of $T$ matrix from MoM calculation of scattered field

Our first application of the method was to a layer of C-shaped dielectric cylinders with relative permittivity limited to a rather small range. The method of calculating the scattering from an individual cylinder was an MoM method based on

the volume integral equation for electric field in terms of polarization current. The method is detailed in Chapter 12 of (Ishimaru 1991). By comparison of MoM solutions for circular cylinders and pipes, we found that the MoM method lost accuracy when  $\epsilon_r$  became as large as 10. (Harrington 1993) makes the comment regarding this problem that pulse basis functions are not in the domain of the linear operator from which the Green's function for this problem is obtained. (Peterson & Mittra 1998) state that a fictitious surface charge density is introduced between each cell through the pulse basis functions. In turn, this produces fictitious discontinuities in the normal E field at each cell boundary.

The MoM method yields a solution for the scattered field as function of location  $(R, \phi_s)$  of observation point for the scattered wave. This calculation is carried out for some finite number  $N_s$  of angles of incidence. We formulated our calculations in terms of the magnetic Hertz potential specifically for the TE or p-polarization case. In this case a complete theoretical solution would have the form

$$E_{sc}(\phi_s; \phi_i) = j\omega\mu_o k_o \sum_{n=-N_p}^{N_p} b_n(\phi_i) H_n^{(2)'}(k_o R) e^{-jn\phi_s} \quad (6.4)$$

for a plane wave incident at angle  $\phi_i$ , and where the terms would be known for  $N_p$  as large as needed. In the numerical computation we obtain  $E_{sc}(R, \phi_s, \phi_i)$  for a fixed fairly large radial distance R and a plane wave incident at angle  $\phi_i$ . This numerical solution has results for the discrete set of scattering angles

$\{\phi_s \quad s = 1, 2, \dots, 2 \cdot N_p + 1\}$ . Let  $N_s = 2 \cdot N_p + 1$ . Then, we numerically compute solutions for  $N_s$  different values of  $\phi_i$ . Probably it is best to use equally spaced values of  $\phi_i$  covering the interval 0 to  $\pi$  measured from grazing from the left to grazing from the right. The values of  $\phi_s$  should span the range of 0 to  $2\pi$ . From these solutions we can find  $N_s$  Discrete Fourier Transforms (FFT method) such that

$$E_{sc}(\phi_s, \phi_i) = \sum_{n=-N_p}^{n=N_p} C_n^{(i)} e^{-jn\phi_s} \quad (6.5)$$

By comparison of equations (6.4) and (6.5)

$$b_n(\phi_i) = C_n^{(i)} / \left( j\omega\mu_o k_o H_n^{(2)'}(k_o R) \right).$$

Thus for any given  $\phi_i$  we can then write formally

$$\begin{bmatrix} b_{-N_p}(\phi_i) \\ \cdot \\ b_{-1}(\phi_i) \\ b_0(\phi_i) \\ b_1(\phi_i) \\ \cdot \\ b_{N_p}(\phi_i) \end{bmatrix} = \overline{\overline{T}} \begin{bmatrix} a_{-N_p}(\phi_i) \\ \cdot \\ a_{-1}(\phi_i) \\ a_0(\phi_i) \\ a_1(\phi_i) \\ \cdot \\ a_{N_p}(\phi_i) \end{bmatrix}$$

where the matrix  $\overline{\overline{T}}$  is unknown at this stage. Next we can write all the solutions for the  $N_s$  different values of  $\phi_i$  side by side in matrix form to obtain a matrix equation

$$\overline{\overline{B}} = \overline{\overline{T}} \cdot \overline{\overline{A}} \quad (6.6)$$

Then to this  $N_s \times N_s$  order,  $\overline{\overline{T}}$  is determined by linear algebra as

$$\overline{\overline{T}} = \overline{\overline{B}} \cdot \overline{\overline{A}}^{-1} \quad (6.7)$$

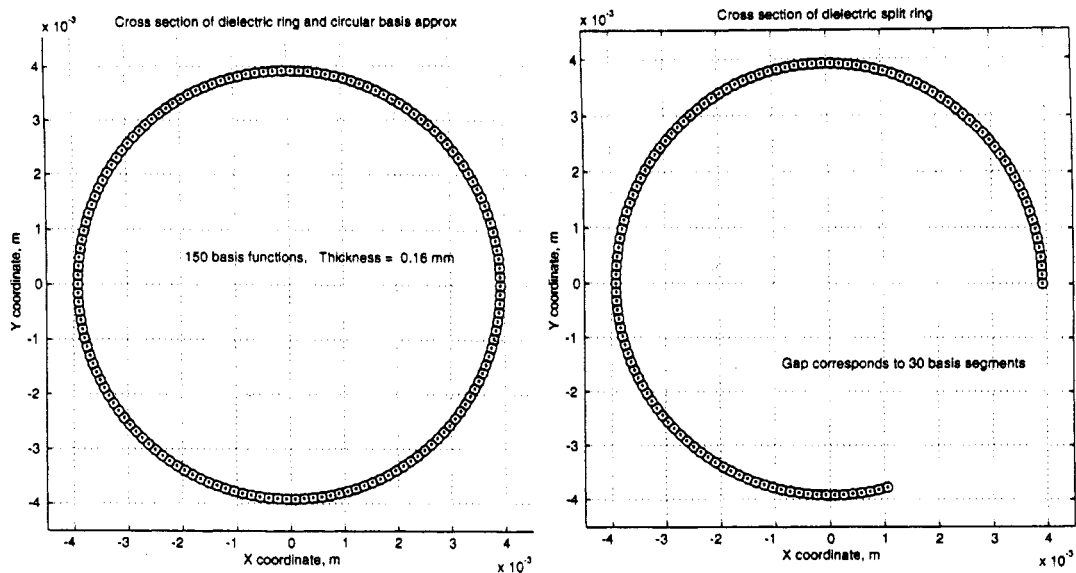
In this procedure we are picking out the central  $N_s \times N_s$  part of a matrix that is countably infinite ( $-\infty$  to  $+\infty$ ) in both row and column indices. The convergence of this procedure may need more investigation, particularly for highly non-isotropic cases.

### 6.3 *Calculations for a dielectric cylinder with $\epsilon_r$ not too large—some plotted results*

I calculated the scattering from a layer of dielectric cylinders of three types. The simplest type was a hollow circular cylinder; i.e., a pipe. The next was a C-shaped cylinder, which was constructed by removing a segment from the hollow pipe. I use a typical gap segment of 72 degrees, although I did explore some other gap sizes less than 90 degrees. The third cylindrical shape had a hollow square cross section with elements taken out of one edge, leaving a cross section similar to a Block C. Figure 6.1 shows MATLAB generated cross sections of these three types. The figure also shows the approximately square cross section volume basis elements used in the MoM computation. These elements are exactly square for the Block C.

The calculation of scattering for a pipe (a circular cylindrical ring) was also carried out exactly by the analytic theory as presented in (Ishimaru 1991), chapter 11. This object is symmetric in revolution about the axis and so the scattering only depends on the angle between the incident angle and the scattering angle. That is, its T matrix is diagonal. But this case provides a useful way to compare to evaluate the accuracy of the MoM method. Figure 6.2 shows an overlay of the analytic method and the MoM method for a case with  $\epsilon_r = 2.5 - j2.5$ . The imaginary part of the field agrees very closely, and this is the dominant part. The real part shows a moderate difference. The total amplitude is thus fairly close.

Scattering from the split ring C shape is summarized in Figures 6.3 through 6.6. Because the scattering depends on both the angle of incidence and angle of scattering, we show only the fractions of power reflected and transmitted for two permittivity values as a function of angle of incidence to the plane of the array. The angle is measured from 0 at grazing incidence. The angle is 0 when incidence is from the positive X direction.



## Cross Sections of 2-D objects in this Chapter

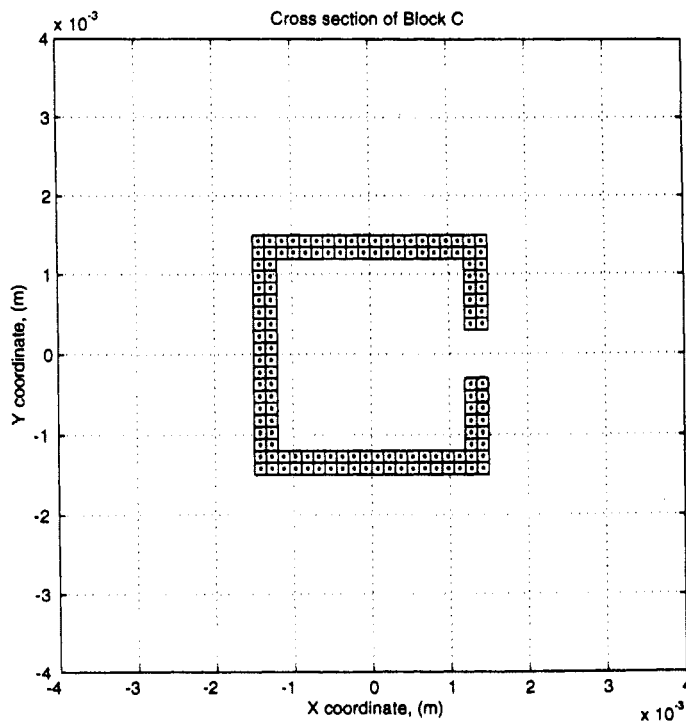
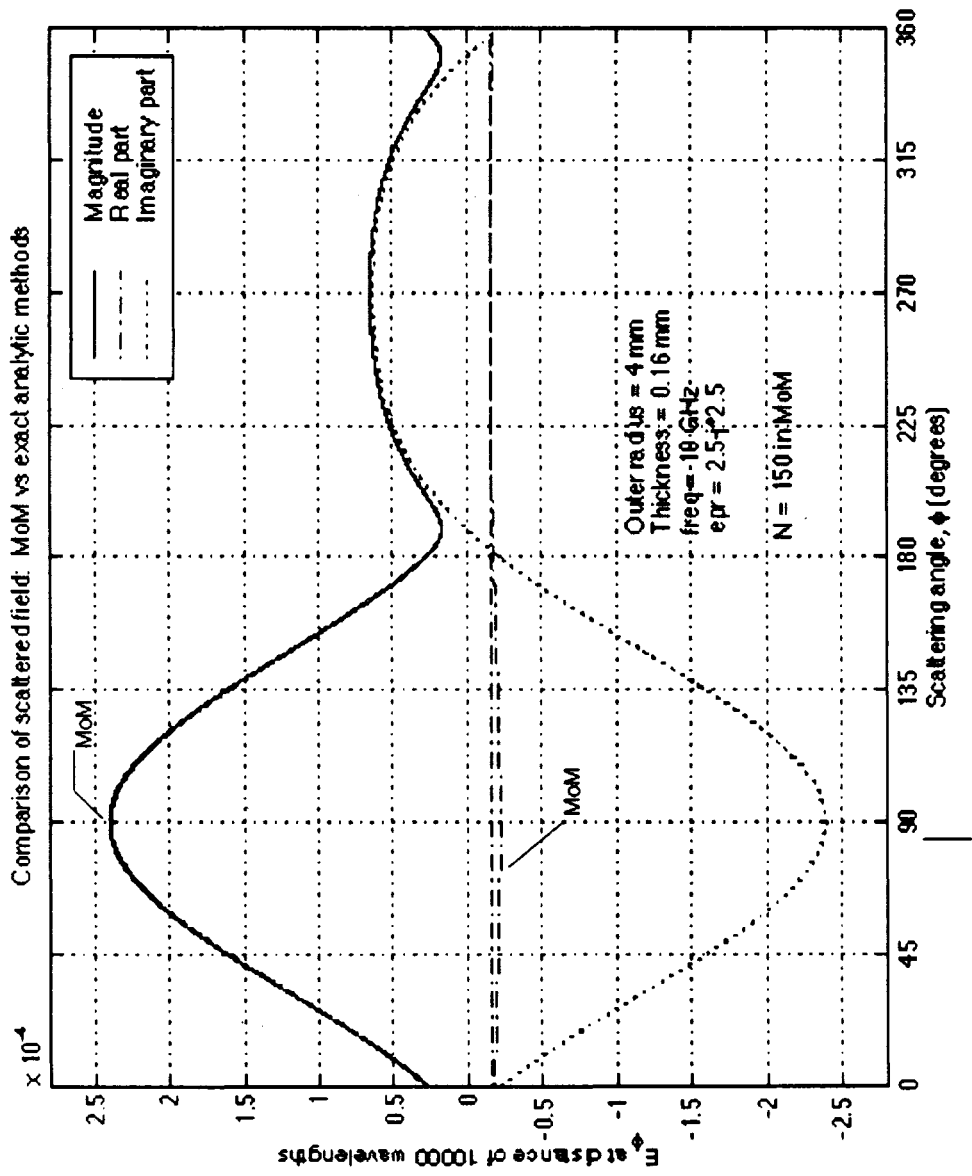


Figure 6.1 MoM Basis Elements for Cylinder Cross Sections

The positive X direction is taken as shown in Figure 6.1 relative to the orientation of the C shape in the lattice.

The derivation of reflected and scattered waves (relative to the lattice) requires more analysis than summarized above because one has to take into account carefully the regions in which the lattice sums as formulated converge (as given by the Graf addition theorem). With these additional derivations, the calculations are straightforward to program. For a lossless dielectric case the result allows a further check. That is, the reflected power plus the transmitted power integrated over all scattering angles should equal the incident power, normalized in this case to unity. For the case of  $\epsilon_r = 2.5$ , the agreement as shown in Figure 6.3 is quite accurate. The individual cylinders in this case scatter quite weakly. Only within about 20 degrees of grazing incidence is the scattering from the array noticeable on this scale. However, if we look at the reflected and transmitted powers only at angles more than 30 degrees from grazing, as shown in Figure 6.4, there is an interesting asymmetry, which presumably shows the effect of the chosen orientation of the C shape.

The same plots for the case  $\epsilon_r = 2.5 - j2.5$  are shown in Figure 6.5 and Figure 6.6. In this case the array absorbs about 4% of the incident power at normal incidence and over 30% at angles within about 5 degrees of grazing. There is also a stronger asymmetry in this case.



$\phi_0 = 90^\circ$  Forward scattering peak  
 Figure 6.2 Field Scattered from a Hollow Dielectric Pipe

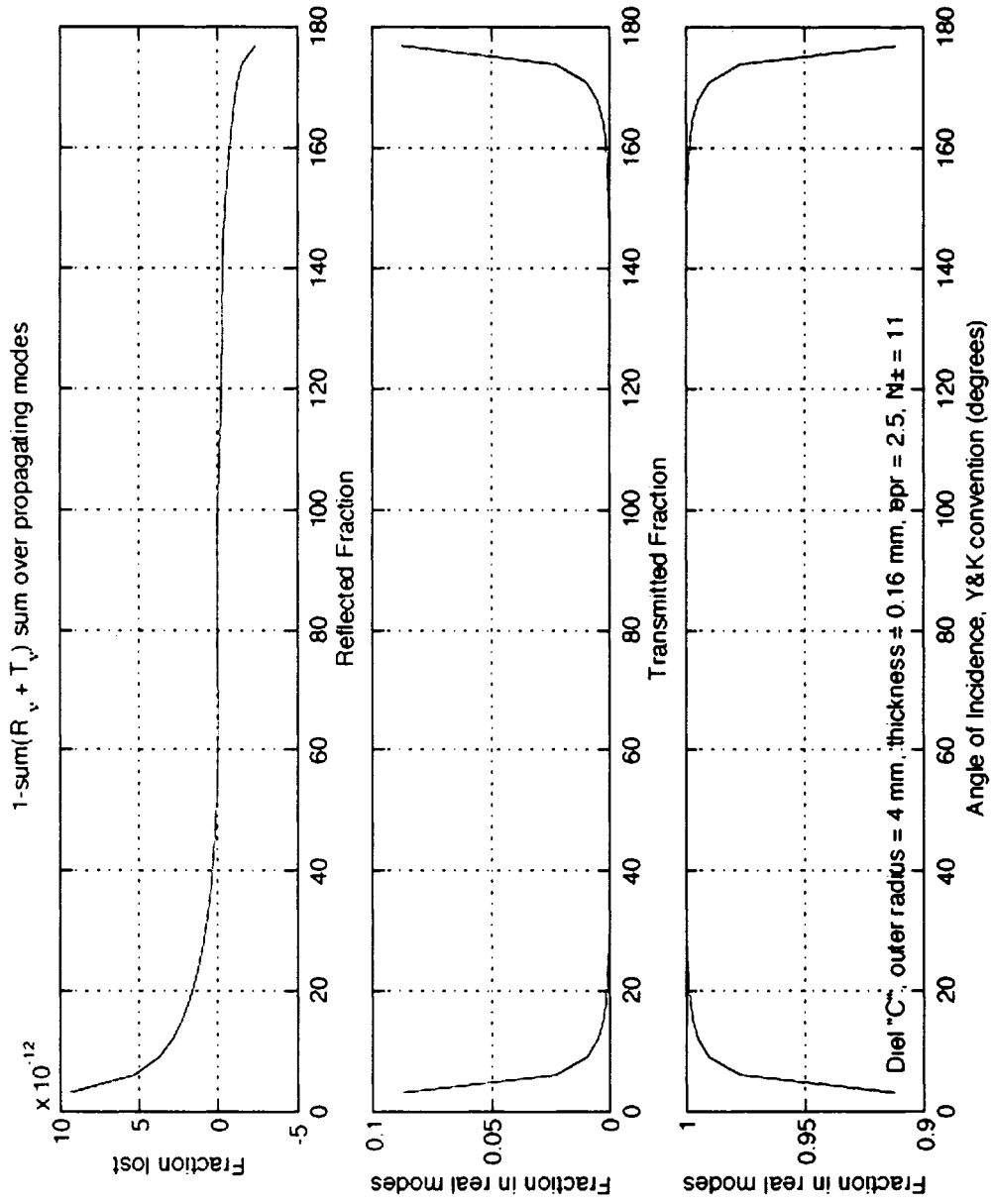


Figure 6.3 Reflected and transmitted power fractions from lossless dielectric C-shaped cylinder

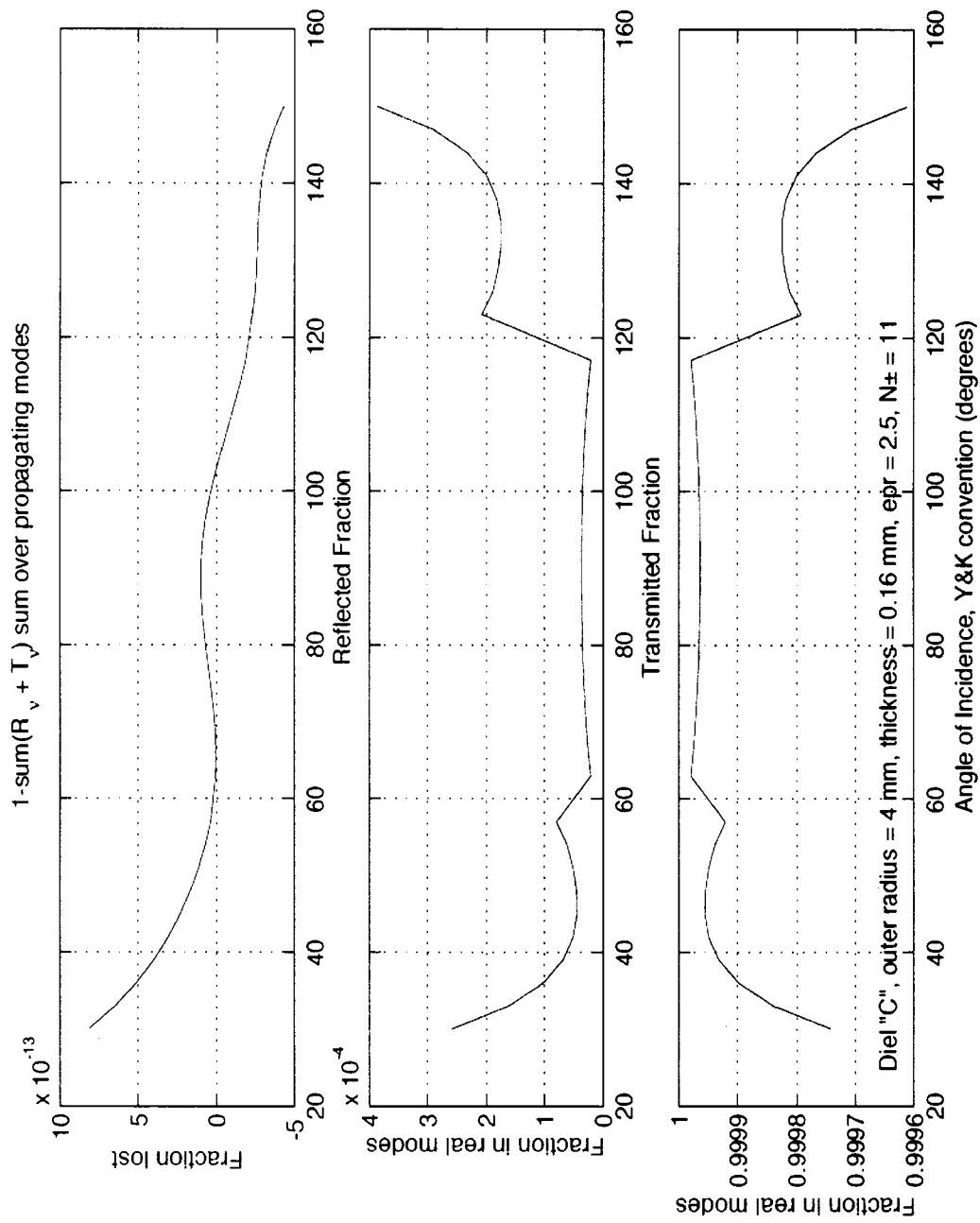


Figure 6.4 Details of reflected and transmitted power fractions from lossless C showing asymmetry

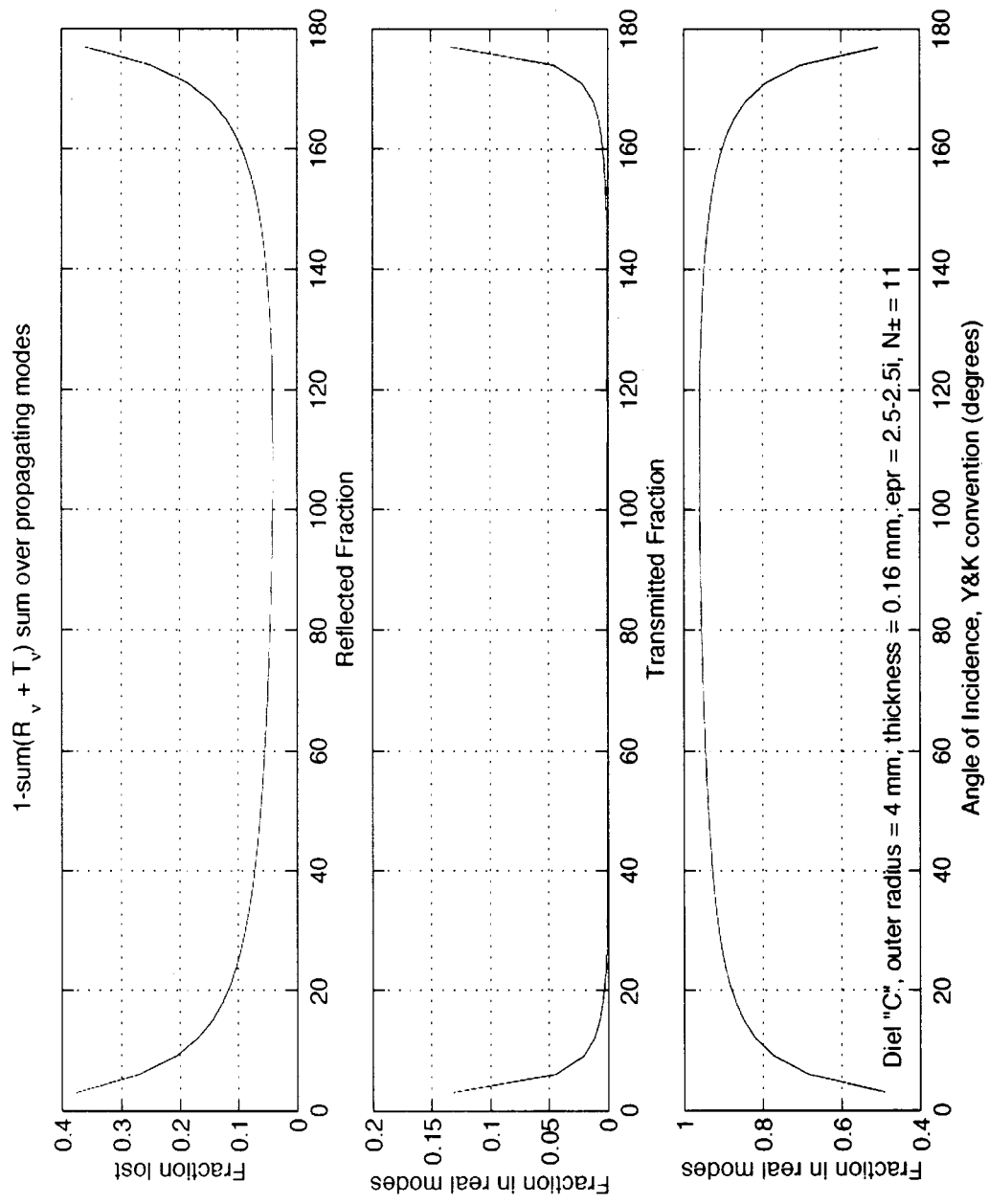


Figure 6.5 Reflected and transmitted power from lossy dielectric C-shaped cylinder

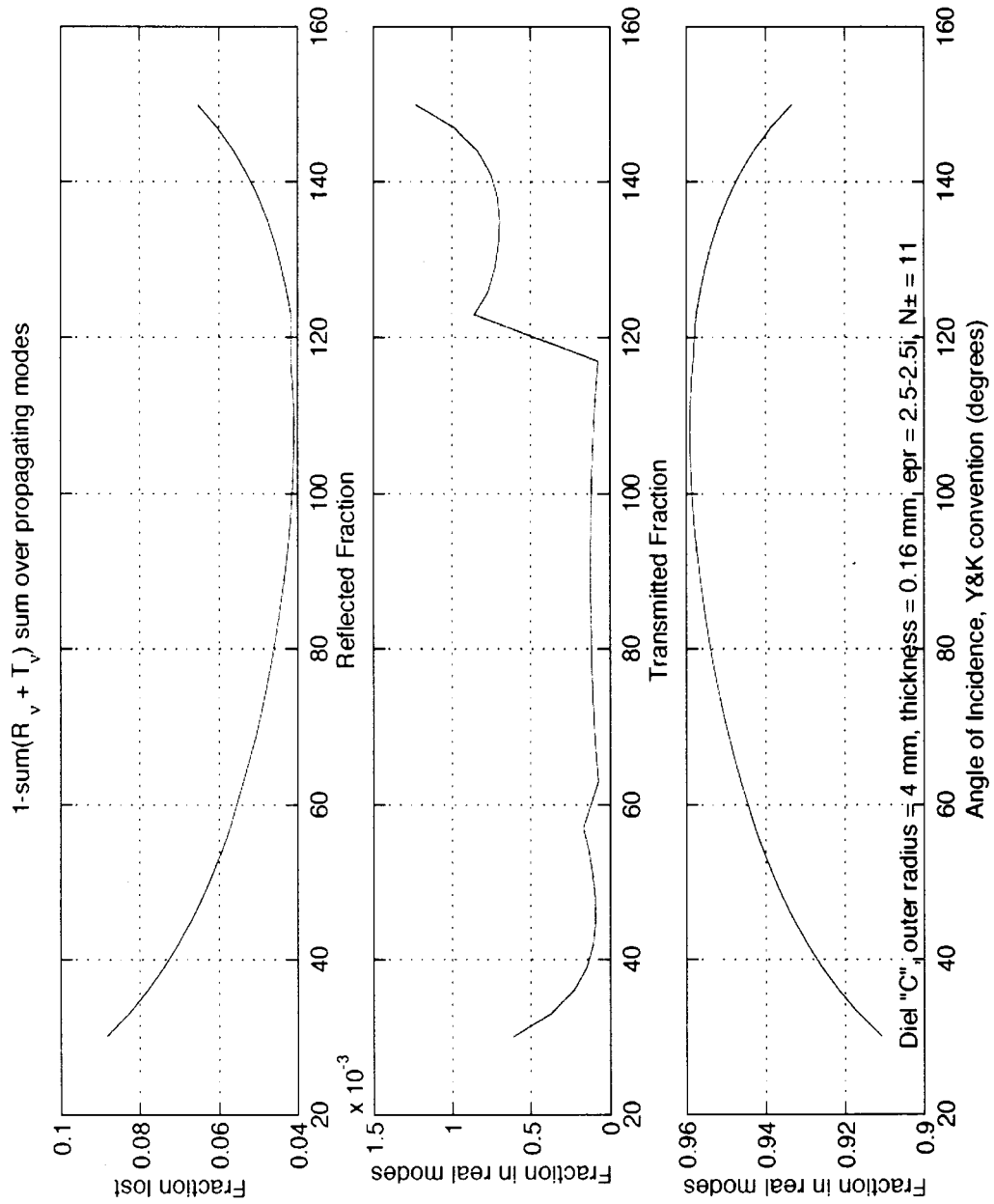


Figure 6.6 Details of reflected and transmitted power fractions from lossy C showing asymmetry and detail of absorbed power

These results were presented in an oral paper (Thomas & Ishimaru 2001) in 2001 and the plots are taken from the computer versions of the transparencies. Many more cases and details are available, but an improved MoM method is needed to handle high dielectric constants, roughly such that  $|\epsilon_r| > 5$ . We started a MoM calculation with a perfectly conducting (PEC) C shape, based on surface currents. The scattered fields showed excellent agreement with the analytic solution in the case of a circular pipe, but the asymmetry introduced by the split ring shape led to a T-matrix that changed considerably as the dimension increased. I feel that this problem deserves a bit more study. The possibility of using global basis functions (i.e., expansion in cylindrical wave harmonics) would seem to provide a more direct approach to solving for the T matrix.

#### 6.4 Notes to Chapter 6

Harrington RF. 1993. *Field Computation by Moment Methods*. Piscataway, New Jersey: IEEE PRESS. 229 pp.

Ishimaru A. 1991. *Electromagnetic Wave Propagation, Radiation, and Scattering*. Englewood Cliffs, New Jersey: Prentice-Hall. 637 pp.

Peterson AFR, Scott L., Mittra R. 1998. *Computational Method for Electromagnetics*. Piscataway, New Jersey: IEEE PRESS. 564 pp.

Thomas JR, Ishimaru A. 2001. Lattice sum approach to scattering by periodic structures. In *PIERS Symposium*. Boston, MA

Yasumoto K, Kushta T. 2000. Efficient Analysis of Scattering by Periodic Arrays of Gyrotropic Cylinders. *Electromagnetic Waves & Electronic Systems* 5: 66-74

Yasumoto K, Yoshitomi K. 1999. Efficient calculation of lattice sums for free-space periodic Green's function. *IEEE Transactions on Antennas and Propagation* 47: 1050-5

## 7. Conclusions and Implications for Future Work

We have shown that a negative index medium (NIM) provides many phenomena that may be called backwards or negative relative to those observed with natural positive index materials. Examples in this thesis are negative refraction, backwards surface waves, backward lateral waves and negative Goos-Hänchen shift. (Veselago 1968) mentions a reversed Doppler shift and a reversed Cerenkov effect. Our approach has been to study the reflected and transmitted waves from a planar layer (finite or filling a half space) of the NIM. This 2-dimensional approach simplifies calculations and analysis in several ways, but the properties of negative refraction and negative-index focusing should extend directly to 3 dimensional pulses and images with some mixing of polarizations.

We investigated how measurements of the reflection and transmission coefficients from a planar slab of any uniform homogeneous medium could be used to determine the permittivity  $\epsilon$  and permeability  $\mu$  of the medium. At least 2 measurements are needed at 2 different angles of incidence. The resulting equations for  $\epsilon$  and  $\mu$  are generally multi-valued with fewer solutions for thinner slabs. Some slabs may yield very little reflection and absorption, and this condition leads to low accuracy in the calculation of  $\epsilon$  and  $\mu$ . Practical measurements utilize a layer or sample of material inside a transmission line. However, good measurements require accurate values for two of the S parameters, say  $S_{11}$  and  $S_{12}$ , which in turn imply that the reflection and transmission coefficients should not be too close to 0 or 1.

We classified the wave types that arise at the boundary between a lossless dielectric (a generalization from a free space) and a medium of arbitrary (but nearly lossless)  $\epsilon$  and  $\mu$ . We presented a diagram that gives the special wave types in terms of regions in  $\text{Re}(\mu) - \text{Re}(\epsilon)$  plane. In addition to the usual (forward) surface wave,

lateral wave, Zenneck wave and evanescent wave, we discovered poles and branch points that correspond to backward surface waves and backward lateral waves. We clarified the meaning of the backward surface waves by looking at how the Poynting vector actually changes sign across the boundary between positive index medium and NIM. We also found an example of the backward lateral wave in the following chapter in a study of 2-dimensional beam waves incident from free space onto a NIM.

Our study of the beam wave packet shows primarily how a beam wave refracts negatively according to Snell's law. The direction of propagation of the packet follows Snell's law for the center frequency of the beam wave. However, the shape of the packet rotates and stretches in a fashion depending on the dispersion of the NIM. If the dispersion of the NIM were too great over the bandwidth of the packet, this coherent description in terms of the center frequency and a refracted distorted packet would break down. The resulting widely distributed wave would no longer form a beam wave packet. Our study derives the results from an analytical asymptotic expansion method and also presents details of an example evaluated exactly by numerical Fourier transform calculations. This example also shows the backward lateral wave emerging from an apparent source that corresponds to a negative Goos-Hänchen shift.

The most detailed part of our study is the investigation in Chapter 5 of negative index focusing by a slab with index  $n_2$  close to  $-1$ . The remarkable and somewhat controversial prediction by (Pendry 2000) that a NIM with  $n_2 = -1$  would provide a perfect focus is what inspired most of the investigations of this thesis. In particular, the question was how do the evanescent waves (relative to a direction of propagation normal to a slab) from a point source get amplified in the NIM slab and then transmitted to yield a perfect image. Part of the answer is that a slab with  $n_2 = -1$  exactly is impossible because any medium other than the ideal vacuum has at least

some small loss associated with it; hence, exact perfect focusing is not possible.

However, evanescent components up to some maximum transverse wave number are amplified by a NIM with  $n_2$  close to  $-1$  and make it possible to achieve better resolution than a large lens of positive index material.

We studied the focusing of a 2-dimensional point source, i.e., a line source, by both an approximate analytical method and a numerical method based on the exact Fourier integral transform solution for a line source incident on a planar slab. We found an approximate expansion of the transmission coefficient in transverse-wave-number  $k_x$  space for a NIM with permittivity  $\epsilon_{2r}$  and permeability  $\mu_{2r}$ . This approximation shows an exponential growth in the transmission coefficient in the evanescent region  $k_x > k_o$  up to a peak value given approximately (for an s-polarized incident wave) by

$$k_p = \sqrt{k_o^2 + (\ln(2/\delta_e)/d_2)^2}$$

where  $d_2$  is the thickness of the slab and  $\delta_e = \epsilon_{2r} + 1$  is the deviation of the permittivity from  $-1$ . This form assumes that the deviation of  $\mu_{2r}$  is of the same order or smaller than  $\epsilon_{2r}$ . With a p-polarized source  $\delta_m = \mu_{2r} + 1$  would replace  $\delta_e$  in the equation for  $k_p$ . This exponential growth balances the exponential evanescent decay. However, at larger values of  $k_x$  the transmission coefficient rolls off exponentially. Hence, the decay of the transmitted spectrum in the NIM focal plane for these high values of  $k_x$  is at twice the rate of the evanescent decay.

Several investigators have arrived at this wave-number space approximation or an equivalent. However, we also calculated the widths of the focal peak by approximate analytic methods and by numerical evaluation of the inverse Fourier transform integrals that give exact solutions. These methods show excellent confirmation of the two approaches and show a qualitative feature of the focusing that has not been noticed (or at least emphasized) by others. As the equation for  $k_p$  (or for

the transverse focal width  $\Delta W$  as given by (5.30)) indicates, a large improvement in focusing over the positive lens limit requires thin slabs. But the focusing in the Z direction, parallel to propagation, has a ridge focus property for thin slabs. That is, in the plane  $x = 0$  the intensity falls off with distance from the exit plane of the NIM slab and the sharpness of this ridge is approximately constant from about half the focal distance out to the theoretical focal distance. Chapter 5, Sections 5.5 and 5.7, provide details and several figures illustrating the ridge focus. For moderately thick slabs, thicker than about 2 wavelengths, the transverse focal width will not be as small, but a peak relative to the Z direction develops around the vicinity of the theoretical focal point and a spot focus develops. This Z-direction focal width at half-magnitude for the  $E_x$  field (or the 6-dB level for power or energy) is almost 2 wavelengths.

We carried out numerical calculations (from exact Fourier transform methods) of all the field components in order to find and demonstrate these focal effects on the Poynting vector and the stored electric and magnetic energy densities. The resulting plots show a variety of interesting patterns, but all show the change from the ridge focusing feature for thin slabs to a spot focus for thicker slabs. Furthermore, the propagation-direction width of the spot is not smaller than the focal width provided by a normal lens, from which evanescent waves do not contribute to the focus.

The last topic of this thesis presented in Chapter 6 is a brief investigation of a possible method for calculating the scattering matrix or the transition matrix of a layer of (general) cylinders. The method was devised by (Yasumoto & Kushta 2000) and we combined a numerical MoM approach with it. We found a reasonable result for nearly transparent cylinders, but did not find a useful beginning point for study of a layer of conductive cylinders, or even more important, for study of multiple layers. Therefore, we did not continue with this topic.

The interesting questions concern what topics should be further investigated based on the work of this thesis. One significant extension that could be done pretty much directly with our numerical Fourier transform methods would be to study the focusing of a 3-dimensional point source, i.e., a dipole. A dipole with moment directed perpendicular to the plane of incidence on the slab can be reduced to a 2-dimensional problem by the symmetry in the azimuthal angle. And this case would have pure TE or TM polarization. Any other orientation will require a 2-dimensional numerical Fourier transform, but the extent in both directions ( $k_x$  and  $k_y$ , for example) would be limited to a maximum of several times  $k_p$ . Possibly, we could find some asymptotic analytic approximations that would provide considerable guidance to the numerical study.

Another interesting extension would be to consider the focusing of a pulse (a beam wave similar to that used in the study in Chapter 4). This problem also would require another dimension of Fourier integration, the frequency-time relation. We need to investigate some wave of this type to find backward surface waves along the NIM layer.

The biggest problem, and perhaps most related to engineering developments, is to find ways to design a metamaterial with any given  $\epsilon$  and  $\mu$  and especially ones with both indexes negative. This has been a classical electromagnetics problem. Powerful fast MoM codes to treat periodic structures of interlinked split rings or small finite helices appear to be the best starting point for this study. The job would presumably be a long one, requiring the building of a library of results for many cases with a study to determine trends. One hint might be useful from our Chapter 4 studies because most resonances seem to be approximated in their dispersion relation by a Drude-Lorentz model. This result seems to arise because a resonance involves a deviation from an equilibrium (resonant) point with a restoration that, near the

resonance, has a linear restoring term corresponding to a classical harmonic oscillator. In this model, the objective is to increase the plasma frequency relative to the electron resonant frequency and the equivalent for the magnetic term.

***Notes to Chapter 7***

Pendry JB. 2000. Negative refraction makes a perfect lens. *Physical Review Letters* 85: 3966-9

Veselago VG. 1968. The electrodynamics of substances with simultaneously negative values of  $\epsilon$  and  $\mu$ . *Soviet Physics USPEKHI* 10: 509-14

Yasumoto K, Kushta T. 2000. Efficient Analysis of Scattering by Periodic Arrays of Gyrotropic Cylinders. *Electromagnetic Waves & Electronic Systems* 5: 66-74

## Bibliography

- Alu, A. and N. Engheta (2006). "Physical insight into the "growing" evanescent fields of double-negative metamaterial lenses using their circuit equivalence." IEEE Transactions on Antennas and Propagation **54**(1): 268-272.
- Born, M. and E. Wolf (1989). Principles of Optics: Electromagnetic Theory of Propagation, Interference and Diffraction of Light. Cambridge, U.K., Cambridge University Press.
- Brillouin, L. (1953). Wave Propagation in Periodic Structures. New York, Dover Publications.
- Brillouin, L. (1960). Wave Propagation and Group Velocity. New York, Academic Press.
- Caloz, C., C.-C. Chang and T. Itoh (2001). "Full-wave verification of the fundamental properties of left-handed materials in waveguide configurations." Journal of Applied Physics **90**(11): 5483-5486.
- Chew, W. C. (1990). Waves and Fields in Inhomogeneous Media. New York, IEEE PRESS (originally Van Nostrand Reinhold).
- Chew, W. C. (2004). "Sommerfeld integrals for left-handed materials." Microwave and Optical Technology Letters **42**(5): 369-73.
- Cummer, S. A. (2003). "Dynamics of causal beam refraction in negative refractive index materials." Applied Physics Letters **82**(13): 2008-2010.
- Cummer, S. A. (2003). "Simulated causal subwavelength focusing by a negative refractive index slab." Applied Physics Letters **82**(10): 1503-1505.
- de Wolf, D. A. (2005). "Transmission of evanescent wave modes through a slab of DNG material." IEEE Transactions on Antennas and Propagation **53**(1): 270-274.
- de Wolf, D. A. (2006). "Transmission of evanescent wave modes through a slab of DNG material II." IEEE Transactions on Antennas and Propagation **54**(1): 263-264.
- Dewar, G. (2005). "A thin wire array and magnetic host structure with  $n < 0$ ." Journal of Applied Physics **97**(10): 10Q101-1 to 10Q101-3.
- Drude, P. (1900). "Zur Electronentheorie der Metalle." Annalen der Physik **1**: 566.

- Eleftheriades, G. V., A. K. Iyer and P. C. Kremer (2002). "Planar negative refractive index media using periodically L-C loaded transmission lines." IEEE Transactions on Microwave Theory and Techniques **50**(12): 2702-2712.
- Engheta, N. and R. W. Ziolkowski (2005). "A positive future for double-negative metamaterials." IEEE Transactions on Microwave Theory and Techniques **53**(4): 1535-1556.
- Felsen, L. B. and N. Marcuvitz (1994). Radiation and Scattering of Waves. New York, IEEE Press.
- Gay-Balmaz, P., C. Maccio and O. J. F. Martin (2002). "Microwire arrays with plasmonic response at microwave frequencies." Applied Physics Letters **81**(15): 2896-2898.
- Grbic, A. and G. V. Eleftheriades (2002). "Experimental verification of backward-wave radiation from a negative refractive index metamaterial." Journal of Applied Physics **92**(10): 5930-5935.
- Grbic, A. and G. V. Eleftheriades (2005). "Practical limitations of subwavelength resolution using negative-refractive-index transmission-line lenses." IEEE Transactions on Antennas and Propagation **53**(10): 3201-3209.
- Gregor, R. B., C. G. Parazzoli, K. Li and M. H. Tanielian (2003). "Origin of dissipative losses in negative index of refraction materials." Applied Physics Letters **82**(14): 2356-2358.
- Gregor, R. B., C. G. Parazzoli, J. A. Nielsen, M. A. Thompson, M. H. Tanielian and D. R. Smith (2005). "Simulation and testing of a graded negative index of refraction lens." Applied Physics Letters **87**(9): -.
- Harrington, R. F. (1993). Field Computation by Moment Methods. Piscataway, New Jersey, IEEE PRESS.
- Huang, X. and W. L. Schaich (2004). "Wave packet propagation into a negative index medium." American Journal of Physics **72**(9): 1232-1240.
- Ishimaru, A. (1991). Electromagnetic Wave Propagation, Radiation, and Scattering. Englewood Cliffs, New Jersey, Prentice-Hall.
- Ishimaru, A., S. Jaruwatanadilok and Y. Kuga (2005). Generalized surface plasmon resonance sensors using metamaterials and negative index materials. Progress in Electromagnetics Research Symposium (PIERS), Elsevier.

- Ishimaru, A., S. W. Lee, Y. Kuga and V. Jandhyala (2003). "Generalized constitutive relations for metamaterials based on the quasi-static Lorentz theory." IEEE Transactions on Antennas and Propagation **51**(10): 2550-2557.
- Ishimaru, A. and J. R. Thomas (2002). Transmission and focusing properties of a slab of negative refractive index. IEEE AP-S/URSI Symposium. Dallas, Texas.
- Ishimaru, A. and J. R. Thomas (2004). Waves in layered negative index media excited by space-time localized source. URSI International Symposium on Electromagnetics Theory, Proceedings, Pisa, Italy.
- Ishimaru, A., J. R. Thomas and S. Jaruwatanadilok (2005). "Electromagnetic waves over half-space metamaterials of arbitrary permittivity and permeability." IEEE Transactions on Antennas and Propagation **53**(3): 915-921.
- Jia, H. and K. Yasumoto (2004). "S-Matrix Solution of Electromagnetic Scattering from Periodic Arrays of Metallic Cylinders with Arbitrary Cross Section." IEEE Antennas and Wireless Propagation Letters **3**(1): 41-44.
- Joannopoulos, J. D., R. D. Meade and J. N. Winn (1995). Photonic Crystals. Princeton, New Jersey, Princeton University Press.
- Kolinko, P. and D. R. Smith (2003). "Numerical study of electromagnetic waves interacting with negative index materials." Optics Express **11**(7): 640-648.
- Lakhtakia, A. (2004). "Positive and negative Goos-Hanchen shifts and negative phase-velocity mediums (alias left-handed materials)." AEU-International Journal of Electronics and Communications **58**(3): 229-231.
- Leskova, T. A., A. A. Maradudin and I. Simonsen (2003). Coherent scattering of an electromagnetic wave from, and its transmission through, a slab of left-handed medium with a randomly rough illuminated surface. Surface Scattering and Diffraction III.
- Loschialpo, P. F., D. L. Smith, D. W. Forester, F. J. Rachford and J. Schelleng (2003). "Electromagnetic waves focused by a negative-index planar lens." Physical Review E **67**(2): -.
- Lu, J., T. M. Grzegorzcyk, B.-l. Wu, J. Pacheco, M. Chen and J. A. Kong (2005). "Effect of poles on subwavelength focusing by an LHM slab." Microwave and Optical Technology Letters **45** (1): 49-53.
- Lu, W. T., J. B. Sokoloff and S. Sridhar (2004). "Refraction of electromagnetic energy for wave packets incident on a negative-index medium is always negative." Physical Review E **69**(2): -.

- Luo, C. Y., S. G. Johnson, J. D. Joannopoulos and J. B. Pendry (2003). "Subwavelength imaging in photonic crystals." Physical Review B **68**(4): -.
- McCall, M. W., A. Lakhtakia and W. S. Weiglhofer (2002). "The negative index of refraction demystified." European Journal of Physics **23**: 353-359.
- Melville, D. O. S. and R. J. Blaikie (2005). "Super-resolution imaging through a planar silver layer." Optics Express **13**(6): 2127-2134.
- Nieto-Vesperinas, M. (2004). "Problem of image superresolution with a negative-refractive-index slab." Journal of the Optical Society of America a-Optics Image Science and Vision **21**(4): 491-498.
- Parazzoli, C. G., R. B. Greigor, K. Li, B. E. C. Koltenbah and M. Tanielian (2003). "Experimental verification and simulation of negative index of refraction using Snell's law." Physical Review Letters **90**(10): -.
- Parazzoli, C. G., R. B. Greigor, J. A. Nielsen, M. A. Thompson, K. Li, A. M. Vetter, M. H. Tanielian and D. C. Vier (2004). "Performance of a negative index of refraction lens." Applied Physics Letters **84**(17): 3232-3234.
- Parazzoli, C. G., B. E. C. Koltenbah, R. B. Greigor, T. A. Lam and M. H. Tanielian (2006). "Eikonal equation for a general anisotropic or chiral medium: application to a negative-graded index-of-refraction lens with an anisotropic material." Journal of the Optical Society of America B-Optical Physics **23**(3): 439-450.
- Pendry, J. B. (2000). "Negative refraction makes a perfect lens." Physical Review Letters **85**(18): 3966-3969.
- Pendry, J. B., A. J. Holden, D. J. Robbins and W. J. Stewart (1999). "Magnetism from conductors and enhanced nonlinear phenomena." IEEE Transactions on Microwave Theory and Techniques **47**(11): 2075-2084.
- Pendry, J. B., A. J. Holden, W. J. Stewart and I. Youngs (1996). "Extremely low frequency plasmons in metallic mesostructures." Physical Review Letters **76**(25): 4773-4776.
- Pendry, J. B. and S. A. Ramakrishna (2003). "Focusing light using negative refraction." Journal of Physics-Condensed Matter **15**(37): 6345-6364.
- Pendry, J. B. and D. R. Smith (2003). "Comment on "Wave refraction in negative-index media: Always positive and very inhomogeneous"." Physical Review Letters **90**(2): 029703-1.

- Peterson, A. F. R., Scott L. and R. Mittra (1998). Computational Method for Electromagnetics. Piscataway, New Jersey, IEEE PRESS.
- Podolskiy, V. A. and E. E. Narimanov (2005). "Near-sighted superlens." Optics Letters **30**(1): 75-77.
- Qing, D. K. and G. Chen (2004). "Goos-Hanchen shifts at the interfaces between left- and right-handed media." Optics Letters **29**(8): 872-874.
- Ruppin, R. (2000). "Surface polaritons of a left-handed medium." Physics Letters A **277**: 61-64.
- Simovski, C. R. and B. Sauviac (2004). "Toward creating isotropic microwave composites with negative refraction." Radio Science **39**(2): -.
- Smith, D. R., W. J. Padilla, D. C. Vier, S. C. Nemat-Nasser and S. Schultz (2000). "Composite medium with simultaneously negative permeability and permittivity." Physical Review Letters **84**(18): 4184-4187.
- Smith, D. R., D. Schurig and J. B. Pendry (2002). "Negative refraction of modulated electromagnetic waves." Applied Physics Letters **81**(15): 2713-2715.
- Smith, D. R., D. Schurig, M. Rosenbluth, S. Schultz, S. A. Ramakrishna and J. B. Pendry (2003). "Limitations on subdiffraction imaging with a negative refractive index slab." Applied Physics Letters **82**(10): 1506-1508.
- Stratton, J. A. (1941). Electromagnetic Theory. New York, McGraw-Hill.
- Thomas, J. R. and A. Ishimaru (2001). Lattice sum approach to scattering by periodic structures. PIERS Symposium. Boston, MA.
- Thomas, J. R. and A. Ishimaru (2002). Transmission properties of material with relative permittivity and permeability close to -1. Complex Mediums III: Beyond Linear Isotropic Dielectrics, Seattle, WA, United States, SPIE--The International Society for Optical Engineering.
- Thomas, J. R. and A. Ishimaru (2005). "Wave packet incident on negative-index media." IEEE Transactions on Antennas and Propagation **53**(5): 1591-1599.
- Valanju, P. M., R. M. Walser and A. P. Valanju (2002). "Wave refraction in negative-index media: Always positive and very inhomogeneous." Physical Review Letters **88**(18): 187401.
- Veselago, V. G. (1968). "The electrodynamics of substances with simultaneously negative values of  $\epsilon$  and  $\mu$ ." Soviet Physics USPEKHI **10**(4): 509-514.

- Yannopapas, V. and A. Moroz (2005). "Negative refractive index metamaterials from inherently non-magnetic materials for deep infrared to terahertz frequency ranges." Journal of Physics-Condensed Matter **17**(25): 3717-3734.
- Yasumoto, K. and T. Kushta (2000). "Efficient Analysis of Scattering by Periodic Arrays of Gyrotropic Cylinders." Electromagnetic Waves & Electronic Systems **5**(1): 66-74.
- Yasumoto, K. and K. Yoshitomi (1999). "Efficient calculation of lattice sums for free-space periodic Green's function." IEEE Transactions on Antennas and Propagation **47**(6): 1050-1055.
- Zhang, Z. M. and K. Park (2004). "On the group front and group velocity in a dispersive medium upon refraction from a nondispersive medium." Journal of Heat Transfer-Transactions of the Asme **126**(2): 244-249.
- Ziolkowski, R. W. (2003). "Design, fabrication, and testing of double negative metamaterials." Ieee Transactions on Antennas and Propagation **51**(7): 1516-1529.
- Ziolkowski, R. W. and N. Engheta (2003). "Metamaterial special issue introduction." IEEE Transactions on Antennas and Propagation **51**(10): 2546-2549.
- Ziolkowski, R. W. and E. Heyman (2001). "Wave propagation in media having negative permittivity and permeability." Physical Review E **64**(5): 056625-1-056625-15.

## Appendix A: Derivation of Equation (2.7)

Recall that we defined subsidiary quantities for the ratio of wave impedances

$$g = \frac{Z_2}{Z_1}$$

and for the angle (in radians)

$$\psi = k_{z2}d = k_o d \sqrt{n_2^2 - \sin^2 \theta_1}.$$

Then equations (2.1) and (2.2) are written more compactly in terms of  $g$  and  $\tan \psi$  as

$$R = \frac{j(g - 1/g) \tan \psi}{D}$$

$$T = \frac{2 \sec \psi}{D}$$

where the denominator  $D$  is given by

$$D = 2 + j(g + 1/g) \tan \psi.$$

Then with the use of the trigonometric identity  $\sec^2 \psi - \tan^2 \psi = 1$ ,

$$\begin{aligned} D^2(1 + R^2 - T^2) &= 4 + 4j(g + 1/g) \tan \psi - (g + 1/g)^2 \tan^2 \psi - (g - 1/g)^2 \tan^2 \psi - 4 \sec^2 \psi \\ &= -4 \tan^2 \psi + 4j(g + 1/g) \tan \psi - 2(g^2 + 1/g^2) \tan^2 \psi \\ &= 4j(g + 1/g) \tan \psi - 2(g + 1/g)^2 \tan^2 \psi. \end{aligned}$$

Then,

$$\begin{aligned} 1 + R^2 - T^2 + 2R &= \\ &= \frac{4j(g + 1/g) \tan \psi - 2(g + 1/g)^2 \tan^2 \psi + 2j(g - 1/g) \tan \psi [2 + j(g + 1/g) \tan \psi]}{D^2} \\ &= \frac{4jg \tan \psi - 2(g + 1/g)^2 \tan^2 \psi - 2(g^2 - 1/g^2) \tan^2 \psi}{D^2} \\ &= \frac{4[jg \tan \psi - (g^2 + 1) \tan^2 \psi]}{D^2}. \end{aligned}$$

Similarly,

$$\begin{aligned}
 1 + R^2 - T^2 - 2R &= \\
 &= \frac{4j(g + 1/g) \tan \psi - 2(g + 1/g)^2 \tan^2 \psi - 2j(g - 1/g) \tan \psi [2 + j(g + 1/g) \tan \psi]}{D^2} \\
 &= \frac{4j(1/g) \tan \psi - 4 \tan^2 \psi - (4/g^2) \tan^2 \psi}{D^2} \\
 &= \frac{4[j(1/g) \tan \psi - (1 + 1/g^2) \tan^2 \psi]}{D^2} = \frac{4[jg \tan \psi - (g^2 + 1) \tan^2 \psi]}{g^2 D^2}.
 \end{aligned}$$

Thus,

$$\frac{1 + R^2 - T^2 + 2R}{1 + R^2 - T^2 - 2R} = \frac{(1 + R)^2 - T^2}{(1 - R)^2 - T^2} = g^2.$$

## Appendix B: Derivations for Section 5.3

**To derive bounds on the integrand in (5.22)**

$$E_2(x) = \frac{-4}{\pi\delta_e^2} \int_{k_p}^{\infty} \exp(-2d_2\sqrt{k_x^2 - k_o^2}) \operatorname{Re}(e^{-jk_x x}) dk_x$$

We would like to find bounds on  $\sqrt{k_x^2 - k_o^2}$  relative to  $k_x$  so that we can evaluate an elementary integral of the form  $\int e^{ak_x} dk_x$ . It is evident that  $\sqrt{k_x^2 - k_o^2} < k_x$  over the range of the integrand, and where we imply positive square roots in these cases that are all real. To get a lower bound on  $\sqrt{k_x^2 - k_o^2}$  we would like a form such that  $\sqrt{k_x^2 - k_o^2} \geq k_x - \text{constant}$ . With some algebra we found that this constant should be  $\Delta = k_p - \sqrt{k_p^2 - k_o^2}$ .

Proof:

$$\begin{aligned} (k_x - k_p)^2 &= k_x^2 - 2k_x k_p + k_p^2 \geq 0 \\ 2k_x k_p &\leq k_x^2 + k_p^2 \end{aligned}$$

Change sign and the order of the inequality changes.

$$-2k_x k_p \geq -(k_x^2 + k_p^2)$$

Multiply by a positive constant  $k_o^2$  and add a positive term  $k_x^2 k_p^2 + k_o^4$  to both sides.

$$k_x^2 k_p^2 - 2k_o^2 k_x k_p + k_o^4 \geq k_x^2 k_p^2 - (k_x^2 + k_p^2)k_o^2 + k_o^4$$

The additive term is large enough to change what was an order relationship between negative quantities into one between positive quantities. Factor each side.

$$(k_x k_p - k_o^2)^2 \geq (k_x^2 - k_o^2)(k_p^2 - k_o^2)$$

We are considering an interval where  $k_x \geq k_p > k_o > 0$ . So both factors on the right side are positive as is the quantity being squared on the right hand side. So we can take positive square roots and maintain the order relationship as

$$k_x k_p - k_o^2 \geq \sqrt{k_x^2 - k_o^2} \sqrt{k_p^2 - k_o^2}$$

Multiply both sides by  $-2$  and the order relationship reverses.

$$-2k_x k_p + 2k_o^2 \leq -2\sqrt{k_x^2 - k_o^2} \sqrt{k_p^2 - k_o^2}$$

Add  $k_x^2 + k_p^2 - 2k_o^2$  to both sides and the order relationship stays the same.

$$k_x^2 - 2k_x k_p + k_p^2 \leq k_x^2 - k_o^2 + k_p^2 - k_o^2 - 2\sqrt{k_x^2 - k_o^2} \sqrt{k_p^2 - k_o^2}$$

Remember that we are using positive square roots. Both sides of this inequality can now be written as squared terms.

$$(k_x - k_p)^2 \leq \left( \sqrt{k_x^2 - k_o^2} - \sqrt{k_p^2 - k_o^2} \right)^2$$

To maintain the order relationship we take the positive square root of each side. Since  $k_x \geq k_p$  this procedure gives

$$k_x - k_p \leq \sqrt{k_x^2 - k_o^2} - \sqrt{k_p^2 - k_o^2}.$$

Or

$$k_x - k_p + \sqrt{k_p^2 - k_o^2} \leq \sqrt{k_x^2 - k_o^2}$$

Furthermore, it is evident that this inequality becomes an equality at the end of the interval where  $k_x = k_p$ . Therefore  $\Delta = k_p - \sqrt{k_p^2 - k_o^2}$  is the smallest quantity (best bound) that can be subtracted from  $k_x$  and maintain  $\sqrt{k_x^2 - k_o^2} \geq k_x - \text{constant}$  over the interval of integration.

**To show that  $e(x)$  given by (5.25) is not greater than 1 in absolute value**

$$e(x) = \frac{4\Theta^2 \cos X - 2X\Theta \sin X}{4\Theta^2 + X^2}$$

where  $\Theta$  is a positive quantity and  $X$  is non negative. So all quantities in  $e(x)$  are real and we want to show

$$|4\Theta^2 \cos X - 2X\Theta \sin X| \leq 4\Theta^2 + X^2$$

To get rid of dealing with the absolute value, this lemma will be true if the same inequality applies to the square of each side.

$$16\Theta^4 \cos^2 X - 16X\Theta^3 \cos X \sin X + 4X^2\Theta^2 \sin^2 X \leq 16\Theta^4 + 8X^2\Theta^2 + X^4$$

Subtract  $16\Theta^4 + 4X^2\Theta^2$  from both sides and the order relationship is preserved. Then apply the identity  $\sin^2 X + \cos^2 X = 1$  in the form  $-1 + \cos^2 X = -\sin^2 X$  for the  $\Theta^4$  term and in the form  $-1 + \sin^2 X = -\cos^2 X$  for the  $X^2\Theta^2$  term.

$$-16\Theta^4 \sin^2 X - 16X\Theta^3 \cos X \sin X - 4X^2\Theta^2 \cos^2 X \leq 4X^2\Theta^2 + X^4$$

Now we recognize the left-hand side as the negative of a square quantity much like the one of the previous equation; that is

$$-(4\Theta^2 \sin X + 2X\Theta \cos X)^2 \leq 4X^2\Theta^2 + X^4$$

Here we have a quantity that can be only zero or negative on the left and a quantity that can be only zero or positive on the right, so this inequality must hold. Reverse the steps for a proof. Furthermore, the inequality is strict unless  $X = 0$ .

## VITA

John Rhodes Thomas was born February 4, 1936, in Seattle, Washington. He graduated from Roosevelt High School, Seattle, in 1953 and obtained the Bachelor of Science degree in Physics with honors from the California Institute of Technology, Pasadena, California in 1957. He carried out graduate studies at the California Institute of Technology, at the University of California and the University of Washington during various intervals from 1957 to 1973.

He worked as an engineer for The Boeing Company, Seattle, from June 1958 until retirement in July of 1995. Within those years he had leaves of absence and part-time arrangements to do graduate work mentioned above. During his last 22 years with Boeing he worked mostly on Electromagnetic Pulse Hardening of many types of airborne weapon systems.

He regained graduate student status in the Electrical Engineering Department at the University of Washington, Seattle, Washington in winter 1997. He earned the M.S.E.E. degree in June 1998 and the Doctor of Philosophy in electromagnetics in June 2006. His current interest is the study of materials created artificially to provide arbitrary, including negative, dielectric constant and magnetic permeability.

### List of publications

#### Journals

- John Rhodes Thomas and Akira Ishimaru, "Wave packet incident on negative-index media," *IEEE Transactions on Antennas and Propagation*, vol. 53, no. 5, pp. 1591-1599, May 2005.

- Akira Ishimaru, John Rhodes Thomas, and Serm Sak Jaruwatanadilok, "Electromagnetic waves over half-space metamaterials of arbitrary permittivity and permeability," *IEEE Transactions on Antennas and Propagation* vol. 53, no. 3, pp. 915-921, Mar. 2005.
- John Rhodes Thomas and Akira Ishimaru, "Transmission properties of material with relative permittivity and permeability close to  $-1$ ," *Proceedings of SPIE*, vol 4806, pp 167-175, 2002.

### Conference papers

- Akira Ishimaru and John R. Thomas, "Waves in layered negative index media excited by space-time localized source," URSI International Symposium on Electromagnetics Theory, *Proceedings* (3 pages), Pisa, Italy., 2004.
- J. R. Thomas and A. Ishimaru. "Transmission properties of material with relative permittivity and permeability close to  $-1$ ," *Complex Mediums III: Beyond Linear Isotropic Dielectrics*, Seattle, WA, United States, SPIE--The International Society for Optical Engineering, 2002
- J. R. Thomas and A. Ishimaru (2001). "Lattice sum approach to scattering by periodic structures," PIERS Symposium, Boston, MA., 2001